

DISSERTATION

# Application of single-molecule microscopy techniques to characterize the T cell receptor on the membrane of T cells

verfasst von

**DI Benedikt Klaus Rossboth, BSc**

01227692

Ausgeführt zum Zwecke der Erlangung des akademischen Grades eines  
Doktors der technischen Wissenschaften

Unter der Leitung von

**Univ. Prof. Dr. Gerhard J. Schütz**

E134

Institut für Angewandte Physik

eingereicht an der Technischen Universität Wien

Fakultät für Physik



Die approbierte gedruckte Originalversion dieser Dissertation ist an der TU Wien Bibliothek verfügbar.  
The approved original version of this doctoral thesis is available in print at TU Wien Bibliothek.

# Kurzfassung

Die Immunologie als Lehre der Abwehrmechanismen eines lebenden Organismus gegen infektiöse Erreger stellt seit der ersten Impfung im Jahr 1796 einen der zentralsten Punkte der modernen Medizin dar. Gerade in Zeiten der immer weiter verbreiteten Impfkritik kann diese Wichtigkeit in unserer Gesellschaft nicht genug betont werden.

Im Gegensatz zu wirbellosen Tieren, verfügen Vertebrata über ein adaptives Immunsystem, ein höchst ausgefeiltes Abwehrsystem, welches sich durch ständige Weiterentwicklung auszeichnet. Dieses adaptive Abwehrsystem basiert auf einigen unterschiedlichen, hoch spezialisierten Zellarten. Unter diesen spielen die T-Zellen die Rolle des Initiators, indem sie Fremdkörper, welche von anderen Zellen präsentiert werden, erkennen, und eine Immunabwehrreaktion in Gang setzen können. Die als „fremd“ erkannte Struktur (das *Antigen*) wird von einem Oberflächenprotein der T-Zelle, dem T-Zell-Rezeptor, erkannt. Dieser stellt somit einen zentralen Punkt in der Abwehrreaktion dar.

Trotz der bedeutenden Rolle des T-Zell-Rezeptors in der Immunabwehr sind nach wie vor einige zentrale Fragen in Bezug auf dessen funktionale und physikalische Charakteristika ungelöst. Eigenschaften des Rezeptors wie dessen Mobilität in der Zellmembran, dessen Aufbau aus mehreren Untereinheiten, oder die Anordnung der Rezeptoren in der Zellmembran, beeinflussen mit hoher Wahrscheinlichkeit seine Funktion im Zuge der Antigen-Erkennung.

In dieser Arbeit widmete ich mich den genannten physikalischen Eigenschaften des T-Zell-Rezeptors, um zu einem besseren Verständnis der von der T-Zelle induzierten Immunabwehrreaktion beizutragen. Hierzu verwendete ich hochauflösende Lichtmikroskopie-Verfahren: Ich untersuchte die Mobilität des T-Zell-Rezeptors mittels der Verfolgung einzelner Rezeptoren in der Zellmembran. Außerdem untersuchte ich die Stöchiometrie der T-Zell-Rezeptor-Komplexe mittels der Einzelmolekül-Methoden TOCCSL, FRET, sowie PA/FCS. Die Verteilung der Rezeptoren in der Zellmembran von T-Zellen konnte durch Einzelmolekül-Lokalisations-Mikroskopie festgestellt, und mittels STED-Mikroskopie verifiziert werden. Durch ausführliche Simulationsstudien wurden die Ergebnisse weiter unterstützt.

Die Resultate dieser Studien zeigen, dass die T-Zell-Rezeptoren vergleichsweise langsam in der Zellmembran diffundieren, aus einer TCR $\beta$  und zwei CD3 $\epsilon$  Untereinheiten aufgebaut sind, und im Wesentlichen zufällig verteilt in der Zellmembran vorliegen. Aufbauend auf diesen Ergebnissen wird ein neues 2-Phasen-Modell vorgeschlagen, welches versucht, die hohe Geschwindigkeit der T-Zellen bei der Identifikation von Fremdkörpern zu erklären.



Die approbierte gedruckte Originalversion dieser Dissertation ist an der TU Wien Bibliothek verfügbar.  
The approved original version of this doctoral thesis is available in print at TU Wien Bibliothek.

# Abstract

The health of any organism critically depends on the correct and efficient functionality of its immune system. Malfunctioning might manifest itself in illnesses such as AIDS, Type 1 Diabetes Mellitus or Multiple Sclerosis. A central constituent of the adaptive immune system are T cells, which are able to distinguish foreign from endogenous substances and can thereby initiate a defensive response on potential threats. The surface protein responsible for the recognition of those threats is the T cell receptor (TCR), which bears the uttermost important role within the adaptive immune response. Nevertheless, the knowledge on many of the receptor's characteristics, which might be pivotal for its function, is still limited and published results are highly controversial.

Within this work, I used novel fluorescence microscopy techniques to strengthen, extend and tackle the current ideas on three specific topics: i) the TCR's mobility within the plasma membrane, ii) the oligomerization state of the TCR/CD3 complex, and iii) the receptors' spatial distribution within the plasma membrane.

Single-molecule tracking and Fluorescence Correlation Spectroscopy were used to measure the diffusion of the TCR. Large discrepancies on this aspect found in the literature motivated these approaches. The TCR/CD3 complex was found to diffuse slowly within the plasma membrane. While about a third of all complexes showed basically no mobility at all, the remaining two thirds were measured to have a diffusion coefficient of  $D \sim 0.045 \mu\text{m}^2/\text{s}$ .

Next, I used FRET, TOCCSL, and PA/FCS to investigate the subunit composition of the TCR/CD3 complex, as there is still a lack of studies tackling this question by using minimally invasive methods. By this, I could confirm the widely favoured model of one TCR $\beta$  and two CD3 $\epsilon$  subunits.

A T cell activation model based on the receptors' spatial distribution within the membrane was recently proposed. The experiments, on which this model is based, were realized using single-molecule localization microscopy (SMLM) methods. In recent years, however, it was shown that these methods come along with major challenges in quantitation. To this end, we used SMLM combined with a novel analysis approach to re-evaluate the receptors' spatial distribution. Additional STED experiments strengthened our results by offering a complementary approach. Both experimental approaches were further supplemented with extensive Monte Carlo simulations. The model of TCR nanoclustering, however, could not be verified by either label-density variation SMLM or STED. Both methods showed that significant nanoclustering of the TCRs is highly unlikely. Based on those findings, a new model for T cell activation is proposed: A two-phase search approach, in which the time for a T cell to identify an agonistic antigen within a majority of endogenous ones is decreased by several orders of magnitude, while preserving the typical high specificity of the TCR.



Die approbierte gedruckte Originalversion dieser Dissertation ist an der TU Wien Bibliothek verfügbar.  
The approved original version of this doctoral thesis is available in print at TU Wien Bibliothek.

# Danksagung

Zuallererst möchte ich mich bei Univ. Prof. Dipl.-Ing. Dr. techn. Gerhard Schütz bedanken. Herzlichen Dank, Gerhard, für dein Vertrauen und die Freiheiten bei der Durchführung der Arbeit. Die zahlreichen, weitreichenden Diskussionen, nicht nur in Bezug zur Forschung, waren ausgesprochen hilfreich und eröffneten mir oftmals neue Sichtweisen.

Vielen Dank an alle beteiligten Projektpartner, allen voran Assoz. Prof. Johannes Huppa, PhD. Ganz herzlich möchte ich mich auch bei Flo, Renè und Iago für die tatkräftige Unterstützung bei der Isolation der Mauszellen und der umfangreichen Proteinsynthese bedanken. Mein weiterer Dank gilt Prof. Dr. Stefan Hell für die Ermöglichung der Festigung unserer Ergebnisse durch STED Messungen. Vielen Dank an Haisen für die tatkräftige Unterstützung bei der Durchführung dieser wichtigen Experimente.

Ein riesiges Dankeschön möchte ich an die gesamte Biophysik-Gruppe richten. Ich habe die wunderschöne Zeit sehr genossen und mich bei euch immer sehr wohl gefühlt. Ganz besonders möchte ich mich bei euch bedanken, Mario und Flo, nicht nur für eure praxisrelevanten Ratschläge und Tipps, die mir die tägliche Arbeit im Labor erleichtert haben, sondern auch für die zahlreichen Diskussionen und die Inspiration, die ihr immer für mich seid. Vielen Dank auch an dich, Elena, für deine großartigen Bemühungen, den Wahnsinn des Laboralltags immer am Laufen zu halten. Auch bei dir, Andi, möchte ich mich bedanken. Nicht nur für die vielen unterhaltsamen Momente, sondern auch für deine Einstellung zum Doktorat – du warst mir damit oft ein großes Vorbild und ich bin froh, dass wir dieses Stück unseres Weges zumindest kurz gemeinsam bestritten haben.

Ich möchte diese Gelegenheit außerdem nutzen, um mich bei meiner wunderbaren Familie zu bedanken.

Mama und Papa, ihr habt mir die gesamte Studienzeit finanziell ermöglicht und dabei niemals Druck ausgeübt. Euer ständiges Interesse und euer Bemühen, meine Studieninhalte zu verstehen, schätze ich sehr. Die Kurzbesuche Zuhause, bei euch, lassen mich jedes Mal wertvolle Kraft tanken. Vielen Dank für all das.

Danke, Katharina, Theresa und Manuel, für die vielen entspannenden, ablenkenden Mittagspausen, Kaffeehausbesuche und gemeinsamen Abende.

Theresa und Christian, ihr seid mein so wichtiger Ruhepol – nicht nur zwischen den Weinreben - und ich genieße die Besuche bei euch jedes Mal sehr.

Danke Jonathan und Vincent, ihr bringt immer Sonnenschein.

Zuletzt möchte ich mich bei dir, Sophia, bedanken, für die großartige Unterstützung in so vielfacher und unterschiedlicher Form. Vor allem aber für die Geduld und die Motivation, die du mir auf jeden Moment perfekt abgestimmt entgegenbringen kannst. Ich freue mich auf unsere weitere Reise, und bin dankbar, so einen wundervollen Menschen an meiner Seite zu haben.



Die approbierte gedruckte Originalversion dieser Dissertation ist an der TU Wien Bibliothek verfügbar.  
The approved original version of this doctoral thesis is available in print at TU Wien Bibliothek.



# Eidesstaatliche Erklärung

Ich erkläre an Eides statt, dass ich die vorliegende Arbeit selbstständig verfasst, andere als die angegebenen Quellen/Hilfsmittel nicht benutzt, und die den benutzten Quellen wörtlich und inhaltlich entnommenen Stellen als solche kenntlich gemacht habe. Das in TISS der TU Wien hochgeladene Textdokument ist mit der vorliegenden Dissertation ident.

.....  
Ort, Datum

.....  
Unterschrift

# Table of Content

|   |           |
|---|-----------|
| Kurzfassung .....   | i         |
| Abstract.....   | iii       |
| Danksagung .....  | v         |
| Eidesstaatliche Erklärung .....                                   | vii       |
| Table of Content .....  | viii      |
| <b>Chapter 0 – Preface .....</b>                                  | <b>1</b>  |
| 0.1. Research Questions and Rationale.....                        | 2         |
| 0.2. Structure of This Work .....                                 | 2         |
| 0.3. Published Articles & Contributions.....                      | 3         |
| <b>Chapter 1 – Introduction .....</b>                             | <b>7</b>  |
| 1.1. Single-Molecule Microscopy Techniques.....                   | 8         |
| 1.1.1. History and Basics of Fluorescence Microscopy .....        | 8         |
| 1.1.2. Single-Molecule Microscopy.....                            | 12        |
| 1.1.3. Single-Molecule Methods in Biology.....                    | 21        |
| 1.2. Immunology and T Cell Biology .....                          | 27        |
| 1.2.1. The Immune System and the Role of T Cells.....             | 27        |
| 1.2.2. The T Cell Receptor Complex.....                           | 31        |
| 1.2.3. Mechanism of T Cell Activation.....                        | 34        |
| <b>Chapter 2 - Materials &amp; Methods.....</b>                   | <b>45</b> |
| 2.1. Cell Biology and Sample Preparation.....                     | 46        |
| 2.1.1. Cell Culture, DNA Constructs, Antibodies and Reagents..... | 46        |
| 2.1.2. Isolation and Transduction of T Cells.....                 | 46        |
| 2.1.3. Protein and Label Preparations .....                       | 47        |
| 2.1.4. Sample Preparation Procedures .....                        | 51        |
| 2.2. Microscopy Imaging .....                                     | 52        |
| 2.2.1. Microscopy Systems.....                                    | 52        |
| 2.2.2. Imaging Protocols.....                                     | 53        |

|  |            |
|--|------------|
| 2.2.3. Image Analysis .....  | 55         |
| 2.2.4. Simulations.....  | 59         |
| <b>Chapter 3 – Results &amp; Discussion.....</b>                     | <b>63</b>  |
| Part A: TCR/CD3 Complex Mobility .....                               | 66         |
| A1) Single-Molecule Tracking of TCR/CD3 Complexes.....               | 66         |
| A2) Discussion .....   | 69         |
| Part B: TCR/CD3 Complex Stoichiometry .....                          | 71         |
| B1) TOCCSL Analysis of TCR/CD3 Complexes.....                        | 71         |
| B2) Two-Color TOCCSL and Single-Molecule FRET Analysis.....          | 73         |
| B3) PA/FCS Analysis of TCR/CD3 Complexes .....                       | 75         |
| B4) Bulk FRET Analysis of TCR/CD3 Complexes .....                    | 77         |
| B5) FRET Analysis of pMHC Oligomerization .....                      | 80         |
| B6) Discussion.....  | 83         |
| Part C: Spatial Distribution of TCR/CD3 Complexes.....               | 87         |
| C1) A System to Analyze Single Fluorophore Blinking.....             | 87         |
| C2) Parameters to Describe Fluorophore Blinking.....                 | 91         |
| C3) Influence of Experimental Settings on Fluorophore Blinking ..... | 92         |
| C4) Ripley’s K Analysis I: Effects of Blinking .....                 | 94         |
| C5) Label-density-variation SMLM of TCR/CD3 Subunits.....            | 96         |
| C6) Ripley’s K Analysis II: T Cell Context.....                      | 105        |
| C7) STED Imaging of TCR/CD3 Subunits .....                           | 109        |
| C8) Estimations of Sensitivity for Cluster Detection.....            | 113        |
| C9) Discussion .....   | 118        |
| C10) A Two-Phase Activation Model for T Cells.....                   | 124        |
| <b>Chapter 4 – Appendix .....</b>                                    | <b>131</b> |
| Abbreviations.....   | 132        |
| List of Figures .....  | 135        |
| Equations.....   | 138        |
| List of Tables .....   | 139        |
| Curriculum Vitae.....  | 140        |
| References.....  | 142        |



Die approbierte gedruckte Originalversion dieser Dissertation ist an der TU Wien Bibliothek verfügbar.  
The approved original version of this doctoral thesis is available in print at TU Wien Bibliothek.

---

# Chapter 0

# Preface

## 0.1. Research Questions and Rationale

Within the presented thesis, the spatiotemporal nanoscale properties of the T cell receptor (TCR) in the T cell plasma membrane are characterized. This is realized by the application of high-end single-molecule fluorescence microscopy.

The TCR is the key membrane receptor on T cells, which plays a major role in initiating an immune reaction via the recognition of foreign pathogens. The function of the TCR is likely influenced by its diffusion characteristics, its oligomeric state and its spatial organization. Several studies aiming to characterize these properties have been performed during the last decades, however, contradicting results have been reported: diffusion coefficients varying by two orders of magnitude, or oligomeric conformations ranging from solely monomers to a mixture of oligomers up to higher order structures.

This thesis aims to use state-of-the-art fluorescence microscopy methods to contribute to the clarification of these inconsistencies. Therefore, the following research questions are addressed:

**A: How does the TCR diffuse within the membrane of T cells?**

**B: What is the oligomerization state of the TCR?**

**C: How is the TCR spatially distributed on the membrane of T cells?**

## 0.2. Structure of This Work

The presented thesis sticks to a classic structure of a research article, starting with an introduction outlining the relevant background in high detail. This includes a comprehensive introduction to light microscopy from the basics of the method and its history to the more advanced methodological aspects relevant for this thesis. In addition to that, an introduction to T cell biology, and the TCR is provided. The Materials and Methods section provides a comprehensive description of the conducted experiments as well as the analyses required for addressing the research questions. This should allow and motivate for easy reproducibility.

The structure of the Results section mirrors the three properties of the TCR studied within this thesis. Besides the results of the experiments and the corresponding analyses, also problems and workarounds encountered during this work are highlighted.

The results are discussed regarding the adaptation of the current status of both T cell biology paradigms and the use of super-resolution microscopy methods.

Additionally, further topics which could not be tackled within this thesis are discussed in order to provide an outlook for potential further studies.

### 0.3. Published Articles & Contributions

The content of this thesis has been published in the following peer-reviewed articles:

- Brameshuber M, Kellner F, Rosboth B, Ta H, Alge K, Sevcsik E, Göhring J, Axmann M, Baumgart F, Gascoigne NRJ, Davis SJ, Stockinger H, Schütz GJ, Huppa JB. **Monomeric TCRs drive T cell antigen recognition.** *Nature Immunology* **19**(5), 487-96 (2018) [2].  
Personal contribution: Performance of TOCCSL and FRET experiments, assistance in PA/FCS experiments and data analyses.
- Rosboth B, Arnold A, Ta H, Platzer R, Kellner F, Huppa JB, Brameshuber M, Baumgart F, Schütz GJ. **TCRs are randomly distributed on the plasma membrane of resting antigen-experienced T cells.** *Nature Immunology* **19**(8), 821-7 (2018) [3].  
Personal contribution: performance of the majority of single-molecule localization microscopy experiments and STED experiments; data analyses; performance of simulations and assistance in manuscript writing.
- Baumgart F, Arnold A, Rosboth B, Brameshuber M, Schütz GJ. **What we talk about when we talk about nanoclusters.** *Methods and Applications in Fluorescence* **7**(013001), (2018) [4].  
Personal contribution: Writing of sections of the article.

Parts of the content of this thesis are currently under peer-review:

- Rosboth B, Platzer R, Baumgart F, Stockinger H, Schütz GJ, Huppa JB, Brameshuber M. **Deriving fluorophore blinking properties for comprehensive PALM analysis.** *In preparation*.  
Personal contribution: Performance of PALM experiments on single fluorophores, data analyses, preparation of manuscript draft.

Additionally, I contributed to the following articles, which will not be included within this thesis:

- Plochberger B, Axmann M, Röhrl C, Weghuber J, Brameshuber M, Rossboth B, Mayr S, Ros R, Bittman R, Stangl H, Schütz GJ. **Direct observation of cargo transfer from HDL particles to the plasma membrane.** *Atherosclerosis* **277**, 53-9 (2018) [5].  
Personal contribution: Performance of experiments and corresponding data analyses.
- Chien M-H, Brameshuber M, Rossboth B, Schütz GJ, Schmid S. **Single-molecule optical absorption imaging by nanomechanical photothermal sensing.** *Proc. Natl. Acad. Sci. USA* **115**(44), 11150-5 (2018) [6].  
Personal contribution: Performance of single-molecule data analyses.
- Zelger P, Kaser K, Rossboth B, Velas L, Schütz GJ, Jesacher A. **Three-dimensional localization microscopy using deep learning.** *Optics Express* **26**(25), 33166-79 (2018) [7].  
Personal contribution: Submission of ideas to the article.

Amongst all co-authors of these articles, I want to particularly highlight the following contributors:

- **Rene Platzer** and **Florian Kellner** for support in protein expression and purification as well as design and creation of the mSav-bio-PS-CFP2 experimental system
- **Carina Viehböck** for support with TCR/CD3 tracking experiments
- **Mario Brameshuber** for support with TOCCSL and FRET experiments
- **Florian Baumgart** for support with SMLM experiments
- **Haisen Ta** for support with PA/FCS and STED experiments
- **Andreas Arnold** for support with simulations for sensitivity estimations





Die approbierte gedruckte Originalversion dieser Dissertation ist an der TU Wien Bibliothek verfügbar.  
The approved original version of this doctoral thesis is available in print at TU Wien Bibliothek.



Die approbierte gedruckte Originalversion dieser Dissertation ist an der TU Wien Bibliothek verfügbar.  
The approved original version of this doctoral thesis is available in print at TU Wien Bibliothek.

---

# Chapter 1

# Introduction

## 1.1. Single-Molecule Microscopy Techniques

### 1.1.1. History and Basics of Fluorescence Microscopy

Basic microscopy methods date back to the start of the 17<sup>th</sup> century, when the Dutch glass-maker Hans Janssen together with his son Zacharias, and at approximately the same time the well-known Galileo Galilei combined concave and convex lenses to achieve optical magnification [8]. By the correction of achromatic aberrations, Huygens improved those minimalistic microscopy systems, and facilitated magnifications up to 50 $\times$  [9]. The ability to grind almost spherical lenses enabled Leeuwenhoek to realize magnifications up to 270 $\times$  by using a single lens [10]. Nevertheless, the physical principles underlying microscopes were not described until the 19<sup>th</sup> century when Ernst Abbe derived a detailed theory to explain the optics of microscopy systems, and set the basis for a first microscope, which was limited in resolution exclusively by the physics of light [11]. Such a microscope was soon after realized in the laboratories of Carl Zeiss.

Modern systems can still be well described by a two-lens analogy: the objective, which creates an image of the focused object in infinite distance, and the tube lens, which focuses the parallel rays to the image plane. The magnification is solely determined by the ratio of the two focal lengths of the objective and the tube lens (**Figure 1A**) [12]. In addition to the magnification, another fundamental property of an objective lens is the numerical aperture (NA) given by

$$NA = n \sin \alpha \quad (1)$$

where  $n$  is the refractive index of the embedding medium and  $\alpha$  is the half opening angle of the objective. This dimensionless number describes the maximum angle at which emitted light can be captured by the objective [12]. In order to reach optimal detection efficiency in single-molecule microscopy, usually a high NA (1.4 – 1.7) is desired. When light traverses from a medium with a high refractive index (e.g. glass:  $n \sim 1.46$ ), into a medium with a lower refractive index (e.g. air:  $n = 1$ ), it is refracted away from the normal. The relationship is described by *Snell's law* of refraction

$$n_1 \sin \theta_1 = n_2 \sin \theta_2 \quad (2)$$

where  $n_1$  and  $n_2$  are the two refractive indices, and  $\theta_1$  and  $\theta_2$  are the angles for the incident and the emerging light beams to the normal. Parts of the light originating from the sample on the glass, thus, will not be captured by the objective (**Figure 1B, right**). Removing this mismatch of refractive indices by adding oil (with  $n \sim 1.5$ ) to

the gap, eliminates refraction at the oil-glass interface, and maximizes the amount of light entering the objective (**Figure 1B, left**).

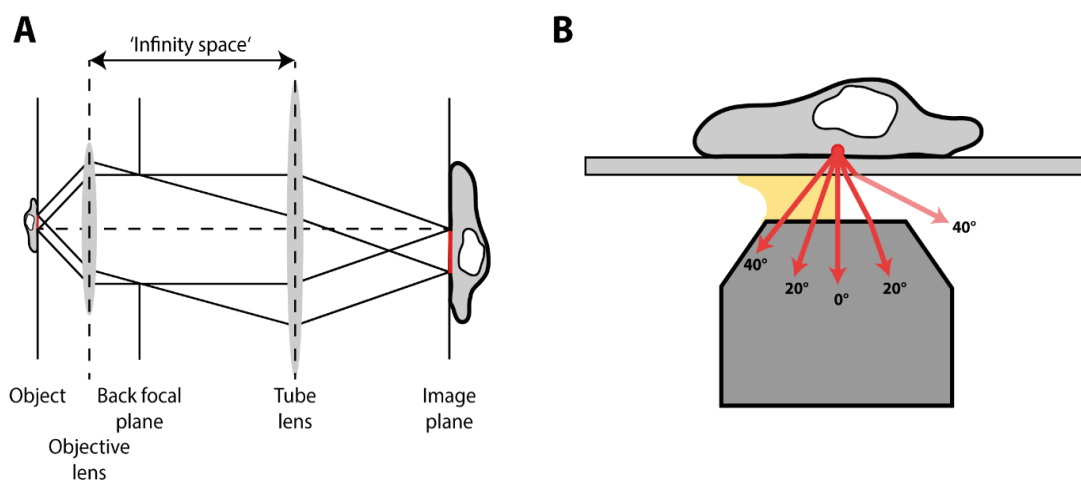


**Figure 1. Principle of a Microscope and of Immersion Oil**

**A)** Image creation in a two-lens analogy: Light of an object in focus is parallel after the first lens (objective). The following tube lens generates an image, which is magnified and inverted at the image plane. **B)** The use of immersion oil adjusts the refractive index of the interspace between the objective and the cover glass, thus enabling the capturing of light rays emitted under an increased angle. In this example, the use of immersion oil enables capturing of light rays emitted at  $40^\circ$ , while they are lost without the oil.

The introduction of fluorescence to the field of microscopy opened up manifold opportunities for biologists. Fluorescence - the emission of light upon excitation - was first described even before the invention of microscopes. In the 16<sup>th</sup> century, fluorescence of the infusion from different tree species was reported [13]. In 1825 the term '*fluorescence*' was introduced by the Irish physicist George Stokes, who named the process based on a mineral called fluorite ( $\text{CaF}_2$ ) [14, 15]. Fluorescence occurs, when an excited orbital electron ( $e^-$ ) relaxes back to its ground state ( $S_0$ ) with a concurrent emission of a photon. The fluorophore - a molecule with the ability to fluoresce - needs to be brought into an excited state ( $S_1$ ) by absorption of a photon. This state is occupied for hundreds of picoseconds up to nanoseconds, after which the molecule relaxes to  $S_0$  by emitting a photon ('*fluorescence*'). Another way to reach  $S_0$  is by intersystem crossing to a triplet state ( $T_1$ ). Relaxation from  $T_1$  happens either via phosphorescence or without radiation. Due to the enhanced lifetime of  $T_1$ , chemical reactions can occur and change the molecular species altogether, which mostly eliminates the fluorescent character ('*photobleaching*'). The process of fluorescence is frequently depicted with *Jablonski diagrams* [16] (**Figure 2A**). Before the  $S_1 \rightarrow S_0$  transition, intramolecular vibrations decrease the energy of the emitted photon, thus increasing the emission wavelength. This *Stoke's shift* [15] is essential

for the use of fluorescence in microscopy, as it enables the separation of emission and excitation light by wavelength-selective (dichroic) mirrors (**Figure 2B**).

In most applications of fluorescence microscopy, emission is not measured at the level of single photons, but the integrated number of emitted photons during illumination is recorded. Two properties of a fluorescent molecule determine the number of photons emitted per time interval [17]: Firstly, the absorption cross section of the dye molecule, which is a measure of the probability of a fluorophore in  $S_0$  to absorb a photon. Secondly, the quantum yield, which describes the probability of an excited fluorophore to relax to  $S_0$  by emission of a photon, or in other words the average number of emitted photons per absorbed photon. In combination with the stochastic character of the lifetime of  $S_1$ , one single fluorophore gives rise to varying numbers of photons emitted during identical exposure times. This distribution of emitted photons, i.e. the brightness, of single fluorophores was described to follow a log-normal distribution [18, 19].

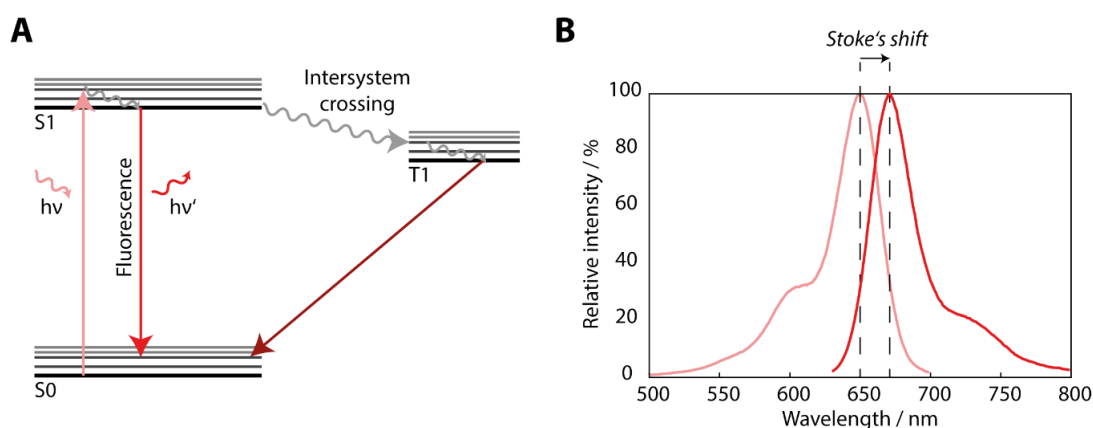


**Figure 2. Jablonski Diagram and Stoke's Shift**

**A)** Fluorescence can be depicted by the Jablonski diagram. The fluorophore is excited from  $S_0$  to  $S_1$ , where it loses energy due to vibrational relaxation and either enters a triplet state ( $T_1$ ) by intersystem crossing or relaxes back to  $S_0$  by emitting a photon. **B)** The loss of energy in  $S_1$  is responsible for a shift towards higher wavelengths of the emitted photon. This process is called Stoke's shift.

In 1941, antibodies showing highly specific binding to their cognate protein were combined with fluorescent dyes for the first time [20]. This approach called immunohistochemistry is widely used in nowadays' research and clinical routine to label and study specific protein species. The used organic dyes show a conjugated structure, resulting in an extended  $e^-$  orbital, with an  $e^-$  donor on the one end and an  $e^-$  acceptor on the other end. The size of this orbital usually scales with the color of the dye: Largely extended orbitals coincide with a spectrum shifted towards high wavelengths [21]. A rigid structure of the dye prevents loss of energy due to rotation

and increases the quantum yield [22]. Dyes can be classified depending on their chromophore - the part of the dye responsible for the color. Well-known representatives include the classes of cyanines (AlexaFluor647, AF647) and rhodamines (AlexaFluor488, AF488), which are shown in **Figure 3A and B**, respectively [23]. An alternative to immunohistochemistry arose when Green Fluorescent Protein (GFP) was extracted from the jellyfish species *Aequorea Victoria* [24] in the mid-20<sup>th</sup> century. Genetic fusion to other non-fluorescent proteins allowed for highly specific and direct observations, without the need for external labeling [25]. This finding was awarded with the Nobel Prize in Chemistry in 2008. Several derivatives of GFP, such as yellow fluorescent protein and cyan fluorescent protein (CFP), have been artificially generated since then [26, 27]. Studies to shift the emission towards even higher emission wavelengths, however, have not been successful until the extraction of another fluorescent protein (FP) from sea anemone *Discosoma Striata*, termed DsRed [28]. Since then, several new FPs have been extracted successfully from *Anthozoa* species, and further derivatives have been developed, giving rise to a wide palette of FPs differing in structure, color and oligomerization [29].

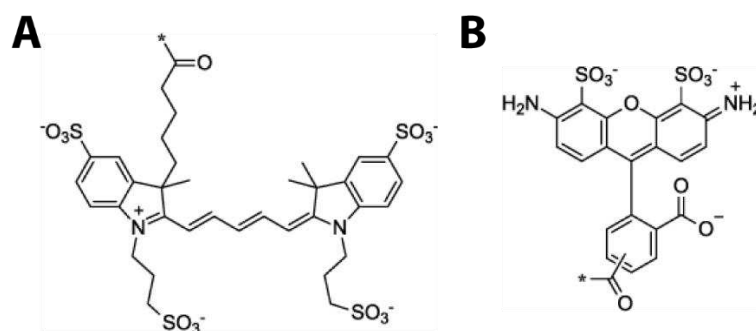


**Figure 3. Major Groups of Organic Dyes**

**A)** A large class of organic dyes is represented by derivatives of cyanine. Shown here is the structure of AlexaFluor647 (AF647). The asterisk marks the position where additional groups are placed, enabling conjugation via NHS-ester or maleimide chemistry. **B)** Another widespread group of organic dyes is based on rhodamines. AlexaFluor488 (AF488) represents one example for such an organic dye. The asterisk marks the position where additional groups are placed, enabling conjugation via NHS-ester or maleimide chemistry.

While labeling with antibodies or antibody-derivatives, such as Fabs [30] or single-chain variable fragments (scFv) [31], does not require any genetic modification of the cell, the fusion of FPs to other proteins has to be realized on a genetic level. Organic dyes are usually much smaller (molecular weight of AF647: 1.2 kDa) than FPs (molecular weight of GFP: 27 kDa), however, antibodies (150 kDa), Fabs (~80 kDa) or scFv (~20 kDa) combined with dyes usually add up to at least the size of FPs.

## 1.1.2. Single-Molecule Microscopy

It was the dream of many biologists to be able to resolve the action of individual biomolecules. These direct single-molecule observations allow for determination of not only averaged values, but the full underlying parameter distributions, potentially revealing heterogeneities or small subsets. Additionally, most biological processes are not synchronized at the molecular level. Hence, when measuring on a population level, effects might be masked or at least biased by temporal fluctuations. Investigating each single molecule on its own removes the need for synchronization [32, 33].

Experiments on single molecules were declared unfeasible by Erwin Schrödinger in 1952 [34, 35]. Nevertheless, in 1976, Hirschfeld was able to demonstrate the detection of a single antibody labeled with 80 – 100 fluorophores using fluorescence microscopy [36, 37]. In the late 1980s, improvements in the sensitivity of the optical systems enabled the detection of even single fluorophores [38-40], and studies of single molecules in biological contexts followed only several years later [41-44]. Even commercial single-molecule microscopy systems are available nowadays, which allow for studying highly distinct parameters ranging from molecular interactions or conformational dynamics to molecular motion or reaction kinetics.

In this work, single-molecule fluorescence microscopy was applied to probe the mobility, the oligomeric state and the spatial distribution of the TCR/CD3 complex in the membrane of T cells.

For the transition from ensemble to single-molecule measurements optimization of contrast is of utmost interest. One experimental approach to facilitate an increase in contrast is called Total Internal Reflection Fluorescence (TIRF) [45, 46]. It is based on *Snell's law* (**Equation (2)**), which determines an angle of incidence - the critical angle ( $\theta_1 = \theta_c$ ) – above which all light is reflected ( $\theta_2 = 90^\circ$ ) at the transition surface between a high ( $n_1$ ) and a low ( $n_2$ ) refractive index medium:

$$\theta_c = \sin^{-1}\left(\frac{n_2}{n_1}\right) \quad (3)$$

In addition to this total reflection, an evanescent wave travelling along the surface is generated.



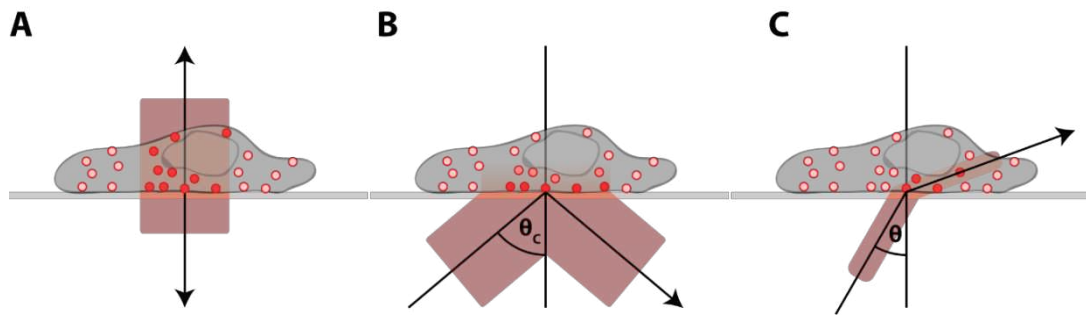


**Figure 4. TIRF and HILO Illumination for Contrast Increase**

**A)** In common non-TIRF illumination, fluorophores localized all along the optical axis are excited. **B)** Contrast is increased by tilting the excitation beam, thus achieving TIRF illumination. Only a layer of  $\sim 150$  nm above the coverslip is illuminated, and the background is efficiently suppressed. **C)** In HILO illumination, only a thin sheet of light is illuminated by tilting the excitation beam.

The amplitude of this evanescent light decreases exponentially with distance, with typical decay lengths of  $\sim 150$  nm. Objective-based TIRF configuration can be implemented by tilting the excitation beam, i.e. shifting the beam away from the center of the objective at the back focal plane [47] (**Figure 4A and B**).

A different way to facilitate an increase in contrast is to condense the measurement to a thin plane, as realized in light-sheet microscopy. Light-sheet illumination enables the selective illumination of a sample plane, thus suppressing background from non-illuminated regions and increasing the contrast. Highly-inclined and laminated optical sheet (HILO) microscopy [48] represents one rather easy way to achieve light-sheet illumination. Here, the illumination beam is, similar to TIRF, shifted in the back focal plane, but to an extent, where total reflection is not yet occurring. The beam gets refracted at the interface between the glass slide and the sample, and enters the sample at an inclined plane, which is selectively illuminated (**Figure 4C**). In contrast to TIRF, HILO enables increased contrast also in apical areas of the sample.

While representing adequate tools for increasing contrast, TIRF or HILO illumination cannot increase the resolving power of the microscope *per se*. The wave characteristics of light provide a physical limitation to the resolution of a light microscope. A first description of the wave nature of light including diffraction was given by Huygens [49]. He stated, that each point of a moving wave front itself can be seen as a source for a new wave front. This *Huygen's principle* is shown in **Figure 5A**.

The most relevant geometry in the case of microscopy is a circular aperture. According to Fraunhofer, the diffraction pattern of an aperture is the square of the Fourier Transform of the aperture itself [50]. Mathematical derivations result in the following description for the intensity:

$$I = I_0 \left[ \frac{2J_1(x)}{x} \right]^2 \quad (4)$$

with  $x = \frac{2\pi}{\lambda} r \sin \theta$ , where  $\lambda$  is the wavelength,  $r$  is the radius of the aperture and  $\theta$  is the angle to the point of observation, and  $J_1$  is the Bessel function of the first order (for geometric definitions see **Figure 5A**). The resulting intensity pattern is called *Airy disc* [51] and shows the first minimum at  $x = 3.83$ . The first minimum of a circular aperture, e.g. a lens with focal distance  $f$ , and small  $\theta \approx \tan \theta \approx \sin \theta = \frac{R}{f}$  is thus given by:

$$R = \frac{3.83 \lambda f}{2r \pi} = 1.22 \frac{\lambda f}{2r} \quad (5)$$

showing dependence on the wavelength  $\lambda$ , the radius of the aperture  $r$ , and the focal distance of the objective  $f$ . For imaging through a microscope, the sample is in focus of the objective, so that each point source within the sample yields a parallel beam after the objective lens. The radius of this parallel light beam is given for an immersion objective by its exit pupil diameter  $r \approx f \cdot NA$ . For the position of the first minimum of the above-mentioned *Airy disc* on the imaging screen this results in:

$$R = 0.61 \frac{\lambda}{NA} = res_{min} \quad (6)$$

The *Rayleigh criterion* defines resolution as the distance, for which the maximum of the intensity distribution obtained from one point emitter is located at the first minimum of the intensity distribution of a second point emitter [52] (**Figure 5B**). This yields the limitation for resolution identical to **Equation (6)** and to an approximate resolution of  $\sim 200$  nm for blue light ( $\lambda = 488$  nm) and a high NA (1.4) objective.

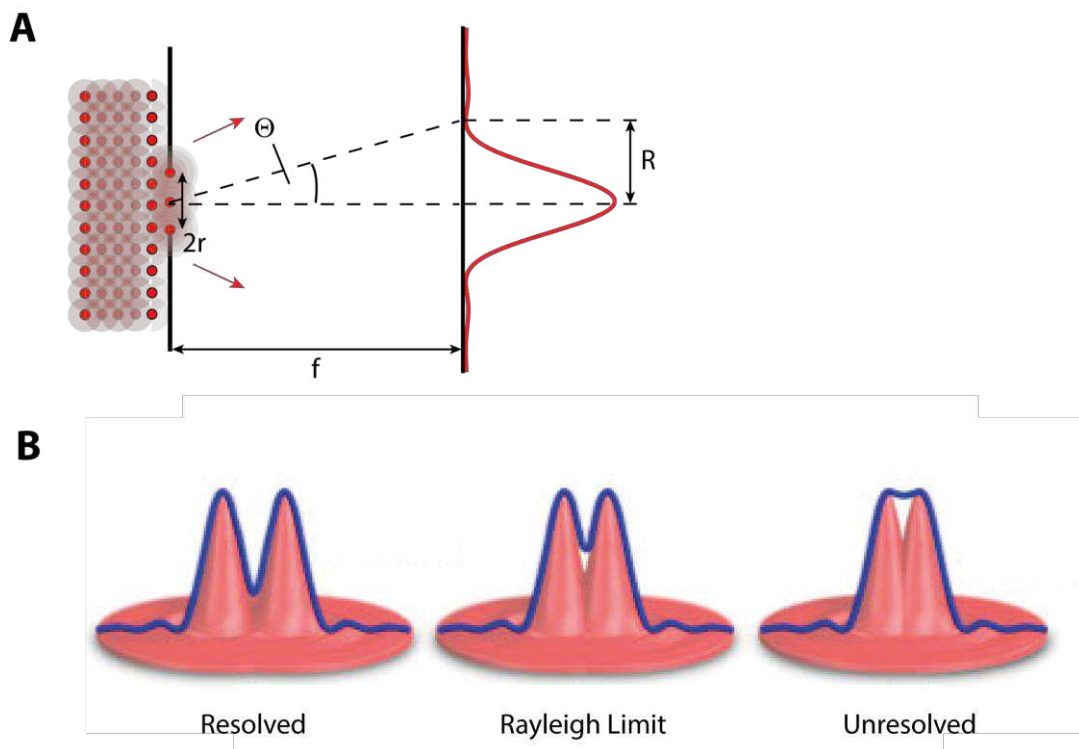


**Figure 5. The Physical Limitation of Resolution**

**A)** Huygens principle states that each point of a moving wave front itself can be considered as starting point for a new wave. Considering this, diffraction on a single slit can be explained: Point sources on the edges of the slit will give rise to spherical emission of the wave front, thus reaching areas on the screen, that cannot be explained solely by pure geometric optics. The geometric considerations for the deduction of the limitations of resolution are displayed. A circular aperture with diameter  $2r$  causes a first minimum on a screen in distance  $f$  at a position  $R$  away from the optical axis.  $\theta$  represents the angle of observation. **B)** Three examples of two signals are shown. Left: The fluorophores are well separated, and the signals are resolved. Middle: A fluorophore is located exactly at the first minimum of the signal of another fluorophore and according to the Rayleigh criterion, the signals are still resolved. Right: The fluorophores are closer to each other and the signals are not resolved anymore. Image adapted from [53].

Insufficient resolution constitutes a major limitation in the estimation of structure sizes, as every sub-diffraction sized structure will give rise to a detected spot of at least  $\sim 200$  nm. To resolve finer structures, determine smaller sizes, or investigate the spatial distribution of dense molecules, alternative approaches are needed. In the following, two methods with increased resolution power used in this work will be presented. Additional super-resolution microscopy techniques are reviewed for example by Huang et al. and Sigal et al. [54, 55].

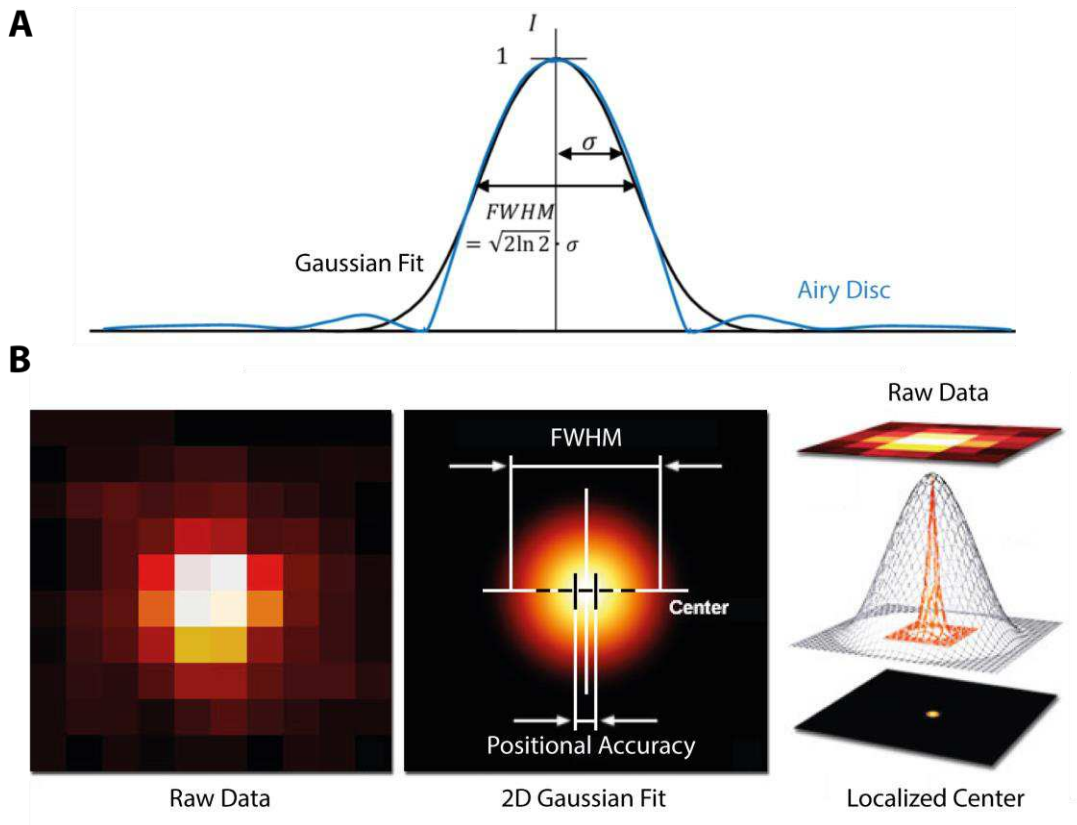


**Figure 6. Gaussian Fitting of the PSF**

**A)** The shape of the PSF is well approximated by a Gaussian Function. Image adapted from [56]. **B)** Fitting of the PSF with a Gaussian Function allows for localization of a single emitter with a positional accuracy down to several nanometers. Image adapted from [57].

Before the first observation of single fluorescent molecules, plastic beads could already be visualized in common light microscopy, as the beads give rise to substantial contrast in transparent samples. Already in the 1980s, first studies succeeded in localizing these beads with a precision down to a few nanometers [58]. Analogous studies were done on single fluorescent signals several years later [59, 60]. The theoretical *Airy disc* and its experimentally realized Point-Spread Function (PSF) of a diffraction-limited microscope are usually well approximated by a 2D Gaussian (**Figure 6A**). This is frequently used to estimate the central position of the fluorescent signal by fitting a Gaussian to the image of a single isolated signal. The PSF is given by:

$$PSF(x, y|\theta) = \frac{\theta_N}{2\pi\theta_\sigma^2} e^{-\frac{(x-\theta_x)^2 + (y-\theta_y)^2}{2\theta_\sigma^2}} + \theta_b \quad (7)$$

where  $\theta = [\theta_x, \theta_y, \theta_\sigma, \theta_N, \theta_b]$  are the free parameters of the fit: the x- and y-coordinate, the sigma-width of the signal, the total number of emitted photons and the background offset, respectively.

To quantify the accuracy of fitting, Thompson et al. derived an analytical expression [61], which was re-evaluated by Quan et al to include the effects of electron-multiplying charge-coupled device cameras on the precision accuracy, yielding [62]:

$$\langle \Delta x^2 \rangle = \frac{2\sigma^2 + a^2/12}{N} + \frac{8\pi\sigma^4 b^2}{a^2 N^2} \quad (8)$$

where  $\sigma$  is the standard deviation of the PSF in nm,  $a$  is the pixel size in nm,  $N$  is the total number of detected photons, and  $b$  is the standard deviation of the residuals between the fitted and the raw background (**Figure 6B**). The precision hereby depends particularly on the total number of detected photons.

When a conclusive image of a molecular species within the cellular context is desired, high expression levels often avert imaging at low densities, thus preventing the localization of single, isolated signals. In the mid-2000's, new methods arose, which succeeded in separating spatially dense signals over time, thereby decreasing the signal density per image: at each acquisition frame, only a minor subset of molecules is imaged, while most fluorophores remain non-fluorescent (**Figure 7A**) [63, 64]. As these specific microscopy methods are based on the iterative localization of single molecules, they are termed Single-Molecule Localization Microscopy (SMLM) methods.

Three major ways to achieve this blinking behavior have emerged and are frequently used by now:

### Direct Stochastic Optical Reconstruction Microscopy (dSTORM)

dSTORM makes use of the inherent blinking properties of organic dyes. Different phenomena are responsible for organic dyes to stay in a non-fluorescent state: Firstly, spontaneous transitions from  $S_1$  to  $T_1$  by intersystem crossing block the renewed excitation of the fluorophore. The lifetime of  $T_1$  in standard, aqueous buffer conditions is in the order of several microseconds, and thus negligible for many imaging experiments. Secondly, by addition of a reduction/oxidation buffer system (ROXS),  $T_1$  gets quenched, as the dye immediately gets reduced when in  $T_1$ . Consecutive oxidation or illumination at ~400 nm recovers the fluorophore to  $S_0$  (**Figure 7B**).

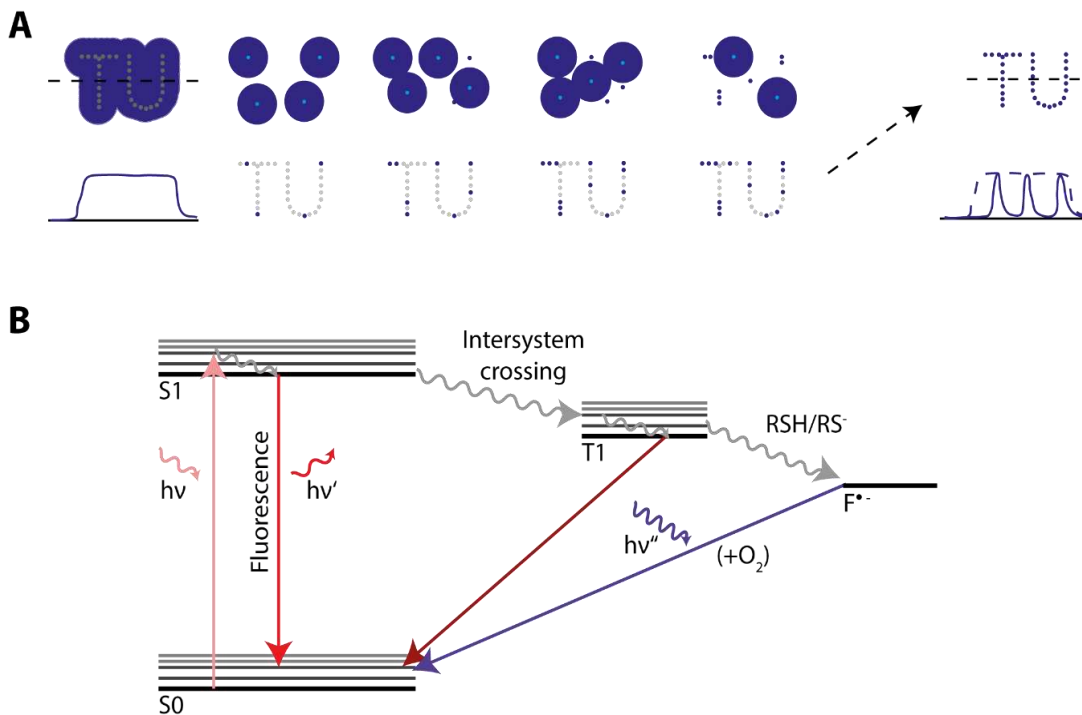


**Figure 7. Single Molecule Localization Microscopy**

**A)** Single-molecule localization microscopy yields increased resolution by separating dense signals in time, enabling the positional determination of single, isolated emitters. In order to image all fluorophores at least once, this process is repeated several thousand times. A final reconstructed super-resolution image is then generated by an overlay of all determined positions. Line-profiles show the improved resolution. **B)** In dSTORM, additional redox buffer systems introduce prolonged dark states of organic dyes.  $T_1$  is quenched by immediate reduction of the fluorophore ( $F^{\cdot-}$ ). Illumination by 400 nm light or subsequent oxidation can bring the fluorophore back to  $S_0$ .

The rates for the oxidation and reduction can be controlled efficiently by the buffer system [65]. dSTORM aims at prolonging the induced *off* states to an extent where single-molecule localization of the remaining dyes can be achieved. Most commonly, the buffer system consists of glucose, glucose oxidase and catalase for quenching  $T_1$  combined with  $\beta$ -mercaptoethylamine for reduction [66]. This approach of SMLM renders super-resolution imaging readily available for common immunofluorescent microscopy, as antibodies conjugated to organic dyes are standard biological tools. However, due to the nature of the ROXS buffer systems and their common goal to minimize oxygen within the sample, live-cell experiments are severely restricted. Additionally, antibody labeling in living cells might artificially crosslink proteins and initiate undesired cellular processes.

Within this work, the enormously increased resolving power of dSTORM will be used to probe the spatial distribution of different subunits of the TCR/CD3 receptor complex.

## Photoactivated Localization Microscopy (PALM)

In contrast to dSTORM, PALM uses FPs which can be turned on deliberately. Stochastic blinking of GFP and its variant yellow fluorescent protein was observed for the first time in 1997 by Moerner et al [67]. Soon after, a genetically modified GFP variant termed photo-activatable GFP (PA-GFP), which allowed for control of the blinking, was produced [68]. PA-GFP needs activation by ultra-violet (UV) light before it effectively turns fluorescent [69]. UV-dependent decarboxylation switches the PA-GFP from a non-fluorescent *off* state into a fluorescent *on* state. This *on* state shows similar spectral characteristics as GFP itself. The transition was described to be unidirectional. Another photo-activatable fluorescent protein (PA-FP) named PAmCherry is derived from red fluorescent protein. It offers a PA-FP in the red spectrum and is also turned on by UV illumination [70]. In contrast to PA-FPs, photo-switchable (PS)-FPs do not show an initial *off* state but shift their spectra upon photo-switching. An important member of this family is represented by the photo-switchable cyan fluorescent protein (PS-CFP) and its derivative PS-CFP2. Upon illumination at ~400 nm, the spectrum is shifted from CFP to GFP, with an accompanying increase in contrast of ~2000x [71, 72]. Red-shifted versions of PS-FPs exist as well, such as mEos3.2 or Dendra2 [72, 73]. In contrast to unidirectional PS-FPs, several other FPs offer an additional *off*-switch. Dronpa can be toggled between its *on* and *off* states with UV and 490 nm illumination, respectively [74]. Fusing a protein to a PS/PA-FP enables the stochastic activation of small protein subsets over time. This realization of SMLM was first applied in 2006 by Betzig et al [63].

Within this work, experiments using PALM on a TCR/CD3 complex subunit will be used to determine the receptor's spatial distribution on the plasma membrane of T cells, even on living T cells. This can be realized, as no ROXS buffer is necessary. Additionally, the paradigm of PA-FPs yielding stoichiometric numbers of localizations will be investigated for the case of the widely used PS-CFP2, in order to estimate the effects of multiple localizations of the same molecule. This facilitates a better interpretation of PALM data.

## Point Accumulation for Imaging in Nanoscale Topography (PAINT)

In PAINT, blinking is not achieved by the photophysics of fluorophores, but by the diffusion and/or the binding of the label molecules. In its first application, the membrane stain NileRed was used to visualize glass supported lipid bilayers, by imaging the incorporation and diffusion of NileRed into and within the bilayer in TIRF configuration [75]. Further developments use the binding kinetics of two complementary DNA strands [76]. In DNA-PAINT, a protein is not labeled fluorescently, but with a probe which is conjugated to a single-stranded DNA. In addition, a fluorescently labeled complementary DNA strand is added to the imaging buffer. During imaging, the fluorescent label might bind to a

complementary DNA strand on a protein in focus, which enables imaging as long as the DNA bond persists. After dissociation, the fluorescent label leaves the focus. As the buffer contains a substantial concentration of fluorescent strands, long illumination times need to be used in order to select for bound, i.e. immobilized signals. This implies increased acquisition times for DNA-PAINT.

### STED Microscopy

In addition to the SMLM methods, other super-resolving microscopy techniques, which do not depend on blinking of fluorophores, have been designed. Amongst them, a noteworthy innovation termed Stimulated Emission Depletion (STED) microscopy is characterized by tackling the resolution limit by directly reducing the size of the PSF [77, 78].

STED microscopy is an advanced variant of confocal microscopy. In confocal microscopy, two pinholes are added to the microscopy system. The first one is placed at the illumination path and is used to generate a point illumination on the sample. A second pinhole at a conjugated plane in front of the detection system cancels out emission light from out-of-focus signals. As only a small point of the sample is illuminated, acquisition of a full image requires scanning. The scanning character allows the use of photomultiplier tubes or avalanche photodiodes (APD) for detection. STED microscopy is based on stimulated emission, a process in which the relaxation of excited fluorophores is triggered by an additional photon [79] (**Figure 8A**). Stimulated emission competes with spontaneous emission, thus fluorescence by spontaneous emission is suppressed in regions where stimulated emission is induced. STED microscopy effectively shrinks the PSF by realizing stimulated emission in an outer ring of the initial, diffraction-limited PSF. In addition to the imaging laser, which yields a diffraction-limited image, a second laser, called depletion laser, is required. The depletion laser is put into a doughnut shape e.g. by adding a  $2\pi$  spiral phase plate [80], and needs to be of a wavelength suitable to induce stimulated emission. The effective width of this ring depends non-linearly on the intensity of the depletion laser (**Figure 8B**). High-laser power is needed to efficiently increase the resolution: a 50% fluorescence reduction of a fluorophore with a  $S_1$  lifetime of 4 ns and a stimulated emission cross-section of  $25 \text{ cm}^2/\text{J}$  will require  $10 \text{ MW}/\text{cm}^2$  [81]. The power needed for 50% reduction is called the saturation intensity. Mathematical derivations for the resolution of a STED microscope result in:

$$res_{min,STED} \approx 0.61 \frac{\lambda}{NA(1 + \varsigma)} \quad (9)$$



showing an increase in resolution by  $(1+\zeta)^{-1}$ , where  $\zeta = \frac{I}{I_s}$  is the ratio of the used laser power and the fluorophore's saturation intensity [82].

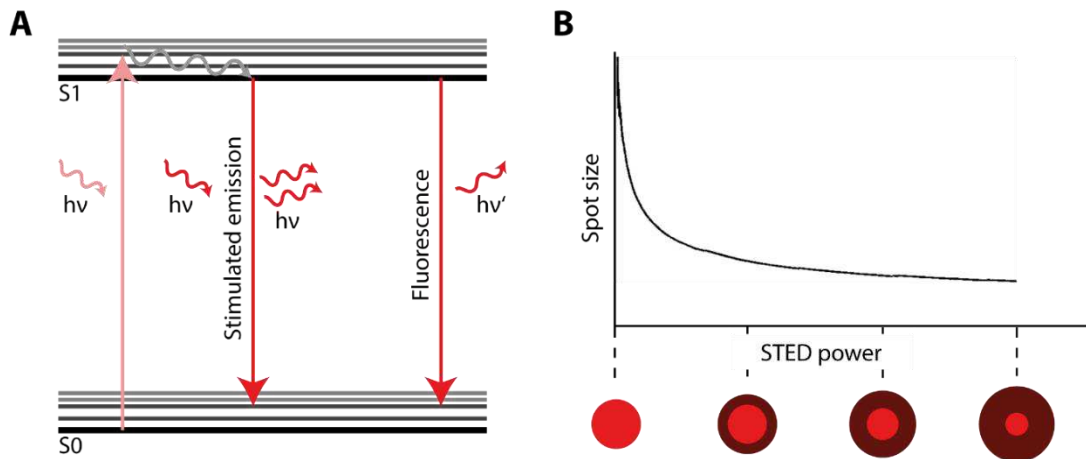


**Figure 8. STED Microscopy**

**A)** The Jablonski diagram for STED microscopy: A fluorophore is excited from  $S_0$  to  $S_1$ . Before relaxing by spontaneous fluorescence, the emission is stimulated by the depletion laser. Fluorophores located in the center of the doughnut of the depletion laser spontaneously fluoresce and get imaged. **B)** The effective decrease of the PSF in size depends on the power of the depletion laser. The saturation intensity  $I_{sat}$  corresponds to the power where more than 50% of the excited fluorophores are experiencing stimulated emission. With increasing power of the depletion laser, the doughnut broadens, thus shrinking the PSF.

Within this work, STED microscopy will be used to confirm dSTORM and PALM data on the spatial distribution of the TCR/CD3 complex on the plasma membrane of T cells, as this method is conceptually different to SMLM approaches and therefore a perfectly suitable method to confirm that the results are derived from biological facts rather than methodological artefacts.

### 1.1.3. Single-Molecule Methods in Biology

The ability to image single molecules enabled the estimation of a multitude of properties relevant to cellular biology. By now, a set of highly diverse single-molecule microscopy methods has accumulated, each of those offering ways to tackle highly specific questions. Selected methods to probe the mobility of single molecules, and the stoichiometry of receptor complexes, are now introduced in brief. This selection is based on the relevance for this thesis, as they were also applied within this work.

#### Single-Molecule Mobility Estimation

Besides directly yielding information on the protein's mobility itself, diffusion studies are also suitable to investigate the underlying mechanisms and structures. A protein's diffusion might, for example, be actively driven along cytoskeletal structures, limited to defined areas by obstacles or barriers, or it might happen

randomly according to *Brownian motion*. The diffusion coefficient  $D$  is frequently used to characterize the mobility of proteins within the cellular context. It shows typical values of a few  $\mu\text{m}^2/\text{s}$  for membrane lipids, and below  $0.5 \mu\text{m}^2/\text{s}$  for most membrane proteins [83].

Estimating the lateral diffusion behavior of molecules can be achieved in several ways:

Single-molecule tracking (SMT) represents a direct way to capture the diffusional behavior of molecules (**Figure 9A**). Molecules need to be labeled at sufficiently low density to ensure identification of single signals by localization methods and correct linking of the respective signals in consecutive images. The mean square displacement (MSD) of all points within a track separated by time  $\Delta t_i = i \cdot t_{lag}$  can be calculated by

$$MSD_{\Delta t=i} = \frac{1}{n-i} \sum_{t=1}^{n-i} (x_t - x_{t+i})^2 \quad (10)$$

where  $n$  is the number of points in the track,  $x$  is the position and  $i$  is the size of the gap introduced. To determine  $D$  from this information, the MSD values are plotted against the respective  $t_{lag}$  and the curve is fitted with an appropriate model. Assuming two-dimensional Brownian motion, the solution of *Fick's second law of diffusion* yields a mean square displacement described by

$$MSD = \langle r^2 \rangle = 4Dt \quad (11)$$

where  $t$  is the observation time and  $r$  is the displacement. The slope of the resulting linear plot corresponds to the value of  $D$ . However, the limited positional accuracy of the signal-fitting procedure introduces a bias manifested as an y-offset, yielding

$$\langle r^2 \rangle = 4D\Delta t + 4\sigma^2 \quad (12)$$

where  $4\sigma^2$  is the localization error. Other modes of mobility, such as directed motion or anomalous diffusion, are described by more complex models and do not yield linearly increasing MSD-vs-t plots [84]. The shape of MSD-vs-t plots thus enables a straight-forward deduction of mobility modes other than *Brownian motion*.

Fluorescence Recovery After Photobleaching (FRAP) is widely applied for bulk mobility estimations. After photobleaching, a certain spot within the sample, the recovery of the signal over time, contains information on the probe's mobility (**Figure 9B**). This facilitates a straight-forward analysis of the immobile and mobile fractions of the probe. Quantitative statements about the diffusion coefficient  $D$ , however, are more intricate, but can be realized by fitting the recovery curve with appropriate models [85].

Correlation-based methods, such as Fluorescence Correlation Spectroscopy (FCS), are an additional alternative for mobility estimations. A fixed spot within the sample is measured over time, and the diffusion of fluorescent probes gives rise to signal fluctuations (**Figure 9C**). By analyzing these fluctuations with auto-correlation analysis, conclusions about the mobility can be drawn. Changing the observation spot size, either directly by variation of the size of the excitation laser, or indirectly by variation of the STED laser power, allows for resolving different diffusive modes within the plasma membrane of living cells [86-88]. Additional sample scanning during FCS measurements enables the determination of spatial heterogeneities in diffusion behavior [89, 90].

Two approaches for mobility estimation of the TCR/CD3 complexes on the membrane of T cell will be applied within this work: Single-molecule tracking and FCS. Both methods are conceptually different, and thus complement each other well.

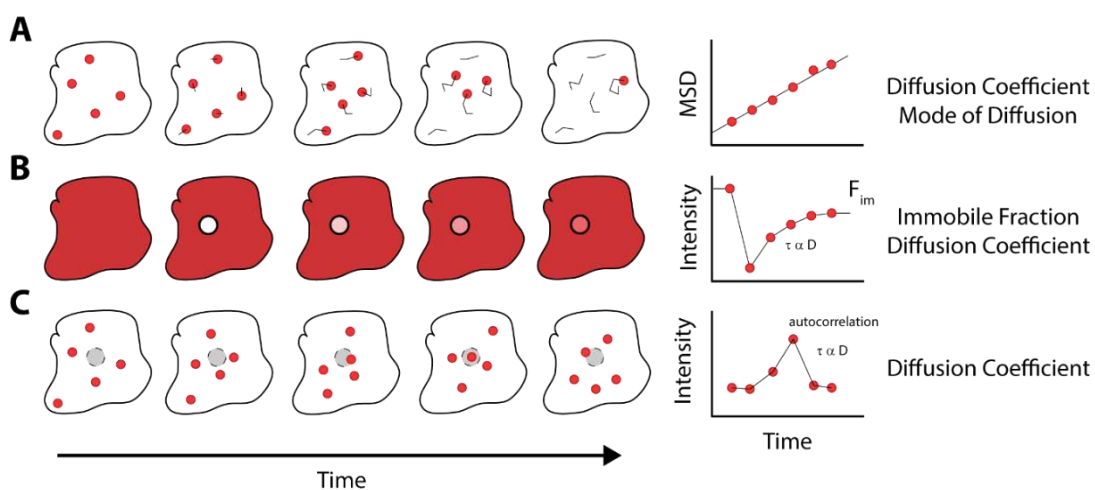


**Figure 9. Methods to Determine Mobility**

**A)** By SMT of molecules, the mobility can be determined at the single-molecule level, and heterogeneities between molecules of the same species can be resolved. Low-density labeling has to be ensured to resolve single molecules and to be able to link the identical molecules within consecutive frames. By analyzing the step lengths at different time lags, the mean-square displacement (MSD) can be analyzed as a function of gap-size. This allows for discrimination between different modes of diffusion. In case of free Brownian motion,  $D$  can be determined by fitting the MSD-vs- $t$  curve with **Equation (12)**. **B)** In FRAP, the bulk mobility and the mobile fraction of a molecular species can be determined. A well-defined area within the fluorescently labeled cell is bleached and the recovery of the fluorescence is recorded. The intensity to which fluorescence recovers can be compared to the initial intensity, thus giving a direct measure of the size of the mobile fraction. By fitting the recovery curve,  $D$  can be determined. **C)** In FCS, the intensity within a fixed spot in the sample is measured over time and its intensity fluctuations are recorded. Analyses of these fluctuations by autocorrelation and additional fitting enables the determination of  $D$ .

## Methods to Estimate Stoichiometry

In addition to the mobility of proteins, measures on their subunit stoichiometry can reveal important information on their function. A higher receptor valency, for example, leads to an elevated re-binding probability [91]. High expression levels, however, often impair straight-forward analyses of the stoichiometry of receptor complexes due to overlapping signals. To accomplish analyses at even high surface densities of molecules, the biophysics group at the Institute of Applied Physics at the Technical University of Vienna under Gerhard Schütz has developed a method termed Thinning Out Clusters while Conserving Stoichiometry of Labeling (TOCCSL). It can be interpreted as a single-molecule implementation of FRAP [92, 93]. By using an aperture in combination with a high-intensity laser pulse, a defined region within the cellular membrane is photobleached. Instead of monitoring the recovery of the integrated intensity within the bleached region, the recovery of single receptor complexes is analyzed. The signals of the individual complexes are then well separated, and their brightness can be determined. Comparing the brightness distribution of the recovered fluorescent signals to the brightness distribution of single fluorophores provides information on the oligomerization status of the probed molecule (**Figure 10**). The addition of a second color allows to determine the degree of co-localization of the recovered probes and enables more sensitive detection of rare interactions [94].

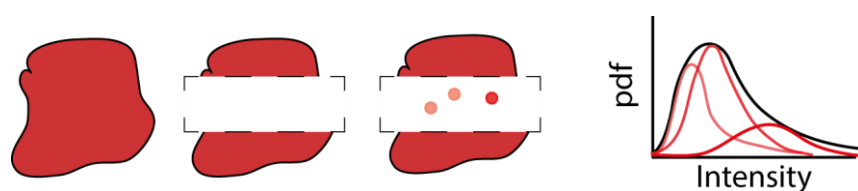


**Figure 10. Thinning Out Clusters while Conserving Stoichiometry of Labeling (TOCCSL)**

*In TOCCSL, a defined region of the cell is bleached and the brightness of separated recovering signals is analyzed. Comparison and fitting of the resulting probability density function (pdf) of brightness with a linear combination of the distribution of signals from single fluorophores yields information on the stoichiometry of the probed molecule.*

Photon-arrival time analysis FCS (PA/FCS) combines the concepts of FCS with photon-arrival time analysis [95-97]. The photons emitted by a single fluorophore are anti-bunched, as the fluorophore needs a certain time to relax to the ground state after photon absorption [98]. Splitting the emission light into multiple channels and using independent APDs allows to count simultaneously emitted photons: A single photon can only follow one path, thus, coincident detections on more than one APD indicate more emitters within the measurement spot. Evaluation of the correlation between the channels at different time lags further gives information whether these emitters move independently, i.e. as monomers. For this, the correlation is evaluated at three different time lags: First, at a maximum time lag, where detected photons

are uncorrelated. Secondly, at an intermediate time lag of one acquisition pulse. The emitter most likely has not yet left the observation spot and emits another photon, which will be detected again, giving rise to increased correlation at this time lag. These two curves act as reference for the third one, which is evaluated at time lag zero. Here, elevated correlation hints towards a higher number of emitters. The use of these three correlation curves combined with a model, which includes photophysics and diffusion, allows for quantification of the number of emitters per diffusing entity [99].

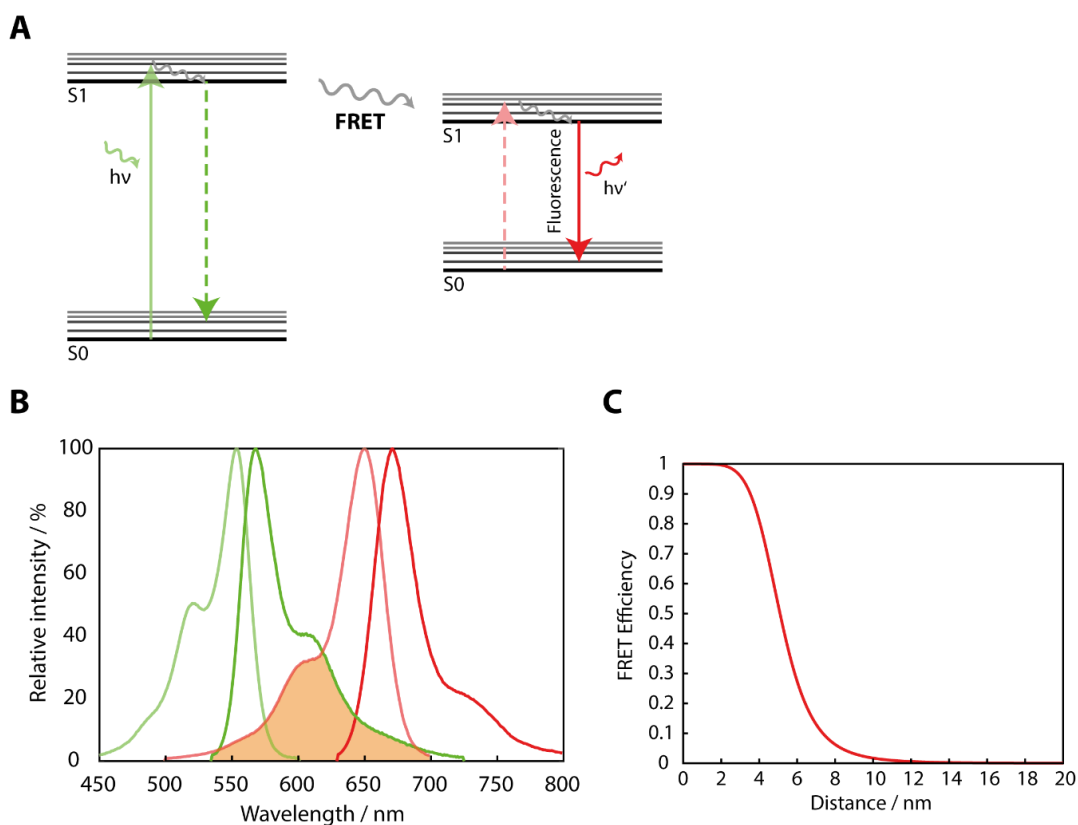


**Figure 11. Förster Resonance Energy Transfer (FRET)**

**A)** The Jablonski diagram can be used to depict FRET: When the fluorophore with the lower excitation wavelength (green) is excited, and another fluorophore of a different species is within near distance ( $<10$  nm), FRET can occur. The fluorophore with the higher excitation wavelength (red) is then excited through energy transfer by non-radiative dipole-dipole coupling, and spontaneously relaxes to its  $S_0$  with the accompanying emission of a photon. **B)** For the appearance of FRET, the emission spectrum of one fluorophore species (dark green, AF555) needs to show overlap with the excitation spectrum of the second fluorophore species (bright red, AF647). The overlap is marked in orange. **C)** The FRET efficiency depends highly on the distance between the two fluorophores. The Förster radius for a pair of fluorophores is the distance, for which 50% FRET efficiency is reached.

Both TOCCSL and PA/FCS require the diffusion of fluorescent probes and do not allow for probing a potential immobile fraction of the protein. When two fluorophores of different species are in close proximity and the emission spectrum

of the first one ('donor') shows at least some overlap with the absorption spectrum of the second one ('acceptor'), Förster Resonant Energy Transfer (FRET) can occur (**Figure 11A and B**). The distance at which 50% FRET appears depends on the spectral overlap, the quantum yield, the relative dipole orientation and the surrounding medium, and is termed Förster radius ( $R_0$ ) [100].

The choice of fluorophores determines the sensitivity of the probes: small spectral overlap enables highly sensitive measurements even at size scales of about 1 nm. FRET is a non-radiative energy transfer via dipole-dipole coupling from the donor to the acceptor, and its rate,  $k_{ET}$ , is highly dependent on the distance between the fluorophores,  $r$ . This relation can be described as follows:

$$k_{ET} = \frac{R_0^6}{\tau_D \cdot r^6} \quad (13)$$

where  $\tau_D$  is the fluorescence lifetime of the donor. This strong dependence on distance turns the method into a powerful tool for probing nanometer distances (**Figure 11C**).

An ensemble way to measure FRET is termed Donor Recovery After Acceptor Photobleaching [101, 102]. After acquisition of a donor image, the acceptor fluorophores are photobleached and the donor fluorophore is imaged again. An increase in brightness in the second donor image compared to the first image indicates FRET. The ratio of the two donor images gives information about the amount of FRET. A more versatile way to check for FRET is sensitized emission [103-105], in which the acceptor signal upon donor excitation is put in reference to the donor signal. However, amongst other obstacles, possible emission crosstalk can decisively bias the results.

The three methods described to study the stoichiometry of molecular complexes (TOCCSL, PA/FCS and FRET) are conceptually different. All of them were applied within this work with the aim to unambiguously resolve the oligomeric state of the TCR/CD3 complexes on the plasma membrane of T cells.

## 1.2. Immunology and T Cell Biology

Immunity, a term derived from the Latin word *immunis*, meaning 'exempt', describes the ability of a biological organism to defend itself against infections, diseases, or other forms of biological invasion while suppressing defense actions against harmless and autologous substances.

References related to immunology, the study of the immune system, date back to as early as 430BC when a group of people was found to be resistant against the Plague, a disease caused by bacterial infection. However, systematic immunological studies were only started in the late 18<sup>th</sup> century, leading to the first successful vaccination against smallpox by Edward Jenner. The systematic classification of causes for infection, i.e. pathogens, the successful vaccination against cholera and the discovery of antibodies in the late 19<sup>th</sup> century depict further important milestones in this field of research.

The infamous example of Acquired Immune Deficiency Syndrome (AIDS) induced by the Human Immunodeficiency Virus (HIV) highlights the uttermost importance of a fully functional immune system. Absence or malfunction of parts within the machinery of the defensive mechanisms transforms common, generally harmless pathogens into dangerous threats. Autoimmune diseases such as Type 1 Diabetes Mellitus, Rheumatoid Arthritis or Multiple Sclerosis originate from a malfunctioning immune system, initiating defense mechanisms against endogenous constituents of the organism.

### 1.2.1. The Immune System and the Role of T Cells

The immune system of vertebrates comprises two distinct yet tightly connected systems:

The innate immune system, acting as a first line of defense, responds to foreign pathogens within hours, but does not enable a long-lasting immunity. This immediate reaction is facilitated by the ability of innate immune cells, such as macrophages or dendritic cells (DCs), to recognize pathogen-associated molecular patterns (PAMPs). PAMPs are abundant on a wide variety of pathogens, such as the cell walls on bacteria, but cannot be found in autologous cells. However, many

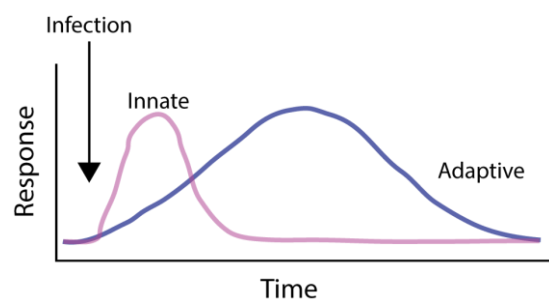


**Figure 12. Response Times of the Innate and Adaptive Immune System**

*Innate responses are initiated within the first few hours after encountering a pathogen, while the cells related to the adaptive responses take multiple hours to several days to be activated. Image adapted from [1].*

pathogens do not contain PAMPs, which preserves them from being detected by the innate immune defense. This weakness of the innate system is compensated by the adaptive system: It enables immune responses evolving and adapting over the lifetime of an organism and even the development of a memory function that provides faster and more efficient responses in case of repeated infections. This is not only characterized by an extremely high level of efficiency in the detection of virtually all exogenous pathogens, but also by an astonishing specificity concerning the distinction between exogenous and endogenous structures. However, these mechanisms require several days to be initiated and to act at their full strength (**Figure 12**). To readily facilitate the recognition of scarce but highly variable pathogens in the absence of PAMPs, a huge variety of receptors with different epitopes exists.

The immune system is based on the interplay of a large variety of cell types (see selected subsets in **Figure 13**), together known as leukocytes or white blood cells. Those cells are derived from hematopoietic stem cells within the bone marrow. A first class of highly important immune cells are professional antigen-presenting cells (APCs) such as Dendritic Cells, Macrophages or Eosinophil Granulocytes. These cells are responsible for the digestion of pathogens and the presentation of fragments thereof on their surface as peptide-loaded Major Histocompatibility Complex of Class II (pMHC-II) molecules.

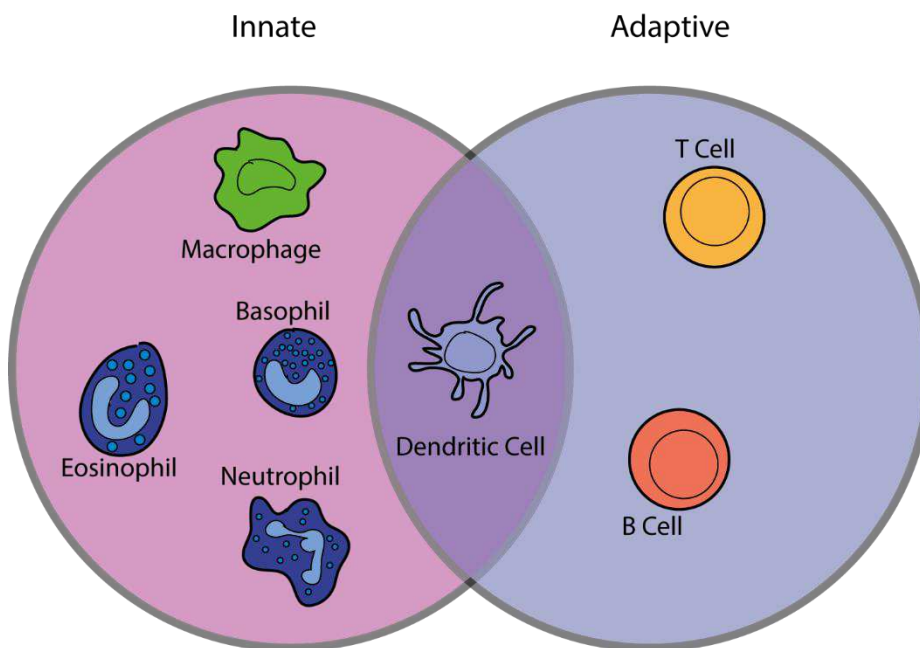


**Figure 13. Selected Cells of the Immune System**

Cells of the innate immune system include professional antigen-presenting cells (APCs) such as macrophages. Leukocytes (baso-, eosino- and neutrophil granulocytes) represent an additional part of the innate system. Dendritic cells have a major role in connecting the innate with the adaptive system. T and B lymphocytes are participating in adaptive immune responses. Image adapted from [1].



To perform this function, the pathogens are taken up by the APCs via pino-, phago- or endocytosis and cleaved by proteases in endo- or (phago)lysosomes. After its synthesis, the MHC-II complex is located at the endoplasmic reticulum (ER) and loaded with a dummy peptide, called the invariant chain. Via the Golgi apparatus, the MHC-II is transferred to late endosomes, where the invariant chain is cleaved and the loading with pathogenic peptides happens. Subsequently, the pMHC-II complex reaches the cell surface. Only antigenic peptides presented by MHC-II can be recognized by T cells (**Figure 14**). Additional cell types of the innate immune system are other types of Granulocytes: the phagocytic Neutrophil Granulocytes, and the histamine-secreting Basophil Granulocytes, which are responsible for inflammation.

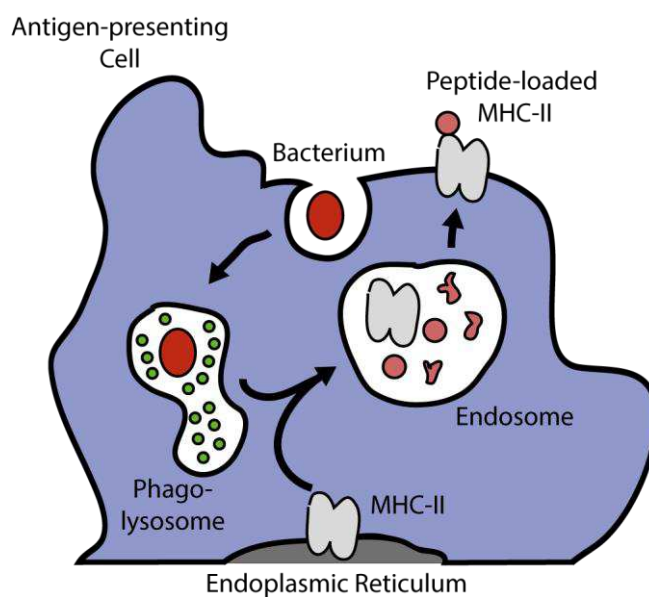


**Figure 14. Antigen Processing and Presentation**

*Foreign pathogens are taken up by professional APCs, dissected, fused with MHC-II molecules in late endosomes, and presented as peptide-loaded MHC-II (pMHC-II) on the surface of the APCs.*

In contrast to Macrophages and Dendritic Cells, T cells and B cells are characterized by highly specific receptors on their surface, which facilitate the recognition and binding of antigens. In case of B cells, these receptors are called B cell receptors (BCRs) which do not need MHC-based presentation of antigens. In most cases, B cell responses depend on additional activation by helper T cells. When an antigen is recognized by a B cell via the BCR, parts of this antigen are subsequently digested and presented to T cells, as described above for professional APCs.

Only after this additional recognition of antigens by T cells, B cells are fully activated, yielding a release of cytokines and antigen specific BCRs in the form of antibodies.

The need of helper T cells for the full activation of B cells highlights the crucial role of T cells.

Interestingly, several different subsets of T cells were identified. Like all hematopoietic cells, T cells are derived from the bone marrow, from where they migrate towards the thymus via the lymphatic system (**Figure 15A**). In the thymus, T cells pass varying stages of maturation, initially expressing neither of the two major co-receptors in antigen recognition (CD4-CD8<sup>-</sup>; double negative, DN). Upon this maturation, the T cells start to express both co-receptors (CD4<sup>+</sup>CD8<sup>+</sup>; double positive, DP), before maturing into either CD8<sup>+</sup> or CD4<sup>+</sup> cells and subsequently migrating towards peripheral tissues as naïve, single positive (SP) T cells.

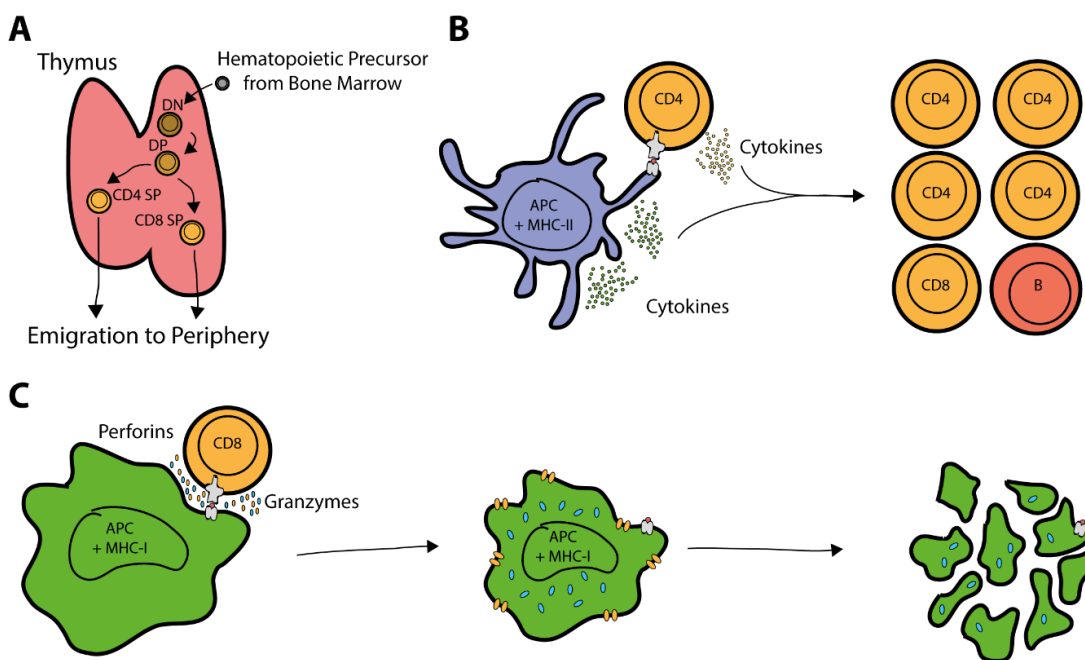


**Figure 15. T Cell Differentiation and Effector Tasks of CD4 and CD8-positive T Cells**

**A)** Hematopoietic precursor cells migrate from the bone marrow to the thymus, where they differentiate into double negative (DN) T cells, before starting expression of CD4 and CD8, thus becoming double positive (DP) T cells. Either CD4 or CD8 expression is then reduced, yielding single positive (SP) T cells, which emigrate to the periphery. **B)** CD4<sup>+</sup> T cells recognize peptides embedded in MHC-II, which, in case of an antigenic peptide, triggers the release of cytokines, and further differentiation of the T cell, besides activation of other immune cells, like CD8<sup>+</sup> T cells or B cells. **C)** CD8<sup>+</sup> T cells recognize peptides embedded in MHC-I. Perforins and granzymes are released and taken up by the APCs. The cellular membrane is destroyed, and the APCs start to disintegrate.

When encountering cognate pMHC, CD8<sup>+</sup> and CD4<sup>+</sup> T cells fulfill distinct tasks. CD4<sup>+</sup>, also known as helper T cells, support other cell types in the immune response by secreting cytokines, thus inducing the maturation of B cells, further activation of CD8<sup>+</sup> cells and proliferation of CD4<sup>+</sup> cells. CD4<sup>+</sup> T cells recognize the peptides within the MHC-II complex and, upon binding, can differentiate further into a wide variety of more specialized helper T cell types (**Figure 15B**). CD8<sup>+</sup>, or cytotoxic T cells, on

the contrary are able to recognize peptides presented by the MHC class I molecule, and, upon binding, they immediately start destroying the cell presenting the antigen. Within the plasma membrane of the APCs, perforins induce pores, which allows the influx of granzymes. These proteases subsequently induce apoptosis of the target cell (**Figure 15C**).

### 1.2.2. The T Cell Receptor Complex

The T cell receptor (TCR), which is expressed on the surface of T cells, represents the key player in the recognition of pMHC. Both BCR and TCR lack signaling activity and require the association with CD79 or CD3, respectively. The TCR is a heterodimeric transmembrane protein that consists of one  $\alpha$  and one  $\beta$  subunit linked by a disulfide bond and is embedded in the membrane by one transmembrane helix per subunit. Alternatively, in the specific case of  $\gamma\delta$ T cells, the TCR is made up of two distinct subunits called  $\gamma$  and  $\delta$ . However, this type of T cells represents only a minor subset of the total number of T cells. The extracellular domain represents the main part of the TCR. It is similar to the Fab part of an antibody and consists of a constant region and a variable region, where the antigen-binding site is located (**Figure 16**).

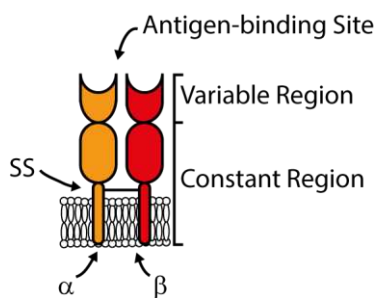


**Figure 16. Structure of the TCR**

*The TCR heterodimer shows structural analogy to Fab fragments: It contains a constant region, which is partly embedded in the membrane, and a variable region, featuring the antigen binding site. The TCR consists of two subunits, the  $\alpha$  and  $\beta$  chain, which are linked by a disulfide bond.*

To facilitate binding of the TCR to the massive variety of abundant pathogenic peptides, a process called gene rearrangement gives rise to TCRs that are specific for a high number of different peptides. This is achieved by varying the variable region in the antigen-binding site. Copies of three different gene segments (V, D and J) contribute to the expression of specific  $\alpha\beta$ TCRs. By randomly selecting these segments, and additionally connecting them in highly diverse ways (*'junctional diversity'*), specificity to approximately  $10^{18}$  different antigens can be achieved in principle. This rearrangement process only affects the variable region of the TCR, while the constant region remains identical for all expressed TCRs.

The TCR lacks a significant cytosolic domain, which renders it incapable of transmitting signals to the intracellular milieu. Therefore, additional proteins are needed to aid in signal transmission. The CD3 protein complex, which is associated with the TCR, provides signaling functionality to the receptor by offering a total of ten immunoreceptor tyrosine-based activation motifs (ITAMs) as targets for

phosphorylation. The proposed subunit stoichiometry of this multi-component complex is the following:

In addition to the heterodimeric TCR $\alpha\beta$ , two further heterodimers (CD3 $\epsilon\gamma$  and CD3 $\epsilon\delta$ ) and one homodimer, CD3 $\zeta$ , constitute the TCR/CD3 complex (**Figure 17**). While each of the CD3 $\epsilon$ , CD3 $\gamma$  and CD3 $\delta$  subunits contain one ITAM, each CD3 $\zeta$  subunit offers three ITAMs [106, 107]. The proposed stoichiometry was obtained in studies based on biochemical data [108, 109] and on atomic-resolution structures of folded domains [110, 111].

After studies suggested two CD3 $\epsilon$  subunits per complex [108, 109], the heterodimeric structures of CD3 $\epsilon\gamma$  and of CD3 $\epsilon\delta$  were identified [112]. Concerning the valency, i.e. the number of  $\alpha\beta$ TCR heterodimers within a complete TCR/CD3 complex, differing indications exist: An erythropoietin receptor-based dimerization assay showed the potential for  $\alpha\beta$ TCR dimerization [113]. Such a bivalent  $\alpha\beta$ TCR complex would result in a neutral net charge of the TCR/CD3 complex. This bivalency was also suggested by co-immunoprecipitation [114]. Blue native-polyacrylamide-gel experiments suggested a mixture of mono- and multivalent complexes [115].

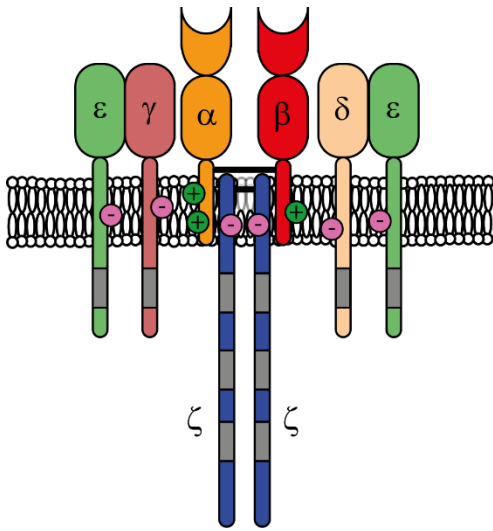


**Figure 17. TCR/CD3 Complex Structure**

The CD3 subunits provide cytosolic signaling capacity to the TCR. The whole TCR/CD3 complex consists of the  $\zeta$  homodimer (blue), linked by a disulfide bond, and it is carrying six ITAMs, the CD3 $\epsilon\delta$  (green/beige) and the CD3 $\epsilon\gamma$  (green/light red) heterodimer, each of them carrying two ITAMs, and the TCR $\alpha\beta$  (orange/dark red). Charges within the transmembrane domains are believed to stabilize the complex.

However, bioluminescence resonance energy transfer and two-color coincidence detection microscopy showed exclusively monovalent presence of the complex [116].

While the structure of the CD3 $\epsilon\delta$  and CD3 $\epsilon\gamma$  heterodimers are similar to each other, the CD3 $\zeta$  homodimer differs substantially. CD3 $\zeta$  is characterized by a short extracellular domain consisting of only nine amino acids followed by a transmembrane helix and a long intracellular tail, on which three ITAMs are located. The two subunits of the CD3 $\zeta$  homodimer are linked to each other via a disulfide bond in their transmembrane regions [111, 112, 117]. The importance of this CD3 $\zeta$

homodimer is substantiated by the fact that it is highly conserved: even non-mammalian CD3 $\zeta$  is able to regain function within TCR/CD3 complexes in mammals [118]. Due to the results of Immuno-blotting assays, it was suggested that CD3 $\zeta$  is the only component of the complex that is able to associate with the actin cytoskeleton [119]. The TCR/CD3 complex is thought to be stabilized mainly by charge interactions. A negatively charged residue within each of the CD3 subunits is speculated to facilitate their association to the three basic transmembrane residues of the  $\alpha\beta$ TCR dimer (**Figure 17**). In addition, also the extracellular domains of CD3 $\zeta$  and the constant parts of TCR $\alpha$  and TCR $\beta$  showed effects on complex association [120-122].

The assembly of the multi-molecular TCR/CD3 complex takes place at the ER, where all subunits except CD3 $\zeta$  are present in excess and retained in the ER by retention motifs located within their transmembrane domains. Upon formation of partial sub-complexes consisting of TCR $\alpha\beta$ -CD3 $\epsilon\delta$ , TCR $\alpha\beta$ -CD3 $\epsilon\gamma$  or CD3 $\zeta$  dimers, retention motifs are blocked [123]. The partial complexes can then progress to the Golgi apparatus, where the full formation of the TCR/CD3 complex is facilitated. The remaining subunits are degraded within four hours, while CD3 $\zeta$  has an increased half-life of 10-20 hours [124]. Various studies showed expression of TCR/CD3-independent CD3 $\zeta$  homodimers at the plasma membrane, which, in combination with the reduced turn-over time, points towards differential recycling processes. If correctly assembled, TCR/CD3 complexes are then trafficked to the plasma membrane [125], while CD3 $\zeta$ -deficient complexes are degraded within lysosomes [126]. Endocytosis of TCR/CD3 complexes occurs either due to natural turn-over or is additionally accelerated by pMHC binding and T cell activation. In both cases, the internalized TCR/CD3 complexes are recycled to the membrane via endosomes or degraded by lysosomes.

The mobility of TCR/CD3 complexes within the plasma membrane has not yet been clarified. Several studies with the aim to elucidate this aspect have been published, however, the results have been rather contradictory [2, 127-135]. While some groups suggested predominantly immobile or slowly diffusing complexes [127, 132] others came to the conclusion of complexes with a rather high mobility of  $D \approx 0.5 \mu\text{m}^2/\text{s}$  [129]. Most studies, however, have used different experimental systems, for example regarding adhesion surfaces, label molecules and cell types (see Table 1). These differences in the experimental setups raise questions about the comparability of the results. The concern is strengthened by Santos et al who identified that the adhesion surface in particular has a significant impact on the results of mobility studies [131].

| Surface        | Cell                        | Label                                  | Method        | D [ $\mu\text{m}^2/\text{s}$ ] | Mobile Fraction | Ref.  |
|----------------|-----------------------------|--|---------------|--------------------------------|-----------------|-------|
| NR             | HeLa                        | T $\zeta\zeta$ -GFP                    | FRAP          | $0.011 \pm 0.001$              | n.d.            | [127] |
| NR             | Human CD4 <sup>+</sup> PBL  | $\alpha\text{CD3}\epsilon$ -Fab-Cy5    | confocal FRAP | $0.064 \pm 0.008$              | $0.96 \pm 0.04$ | [128] |
|                | Human CD4 <sup>+</sup> CBTL |  |               | $0.048 \pm 0.008$              | $1.00 \pm 0.05$ |       |
| SLB            | 5c.c7 T cells               | CD3 $\zeta$ -eGFP/mCherry              | dcFCCS        | $\sim 0.5$                     | n.d.            | [129] |
| SLB            | Jurkat                      | $\alpha\text{CD3}\epsilon$ -QDot655    | SMT           | $0.091 \pm 0.001$              | $0.66 \pm 0.03$ | [130] |
| PLL            | Jurkat                      | $\alpha\text{CD3}\epsilon$ -Fab        | SMT           | $0.018 \pm 0.01$               | n.d.            | [131] |
| Agarose        |                             |  |               | $0.18 \pm 0.07$                |                 |       |
| PLL on Agarose |                             |  |               | $0.04 \pm 0.03$                |                 |       |
| PLL            | Jurkat                      | $\alpha\text{CD3}\epsilon$ -Fab-AF488  | SMT           | $0.005 \pm 0.005$              | n.d.            | [132] |
| IgG            |                             |  | SMT (apical)  | $0.093 \pm 0.038$              |                 |       |
|                |                             |  | SMT           | $0.068 \pm 0.021$              | 0.75            |       |
| NR             | TCR $\beta$ -Jurkat         | V $\beta$ 3-GFP & V $\alpha$ 1.2       | confocal FRAP | $0.12 \pm 0.01$                | $0.95 \pm 0.02$ | [133] |
| NR             | Jurkat                      | TCR $\beta$ -HaloTag-TMR               | SMT (apical)  | $0.11 \pm 0.007$               | n.d.            | [134] |
| NR             | T cell hybrido ma           | $\alpha\text{TCR}\beta$ -Fab-AF488/647 | FCS (apical)  | $0.06 \pm 0.01$                | n.d.            | [135] |
| SLB            | 5c.c7 T cells               | scFv-AF647                             | FRAP          | n.d.                           | $0.73 \pm 0.06$ | [2]   |

**Table 1. Summary of reported mobility estimations of the TCR/CD3 complex**

T $\zeta\zeta$  describes a fusion protein of the extracellular part of the human IL-2 receptor  $\alpha$  chain, which is linked to transmembrane and cytoplasmic parts of CD3 $\zeta$  and GFP. Abbreviations: peripheral blood T lymphocytes (PBL); cord blood T lymphocytes (CBTL); not determined (n.d.); Poly-L-Lysine (PLL); Tetramethylrhodamine (TMR); not reported (NR).

### 1.2.3. Mechanism of T Cell Activation

The recognition of an antigenic pMHC by the corresponding TCR/CD3 complex initiates a multitude of signaling events. Major participating constituents, as well as their abbreviations and functions are listed in **Table 2**. While the key events in T cell activation are rather well described, the decisive triggering mechanism is still largely

unknown. The currently most prominent suggestion of the T cell activation pathway is the following:

The central, decisive trigger for T cell signaling is the binding of the TCR to antigenic pMHC. A first proximate and cytosolic indicator is the phosphorylation status of the ITAMs on the cytosolic parts of the CD3 subunits. While CD45 removes phosphate groups from those ITAMs [136-138], the kinase Lck phosphorylates them (**Figure 18A**) [139]. This phosphorylation of ITAMs by Lck, via still unresolved mechanisms, is boosted upon binding of antigenic pMHC. It further allows the kinase ZAP-70 to bind to phosphorylated ITAMs, a process in which ZAP-70 itself is phosphorylated by Lck [140]. Once phosphorylated, ZAP-70 transmits the signal to LAT, a process again facilitated via phosphorylation [141]. Several proteins, that are associated with the signaling process, accumulate into a large multi-protein complex termed LAT signalosome [142-144]. Amongst others, SLP-76 plays a major role as a linker protein in this process [145]. Other proteins on the APCs, that are involved, include B7-1 and ICAM-1. B7-1 may lead to differing effects, depending on the associated binding partner: while binding to CD28 stimulates the signaling process, the association with CTLA-4 leads to its inhibition [146]. ICAM-1 facilitates adhesion of the T cell by binding LFA-1, additionally inducing inside-out integrin signaling [147, 148].

Three major effects are induced during the process of T cell activation:

Firstly, the actin cytoskeleton is remodeled via the proto-oncogene *vav* (VAV-1) [144]. This supports the formation of larger scale signaling clusters termed micro-clusters, which contain TCR/CD3, CD4 and Lck, and their transport to the central supramolecular activation cluster (cSMAC; orange areas in **Figure 18B**) [149]. In the final state of the remodeling process, the cSMAC is surrounded by the peripheral SMAC (pSMAC; red areas in **Figure 18B**), where the major T cell integrin LFA-1 is accumulated. On the borders of the attachment area of the T cell the distal SMAC (dSMAC; gray areas in **Figure 18B**) emerges. In this dSMAC the phosphatase CD45 is located [150]. Secondly, inside-out signaling of integrins is triggered by the LAT signalosome [144]. Thirdly, the breakdown of PIP<sub>2</sub> into DAG and IP<sub>3</sub> is initiated via PLCγ1 [151]. This results in proliferation and differentiation of the cells, a process that is induced by changes in expression patterns of associated transcription factors. Amongst these, NFAT-, NF-κB- and MAPK-transmitted changes play major roles [152]. Within the latter signaling pathway, Ca<sup>2+</sup> fluxes into the cytosol of the T cell are initiated [153]. Additionally, cytokines, such as IL-2, are released and stimulate T cell proliferation [154].

| Abbreviations  | Full Name | Function                              |
|----------------|-----------|---------------------------------------|
| B7-1<br>(CD80) |           | Costimulatory protein on APCs         |
| CD3            |           | Signaling unit of the TCR/CD3 complex |

|  |  |  |
|--|--|--|
| <b>CD4</b>   |  | Coreceptor binding to MHC  |
| <b>CD28</b>  |  | Costimulatory receptor for B7-1  |
| <b>CD45</b>  |  | Tyrosine phosphatase for ITAMs   |
| <b>CTLA-4 (CD152)</b>                                  | Cytotoxic T-lymphocyte-associated protein 4                        | Inhibitory receptor for B7-1   |
| <b>DAG</b>   | Diacylglycerol   | Second messenger signaling lipid; product of PIP <sub>2</sub> hydrolysis |
| <b>GADS</b>  | GRB2-related adaptor downstream of Shc                             | Adaptor protein  |
| <b>ICAM-1 (CD54)</b>                                   | Intercellular Adhesion Molecule 1                                  | Adhesion molecule binding to LFA-1                                       |
| <b>IL-2</b>  | Interleukin 2  | Cytokine; stimulates T cell proliferation                                |
| <b>IP<sub>3</sub></b>                                  | Inositol 1,4,5-triphosphate  | Second messenger; product of PIP <sub>2</sub> hydrolysis                 |
| <b>LAT</b>   | Linker for activation of T cells                                   | Central adaptor protein; substrate for ZAP-70                            |
| <b>Lck</b>   | Lymphocyte-specific tyrosine kinase                                | Tyrosine kinase for ITAMs and ZAP-70                                     |
| <b>LFA-1 (<math>\alpha_L\beta_2</math>, CD11aCD18)</b> | Lymphocyte function-associated antigen 1                           | Integrin; ligand to ICAM-1; costimulatory                                |
| <b>MAPK</b>  | Mitogen-activated protein kinase                                   | Protein kinase specific to Serine and Threonine                          |
| <b>NFAT</b>  | Nuclear factor of activated T-cells                                | Family of transcription factors  |
| <b>NF-<math>\kappa</math>B</b>                         | Nuclear factor $\kappa$ -light-chain-enhancer of activated B cells | Controls transcription of cytokine production                            |
| <b>PIP<sub>2</sub></b>                                 | Phosphatidylinositol 4,5-biphosphate                               | Hydrolysis substrate for PLC $\gamma$ 1                                  |
| <b>PLC<math>\gamma</math>1</b>                         | Phospholipase C $\gamma$ 1   | Catalysator for PIP <sub>2</sub> hydrolysis; binds to SLP-76 and LAT     |
| <b>SLP-76</b>  | SH2 domain-containing leukocyte protein of 76kDa                   | Adaptor protein; substrate of ZAP-70                                     |
| <b>ZAP-70</b>  | $\zeta$ -chain associated protein kinase 70                        | Tyrosine kinase for LAT; binds to phosphorylated ITAMs                   |

Table 2. Proteins involved in T cell activation



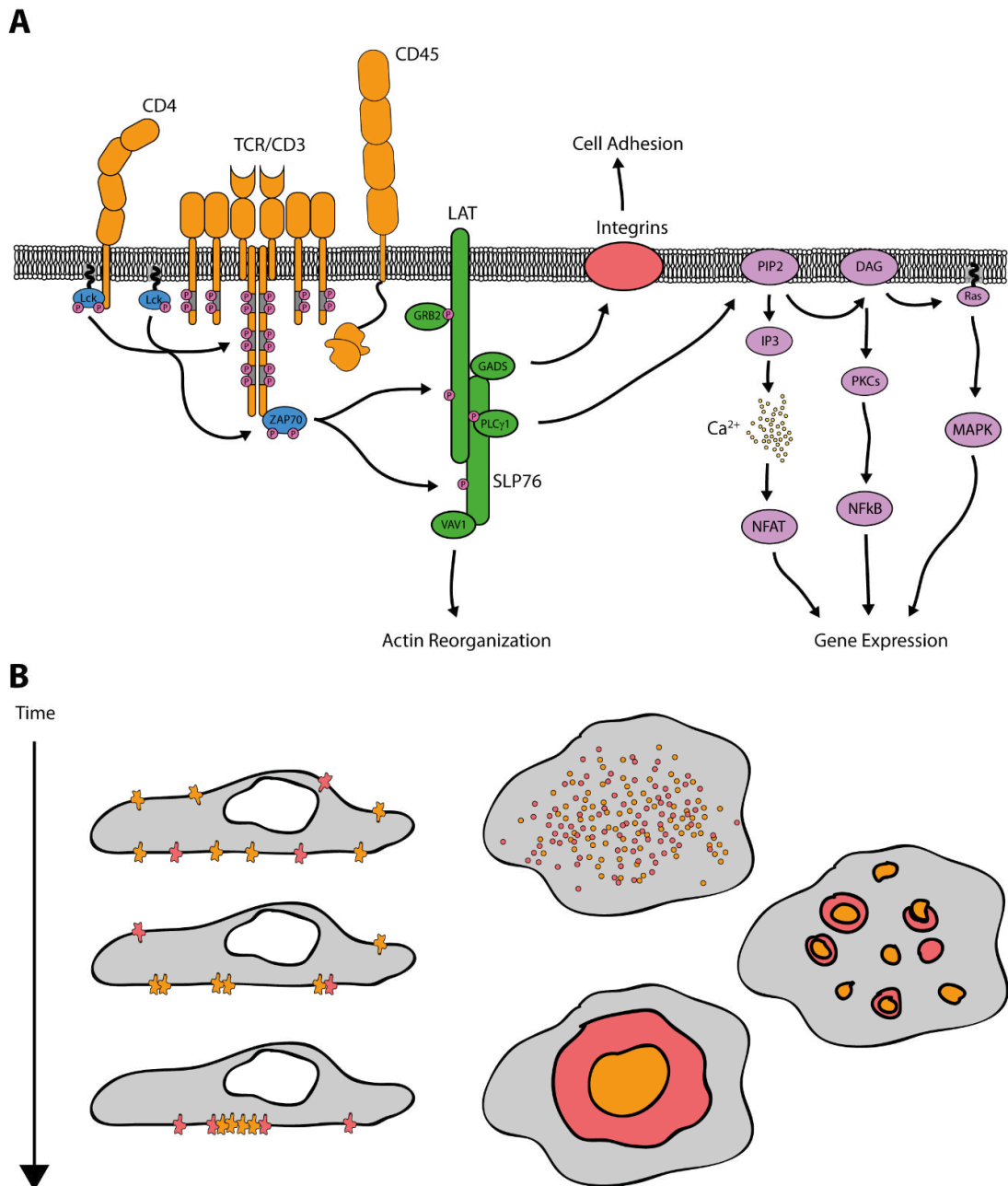


**Figure 18. Signaling pathway and spatial redistribution induced by T cell activation**

**A)** Upon ligand binding, the ITAMs present on CD3 subunits are phosphorylated by Lck. The signal is transmitted to the LAT signalosome by ZAP-70, which leads to altered Actin organization, cell adhesion and gene expression. **B)** The TCR/CD3 complex, CD4 and Lck are transported to the center of the interface area (yellow; cSMAC), which is surrounded by adhesion molecules (e.g. LFA-1, red, pSMAC). The pSMAC is furthermore surrounded by the dSMAC, where the phosphatase CD45 is located (gray).

A plethora of studies gave rise to different models of how a T cell transmits the TCR binding event into cytosolic signaling and how it translates to decision making.

Amongst the more prominent models are the kinetic proof-reading model, which is based on affinity of the TCR to the pMHC, and the kinetic segregation model, which describes the activation process by size-exclusion of the large phosphatase CD45. Other proposed models are based on mechanical properties, conformational changes, changes in receptor environment, or changes in the spatial distribution of receptors. Most of these models are not exclusive and some are outlined in the following:

### Kinetic Proof-Reading

The kinetic proof-reading model (**Figure 19**) proposes that TCR signaling depends mainly on the binding time between pMHC and the TCR. Only if the binding is sustained for a sufficient period of time, all intermediate signaling steps can be realized [155, 156].

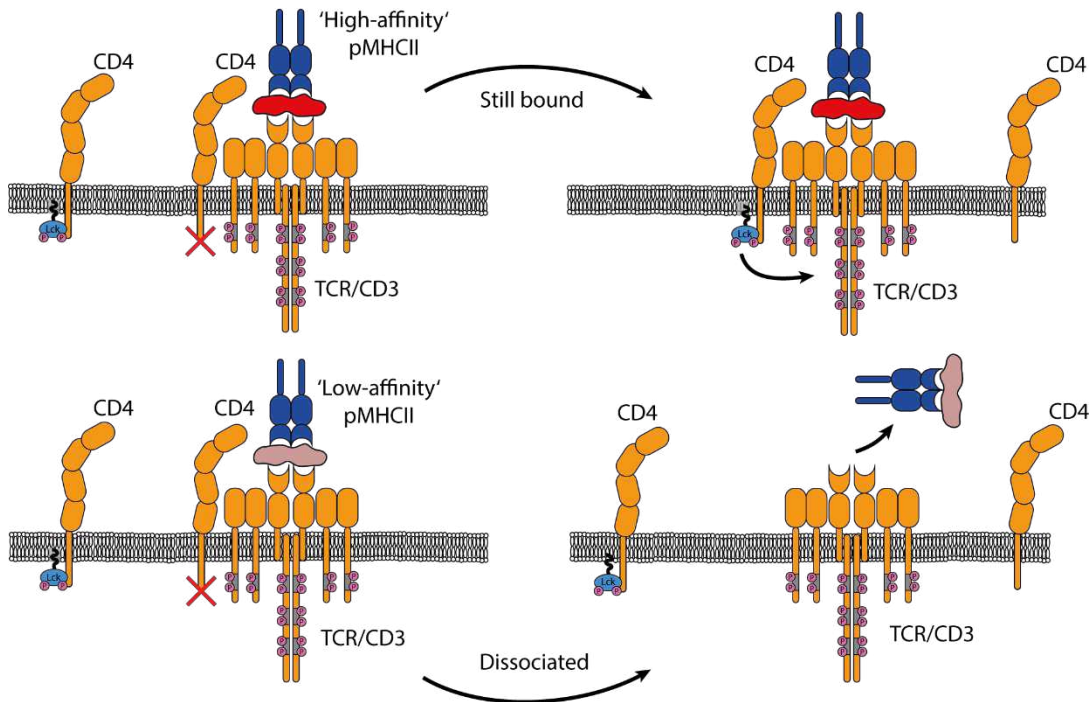


**Figure 19. Proposed Activation Models: Kinetic Proof-Reading Model**

*Top: Upon binding to a high-affinity ligand, the bond of TCR and pMHC persists and thus the probability for downstream events is increased. This includes phosphorylation, but also other events such as ZAP-70 recruitment, or the emergence of the LAT signalosome. Bottom: For low-affinity ligands, the binding time is not long enough for downstream events to be initiated. The T cell is therefore not activated.*

In contrast, dissociation before completion of all key events abruptly stops and reverses all previously triggered steps [157]. This model is independent of the

molecular mechanism of the initial triggering event and can be further supplemented by the following models. Most recently, application of an opto-genetic system, which enabled selective control of ligand binding dynamics, further supported the kinetic proof-reading model [158].

### Kinetic Segregation

Another well-known model is the kinetic segregation model, which was initially proposed by Springer in 1990 [159] and given its name by Dustin et al in 2000 [160]. It is based on size exclusion of CD45, which is responsible for the de-phosphorylation of the ITAMs on the CD3 subunits (**Figure 20**) [161]. CD45 shows a large extracellular domain with approximately 20-50 nm in length, depending on its splicing variant [162]. Due to the fact that no external restrictions on the movement and the accessibility of the TCR and CD45 are present in the basal state of the T cell, an equilibrium state between phosphorylation and de-phosphorylation of the ITAMs by Lck and CD45, respectively, exists. Binding of the TCR to pMHCs, however, locally reduces the available extracellular space to a distance equal to the combined TCR:pMHC size of 10-15 nm [163] by aligning the cellular membranes of the APC and the T cell. Thus, CD45, due to its large extracellular domain, is excluded, the equilibrium is shifted towards phosphorylation, and T cell activation is initiated.

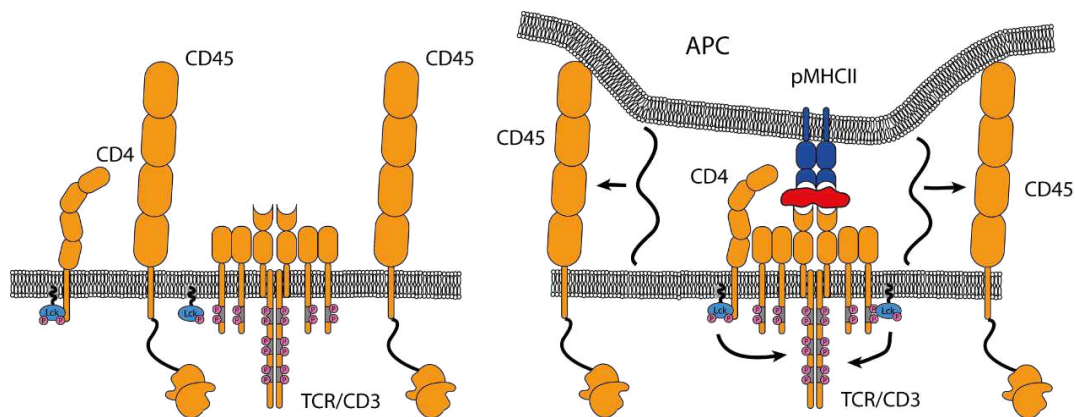


**Figure 20. Proposed Activation Models: Kinetic Segregation**

The kinetic segregation model describes T cell activation by a shift in (de-)phosphorylation equilibrium by steric exclusion of the phosphatase CD45. Thus, the equilibrium is shifted towards phosphorylation of the ITAMs and T cell activation is induced.

### Conformational Changes and Force

Ligand binding induces conformational changes and is responsible for signal transmission across the membrane in many receptor species. For the TCR, most of the identified structural changes upon binding pMHC localize to the binding site itself [164]. However, a model was proposed recently, in which the availability of the ITAMs plays a crucial role. CD3 subunits contain basic-rich sequences in their cytoplasmic domains, which result in binding to the negatively charged inner leaflet of the T cell membrane [165], and in burying of the tyrosine residues within the membrane (Figure 21) [166].

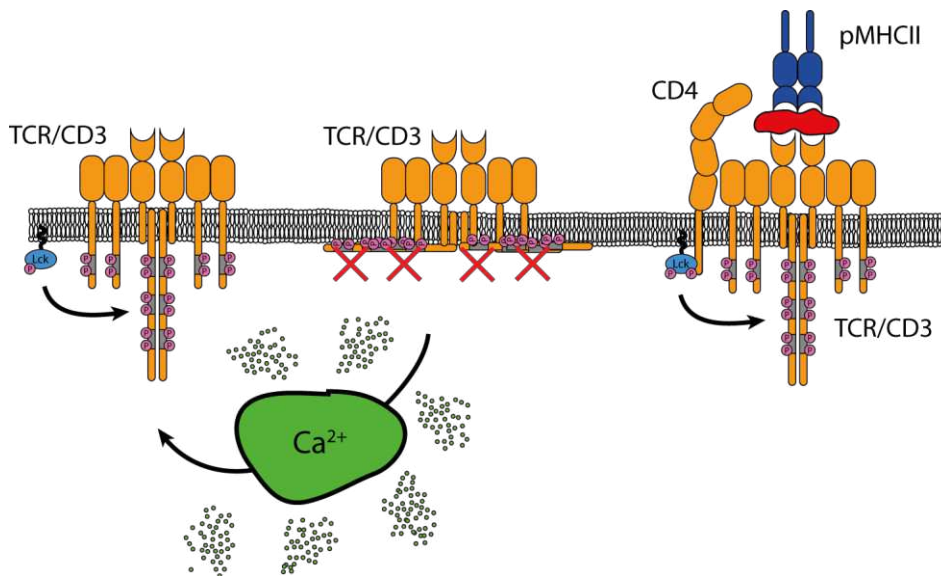


**Figure 21. Proposed Activation Models: Membrane-Associated ITAMs**

The availability of ITAMs for phosphorylation might be diminished in resting T cells. Due to basic regions, the CD3ε and CD3ζ subunits are positively charged, and are therefore able to bind negatively charged lipids at the inner leaflet of the cellular plasma membrane. As a result, the ITAMs are buried within the membrane and not accessible to phosphorylation. Conformational changes, changes in charge distribution or changes in the lipid environment may give rise to accessible ITAMs and consequently to their phosphorylation and the activation of T cells.

Ligand binding, conformational changes, locally changed charge distributions [167] or altered lipid environments [168] might free the cytoplasmic domains from the membrane, rendering them available for phosphorylation. An allosteric model proposes that cholesterol binding to the TCRβ inhibits activation and only spontaneous unbinding of cholesterol renders the TCR ready for phosphorylation ('primed' TCR; Figure 22). This primed state is further stabilized by ligand binding [169]. However, direct causes for hypothesized conformational changes still need to be addressed. Furthermore, several studies propose the TCR to be a mechanosensitive receptor (Figure 23) [170]. Lateral forces, experimentally realized by optical tweezers, were found to be responsible for conformational changes [171-

173]. Such forces were also reported to be the basis for a binding-induced 'closing' of the CD3 $\zeta$  homodimer (Figure 24) [174].

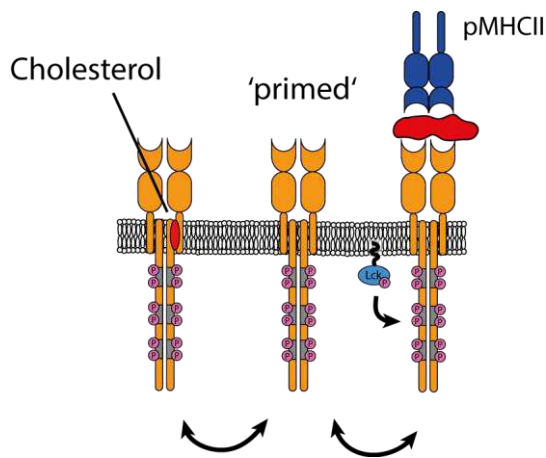


**Figure 22. Proposed Activation Models: Cholesterol Allostery**

Binding of Cholesterol might prevent the TCR to switch to a 'primed' state, in which phosphorylation can occur. From this primed state only, ligand binding and further T cell activation can be initiated.

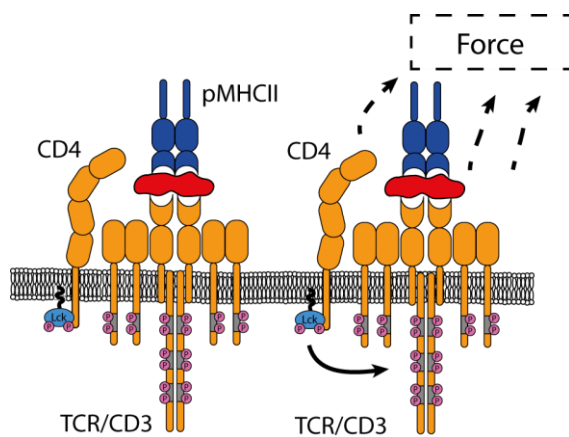


**Figure 23. Proposed Activation Models: Force Sensing**

Some studies showed that the force applied on the TCR complex influences the receptor's activation process.

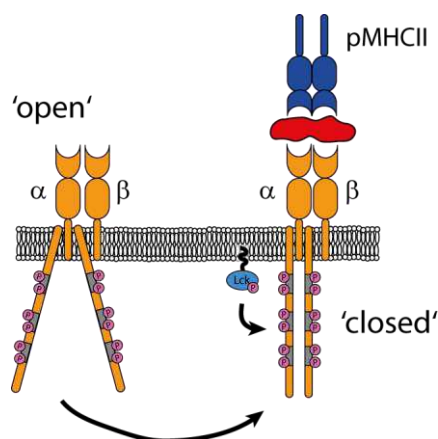


**Figure 24. Proposed Activation Models: Conformational Changes**

Binding of a ligand induces changes in the angle between the two  $\zeta$  subunits of the  $\zeta$  homodimer. Upon binding, the conformation changes to a closed state, and phosphorylation of the ITAMs can happen.

### Role of Clustering in Signal Initiation

Since the fluid lipid bilayer model has been put forward by Singer and Nicolson in 1972 [175], the cellular membrane has been imagined as a surface consisting of randomly mixed lipids and proteins. However, in the 1980's, a study reported high compartmentalization within cellular membranes [176]. The existence of domains enriched in cholesterol, sphingolipids and certain proteins was proposed and termed lipid rafts [176-178]. Using more advanced and less invasive methods, the spatiotemporal scale of potentially existing domains could be narrowed down substantially. If those domains existed, they would have to be very small and short-lived [86, 179-181]. A different model for membrane compartmentalization is based on observed restrictions to lateral diffusion of membrane proteins and lipids [182]. These diffusion barriers are thought to be attributed to the underlying cytoskeleton acting as a fence within the membrane [183].

In regard to T cell activation, a further model has been put forward, which defines the mechanism of triggering being based on the (re)distribution of the involved key proteins, such as the TCR/CD3 complex, Lck or LAT. This model emerged from the first observation of spatial protein domains on membrane sheets. Contrary to lipid rafts, these domains were termed protein islands. Lillemeier et al described clustering of nearly all membrane proteins within cholesterol-enriched and actin-linked areas on the membrane by using transmission electron microscopy (EM) [184]. In a follow-up study, this concept was supported by SMLM experiments on T cells. The TCR/CD3 complex and LAT were described to be aggregated in separated clusters of about 7-20 molecules with 35-70 nm radius [129]. Additional studies revealed clustering also for ZAP70, PLC $\gamma$ 1, SLP-76, Lck and CD4 [185-187]. The SMLM studies on the TCR/CD3 complex are furthermore in accordance with earlier biochemical and EM data, with which higher order oligomers were identified. For LAT and Lck, however, only monomers were detected by biochemical methods [115]. Also, the reported numbers of molecules per cluster vary significantly, questioning the quantitative character of the used methods: While SMLM analysis proposed 7-20 molecules per cluster, EM studies showed clusters with more than 7 molecules in only 1.4% of detected clusters [115, 129]. While the molecular mechanisms for these potential aggregations are still unresolved, dependence on cholesterol and sphingomyelin highlights similarities to lipid rafts [115, 188]. The large redistribution of membrane proteins upon T cell activation into microclusters as well as varying extents of aggregation between different subtypes of T cells, strengthens the hypothesis that T cells actively regulate clustering [129, 189, 190].

In a recent study by Pigeon et al [191], a potential functional role was ascribed to these nanoclusters. According to this model, the receptor-receptor spacing determines the probability for a single TCR to initiate signaling. Hence, TCRs residing in clusters show increased activation probabilities. The importance of receptor spacing during the process of T cell activation was recently confirmed by using nanofabricated array platforms [192].

While the role of clustering for activation is undisputed, the existence of nanoclusters in non-activated T cells is still controversial. There is justifiable uncertainty on how much the variability in published results is derived from non-appropriate choices of methodological approaches. This highlights the need for confirmation by more reproducible and more direct, while less invasive means, as will be realized within this work.



Die approbierte gedruckte Originalversion dieser Dissertation ist an der TU Wien Bibliothek verfügbar.  
The approved original version of this doctoral thesis is available in print at TU Wien Bibliothek.



---

## Chapter 2

# Materials & Methods

## 2.1. Cell Biology and Sample Preparation

### 2.1.1. Cell Culture, DNA Constructs, Antibodies and Reagents

All chemicals and cell culture supplies used to perform the experiments in this work were purchased from Sigma-Aldrich if not stated otherwise.

Primary 5c.c7 transgenic murine T cells were isolated from lymph nodes or the spleen and cultured in RPMI 1640 with 10% fetal bovine serum (FBS), 2 mM L-glutamine, 1 kU/ml Penicillin-Streptomycin, 50  $\mu$ M  $\beta$ -mercaptoethanol and 1 mM sodium pyruvate. For retroviral infection of T cells, the phoenix packaging cell line was used. Cells were cultured in DMEM medium with 10% FBS, 2 mM L-glutamine, 1 kU/ml Penicillin-Streptomycin. Both the murine T cells and the Phoenix cell line were grown in a humidified atmosphere at 37°C and 5% CO<sub>2</sub>.

For the expression of the CD3 $\zeta$ -PS-CFP2 fusion protein in murine T cells, the sequence of murine CD3 $\zeta$  was cloned, in frame with PS-CFP2, into the pIB2 retroviral expression vector.

Within this work, two different antibodies were used, one of which was specific for TCR $\beta$  (clone: H57), the other one for CD3 $\epsilon$  (clone: KT3). H57 conjugated to AF647 was purchased from Biolegend with an average degree of labeling (DOL) of 7.4. KT3 was purchased unconjugated from AbD Serotec/Bio-Rad Technologies and conjugated to AF647 using NHS-ester chemistry according to the supplier's instructions. Unreacted dye was removed using Zeba desalting columns (Thermo Fisher Scientific). An average DOL of 3.8 was determined for the dye-conjugated KT3 antibody.

### 2.1.2. Isolation and Transduction of T Cells

The isolation and expansion of T cells was performed as described by Huppa et al [193].

Retroviral transduction of the T cells was conducted based on the methods stated by Zhong et al [194], however, slight adaptations have been performed. The retroviral transduction is described briefly in the following: On Day 1 after T cell isolation, 80% confluent Phoenix cells were co-transfected with 9  $\mu$ g pL-eco and 15  $\mu$ g pIB2-CD3 $\zeta$ -PS-CFP2 using TurboFect (Invitrogen Life Technologies). After two days of virus production, the medium containing the virus was collected, spun down to eliminate cell debris and used to infect 10<sup>6</sup> cells per ml virus via spin-infection in the presence of 10  $\mu$ g/ml polybrene and 50 U/ml interleukin-2. On Day 4 after T cell isolation, 10  $\mu$ g/ml blasticidine was added to achieve selection for transduced cells. The cells were afterwards expanded until Day 6 and dead cells were removed by density-dependent centrifugation using Histopaque-1119.

The experiments, in which the transduced T cells were used, were performed between Day 7 and Day 9 after the isolation.

### 2.1.3. Protein and Label Preparations

#### His<sub>12</sub>-pMHC Variants

His<sub>12</sub>-pMHC was prepared as reported earlier by Huppa et al [195]. To summarize the process briefly: expression of His<sub>6</sub>-I-E<sup>k</sup> $\alpha$  and His<sub>6</sub>-I-E<sup>k</sup> $\beta$  in *E. coli* was followed by refolding and loading with MCC<sub>88-103</sub> or MCC(ANP) space-holder peptide (Elim Biopharmaceuticals). Subsequent purification with a Ni<sup>2+</sup>-NTA resin affinity chromatography and consecutive size-exclusion chromatography with an Äkta Purifier system (GE Healthcare Life Sciences) ensured correctly folded and monomeric pMHC. Cysteine residues on the C- or N- terminus of purified peptides were conjugated to AF555 or AF647 via maleimide chemistry. In a subsequent step, purification of the dye-conjugated peptides was performed via HPLC (C18 reverse-phase HPLC; Thermo Fisher Scientific). The amino acid sequences of the peptides were CSDLIAYLKQATKGG for N-terminal labeling and SSDLIAYLKQATKGGSC for C-terminal labeling. MCC(ANP) loaded pMHC was mixed with the fluorescent peptides in PBS and 100 mM citric acid at pH 5.1 in 20-fold excess for two days. Consecutive S-200 size chromatography ensured the selection of properly folded and fluorescently labeled pMHC [2].

#### Bio-PS-CFP2

PS-CFP2 (Evrogen) was tagged with AVI (GLNDIFEAQKIEWHE) at the C terminus. This enabled site-specific biotinylation by the BirA ligase. The AVI tag was followed by a His<sub>12</sub>-Tag, which was cleavable by a 3C protease (LEVLFQGP; see **Figure 25**). MWG Operon (Eurofins) was used to synthesize this construct before it was integrated into the pET21a(+) vector by NdeI and HindIII. The expression of the construct was done in *E. coli* at 30°C for 3h. After the application of ultrasound to the *E. coli* cells, a Ni-binding buffer (50 mM Tris-HCl pH 8, 300 mM NaCl, 10 mM imidazole and 1 mM phenylmethylsulfonylfluorid) with a temperature of 4°C and a protease inhibitor cocktail (complete<sup>TM</sup>, Roche) were added to the cells. The cells were centrifuged, and the supernatant was filtered (Filtropur S 0.2  $\mu$ m, Sarstedt).

(A)

MSKGAELFTGIVPILIELNGDVNGHKFSVSGEGEGDATYGKLTLLKFICTTGKLPVPWPTLVATLSYGV  
 QCFSRYPDHMKQHDFFKSAMPEGYIQERTIFFEDDGNYKTRAEVKFEKDTLVSRIELTGTDFKEDGNI  
 LGNKMEYNYNATNVYIVADKARNGIKVNFKVRHNIKDGSVQLADHYQQNTPIGDGPVLLPDNHYLSTQ  
 SALS KDPNEKR DDMIYLEFVTAAAI THGMDELYKGGGSLNDIFEAQKIEWHEGSGGLEVLFGPPHHH  
 HHHHHHHH--

(B)

**CATATGAGCAAGGGCGCCGAGCTGTTACCGGCATCGTGCCCATCCTGATCGAGCTGAATGGCGATGT**  
 GAATGGCCACAAGTTCAGCGTGAGCGGGCAGGGGCGAGGGCGATGCCACCTACGGCAAGCTGACCCCTGA  
 AGTTCATCTGCACCACCGGCAAGCTGCCTGTGCCCTGGCCCACCCTGGTGCCACCCTGAGCTACGGC  
 GTGCAGTGCTTCTCACGCTACCCCGATCACATGAAGCAGCAGCACTTCTTCAAGAGCGCCATGCCTGA  
 GGGCTACATCCAGGAGCGCACCATCTTCTTCGAGGATGACGGCAACTACAAGACGCGCGCCGAGGTGA  
 AGTTCGAGGGCGATAACCCTGGTGAGTCGCATCGAGCTCACCGGCACTGATTTCAAGGAGGATGGCAAC  
 ATCCTGGGCAATAAGATGGAGTACAAC TACAACGCCACCAATGTGTACATCGTGGCCGACAAGGCCAG  
 GAATGGCATCAAGGTGAAC TCAAGGTCCGCCACAACATCAAGGATGGCAGCGTGCAGCTGGCCGACC  
 ACTACCAGCAGAAATACCCCATCGGGGATGGCCCTGTGCTGCTGCCCGATAACCACTACCTGTCCACC  
 CAGAGCGCCCTGTCCAAGGACCCCAACGAGAAGCGCGATCACATGATCTACCTCGAGTTCGTGACCCG  
 CGCCGCCATACCCACGGCATGGATGAGCTGTACAAGGGTGGCGGATCCGGCCTGAACGATATTTTTG  
 AAGCGCAGAAAATTGAATGGCATGAA GGTAGCGCGGTCTGGAAGTTCTGTTTCAAGGTCCGCATCAC  
 CATCACCATCACCACCACCATCATCATCAATAAAAGCTT

**Figure 25. Amino acid sequence and DNA sequence of the PS-CFP2-AVI-3C-His12 construct**

A) Amino acid sequence: black: PS-CFP2 protein, magenta: BirA ligase recognition site, brown: 3C protease cleavage site, red: His12 tag, green: linker sequences. B) DNA sequence: black: PS-CFP2 protein, magenta: BirA ligase recognition site, blue: 3C protease cleavage site, red: His12 tag, green: linker sequences. The construct is cloned within the 5' restriction enzyme *NdeI* and the 3' restriction enzyme *HindIII*, of which the cleavage sites are both highlighted in bold letters.

This process was followed by Ni<sup>2+</sup>-NTA affinity chromatography (Thermo Scientific). Further purification included anion exchange chromatography (MonoQ 5/50 GE Healthcare Life Sciences) and gel filtration (Superdex-200 10/300 GE Healthcare Life Sciences). After increasing the concentration of the monomeric PS-CFP2 fraction with Amicon Ultra-4 filters (10 kDa, Merck Millipore), biotinylation was realized via the BirA ligase (Avidity). Before checking the maturation of PS-CFP2 photometrically by absorbance measurements at 280 and 400 nm, His<sub>12</sub> was removed by digestion with the 3C protease (GE Healthcare Life Sciences), yielding the first part of the used probe, termed bio-PS-CFP2.

### 3xHis<sub>6</sub>-mSav-AS635

Monovalent streptavidin with an included cysteine mutation was produced as reported earlier [196, 197]. A. Ting (Massachusetts Institute of Technology, USA) kindly provided vectors encoding for active and inactive streptavidin subunits. Cation exchange chromatography was enabled by exchange of the His<sub>6</sub> tag with a glutamate tag (Glu<sub>6</sub>) on the active subunit. For further removal of Glu<sub>6</sub>, a recognition site for the 3C protease was added (see **Figure 26**).

(A)  
 MAEAGITGTWYNQLGSTFIVTAGADGALTGTYESAVGNAESRYVLTGRYDSAPATDGS~~GTALGWTVAW~~  
 (C)  
 KNNYRNAHSATTWSGQYVGGAEARINTQWLLTSGTTEANAWKSTLVGHDTFTKVKPSAASGG**LEVL**FQ  
**GP**EEEEEE-

(B)  
**CATATG**GCTGAAGCTGGTATCACCGGCACCTGGTACAACCAGCTGGGATCCACCTTCATCGTTACCGC  
 TGGTGTGACGGTGTCTGTGACCGGTACCTACGAATCCGCTGTTGGTAACGCTGAATCTAGATACGTTT  
 TGACCGGTTCGTTACGACTCCGCTCCGGCTACCGACGGTTCGGGAACCGCTCTGGGTTGGACCGTTGCT  
 TGGAAAAACAACCTACCGTAACGCTCACTCCGCTACCACCTGGTCTGGCCAGTACGTTGGTGGTGTGCTGA  
 (TGC)  
 AGCTCGTATCAACACCCAGTGGTGTGTTGACCTCCGGCACCACCGAAGCCAACGCGTGGAAATCCACCC  
 TGGTTGGTCACGACACCTTCACCAAAGTTAAACCGTCCGCTGCTTCCGGTGGT**CTGGAAGTCTGT**TT  
**CAAGGTCCGGAAGAGGAAGAGGAGTAATAAAAGCTT**

**Figure 26. Amino acid sequence and DNA sequence of the active streptavidin subunit construct**

**A)** Amino acid sequence: black: streptavidin, blue: 3C protease cleavage site, red: Glu<sub>6</sub> tag. For site-specific labeling, the alanine at position 106 was substituted by cysteine. **B)** DNA sequence: black: streptavidin, blue: 3C protease cleavage site, red: Glu<sub>6</sub> tag, sequence in braces: A106C mutation site. The construct is cloned within the 5' restriction enzyme NdeI and the 3' restriction enzyme HindIII, of which the cleavage sites are both highlighted in bold letters.

(A)  
 MAEAGITGTWYQLGDTFIVTAGADGALTGTYEAAVGNESRYVLTGRYDSAPATDGS~~GTALGWTVAW~~  
 KNNYRNAHSATTWSGQYVGGAEARINTQWLLTSGTTEANAWKSTLVGHDTFTKVKPSAASLEHHHHHH  
 -

(B)  
**CATATG**GCTGAAGCTGGTATCACCGGCACCTGGTACGCCAGCTGGGAGACACCTTCATCGTTACCGC  
 TGGTGTGACGGTGTCTGTGACCGGTACCTACGAAGCCGCTGTTGGTAACGCTGAATCTAGATACGTTT  
 TGACCGGTTCGTTACGACTCCGCTCCGGCTACCGACGGTTCGGGAACCGCTCTGGGTTGGACCGTTGCT  
 TGGAAAAACAACCTACCGTAACGCTCACTCCGCTACCACCTGGTCTGGCCAGTACGTTGGTGGTGTGCTGA  
 AGCTCGTATCAACACCCAGTGGTGTGTTGACCTCCGGCACCACCGAAGCTAACGCGTGGAAATCCACCC  
 TGGTTGGTCACGACACCTTCACCAAAGTTAAACCGTCCGCTGCTTCC**CTCGAGCACCACCACCAC**  
**CACTGA**

**Figure 27. Amino acid sequence and DNA sequence of the inactive streptavidin subunit construct**

**A)** Amino acid sequence: black: streptavidin, green: His<sub>6</sub> tag. **B)** DNA sequence: black: streptavidin, green: His<sub>6</sub> tag. The construct is cloned within the 5' restriction enzyme NdeI and the 3' restriction enzyme HindIII, of which the cleavage sites are both highlighted in bold letters.

The inactive subunits were additionally equipped with His<sub>6</sub> at the C terminus (**Figure 27**). For site-specific conjugation, a cysteine mutation was realized at position 106 (A106C) for the active subunit (**Figure 26**). Expression of the subunits was again realized by incubation of transformed *E. coli* at 37°C for 4h. In a subsequent step, refolding from inclusion bodies was facilitated via rapid dilution in PBS [197]. Concentration of tetramers was increased in two subsequent steps: first, in a stirred ultrafiltration cell (10 kDa, Merck Millipore) and afterwards, using Amicon Ultra-4 centrifugal filters (10 kDa, Merck Millipore). During the second step

of increasing the concentration, the buffer was exchanged to 20 mM Tris-HCl pH8. Anion exchange chromatography (MonoQ 5/50 GE Healthcare Life Sciences) with a gradient from 0.1 - 0.4 M NaCl was performed to select monovalent streptavidin tetramers.

Concentration was again increased by filtration with Amicon Ultra-4 centrifugal filters and purification of the tetramers by gel filtration (Superdex-200 10/300 GE Healthcare Life Sciences). Site-specific labeling with AbberiorSTAR635 via maleimide chemistry was performed according to the supplier's protocol [198], which yielded the second part of the used probe, termed 3xHis<sub>6</sub>-mSav-AS635.

In order to reduce unspecific binding of bio-PS-CFP2 to the adhesive surface, we realized the conjugation to mSav beforehand. Bio-PS-CFP2 was mixed with 3xHis<sub>6</sub>-mSav-AS635 at 12x excess at room temperature for 2 h. The bio-PS-CFP2: 3xHis<sub>6</sub>-mSav-AS635 complex was consequently purified by gel filtration (Superdex 200 10/300, GE Healthcare Life Sciences).

To validate the probe, SDS-PAGE and silver staining was used. After mixing with 4x loading buffer (252 mM Tris-HCl, 40% glycerol, 8% SDS, and 0.04% bromophenol blue, pH 6.8) and 20 mM dithiothreitol (Merck), the sample was offered non-reducing and reducing conditions, respectively. Gel electrophoresis was performed using 10% SDS-PAGE in running buffer (25 mM Tris-HCl, 192 mM glycine and 0.1% SDS, pH 8.2). For the visualization of protein bands on the gel, silver staining was done as reported previously [199].

### Preparation of Single-Chain Fragments for TCR/CD3 Complex Labeling

Single-chain fragments specific to TCR $\beta$  (clone: H57) or CD3 $\epsilon$  (clone: KT3) were prepared and labeled with AF647, AF488, AS635 or AS635P as described by Huppa et al and Brameshuber et al [2, 195]. To describe the process briefly, H57-597 or KT3 hybridoma (American Type Culture Collection) were used to prepare mRNA, which then served for 5' rapid amplification of cDNA ends (RACE, Invitrogen). The variable-region domains V<sub>H</sub> and V<sub>L</sub> were fused and a cysteine mutation was introduced by application of the Quikchange protocol (Stratagene) [200]. Inclusion bodies were refolded and a S-200 size-exclusion column (GE Healthcare) was used to purify the single-chain fragments. The introduced cysteine was used for site-specific conjugation via maleimide chemistry to AF488, AF647, AS635 and AS635P by incubation for 2 h in 50  $\mu$ M tris(2-carboxyethyl) phosphine hydrochloride (TCEP, Pierce). S-75 size-exclusion chromatography (GE Healthcare) was used to purify monomeric, fluorescently labeled scFv.

A DOL of close to one was achieved for all fluorescent labels except AS635. For H57-scFv-AS635, a maximum DOL of 0.55 was reached, which disqualified the probe for most experiments except single-molecule tracking.

For the experiments in which streptavidin-crosslinked scFv was used, a cysteine was added to the C-terminus of both donor and acceptor scFv probes. The donor was conjugated to TCO (Jena Bioscience) via maleimide chemistry and further labeled with a biotinylated linker peptide (biotin-GGGGSY(GGGGS)<sub>2</sub>KGGGGSC-maleimide-6-Me-tetrazine, Elim Biopharmaceuticals). The biotinylated donor scFv

was conjugated to AF555 at the lysine residues (underlined in aforementioned brackets depicting the biotinylated linker peptide) by NHS ester chemistry. The acceptor probe was conjugated to DBCO (Jena Bioscience) via maleimide chemistry and further labeled with a biotinylated linker peptide (biotin-GGCGS(GPGGA)<sub>5</sub>GGKYGGSK-azide, INTAVIS). The biotinylated acceptor scFv was conjugated to AF647 at the primary amine of the lysine (underlined in aforementioned brackets depicting the biotinylated linker peptide) by NHS ester chemistry. Before conjugation of the scFv to the biotinylated peptides, the peptides were purified by C18 reverse-phase HPLC.

### 2.1.4. Sample Preparation Procedures

#### Glass-supported Lipid Bilayer (SLB) Preparation

All lipids were purchased from Avanti Polar Lipids. T cell experiments were performed on bilayers consisting of 90% 1-palmitoyl-2-oleoyl-sn-glycero-3-phosphocholine (POPC) and 10% 1,2-dioleoyl-sn-glycero-3-[(N-(5-amino-1-carboxypentyl)iminodiacetic acid)succinyl] (nickel salt) (18:1 DGS-NTA(Ni)). Vesicles were produced following the protocol described in Huppa et al [195] and used in a dilution of 1:10 in PBS for bilayer formation. To create immobile bilayers, 100 µg DPPC and 0.75 µg DGS-NTA(Ni) were mixed in chloroform. The mixture was dried with N<sub>2</sub>, dissolved in 1 ml pre-heated 50°C PBS and sonicated at 50°C for 15 min. The vesicle solution was not diluted further and used for experiments within two days.

After plasma cleaning of the glass cover slides (#1.5, 24x60 mm, Menzel) and attaching them to 8-well LabTek chambers (Nunc), they were incubated with the vesicle suspension for 10 min at either room temperature or 50°C for POPC/DGS-NTA(Ni) and DPPC/DGS-NTA(Ni), respectively. Glass slides were rinsed extensively with PBS and functionalized with either of the following:

- i) His<sub>10</sub>-ICAM-1 (sinobiological),
- ii) His<sub>10</sub>-ICAM-1, His<sub>10</sub>-B7-1 (sinobiological) and His<sub>12</sub>-pMHC or
- iii) 3xHis<sub>6</sub>-mSav-AS635:bio-PS-CFP2.

For FRET experiments, a mixture of His<sub>12</sub>-tagged MCC/IE<sup>k</sup>-AF555, MCC/IE<sup>k</sup>-AF647, His<sub>10</sub>-ICAM-1 and His<sub>10</sub>-B7-1 was used. In those experiments, the pMHC molecules were both either conjugated at the C-or the N-terminus, yielding four different combinations.

After an incubation time of 75 min, the bilayers were rinsed extensively with PBS. For T cell experiments, the buffer was subsequently changed to imaging buffer (HBSS + 2% FBS) by sequential dilution.

### Labeling of T Cells with Antibodies or scFv

All TCR labeling steps were performed at 4°C with approximately  $10^6$  T cells.

For tracking experiments, T cells were labeled at low densities with H57-scFv-AF647, H57-scFv-AF488 or H57-scFv-AS635 by using a dilution with non-fluorescent H57-scFv at a molar ratio of 1:5 for 15 min.

For TOCCSL, PA/FCS, FRET and STED experiments, T cells were labeled with saturating concentrations of the probes as indicated for 15 min. For reliable estimation of the PSF of the STED system, H57-scFv-AS635P was mixed with non-fluorescent H57-scFv at a molar ratio of 1:10 which leads to fluorescent labeling of T cells at single-molecule density.

Labeling for dSTORM experiments was performed using full antibodies ( $\alpha$ TCR $\beta$  and  $\alpha$ CD3 $\epsilon$ ). Therefore, unspecific binding sites were blocked by incubation with 5% BSA for 25 min. For label variation microscopy, it is necessary to use varying concentrations of antibody: T cells were incubated with 0.05, 1, 5 and 10  $\mu$ g/ml H57-AF647, or 0.02, 0.2, 2, 10 and 20  $\mu$ g/ml KT3-AF647 for 20 min. To achieve non-activating conditions while facilitating labeling with KT3-AF647, the T cells were in this case labeled after adhesion and fixation.

To follow micro-cluster formation in advance to the PALM experiment using CD3 $\zeta$ -PS-CFP2, the T cells were additionally labeled with H57-scFv-AF647.

The T cells were washed twice before addition to the SLBs. Settling times of 15 min and 5 min were chosen on non-activating and activating SLBs, respectively. No further processing of the sample was performed for live-cell experiments (SMT, TOCCSL, PA/FCS, FRET and PALM).

Fixation of cells was conducted using 4% paraformaldehyde (PFA; Polysciences) with 0.2% glutaraldehyde (GA) at room temperature for 10 min. As labeling with KT3-AF647 in non-activating experiments was done after fixation, the sample was fixed again for 10 min after finishing the antibody labeling procedure.

In calcium imaging experiments, Fura2-AM (Molecular Probes) labeling at 5  $\mu$ g/ml for 20 min at room temperature preceded all further labeling steps. The cells were washed twice in imaging buffer before the TCR labeling was performed as described above.

## 2.2. Microscopy Imaging

### 2.2.1. Microscopy Systems

#### Single Molecule System

All SMT, TOCCSL, FRET and SMLM experiments were performed on the following microscopy system:

A high NA (1.46) 100x Plan-Apochromat (Zeiss) objective was used within an inverted Zeiss Axiovert 200 microscope. TIRF configuration was realized using a piezo-controlled mirror to move the laser beam away from the center of the objective, thus reaching illumination at the critical angle. 405 nm (diode, iBeam smart 405, Toptica), 488 nm (optically pumped semiconductor, Sapphire, Coherent),



532 nm (solid-state, Millennia Pro, Spectra-Physics) and 640 nm (diode, iBeam smart 640, Toptica) laser lines were used and partly (488 and 532 nm) controlled by acousto-optic modulators (AOM) using a homemade Labview software package. TOCCSL data was recorded on a back-illuminated, liquid N<sub>2</sub>-cooled coupled-charge device camera (Micro-Max, Roper Scientific). All other data was recorded on an iXon DU897 electron multiplying coupled-charge device camera (Andor).

In SMT, TOCCSL and dSTORM experiments, the excitation and emission lines were separated by a zt488/640rpc dichroic mirror (Chroma) and the emission was filtered by a FF01-548/685-25 filter (Semrock). For two-color TOCCSL, a custom-made dichroic wedge (Chroma) was used to split the two colors.

For two-color PALM experiments ( $\zeta$ -PS-CFP2 and H57-scFv-AF647, or bio-PS-CFP2: 3xHis<sub>6</sub>-mSav-AS635), a dual view system (Photometrix), including a 640dcsr dichroic mirror and FF01-525/45 and HQ700/75m emission filters (all Chroma) was used.

For FRET experiments, the Dual View system was again utilized. Emission was separated from excitation by a quad filter (R405/488/532/635, Semrock), and split up by a 640dcsr dichroic mirror. Emission was further selected by HQ585/40m and HQ700/75m band-pass filters (all Chroma).

### Calcium Imaging

An Axiovert 200M (Zeiss) microscope equipped with a 20x objective (Olympus) was used in combination with a monochromatic light source (Polychrome V, TILL Photonics) to facilitate illumination at 340 nm and 380 nm. A longpass filter (T400lp, Chroma) and an emission filter were used (510/80ET, Chroma) to selectively measure the emission, and an iXon Ultra (Andor) electron multiplying coupled-charge device camera was used to facilitate the recording.

### PA/FCS and STED system

A custom-built STED system consisting of a 635 nm (< 100 ps pulsed diode, LHD-D-C-635, PicoQuant) and an 800 nm (Ti:Al<sub>2</sub>O<sub>3</sub>, Mira900, Coherent) laser line was used for excitation and STED, respectively. An oil-immersion objective (HC PL APO 100x/1.4 CS2, Leica) was used for excitation and emission. The emission light was de-coupled via a dichroic mirror (zt625-745rpc, Chroma) and split into four channels by 50:50 beam splitters. The light was further band-pass filtered (685/70ET, Chroma) and led to four avalanche photodiodes (SPCMAQR-13-FC, Perkin Elmer Optoelectronics) via multimode fibers. Additionally, STED light was blocked by a short pass filter (ET750sp-sp, Chroma). Scanning of the sample was realized by a 3-axis piezo stage (Tritor 102 Cap, Piezosystem Jena).

## 2.2.2. Imaging Protocols

### Ca<sup>2+</sup> Imaging

Image acquisition for Ca<sup>2+</sup> experiments was started before the addition of T cells, in order to capture the very first activities of the cells, when encountering the SLBs.

Imaging was conducted for at least 10 min at 1 Hz, with illumination times of 50 and 10 ms at 340 and 380 nm, respectively. The sample was embedded in imaging buffer for all these experiments.

### SMT

For SMT experiments of the TCR/CD3 complex, 200 images were acquired at 20 Hz with illumination times of 2 – 5 ms. The laser power was adjusted to prevent excessive photo-bleaching during the acquisition time.

The immobile character of the DPPC-based bilayer was verified by tracking the 3xHis<sub>6</sub>-mSav-STAR635:bio-PS-CFP2 complex over pro-longed time. Images were acquired at 0.5 Hz with ~1.5 kW/cm<sup>2</sup> and tracked for up to 120 frames. Furthermore, the 3xHis<sub>6</sub>-mSav-STAR635:bio-PS-CFP2 complex was tracked for a shorter period to determine its average position, right before starting the PALM imaging experiment. This tracking was conducted with an image acquisition rate of 100 mHz at ~1.5 kW/cm<sup>2</sup> 640 nm. The complex was imaged for at least 50 frames.

### TOCCSL

The first step of the TOCCSL measurements was the recording of a pre-bleach image (5 ms illumination time, 1 kW/cm<sup>2</sup>). Consecutively, a bleach pulse was applied (400 ms, 5 kW/cm<sup>2</sup>), which was followed by an image acquired with 1 ms delay verifying complete photo-bleaching. Afterwards, the molecules were allowed to recover for 2 – 10 s. The same illumination time and laser power were then used to record up to 18 images at 50 Hz. In two-color TOCCSL measurements, a delay of 20 ms between the pre-bleach images was introduced, while the bleach pulse was applied in both color channels simultaneously. The images of recovered complexes were either recorded simultaneously (for TOCCSL analysis) or with a delay of 1 ms (for FRET event analysis).

### PA/FCS

PA/FCS measurements were recorded for 180 s at 1 μW laser power at the back aperture. Controls on the probes in solution were recorded for 30 min at 5 μW. Additionally, the glass slide was coated with biotinylated BSA (Sigma-Aldrich) to prevent unspecific adhesion of the probe.

### FRET

To realize donor recovery after acceptor photobleaching, the following imaging protocol was applied: first, an image in the red channel was acquired, which was followed by a pre-bleach image in the AF555 channel. Both images were recorded with 5 ms illumination time at approximately 100 W/cm<sup>2</sup>. After application of 5 kW/cm<sup>2</sup> of 647 nm laser light for 200 ms, the red channel was sufficiently bleached. Another image in the AF555 channel was recorded to detect possible intensity increase by FRET quenching. In order to validate bleaching in the red channel, an additional image was recorded in the red channel.

## SMLM

dSTORM experiments on fixed T cells were performed at 100 – 167 Hz with illumination times of 2 – 3 ms. 7,500 – 10,000 frames were acquired at 640 nm with 1.5 – 3 kW/cm<sup>2</sup> and with an additional 405 nm illumination at 20 – 30 W/cm<sup>2</sup>. All experiments were performed in dSTORM buffer consisting of PBS, 10% glucose, 500 µg/ml glucose oxidase, 40 µg/ml catalase and 50 mM cysteamine [66].

PALM experiments were performed at 100 – 167 Hz with illumination times of 2 – 3 ms. 4,000 or 10,000 frames were acquired at 488 nm with 1.5 – 3 kW/cm<sup>2</sup> and with an additional 405 nm illumination at 20 – 30 W/cm<sup>2</sup> for live and fixed T cells, respectively.

For the evaluation of PS-CFP2 blinking, 488 nm power was either ~0.4 kW/cm<sup>2</sup> (for 15 ms illumination time) or ~3 kW/cm<sup>2</sup> (for two ms illumination time). Thus, the energy density on the sample was constant. PALM experiments were performed in imaging buffer when imaging T cells, and in PBS when evaluating PS-CFP2 blinking. For experiments evaluating the influence of reducing milieu, 10 mM glutathione was added to the sample in a ratio of 1:1, yielding an effective concentration of 5 mM glutathione.

## STED

In STED experiments, the sample was scanned with a pixel dwell time of 100 µs at a pixel size of 20 nm. Excitation was conducted with 50 fJ 635 nm, and depletion was realized with 1.6 nJ 700 nm. The laser power was measured at the back aperture of the objective. The gating time was set to 0.8 – 7 ns relative to the excitation. STED experiments were performed in a ROXS buffer system to minimize bleaching effects. This buffer consisted of 2 mM Trolox, 1 mM methylviologen-dichloride hydrate, 50 µM glucose oxidase, 300 U/ml catalase and 5%wt glucose [65].

### 2.2.3. Image Analysis

#### Single-Molecule and Single-Cell Localization, Tracking and Post-Processing

For single-cell tracking in Ca<sup>2+</sup> data, an inhouse implementation of the algorithm described by Gao et al [201] was used for localization of the cells.

Fitting of single molecules in data derived from tracking, SMLM and STED experiments was performed using the ImageJ plug-in thunderSTORM [202]. Briefly, a wavelet filter was applied, local maxima were identified by thresholding, and a Gaussian intensity distribution was fitted using maximum likelihood estimation (MLE). The thereby identified signals were further filtered for intensity,  $\sigma$  and the positional accuracy of the fit.

MLE-fitting of single molecules in TOCCSL data was conducted as described earlier [93].

Tracking of Ca<sup>2+</sup> and SMT data was again realized by an inhouse implementation of the algorithm described by Gao et al [201]. The respective parameters for tracking

were adapted to the expected mobility and the time lag used. Evaluation of the tracks was conducted using an inhouse implementation of the msd-vs-t analysis method. Additionally, a bi-exponential fit to the cumulative density function (cdf) of the MSD can report on the immobile fraction of TCR/CD3 complexes [203]. The *cdf* was fit to:

$$cdf = 1 - \alpha \cdot \exp\left(-\frac{r^2}{msd_1^2}\right) + (1 - \alpha) \cdot \exp\left(-\frac{r^2}{msd_2^2}\right) \quad (14)$$

with  $\alpha$ ,  $msd_1$  and  $msd_2$  being the fit parameters, and  $r^2$  the square displacements.

In dSTORM experiments, signals were merged with a maximum off-time of 50 frames and within a radius of the approximate positional accuracy, which was 35 nm. For reasons of comparability [129], CD3 $\zeta$ -PS-CFP2 signals were merged only if they appeared in consecutive frames and within a radius of half the pixel size, which equals 80 nm.

### Aberration Correction

In order to achieve an accurate overlay of the blue and red color channels, 200 nm diameter Tetraspeck (Thermo Fisher Scientific) fluorescent microspheres were imaged and a linear transformation was calculated, which facilitated that the color channels could be registered by shifting and stretching. This was applied for all two-color experiments.

### FRET Efficiency Determination

The fluorescence intensities were corrected by background subtraction to determine FRET efficiencies. The intensities within specified regions of interest (ROIs) were determined. The ROIs were either the full adhesion area of the cell, the cSMAC, or synaptic microclusters of the TCR/CD3 complex or pMHC. The intensities after ( $I_{post}$ ) and before ( $I_{pre}$ ) photo-bleaching of AF647 were used to determine the FRET efficiency:

$$E = \frac{I_{post} - I_{pre}}{I_{post}} \quad (15)$$

The image sequence was also run without a bleaching pulse, which enabled the correction of  $E$  for bleaching due to the imaging process itself.

### Estimation of Blinking Statistics and Surface Density

To estimate the blinking statistics of probes (H57-AF647, KT3-AF647 and CD3 $\zeta$ -PS-CFP2) used in SMLM experiments, cells labeled at low antibody concentrations and cells with a low expression level of CD3 $\zeta$ -PS-CFP2 were analyzed. This ensures that only single labels are analyzed. All localizations within a radius of one pixel to the first appearing signal were considered to belong to the same label. In addition to the

total number of appearances ( $N$ ), the number of consecutive frames a signal is emitting in the analyzed time period ( $t_{on}$ ), the duration of non-emissive dark states ( $t_{off}$ ) and the starting frame ( $t_{start}$ ) were evaluated.

For blinking evaluation of bio-PS-CFP2, only signals located within a radius of one pixel to a 3xHis<sub>6</sub>-mSav-AS635 signal were used for analysis. These 3xHis<sub>6</sub>-mSav-AS635 signals were additionally pre-filtered according to their nearest neighbors, and signals within a radius of four pixels to another 3xHis<sub>6</sub>-mSav-AS635 were eliminated. This rigorous filtering prevents false allocation of bio-PS-CFP2 signals. The surface density and the expression level of the TCR, CD3 and ζ-PS-CFP2 on T cells were estimated based on the total number of localizations within a full SMLM acquisition divided by the average number of localizations per label ( $N$ ).

### Determination of $\varrho$ and $\eta$

For the determination of  $\varrho$  and  $\eta$ , cluster maps were generated by inhouse MatLAB scripts in the following way: All localizations were convolved with a 2D Gaussian with fixed  $\sigma$  width of 35 nm. Consecutive summation of the Gaussians yielded higher values for neighboring molecules, i.e. clusters. A binary map was created by thresholding. According to the position of the localization, it was categorized as clustered or not. To avoid artificially enlarged clusters, the 2D Gaussians were cut and set to zero above  $2\sigma$ .

The relative clustered area  $\eta$  was calculated as the ratio of clustered area and total ROI area.  $\varrho$ , which reflects the density within the clustered area, was calculated as the total localizations within clusters divided by the clustered area. To determine  $\varrho_0$ , the data was fitted to the following polynomial:

$$\varrho = \varrho_0(1 + \alpha\eta^\beta) \quad (16)$$

with  $\alpha = 1.4$  and  $\beta = 4$  [204].

### Ripley's K Analysis

Ripley's K curves were generated by selection of a rectangular ROI within the cell borders.  $L(r) - r$  was evaluated at steps of 5 nm up to 750 nm. The analysis was realized by an inhouse MatLAB implementation.

### Image Auto-Correlation Analysis

For image auto-correlation analysis of STED images and simulations, a MatLAB script based on the correlation function *xcorr2* was used. Further angular averaging was performed using code provided by Sengupta et al [205]. To summarize the approach briefly, the level of background signal was estimated from non-cell regions and TCR densities were determined by dividing the mean intensity on the cell by the mean single-molecule intensity. Five different  $2 \times 2 \mu\text{m}$  ROIs per cell were selected for analysis, in a way that ensured that no cellular borders, or stacked membranes

were included. The results were compared to simulated images of random distributions with equal densities.

### Calcium Analysis

To identify and track single cells, the ratiometric acquisitions of Fura2-AM were summed pairwise. This enabled a more robust identification of single cells. The coordinates of the tracks were consequently used as basis for extracting the intensities from the ratio images. The traces were normalized to the initial values.

### Correlation analysis for PA/FCS

PA/FCS data was analysed as described previously (by Sykora et al) [99]. For small lag times, correlation functions were fitted by

$$A + B \sum_{j=0}^{\infty} e^{\left(-\frac{|t-jT_{rep}|}{\tau}\right)} - C e^{\left(-\frac{t}{\tau}\right)}. \quad (17)$$

The correlation curve for infinite lag time was fitted by

$$A' + B' \sum_{j=0}^{\infty} e^{\left(-\frac{|t-jT_{rep}|}{\tau}\right)}. \quad (18)$$

In both equations,  $T_{rep}$  is the repetition time of laser pulses and  $A$ ,  $B$ ,  $C$ ,  $A'$ ,  $B'$  and  $\tau$  are free fitting parameters, where  $\tau$  represents the fluorescence lifetime. Neglecting blinking, the mean number of emitters per entity is determined by  $n_{nt} = \frac{B-B'}{C}$ .

For the determination of the triplet population of AS635P, the FCS curves were fitted with 2D (on the plasma membrane) or 3D (in solution) diffusion models, taking one triplet state into account as follows:

$$2D: G^2(t) = \frac{\alpha + \beta e^{\left(-\frac{t}{\gamma}\right)}}{1 + \frac{t}{\delta}} + \sigma \quad (19)$$

$$3D: G^2(t) = \frac{a + b e^{\left(-\frac{t}{c}\right)}}{\left(1 + \frac{t}{d}\right) \sqrt{1 + \frac{t}{e}}} + f \quad (20)$$

Here, the fitting parameters are  $\alpha$ ,  $\beta$ ,  $\gamma$ ,  $\delta$ ,  $\sigma$ ,  $a$ ,  $b$ ,  $c$ ,  $d$ ,  $e$  and  $f$ .

These values were then used to correct the number of emitters per entity as follows:

$$n_{2D} = \frac{B - B' \alpha + \beta + \sigma}{C \alpha + \sigma} \quad (21)$$

$$n_{3D} = \frac{B - B' a + b + f}{C a + f} \quad (22)$$

## 2.2.4. Simulations

### Simulation of Spatial Distributions

The initial step for all simulations was the positioning of cluster centers and the consecutive generation of a probability mask. The density of clusters (clusters per  $\mu\text{m}^2$ ) and the cluster size were defined as input parameters. The clusters were described by a Gaussian profile with a  $\sigma$  of the cluster size, which was truncated at the cluster radius; overlapping regions were set to a probability of 0.9 to avoid unnatural high densities in these regions. Subsequently, the clusters were randomly filled until a fixed fraction of the total molecules (fraction of clustered molecules) were positioned. Additionally, non-clustered molecules were placed randomly around the clusters. A random distribution was described by a density of clusters of 0 per  $\mu\text{m}^2$ .

Depending on the degree of labeling, fluorescent labels were allocated to the molecular positions. In case of simulations for the label-variation method, the labeling probability was additionally varied (5% to 95%).

### Simulation of Blinking Localizations

To accord for blinking, each label was allocated a certain number of detections. The number was determined from the blinking characteristics recorded in the respective experiments. In case of label-density-variation SMLM, these were the experiments at low antibody concentrations or with cells expressing only low levels of CD3 $\zeta$ -PS-CFP2. Each detection was additionally shifted to a random direction to account for positional accuracy of the measurement system.

### Image Simulations

In order to further simulate images, the underlying distribution of labels was convolved with the PSF of the microscopy system, which was derived from single-molecule signals inherent to SMLM movies or for the STED system from sparsely labeled T cells. The intensity distribution of the single-molecule signals was fitted with a log-normal distribution [18]. We found that the width of the PSF,  $\sigma$ , depends on the intensity, and therefore fitted the following equation to this dependency:

$$\sigma(I) = a \left( 1 - \exp\left(-\frac{I}{b}\right) \right) \quad (23)$$

Simulated STED images were subsequently generated by distributing the molecular positions at a defined density and convolving these positions with a randomly sampled form of the PSF. For this, the intensity was selected from the log-normal distribution and a corresponding  $\sigma$  was calculated. Additionally, different types of noise were included: first, line-scanning was taken into account by shifting each line randomly by a value of -1, 0 or 1 pixel. Afterwards, the background intensity in experimental STED images was estimated to be 0.86 on average. This background was included as Poisson-distributed noise.

### Simulation of FRET Efficiencies

Random positions of molecules at defined surface densities according to densities of TCR or pMHC were simulated as described for the simulation of spatial distributions. Every acceptor molecule was assigned a FRET efficiency value according to its distance to the nearest donor molecule, according to:

$$E = \frac{1}{1 + \frac{d^6}{R_0^6}} \quad (24)$$

with the Förster radius  $R_0 = 5.1$  nm. The average value of  $E$  per acceptor was derived and the simulation was run 20 times.





Die approbierte gedruckte Originalversion dieser Dissertation ist an der TU Wien Bibliothek verfügbar.  
The approved original version of this doctoral thesis is available in print at TU Wien Bibliothek.



Die approbierte gedruckte Originalversion dieser Dissertation ist an der TU Wien Bibliothek verfügbar.  
The approved original version of this doctoral thesis is available in print at TU Wien Bibliothek.

---

## Chapter 3

# Results & Discussion

The translation from TCR ligand-binding to signal initiation and activation of the T cell is still highly enigmatic. As a starting point towards a better understanding, a comprehensive characterization of the spatiotemporal properties of the TCR/CD3 complexes on non-activated, or resting, T cells is indispensable. Three aspects are of particular interest:

- A) the diffusion of the TCR/CD3 complexes within the plasma membrane,
- B) the stoichiometry of single TCR/CD3 complexes, and
- C) the spatial distribution of the TCR/CD3 complexes on the cell membrane.

All three aspects may affect ligand-binding properties [206-208] and were studied via (single-molecule) fluorescence microscopy within this thesis.

### Characterization of the Experimental System

As T cells are highly sensitive to external influences, a thorough characterization of the experimental system regarding potentially induced activation states is key for providing a basis for further experiments. Thus, the experimental system used throughout this work was evaluated regarding its potency to induce T cell activation. One swift manifestation of T cell activation is an increase in cytosolic  $\text{Ca}^{2+}$  concentration by  $\text{Ca}^{2+}$  release from the ER and also by influx from extracellular  $\text{Ca}^{2+}$ . Cytosolic  $\text{Ca}^{2+}$  levels were measured by ratio-metric imaging using the indicator dye Fura2-AM.

Supported lipid bilayers functionalized with ICAM-1 ('non-activating') and additionally with B7-1 and MCC/IE<sup>k</sup> ('activating') were tested for their ability to induce  $\text{Ca}^{2+}$  flux in unlabeled or fluorescently labeled T cells (**Figure 28**). While activating supported lipid bilayers induced  $\text{Ca}^{2+}$  signaling in unlabeled 5c.c7 T cells (**Figure 29, black**), non-activating supported lipid bilayers did not (**Figure 29, blue**). Furthermore, none of the tested labels, i.e. H57-AF647, H57-scFv-AS635P and KT3-scFv-AS635P, did induce  $\text{Ca}^{2+}$  signaling on non-activating supported lipid bilayers (**Figure 29, magenta, green and orange**).

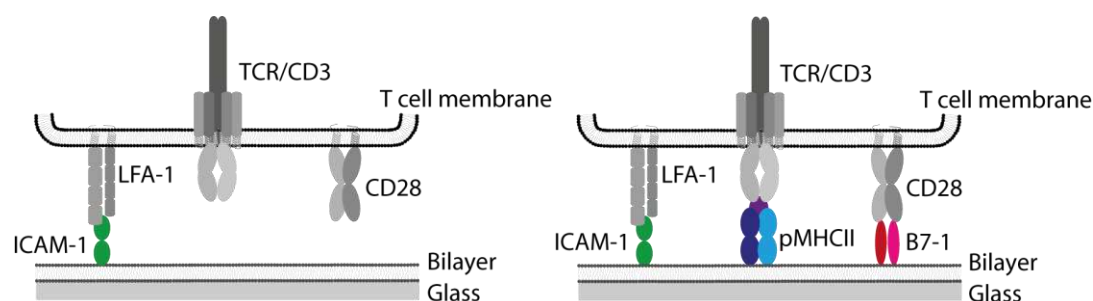


**Figure 28. Experimental System**

5c.c7 T cells were placed on SLBs containing ICAM-1 ('non-activating', left) or on SLBs containing ICAM-1, B7-1 and MCC/IE<sup>k</sup> (here: pMHCII; 'activating', right).

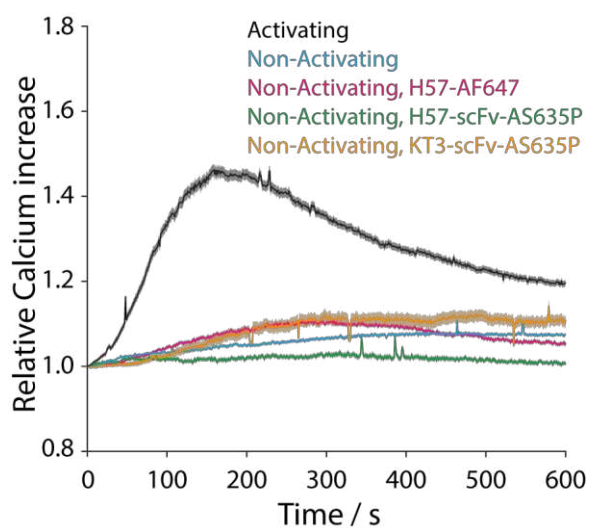


**Figure 29.  $Ca^{2+}$  experiments**

$Ca^{2+}$  imaging was performed using the  $Ca^{2+}$  indicator Fura2-AM for the following conditions: unlabeled on activating SLBs (black;  $n = 2,128$  cells from 7 experiments), unlabeled on non-activating SLBs (blue;  $n = 2,362$  cells from 7 experiments), H57-AF647 labeled on non-activating SLBs (magenta;  $n = 763$  cells from 2 experiments), H57-scFv-AS635P labeled on non-activating SLBs (green;  $n = 293$  cells from 3 experiments) and KT3-scFv-AS635P labeled on non-activating SLBs (orange;  $n = 1,205$  cells from 4 experiments). Shown is median  $\pm$  s.e. of median.

## Part A: TCR/CD3 Complex Mobility

Within this thesis, the aim was to estimate the TCR/CD3 complex mobility in the context of the used experimental system in order to be able to estimate its effects on live-cell experiments such as TOCCSL, PA/FCS and FRET (**Part B**) or SMLM (**Part C**).

To evaluate the TCR/CD3 mobility on the plasma membrane of T cells, we performed single-molecule tracking experiments on differently coated coverslip surfaces (PDL and supported lipid bilayers), using different fluorophores (AF488, AF647 and AS635) and illumination techniques (TIRF and HILO).

### A1) Single-Molecule Tracking of TCR/CD3 Complexes

5c.c7 T cells were labeled with H57-scFv-AF647, a label which binds specifically to TCR $\beta$ , and added onto non-activating supported lipid bilayers. Single-molecule tracks were recorded in TIRF configuration and analyzed by fitting the MSD-vs-t curve with a free diffusion model, yielding a mean diffusion constant  $D = 0.037 \pm 0.002 \mu\text{m}^2/\text{s}$  (**Figure 30A**).

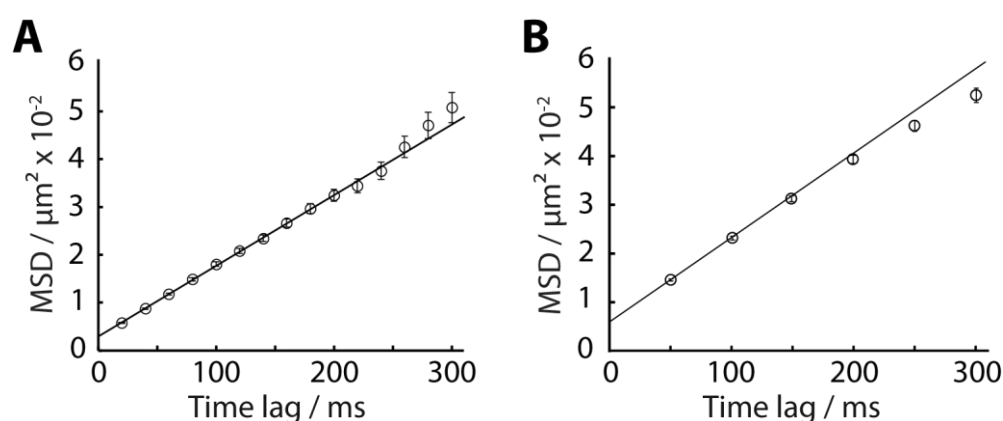


**Figure 30.** TCR/CD3 mobility determination with two different fluorophores

TCR $\beta$  was labeled at low concentration with H57-scFv-AF647 or H57-scFv-AS635 and cells were added onto non-activating SLBs. The measured square displacements were fitted with **Equation (12)** ( $\text{MSD} = 4D\Delta t + 4\sigma^2$ ). **A)** MSD-vs-t analysis of the recorded tracks from  $n = 21$  cells revealed a low mobility of TCR $\beta$  of  $D = 0.037 \pm 0.002 \mu\text{m}^2/\text{s}$ , when labelled with H57-scFv-AF647. **B)** MSD-vs-t analysis of the recorded tracks from  $n = 9$  cells confirmed a low mobility of TCR $\beta$  of  $D = 0.043 \pm 0.002 \mu\text{m}^2/\text{s}$ , when labelled with H57-scFv-AS635. Error bars

In order to validate these results and check for potential influences of the used organic dye AF647, experiments were repeated with an H57-scFv conjugated to AS635. The resulting average  $D = 0.043 \pm 0.002 \mu\text{m}^2/\text{s}$  was only slightly higher (**Figure 30B**), thus, the compared probes either show a similar effect on the complex's mobility, or do not interfere.

Further changing the fluorophore on the H57-scFv to AF488 yielded a similar average  $D$  when measured on non-activating supported lipid bilayers ( $0.046 \pm 0.014 \mu\text{m}^2/\text{s}$ ; **Figure 31A**). To control for potential interactions of the probe (H57-scFv) with

the surface, single-molecule tracking experiments were repeated on T cells which were adhered to PDL-coated slides and labeled with H57-scFv-AF488. The average mobility  $D = 0.044 \pm 0.011 \mu\text{m}^2/\text{s}$  agreed with the measured average  $D$  on supported lipid bilayers, rendering label-surface interactions highly unlikely.

In addition, the apical membrane of T cells was probed using HILO illumination. For these experiments, T cells were adhered to PDL. Single-molecule tracking of TCR/CD3 complexes labeled via H57-scFv-AF488 showed an average mobility  $D = 0.035 \pm 0.001 \mu\text{m}^2/\text{s}$  (**Figure 31B**), which is slightly smaller than the average  $D$  measured in TIRF configuration. This reduced apparent mobility might arise from the inability to capture motion in axial direction by the HILO measurements: When imaging the projection of a fluorophore's trajectory, an axial component in the diffusion gives rise to reduced estimated distance measures and thus a reduced  $D$  [209]. The basal plasma membrane of T cells at the adhesion interface usually flattens out, thereby aligning the membrane planar to the imaging plane and reducing bias by axial diffusion. The untethered top membrane of the cell, however, will preserve structures such as membrane ruffles, which might contribute to a bias during HILO experiments.

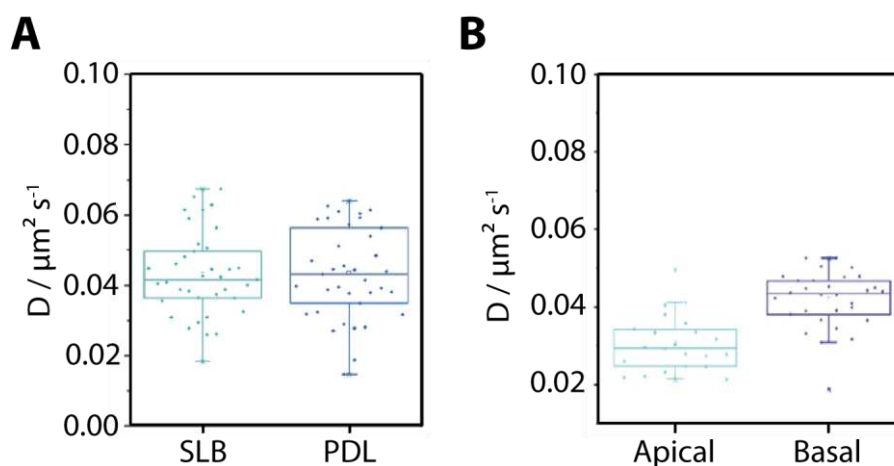


**Figure 31. TCR Mobility Estimation in T cells placed on two different surfaces using two different illumination configurations**

**A)** TCR $\beta$  was labeled at low density with H57-scFv-AF488. T cells were added to non-activating SLBs ( $n = 34$  cells) or PDL ( $n = 36$  cells). Shown are boxplots (with median, 1<sup>st</sup> and 3<sup>rd</sup> quartile and the 1.5 interquartile range) of  $D$  from single-cell msd-vs- $t$  analysis. The mean  $D$  was  $0.046 \pm 0.014 \mu\text{m}^2/\text{s}$  and  $0.044 \pm 0.011 \mu\text{m}^2/\text{s}$  for cells placed on SLBs and PDL, respectively. **B)** TCR $\beta$  was labeled at low density with H57-scFv-AF488. T cells were added to slides coated with PDL. Movies were recorded in TIRF configuration at the bottom surface ( $n = 29$  cells) or in HILO configuration at the top surface ( $n = 22$  cells). Shown are boxplots (with median, 1<sup>st</sup> and 3<sup>rd</sup> quartile and the 1.5 interquartile range) of  $D$  from single-cell MSD-vs- $t$  analysis. The mean  $D$  was  $0.035 \pm 0.001 \mu\text{m}^2/\text{s}$  and  $0.044 \pm 0.011 \mu\text{m}^2/\text{s}$  at the top and the bottom membrane, respectively.

The presented values of  $D$  depict the averaged values for all TCR/CD3 complexes. Additionally, single-molecule tracking offers the possibility to study the distribution of the acquired single displacement steps. Analyzing this distribution of square displacements allows for the identification of sub-populations with different

mobilities [203]. This can be achieved by fitting the cumulative density function (CDF) of the displacements to a bi-exponential function.

The two-component analysis revealed a slow fraction of  $36 \pm 3\%$  of receptor complexes diffusing with  $D = 0.003 \mu\text{m}^2/\text{s}$  and a fast fraction with  $D = 0.047 \mu\text{m}^2/\text{s}$  for experiments on supported lipid bilayers and H57-scFv-AF647 (**Figure 32**).

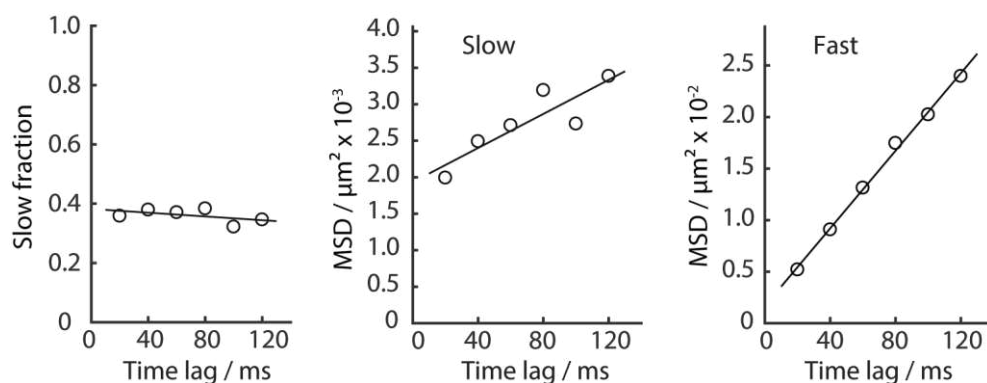


**Figure 32. TCR Mobility Estimation**

TCR $\beta$  was labeled at low density with H57-scFv-AF647. Cells were added to non-activating SLBs. Fitting the cumulative density function of the MSDs to a bi-exponential model yielded two populations of the TCR: one nearly immobile fraction of 36% of TCRs and a mobile fraction of 64% (left). Further analysis of the two subfractions via MSD-vs-t analysis revealed  $D = 0.003 \mu\text{m}^2/\text{s}$  (middle) and  $D = 0.047 \mu\text{m}^2/\text{s}$  (right), respectively.

| Surface        | Label          | Illumination | D [ $\mu\text{m}^2/\text{s}$ ] | Fig.         |
|----------------|----------------|--------------|--------------------------------|--------------|
| Non-activating | H57-scFv-AF647 | TIRF         | $0.037 \pm 0.002$              | Figure 30A   |
| Non-activating | H57-scFv-AS635 | TIRF         | $0.043 \pm 0.002$              | Figure 30B   |
| Non-activating | H57-scFv-AF488 | TIRF         | $0.046 \pm 0.014$              | Figure 31A   |
| PDL            |                |              | $0.044 \pm 0.011$              | Figure 31A,B |
|                |                | HILO         | $0.035 \pm 0.001$              | Figure 31B   |

**Table 3. Summary of tracking experiments**

None of the combinations of fluorophores, surfaces and illumination configurations that have been studied within this thesis revealed substantial differences in the average diffusion coefficient of the TCR/CD3 complexes ( $D = 0.035 - 0.046 \mu\text{m}^2/\text{s}$ ; **Table 3**). In addition, a nearly immobile fraction of 36% of TCR/CD3 complexes was determined.



## A2) Discussion

The experiments performed on the diffusion of the TCR/CD3 complex were motivated by the inconsistency of previously published results on the complexes' mobility (see **Table 1** in **Chapter 1**) and the direct relevance to live-cell measurements. Previous results range from  $D = 0.005 \mu\text{m}^2/\text{s}$  to  $D = 0.5 \mu\text{m}^2/\text{s}$  [129, 132]. Valid comparisons, however, are hardly possible due to differences in cell lines, adhesion surfaces, labels and methods applied. In the following, I discuss two important publications on this topic: i) the immobilization of TCR/CD3 complexes when measured on PLL reported by Santos et al and Ponjavic et al [131, 132], and ii) the comparably high mobility of  $D \sim 0.5 \mu\text{m}^2/\text{s}$  reported by Lillemeier et al [129].

Poly-L/D-Lysine is amongst the most widely used adhesive coatings for studies of the T cell plasma membrane. The unspecific adhesion of cells is based on the interaction of the positively charged amino group on the lysine residue with the negative surface charges of the cell [210]. It was not until 2018 that a thorough study on the influences of PLL adhesion on the T cell's state has been performed [131, 132]. PLL was not only found to induce  $\text{Ca}^{2+}$  flux in primary murine T cells and Jurkat cells, but also to reduce the mobility of the TCR/CD3 complex from  $D \approx 0.068 \mu\text{m}^2/\text{s}$  on the apical surface to  $D \approx 0.018 \mu\text{m}^2/\text{s}$ . Many other causes for this behavior such as influence of the  $\text{Ca}^{2+}$  indicator or the PLL concentration, incubation time and polymer size were carefully investigated by the authors and could be excluded. A reduction of  $\text{Ca}^{2+}$  flux in Jurkat cell lines which lack Lck (JCam1.6) or TCR $\beta$  (J.RT3-T3-5) further supported the specific link to T cell signaling. A comprehensive study of variations in the used label and the fluorophore was, however, not included, and the diffusion of TCR/CD3 complexes was studied solely by using UCHT1-Fab-AF488 against the CD3 $\epsilon$  subunit. While within this thesis, no differences have been identified in diffusion between complexes labeled with H57-scFv conjugated to the fluorophores AF488, AS635 or AF647, a study of different types of label proteins (Fab, full antibody or scFv) was again not realized.

In addition to potential issues with label-polymer interactions, a further uncertainty comes from the use of rigid surfaces such as PDL/PLL or Fibronectin for mobility measurements. To this end, supported lipid bilayers presenting the adhesion molecule ICAM-1 represent an elegant way to provide the T cell with an adhesive surface which itself has no large restrictions in mobility.

Contrary to these quasi-immobile TCR/CD3 complexes, Lillemeier et al. reported a rather large mobility of  $D = 0.5 \mu\text{m}^2/\text{s}$  measured by FCS [129]. The probed molecule was not labeled externally, but the primary mouse T cells were retrovirally transfected with CD3 $\zeta$ -eGFP. The potential residual expression of endogenous CD3 $\zeta$  raises questions about dimerization preferences of either of the two CD3 $\zeta$  species, possibly even allowing monomeric CD3 $\zeta$ -eGFP to reach the plasma membrane [211]. Diffusion of such a monomeric CD3 $\zeta$  would most likely differ from CD3 $\zeta$  embedded within the full TCR/CD3 complex. In addition, retroviral transfection increases background fluorescence as the cytosolic fraction of CD3 $\zeta$ -eGFP also contributes to the image; cytosolic diffusion will be increased significantly compared to diffusion within the plasma membrane. In addition, FCS is highly sensitive to

fluorophore blinking and bleaching which both bias the measured mobility towards increased values. This effect manifests particularly when measuring molecules with slow mobility, as might be the case for the TCR/CD3 complex.

To conclude, the described studies of Ponjavic et al and Santos et al [131, 132] demonstrate the necessity to refrain from using PLL as adhesion surface if considering diffusion measurements within the adhered part of the plasma membrane. Additionally, despite the variations in experimental setups between the mentioned studies (**Table 1; Chapter 1**), the average  $D$  of the TCR/CD3 complex lies within the range of  $0.04 - 0.2 \mu\text{m}^2/\text{s}$ , as values below were exclusively measured on PLL, and values above were only reported once by Lillemeier et al [129].

Regarding the mobile fraction of TCR/CD3 complexes, the value of  $\sim 64\%$  obtained in this thesis is in line with values reported by FRAP or SMT in TIRF [2, 130, 132]. However, other experiments using confocal FRAP reported almost exclusively mobile complexes (mobile fraction  $\sim 95\%$ ; [128, 133]). A possible reason for overestimation of the mobile fraction in confocal FRAP experiments is bleaching of immobile complexes before the actual recording of the recovery curve. Confocal microscopy is particularly susceptible to pre-bleaching effects, as high laser intensities are used for observation.

We are confident that the resulting diffusion coefficient  $D \sim 0.04 \mu\text{m}^2/\text{s}$  and the mobile fraction of  $\sim 64\%$  of TCR/CD3 complexes represent reliable estimates for the diffusion of this complex on the plasma membrane of T cells within the used experimental setup. This result, however, affects the design of stoichiometry measurements: Both the quasi-immobile and the mobile fraction need to be captured by the experiments.

## Part B: TCR/CD3 Complex Stoichiometry

The existence of multivalent TCR/CD3 complexes has been speculated for a long time [212], but the complexes' oligomerization and valency have been investigated only rarely by other than biochemical means. Oligomerization of the TCR/CD3 complex upon ligand binding represents a tempting model which is inspired by other receptors such as Epidermal Growth Factor receptors [213]. The model is supported by studies showing that proteins with more than one epitope against a subunit of the TCR/CD3 complex, such as soluble pMHC dimers or bivalent antibodies, show the ability to activate T cells. However, monovalent binding proteins including Fabs and scFvs derived from antibodies or monomeric soluble pMHC do not activate T cells [214-216]. Most of the recent studies, however, were indirect and involved harsh preparation methods such as detergent solubilization [115, 190]. A direct observation of the oligomerization state of the TCR in living, (non-)activated T cells has been realized only once. In this study, monomeric TCR/CD3 complexes were reported in a T cell hybridoma line [135], which contradicted all previous reports.

We applied four different methodologies to tackle the question of TCR/CD3 subunit composition in living T cells: single-molecule brightness analysis (TOCCSL), single-molecule co-localization analysis (two-color TOCCSL), photon arrival time analysis with fluorescence correlation spectroscopy (PA/FCS), and Förster Resonance Energy Transfer analysis (FRET) to probe the TCR/CD3 stoichiometry in resting T cells and during the initial stage of T cell activation. While TOCCSL, smFRET and PA/FCS are based on the recovery of unbleached fluorescent molecules into the observation area and thus fail to probe immobile or slowly diffusing molecules, bulk FRET measurements allow to probe the entirety of TCR/CD3 complexes, yet with reduced sensitivity for minority populations.

### B1) TOCCSL Analysis of TCR/CD3 Complexes

To perform TOCCSL experiments, 5c.c7 T cells were labeled with a H57-scFv conjugated to AF647 in a 1:1 stoichiometry and added onto non-activating supported lipid bilayers. Briefly, a high-intensity bleach pulse was applied to a small part of the cell, which was defined by imaging a rectangular aperture onto the cell. 1 ms after bleaching, an image was acquired to confirm the absence of residual fluorescence. After an additional recovery time of 3-10 s, the first mobile TCR/CD3 complexes had moved into the photobleached area and could be imaged as single, well-resolved complex entities (**Figure 33A**).

The probability density function (*PDF*) of the recorded brightness of these entities,  $q(B)$ , was compared to the brightness distribution of single H57-scFv-AF647 labels,  $q_1$ , which was recorded on sparsely labeled T cells. Based on  $q_1$ , a linear combination of  $n$ -mer contributions was fit to  $q(B)$ . A minor dimer fraction of  $3 \pm 4\%$  was detected (**Figure 33B, top and Figure 33C, left**). Such minute fractions, however, are close to the methods detection sensitivity [217].

Contrary to TCR $\beta$ , the proposed number of CD3 $\epsilon$  subunits per complex is two. To verify this, we performed similar experiments with a scFv, derived from a KT3 antibody, against the CD3 $\epsilon$  subunits of the TCR/CD3 complex (KT3-scFv-AF647). The results revealed a dimer fraction of  $74 \pm 4\%$ , but no higher-order complexes (**Figure 33B, bottom and Figure 33C, right**).

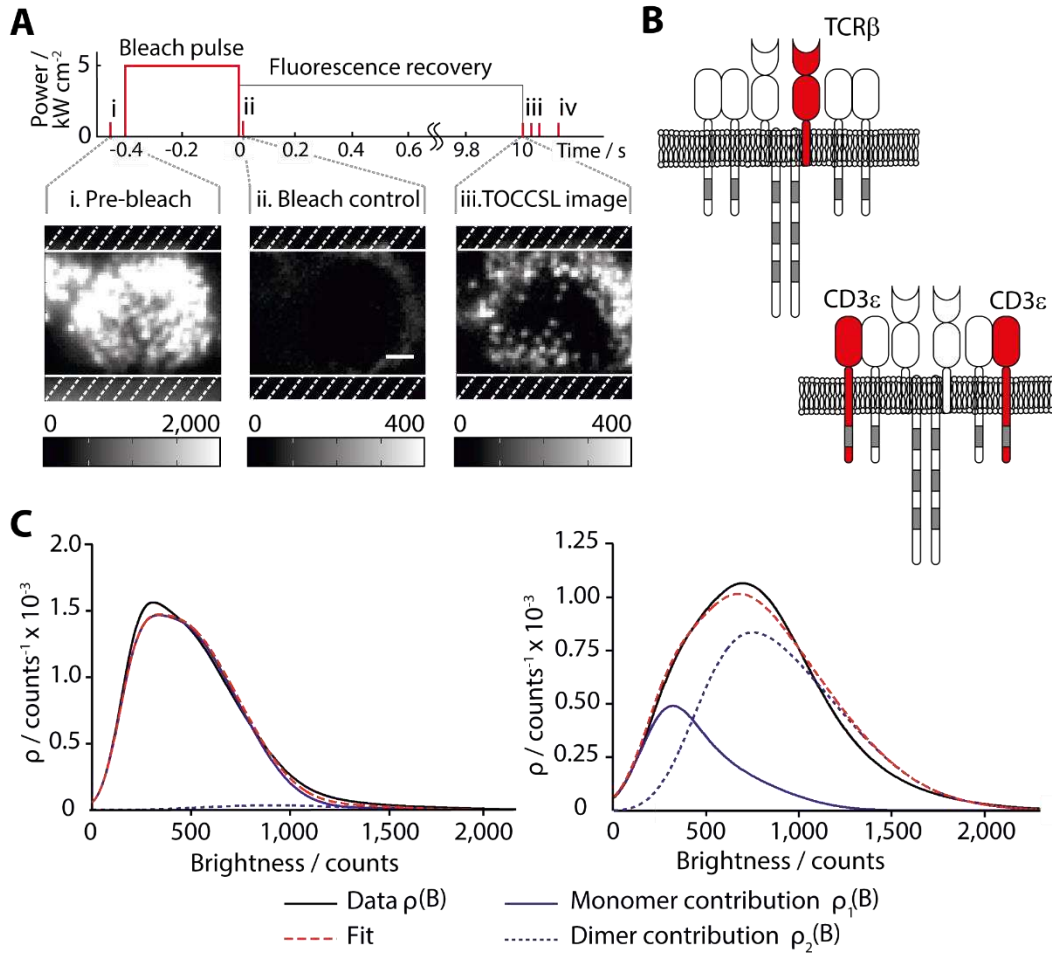


**Figure 33. TOCCSL studies on TCR/CD3 complex stoichiometry**

**A**) Illumination scheme for a TOCCSL experiment with the corresponding exemplary images (Scale bar, 2 $\mu$ m). **B**) Sketch of the TCR/CD3 complex with the labeled subunit highlighted in red for panel C, left (top) and right (bottom). **C**) left: Measured probability density function (pdf) of H57-scFv-AF647 data (black) with a fitted linear combination (red) of mono- and dimer (blue) contributions ( $n = 30$  cells). Right: Measured pdf of KT3-scFv-AF647 data (black) with a fitted linear combination (red) of mono- and dimer (blue) contributions ( $n = 41$  cells).

Due to the restricted accessibility of CD3 $\epsilon$  to the KT3-scFv [2] the estimated dimer fraction represents a minimum level of the number of CD3 $\epsilon$  per TCR. Taken together, the TOCCSL results confirmed the stoichiometry of mobile TCR/CD3 complexes to one TCR $\beta$  and two CD3 $\epsilon$  subunits per complex (**Table 4**; [112]).

| Surface        | Label          | Dimer Fraction | Fig.       |
|----------------|----------------|----------------|------------|
| Non-activating | H57-scFv-AF647 | $3 \pm 4\%$    | Figure 33C |
| Non-activating | KT3-scFv-AF647 | $74 \pm 4\%$   | Figure 33C |

Table 4. Summary of TOCCSL experiments

## B2) Two-Color TOCCSL and Single-Molecule FRET Analysis

The width of the brightness distribution of a single fluorophore impedes the detection of rare oligomers with TOCCSL. Nonetheless, a dual-color approach allows for the detection of interactions with probabilities as low as 0.1% [94]. We thus used two-color TOCCSL to check for rare oligomeric TCR/CD3 complexes.

5c.c7 T cells were labeled in a 1:1 molar ratio with H57-scFv-AF488 and H57-scFv-AF647, and two-color TOCCSL experiments were conducted (**Figure 34A and Figure 34B, top**). The acquisition timings were similar to the single-color experiments. Both fluorophores were excited simultaneously and their emission was split spectrally. The recovered signals were fitted, chromatically corrected and their co-localization was analyzed. Signals occurring in both channels within a radius of 200 nm were defined as co-localized (**Figure 34A, yellow arrows**). Only a minor fraction of 0.4% of all probed TCR $\beta$  subunits showed a neighboring signal in the other color channel (**Figure 34C, left**). Additional experiments were performed with the excitation of the channels delayed for 1 ms. This enabled the identification of FRET events which would have hampered the detection of co-localization events. Only a minority of 0.15% events did show FRET. These events most likely arose from random encounters of complexes.

When performing the experiments with KT3-scFv probes conjugated to AF488 and AF647, an increased fraction of 10% showed co-localization, and a fraction of 2.5% showed FRET (**Figure 34B, bottom and Figure 34C**). Still, these co-localization rates are low, when compared to the expected 50% for TCR/CD3 complexes with two CD3 $\epsilon$  subunits. This might be due to a limited accessibility of CD3 $\epsilon$  by KT3-scFv, as also an increased amount of KT3-scFv is needed to reach saturation of labeling [2]. Additionally, KT3-scFv showed a decreased half-life of binding compared to 44 min at room temperature for H57-scFv [2].

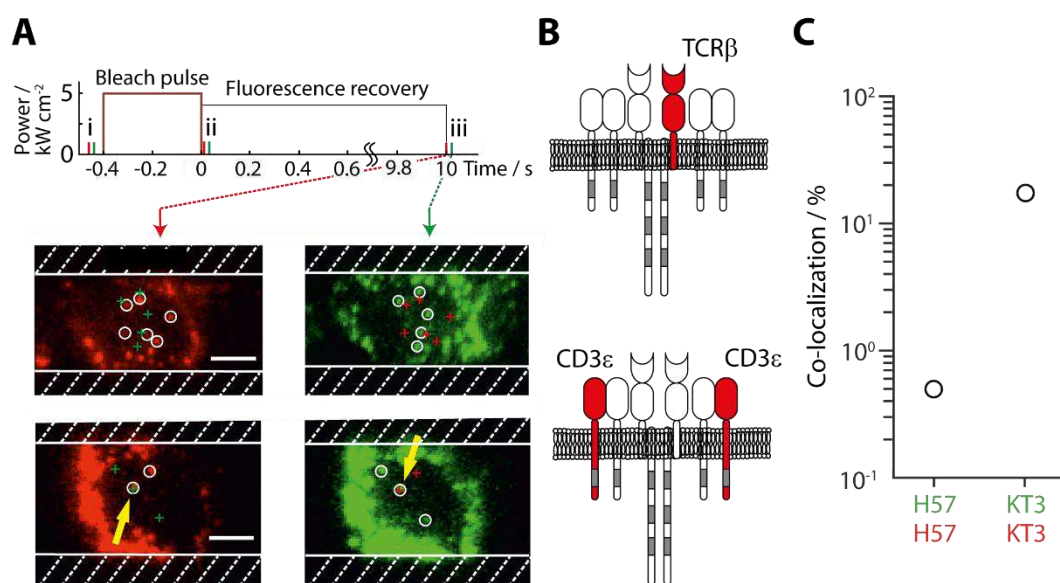


**Figure 34. Two-color TOCCSL studies on TCR/CD3 complex stoichiometry**

**A**) Illumination scheme for a two-color TOCCSL experiment with the corresponding exemplary images (Scale bars, 4 μm). The yellow arrow highlights co-localized fluorophores. **B**) Sketch of the TCR/CD3 complex with the labeled subunit highlighted in red. **C**) The co-localization percentage is dependent on the used label, revealing an increased co-localization rate for KT3-scFv ( $n = 47$  and 31 cells for H57-scFv and KT3-scFv, respectively).

The results of the two-color TOCCSL and single-molecule FRET experiments confirmed the complex stoichiometry of one TCRβ and two CD3ε subunits as seen by the preceding single-color TOCCSL measurements (Table 5). However, both versions of TOCCSL are only sensitive to long-lived (3-10 s) oligomers because of the rather long bleaching pulse and recovery phase. Oligomers with a shorter lifetime would dissociate during this time, thus, evade detection.

| Surface        | Donor          | Acceptor       | Fraction of positive events (%) | Fig.       |
|----------------|----------------|----------------|---------------------------------|------------|
| Non-activating | H57-scFv-AF488 | H57-scFv-AF647 | 0.4 (TOCCSL) / 0.15 (smFRET)    | Figure 34C |
| Non-activating | KT3-scFv-AF488 | KT3-scFv-AF647 | 10 (TOCCSL) / 2.5 (smFRET)      | Figure 34C |

**Table 5. Summary of two-color TOCCSL and single-molecule FRET experiments**

### B3) PA/FCS Analysis of TCR/CD3 Complexes

To probe for the presence of shorter-lived oligomers, we used a combination of photon-arrival time analysis and FCS, termed PA/FCS. The number of photons detected within the measurement spot directly correlates to the number of fluorophores. By analyzing the temporal correlation of the recorded signals, the spatial dependency between the multiple detected signals can be deduced: signals originating from oligomers move in a correlated manner, i.e. enter and leave the observation area at the same time, while signals from monomers diffuse independently through the observation spot, thus do not show any temporal correlation.

5c.c7 T cells were labeled with H57-scFv-AS635P, put on non-activating bilayers, and PA/FCS experiments were performed. The autocorrelation was determined with zero lag time, with an additional small lag time (100 or 400 ns; '1<sup>st</sup> period') and with a lag time of 2 s. The relation of these three autocorrelation curves allows for determination of the number of emitters per complex (see **Chapter 2**). For T cells bearing H57-scFv-AS635P, the correlation curve at zero lag time was identical to that at infinite lag time (**Figure 35A**). Fitting the auto-correlation curves with empirical models that include photophysics as well as diffusion [99], lead to a mean number of emitters of  $1.09 \pm 0.08$  (**Figure 35A**), confirming the number of TCR $\beta$  subunits per TCR/CD3 complex to be one. As control, H57-scFv-AS635P was measured in solution, and fitting revealed  $1.17 \pm 0.01$  emitters per scFv (**Figure 35C**). Using KT3-scFv-AS635P instead of H57-scFv-AS635P showed increased correlation at zero lag time (**Figure 35B**), with the fit resulting in  $1.86 \pm 0.22$  emitters, compared to  $1.14 \pm 0.01$  emitters for KT3-scFv-AS635P measured in solution (**Figure 35C**). This confirms the 1:1 conjugation of the probe, KT3-scFv, to the organic dye AS635P, as well as the presence of two CD3 $\epsilon$  subunits per TCR/CD3 complex. Additionally, fitting the FCS data with a model for two-dimensional diffusion yielded a  $D$  of  $0.034 \pm 0.014 \mu\text{m}^2/\text{s}$  which is in agreement with the diffusion data from the single-molecule tracking experiments (**Part A**). PA/FCS did not indicate the presence of any short-lived TCR/CD3 oligomers (**Table 6**).

| Surface                    | Label           | <N>             | Fig.         |
|----------------------------|-----------------|-----------------|--------------|
| Non-activating<br>Solution | H57-scFv-AS635P | $1.09 \pm 0.08$ | Figure 35A,C |
|                            |                 | $1.17 \pm 0.01$ | Figure 35C   |
| Non-activating<br>Solution | KT3-scFv-AS635P | $1.86 \pm 0.22$ | Figure 35B,C |
|                            |                 | $1.14 \pm 0.01$ | Figure 35C   |

Table 6. Summary of PA/FCS experiments

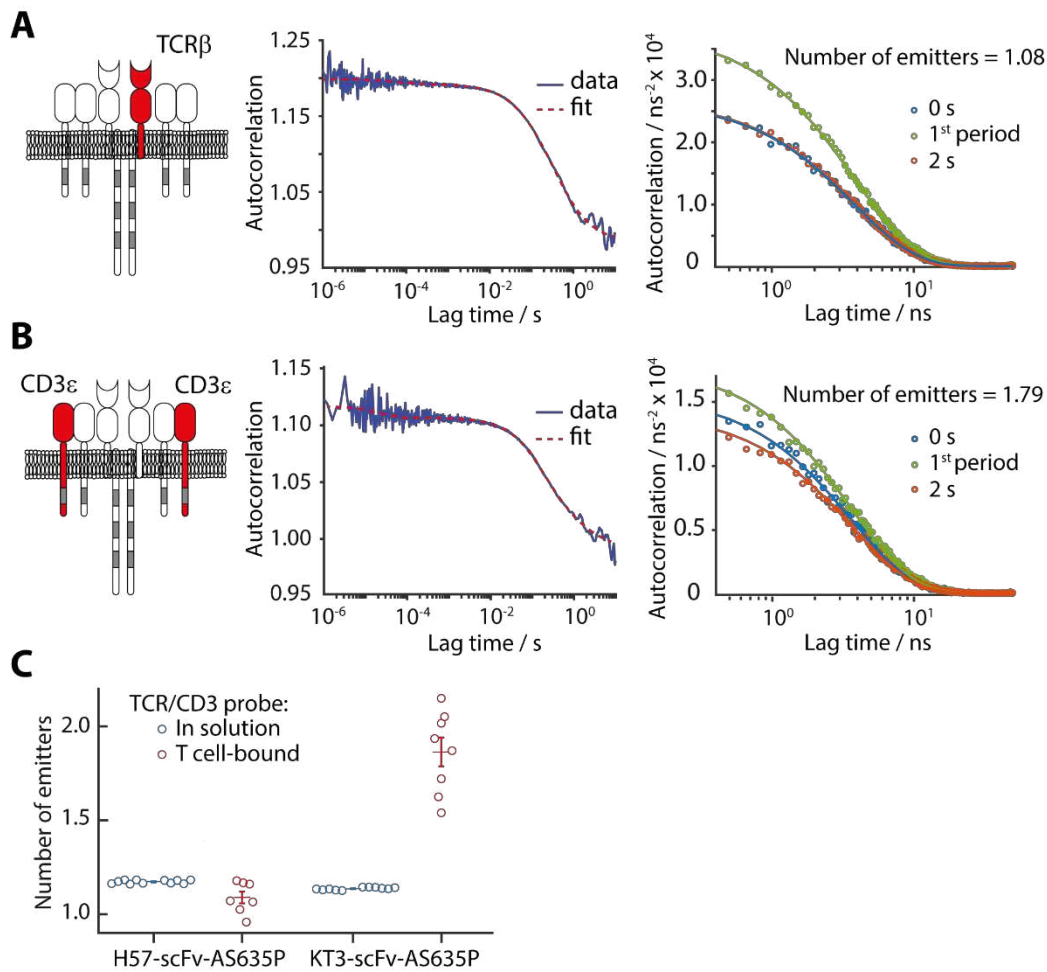


**Figure 35. Studies on TCR/CD3 complex stoichiometry by PA/FCS**

**A)** PA/FCS analysis of TCR $\beta$ . Left: Sketch of the TCR/CD3 complex with the labeled subunit highlighted in red. Middle: A two-dimensional diffusion model (red) was fitted to the normalized autocorrelation function (blue) yielding a diffusion coefficient of  $D = 0.034 \pm 0.014 \mu\text{m}^2/\text{s}$ . Right: Fitting the autocorrelation functions at lag time zero (blue) and 2 s (red) allows to determine the number of emitters per TCR/CD3 complex. Here, the autocorrelation functions at both lag times are equal, the emitters thus diffuse independently through the observation spot. **B)** PA/FCS analysis of CD3 $\epsilon$ . Left: Sketch of the TCR/CD3 complex, with the labeled subunit highlighted in red. Middle: A two-dimensional diffusion model (red) was fitted to the normalized autocorrelation function (blue). Right: Fitting the autocorrelation functions at lag time zero (blue) and 2 s (red) allows to determine the number of emitters per TCR/CD3 complex. Here, the autocorrelation functions at both lag times differ, the emitters thus diffuse correlatedly through the observation spot. **C)** Averages for measurements in solution (blue) or on T cells (red) for the indicated probe.  $N = 11$  measurements for H57-scFv-AS635P in solution;  $n = 7$  cells for cell-bound H57-scFv-AS635P;  $n = 11$  measurements for KT3-scFv-AS635P in solution and  $n = 8$  cells for cell-bound KT3-scFv-AS635P.



## B4) Bulk FRET Analysis of TCR/CD3 Complexes

While TOCCSL and PA/FCS rely on the diffusion of TCR/CD3 complexes into the observation area, and thus only probe mobile complexes, ensemble FRET measurements also include information on the immobile fraction.

5c.c7 T cells were labeled with H57-scFv-AF555 and H57-scFv-AF647 and seeded on non-activating or activating supported lipid bilayers. Labeling with H57-scFv was shown not to interfere with binding to pMHC of T cells [195, 218]. Conjugation of the H57-scFv to dyes at a position next to the paratope minimized bias in FRET results by increased dye distances [2]. For stoichiometric measurements, labeling of the entirety of TCR/CD3 complexes is needed, however, the TCR/CD3 surface level expression of  $\sim 70$  complexes/ $\mu\text{m}^2$  [2] is too high for single-molecule FRET measurements. For this reason, FRET efficiencies were determined using donor recovery after acceptor photo-bleaching, and calculated according to:

$$E = \frac{I_{post} - I_{pre}}{I_{post}} \quad (25)$$

with  $I_{post}$  and  $I_{pre}$  being the background-corrected intensities after and before acceptor photo-bleaching, respectively.

When fluorescently labeled T cells were placed on non-activating supported lipid bilayers, a small increase in FRET was measured (**Figure 36A-C**). This increase, however, can be quantitatively explained by random encounters of donor and acceptor, also termed bystander FRET, as demonstrated by Monte Carlo simulations (**Figure 36D**). For those simulations, the positions of fluorophores of two different species were simulated randomly at respective densities. For each simulated donor molecule, the distance to the nearest acceptor was determined and the corresponding FRET efficiency was calculated.

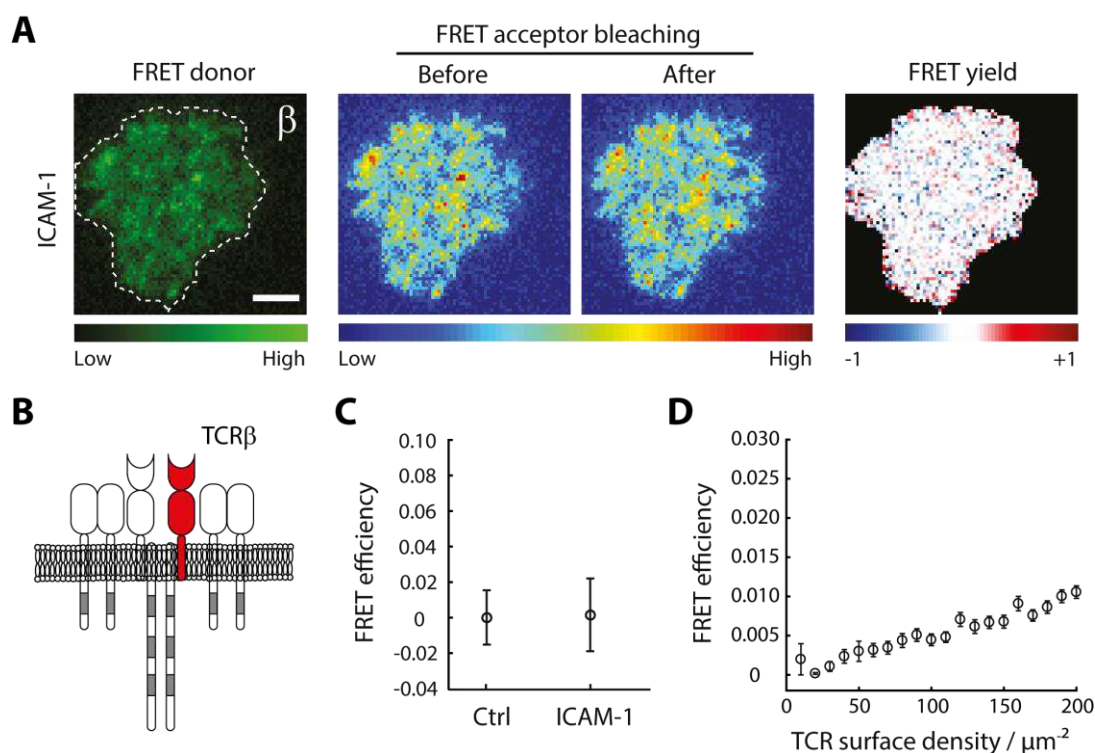


**Figure 36. H57-scFv FRET experiments on non-activating SLBs.**

**A**) Exemplary data of an adhered T cell (Scale bar: 3  $\mu\text{m}$ ). FRET efficiency was calculated according to **Equation (15)**. **B**) Sketch of the TCR/CD3 complex with the labeled subunit highlighted in red. **C**) Analysis of FRET efficiencies did not show an increase in FRET after adhesion to non-activating bilayers ( $n = 21$  cells for ctrl and  $n = 20$  cells for ICAM-1; shown is mean  $\pm$  s.e.m.). **D**) Simulated FRET efficiencies at different TCR surface densities ( $n = 20$  simulations per data point; shown is mean  $\pm$  s.e.m.).

On activating supported lipid bilayers (**Figure 37A-C**), FRET remained low. When confining the analysis region to smaller ROIs, i.e. cSMACs or micro-clusters, no increase in FRET was detected (**Figure 37D**). Instead of an expected increase in FRET due to the elevated fluorophore density in these areas, a slight reduction in FRET was observed, hinting towards active mechanisms keeping the TCR/CD3 complexes apart.

As a positive control, biotinylated H57-scFv FRET probes were used to label T cells. After crosslinking via 1 or 10 nM divalent streptavidin, cells were put on non-activating supported lipid bilayers and increased FRET was measured at the lower streptavidin concentration (**Figure 38A-C**), confirming the sensitivity of the FRET-based experiments. Upon increasing the divalent streptavidin concentration, reduced FRET was observed, which might be derived from the saturation of biotin on the H57-scFv FRET probes (**Figure 38C**).

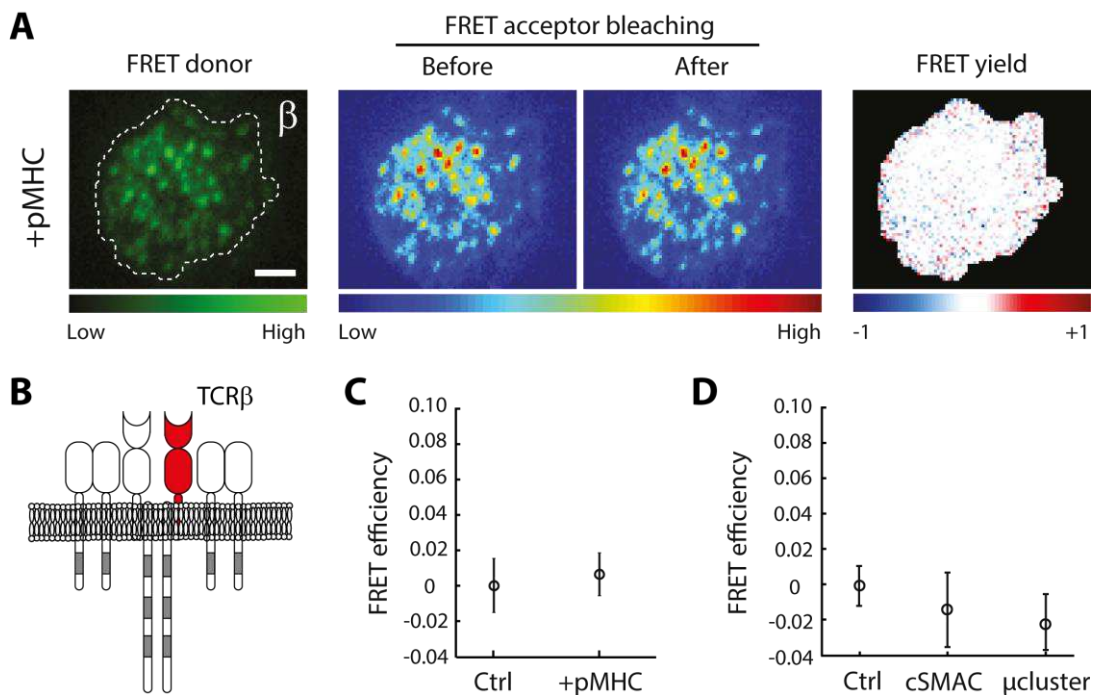


**Figure 37. H57-scFv FRET experiments on activating SLBs**

**A)** Exemplary data of an adhered T cell (Scale bar: 3 μm). **B)** Sketch of the TCR/CD3 complex with the labeled subunit highlighted in red. **C)** Analysis of FRET efficiencies did not show an increase in FRET after adhesion on activating bilayers ( $n = 21$  cells for both data points; shown is mean  $\pm$  s.e.m.). **D)** Analysis of FRET efficiencies restricted to cSMAC ( $n = 13$  cells) or micro-cluster ( $n = 24$  micro-clusters) regions did not show increased FRET ( $n = 20$  cells for ctrl; shown is mean  $\pm$  s.e.m.).

Bulk FRET experiments could again neglect the presence of TCR $\beta$  oligomers as summarized in Table 7.

| Surface                              | Donor (AF555) | Acceptor (AF647) | ROI           | FRET | Fig.       |
|--------------------------------------|---------------|------------------|---------------|------|------------|
| Non-activating                       | H57-scFv      | H57-scFv         | Synapse       | -    | Figure 36C |
| Activating                           | H57-scFv      | H57-scFv         | Synapse       | -    | Figure 37C |
|                                      |               |                  | cSMAC         | -    | Figure 37D |
|                                      |               |                  | $\mu$ Cluster | -    | Figure 37D |
| Non-activating<br>1 mM Streptavidin  | Bio-H57-scFv  | Bio-H57-scFv     | Synapse       | +    | Figure 38C |
| Non-activating<br>10 mM Streptavidin |               |                  |               | -    |            |

**Table 7. Summary of donor recovery after acceptor photobleaching TCR/CD3 FRET experiments**

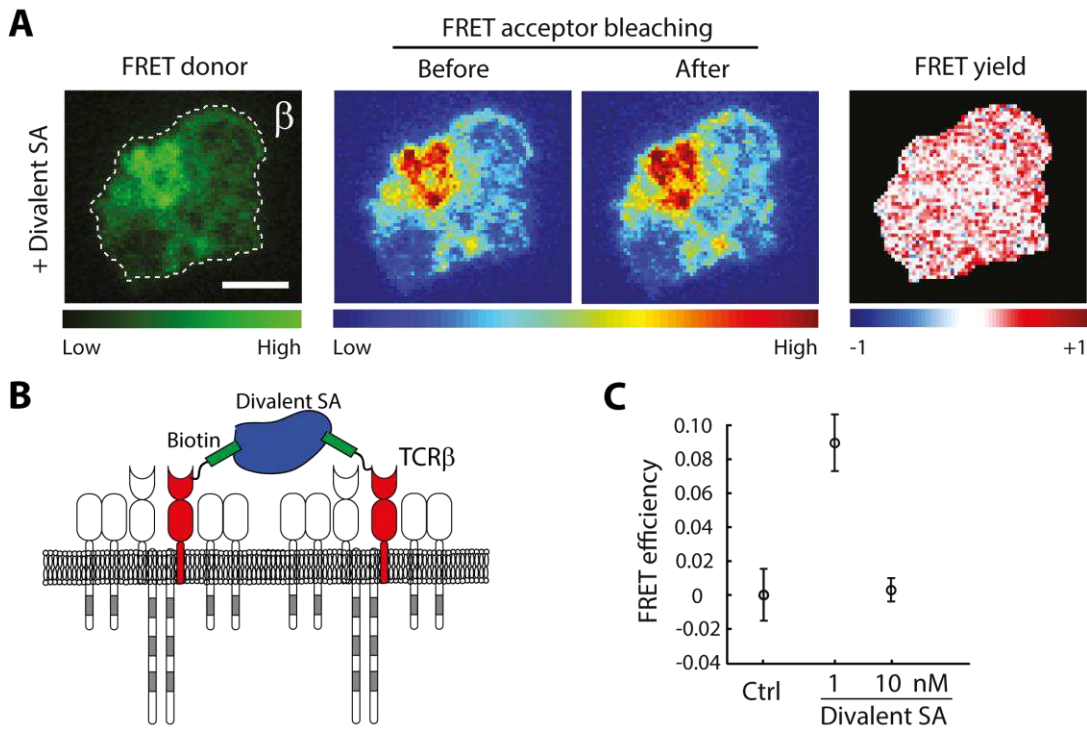


**Figure 38.** *H57-scFv FRET experiments on non-activating SLBs with streptavidin crosslinking*

**A)** Exemplary data of an adhered T cell with crosslinked TCRs (Scale bar:  $3\mu\text{m}$ ). **B)** Sketch of the TCR/CD3 complex with the labeled subunit highlighted in red. **C)** Analysis of FRET efficiencies did show increased FRET after adhesion on non-activating SLBs and crosslinking with 1 nM divalent Streptavidin ( $n = 21$  cells for ctrl,  $n = 10$  cells for 1 nM divalent streptavidin and  $n = 11$  cells for 10 nM divalent streptavidin; shown is mean  $\pm$  s.e.m.). Crosslinking with 10 nM divalent streptavidin did abandon the increase in FRET.

## B5) FRET Analysis of pMHC Oligomerization

Prevention of oligomerization by the label H57-scFv could account for absence of FRET on activated T cells. To circumvent this potential problem, we tested a different labeling strategy: Instead of the TCR/CD3 complex, we labeled MCC/IE<sup>k</sup> in two colors and probed for FRET.

The MCC peptide was labeled site-specifically either at the N- or the C- terminus with AF647 or AF555, loaded to his-tagged MHC-II and linked to the supported lipid bilayers at a density of at least 100 molecules/ $\mu\text{m}^2$ . Without the addition of T cells, all tested combinations (555N/647N, 555C/647C and 555N/647C) gave rise to low levels of FRET. These levels were consistent with simulations for bystander FRET due to random encounters at all measured densities (**Figure 39**).

The simulations for bystander FRET of MCC/IE<sup>k</sup> were realized as described earlier for TCR/CD3 complex FRET experiments. After addition of T cells to activating supported lipid bilayers, the formation of clusters of MCC/IE<sup>k</sup> molecules occurred, corresponding to TCR micro-clusters induced by activation (**Figure 40A and B**). Restriction of the analysis to areas that are most likely involved within the signaling process, i.e. microclusters and cSMACs, did not show elevated levels of FRET

(Figure 40C). Surprisingly, the FRET levels measured were even below the random FRET observed on the supported lipid bilayers before cell addition (Figure 13D), hinting again towards an active mechanism that keeps the TCR-engaged pMHCs apart. However, due to the small size of the measured effect, this potential separation remains subject to further investigations. The combinations of labels, ROIs and the figure number showing the experimental results are listed in Table 8.

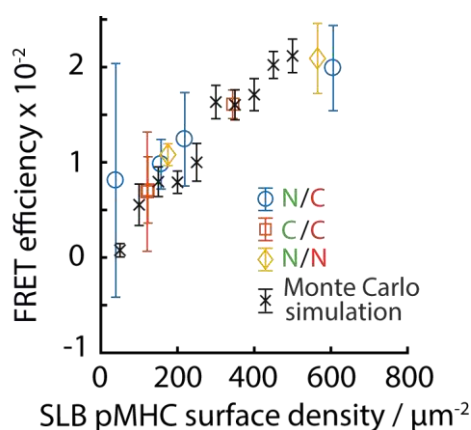


**Figure 39.** MCC/IE<sup>k</sup> FRET simulations

FRET was measured on activating SLBs containing combinations of MCC/IE<sup>k</sup>(C)-AF555 and MCC/IE<sup>k</sup>(C)-AF647, MCC/IE<sup>k</sup>(N)-AF555 and MCC/IE<sup>k</sup>(C)-AF647 or MCC/IE<sup>k</sup>(N)-AF555 and MCC/IE<sup>k</sup>(N)-AF647 ( $n=8$  regions per surface density; shown is mean  $\pm$  s.e.m.). Additional simulations confirmed the corresponding increase in FRET efficiency with increasing surface density ( $n=20$  simulations; shown is mean  $\pm$  s.e.m.).

| Surface    | Donor (AF555)           | Acceptor (AF647)        | ROI           | Fig.       |
|------------|-------------------------|-------------------------|---------------|------------|
| Activating | MCC/IE <sup>k</sup> (N) | MCC/IE <sup>k</sup> (C) | $\mu$ Cluster | Figure 40C |
|            | MCC/IE <sup>k</sup> (C) | MCC/IE <sup>k</sup> (C) |               |            |
|            | MCC/IE <sup>k</sup> (N) | MCC/IE <sup>k</sup> (N) |               |            |
| Activating | MCC/IE <sup>k</sup> (N) | MCC/IE <sup>k</sup> (C) | Bilayer       | Figure 40D |
|            | MCC/IE <sup>k</sup> (N) | MCC/IE <sup>k</sup> (C) | Synapse       |            |
| Activating | MCC/IE <sup>k</sup> (C) | MCC/IE <sup>k</sup> (C) | Bilayer       | Figure 40D |
|            | MCC/IE <sup>k</sup> (C) | MCC/IE <sup>k</sup> (C) | Synapse       |            |
| Activating | MCC/IE <sup>k</sup> (N) | MCC/IE <sup>k</sup> (N) | Bilayer       | Figure 40D |
|            | MCC/IE <sup>k</sup> (N) | MCC/IE <sup>k</sup> (N) | Synapse       |            |

**Table 8.** Summary of MCC/IE<sup>k</sup> FRET experiments

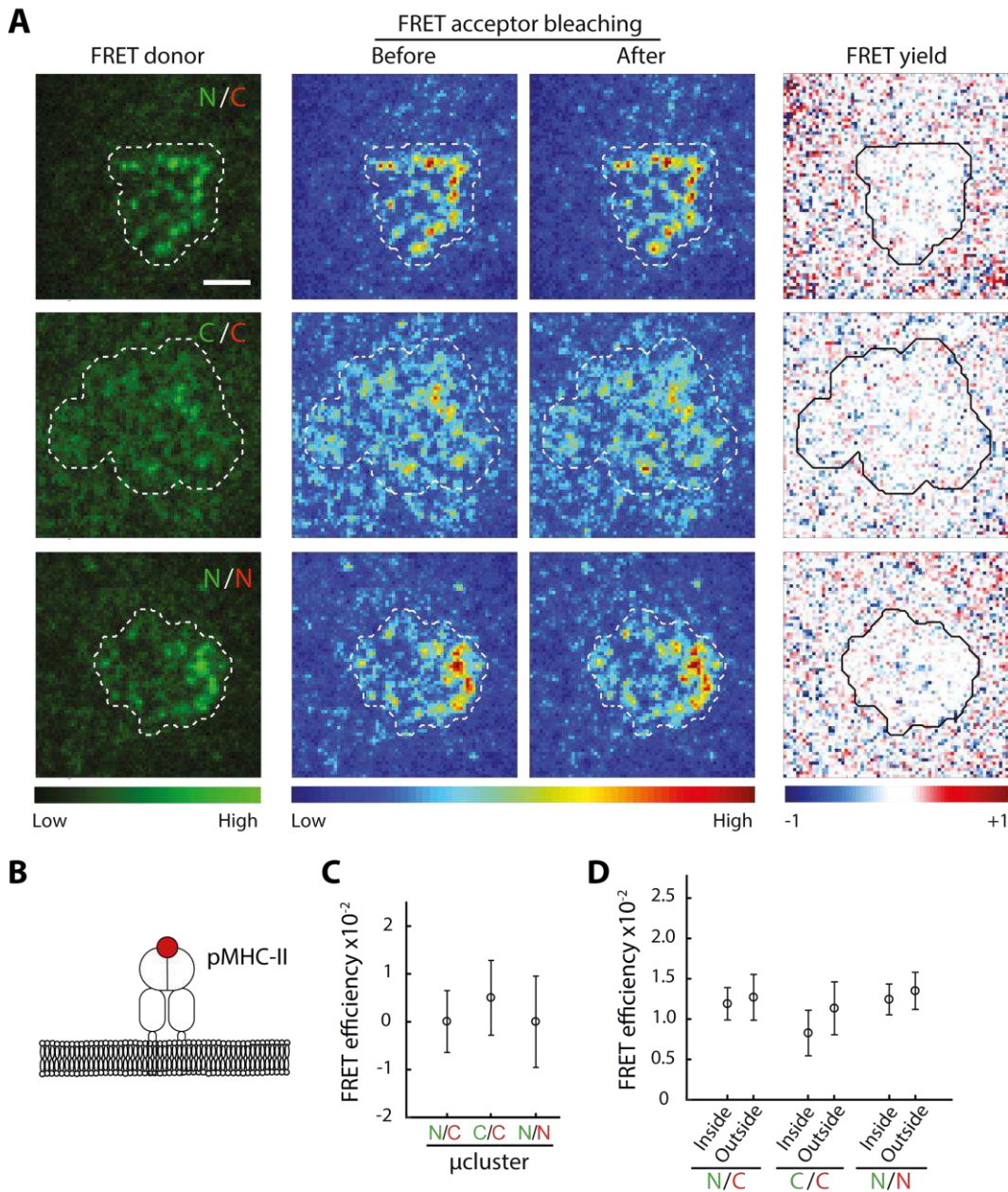


**Figure 40. MCC/IE<sup>k</sup> FRET experiments on SLBs**

**A)** Exemplary data of adhered T cells on activating SLBs with varying combinations of fluorescent MCC/IE<sup>k</sup> (Scale bar: 3  $\mu$ m; combinations as indicated). **B)** Sketch to clarify probed molecule, here: peptide within MCC/IE<sup>k</sup>. **C)** Analysis of FRET efficiencies did not show increased FRET in MCC/IE<sup>k</sup> enriched regions (micro-clusters) after adhesion of unlabeled T cells on activating SLBs ( $n=53$  micro-clusters on 17 cells for N/C,  $n=31$  micro-clusters on 18 cells for C/C and  $n=40$  micro-clusters on 15 cells for N/N; shown is mean  $\pm$  s.e.m.). **D)** Analysis of FRET efficiencies did not show increased FRET in the complete synapse area after adhesion of unlabeled T cells on activating SLBs. FRET was also determined in areas outside the synapse region ( $n=19$  cells for N/C,  $n=18$  cells for C/C and  $n=15$  cells for N/N; shown is mean  $\pm$  s.e.m.).

## B6) Discussion

Using a different complementary (single-molecule) methods, we revealed the stoichiometry of the accessible TCR/CD3 complexes, yielding one TCR $\beta$  and two CD3 $\epsilon$  subunits per complex. The applied methods addressed both mobile complexes (via TOCCSL, PA/FCS and single-molecule FRET) and quasi-immobile complexes (via donor recovery after acceptor photobleaching FRET): The presence of hypothetical multi-unit complexes with lifetimes down to 100 ms [2] could be excluded using PA/FCS, while more stable complexes could be discarded by TOCCSL and single-molecule FRET. The results regarding the oligomerization of the TCR/CD3 complex are summarized in **Table 9**.

| Method                | Probed Population       | TCR $\beta$ | CD3 $\epsilon$ | MCC/IE <sup>k</sup> |
|-----------------------|-------------------------|-------------|----------------|---------------------|
| (Two-Color)<br>TOCCSL | Mobile                  | Monomers    | Dimers         | -                   |
| PA/FCS                | Mobile                  | ~1 emitter  | ~2 emitters    | -                   |
| FRET                  | Mobile & Quasi-immobile | No FRET     | -              | No FRET             |

*Table 9. Summary of experiments on the TCR/CD3 complex stoichiometry*

In the following, I summarize additional experiments performed by my colleagues that strengthen our conclusions further.

Within this work, all experiments probing the number of TCR $\beta$  units per TCR/CD3 complex were performed using scFvs to the H57 epitope on TCR $\beta$ . However, it could not be excluded that the binding of one H57-scFv to TCR $\beta$  blocks the binding of another H57-scFv to a potential second TCR $\beta$  present within the complex. To this end, studies applying the same experimental methods with a Fab specific to the KJ25 epitope of the TCR $\beta$  subunit confirmed the presence of one TCR $\beta$  per TCR/CD3 complex [2]. The KJ25-Fab targets the variable region responsible for antigen-binding. This Fab, thus, should be able to label all TCR/CD3 complexes relevant for pMHC binding [219]. Using this Fab, not only homo-colocalization studies were realized, but it was also used in combination with H57-scFv. Two-color TOCCSL experiments with KJ25-Fab-AF488 and H57-scFv-AF647 gave rise to over 20% of all signals being detected as colocalized [2] confirming the sensitivity of our approach. PA/FCS measurements with KJ25-Fab-AS635P resulted in 1.16 emitters per probed complex, which is slightly higher than the value of 1.09 reported within this work. This elevated number most likely arose from the Fab carrying more than one fluorophore as the conjugation was realized not site-specifically, in contrast to H57-scFv. Similar to the two-color TOCCSL experiments, no FRET was reported when using KJ25-Fab-AF555 paired with KJ25-Fab-AF647, while exchanging one of the labels to H57-scFv lead to elevated FRET efficiencies [2]. Taken together, the use of KJ25-Fab in further studies as an alternative label to H57-scFv could redress

concerns about the inability of the scFv to detect oligomers of TCR $\beta$  [2]. The results are summarized in **Table 10**.

| Method              | Label 1  | Label 2  | Result        | Ref. |
|---------------------|----------|----------|---------------|------|
| Two-Color<br>TOCCSL | scFv-H57 | scFv-H57 | 0.4% coloc.   | -    |
|                     | Fab-KJ25 | Fab-KJ25 | 0.1% coloc.   | [2]  |
|                     | Fab-KJ25 | scFv-H57 | 21% coloc.    | [2]  |
| PA/FCS              | scFv-H57 |          | 1.09 emitters | -    |
|                     | Fab-KJ25 |          | 1.16 emitters | [2]  |
| FRET                | scFv-H57 | scFv-H57 | No FRET       | -    |
|                     | Fab-KJ25 | Fab-KJ25 | No FRET       | [2]  |
|                     | scFv-H57 | Fab-KJ25 | FRET          | [2]  |

**Table 10.** Summary of experiments by Brameshuber et al. using Fab-KJ25, and comparison to results obtained within this work

Temperature has significant influences on cell properties, including diffusion, mechanical properties or membrane permeability [220-223]. The Saffman-Delbrück model describes the lateral diffusion within a lipid membrane as a function of absolute temperature [10, 11]. This relationship is widely acknowledged and has also been confirmed in experiments [12, 13]. Increased temperature also comes along with faster binding kinetics, thus increasing the unbinding rate  $k_{off}$  of the used H57-scFv significantly. The half-life of this bond was reported to drop from 50 min at 22.5°C to 6.8 min at 37°C [195]. This highly reduced lifetime was the main motivation to conduct the live-cell experiments at a temperature of ~22°C. Importantly, the recognition of antigenic pMHC by the TCR/CD3 complex is unaffected by such a change in temperature [195]. Nevertheless, efforts were taken to repeat two-color TOCCSL measurements using H57-scFv at 37°C, but also those experiments did not lead to the detection of TCR/CD3 oligomers [2]. In FRET experiments at 37°C on directly dye-conjugated pMHCs, resembling those used within this thesis, the finding of monomeric TCR/CD3 complexes could be further confirmed [2].

The selection of the organic dyes, AF488 or AF555 and AF647, defined the Förster radii to 5.6 or 5.1 nm, respectively. This equals approximately the size of the TCR (**Figure 41**). However, the resulting FRET sensitivity might be too low to detect dimeric TCR $\beta$  conjugates if they were assembled in one of the proposed arrangements (**Figure 41A, left**; [193]). Changing the donor fluorophore to AF568 increases the Förster radius to  $R_0 = 8.3$  nm (**Figure 41B**) but leads to similar results in FRET experiments based on H57-scFvs [2]. In addition, a high donor-to-acceptor ratio of  $\geq 1$  can lead to significant underestimation of FRET efficiencies. To test for such effects, the acceptor concentration was increased to achieve a molar ratio of donor to acceptor of 1:3. However, no FRET was found with these adjusted label concentrations [2].



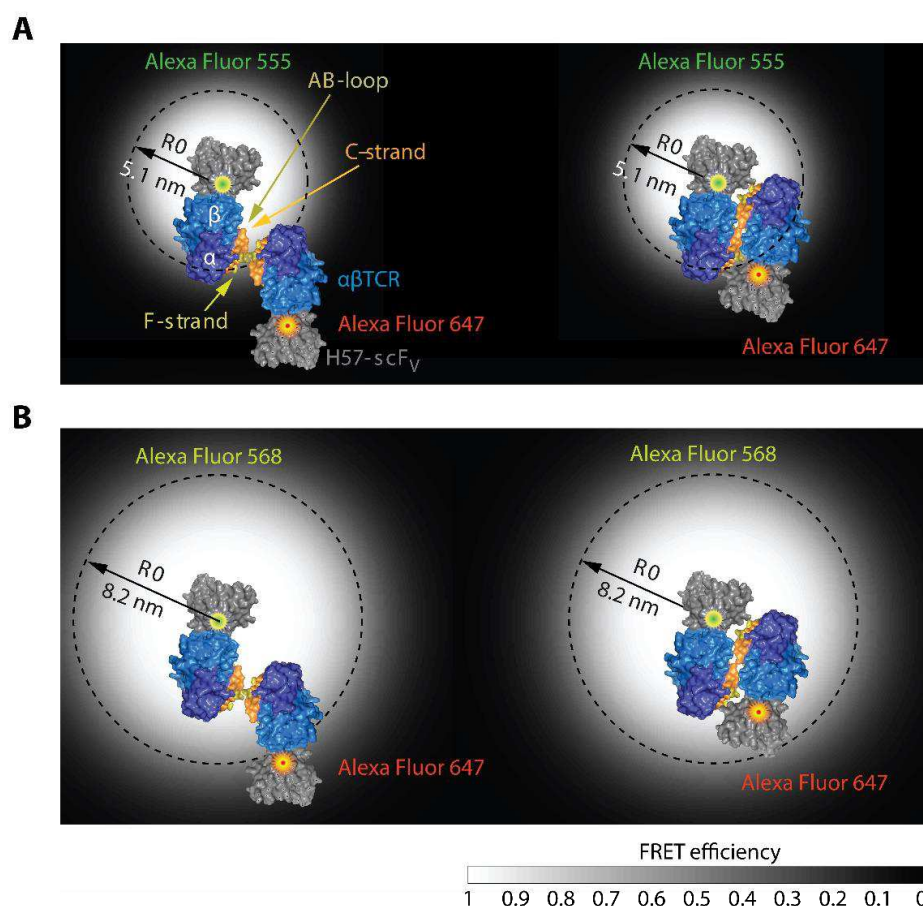


**Figure 41. FRET efficiencies of AF dyes**

**A)** FRET efficiencies of AF555 and AF647 on the TCR sub-complex in two different proposed conformations. **B)** The same arrangements with AF568 instead of AF55 gives rise to an increased FRET distance.

For quantitative interpretation of FRET data, the dyes have to be able to rotate freely within the sample and fast in comparison to the emission time, so that the assumption of  $\kappa^2=2/3$  is valid [100], [224]. However, restrictions in rotation can change  $\kappa$  and thereby  $R_0$ . The unhindered rotation of all used labels was demonstrated by anisotropy measurements [2].

The rather low FRET efficiency of  $\sim 0.09$  measured on TCR/CD3 complexes crosslinked by bivalent streptavidin raised concerns on the sensitivity of the FRET measurements. The aforementioned FRET experiments that were realized using Fab-KJ25 in combination with scFv-H57, resulted in increased FRET efficiencies of up to 0.2 [2]. Additionally, FRET experiments on the CD3 $\epsilon$  subunit using a scFv-KT3 showed average FRET efficiencies of  $\sim 0.2$ , when used in combination with scFv-H57 even  $\sim 0.25$  [2]. This elevated FRET efficiencies confirmed the sensitivity of our measurements and implicate an imperfect labeling and crosslinking by the bivalent streptavidin. The experiments with scFv-KT3 additionally confirmed the existence of two CD3 $\epsilon$  subunits per TCR/CD3 complex as measured with TOCCSL and PA/FCS within this work.

FRET experiments investigating the stoichiometry of the TCR/CD3 complexes upon activation by antigenic pMHC, were started approximately 5 min after cell addition to the bilayer. The measurements, thus, could have missed the very first events of the activation process. Within these early processes, temporary oligomerization could still be of relevance. Experiments were hence repeated on membrane areas, where ZAP70 activity was observed. These regions are presumably actively involved in signaling. The measurements were started as soon as first the signs of ZAP70 recruitment were observable. Nevertheless, no increased FRET efficiency was reported in these areas, also highlighting the absence of oligomerization in early T cell signaling [2].

Dimers of pMHC have already been reported in the 1990s by crystal structure analysis [225, 226], and in a cellular context using biochemical approaches [227]. Reich et al demonstrated the oligomerization of antigenic pMHC and TCR in solution to aggregates of about 2 to 6 complexes [228]. Mixing soluble pMHC dimers containing one agonistic peptide and one endogenous peptide with T cells did result in activation for some selected combinations, while monomeric pMHC did not activate the T cells [214]. These results were taken as indication for the existence and physiological importance of dimeric pMHC complexes and were taken as the basis for computational studies. A model was developed stating that the dimerization of agonist pMHC with endogenous pMHC enhances the transport of dimeric pMHCs to the cSMAC [229]. Despite all these studies, no direct observation of pMHC oligomerization on living APCs has been described so far. While the supported lipid bilayer system used within this work represents such a living APC only remotely, the results negate passive oligomerization of pMHC without an active role of the APC. In the hypothetical case of pMHC aggregation within the cellular context of living APCs, this had to be achieved by means of active involvement of the APCs.

From the T cells' perspective, it seems that pMHCs are actively kept apart from each other, thus being prevented from oligomerization. However, the observed decreases in FRET efficiencies were, while consistently measured in TCR and pMHC experiments, only minute. The minute effects were also shown to be maintained after Nocodazole and Latrunculin B application, which shows independence of F-Actin or microtubules [2].

## Part C: Spatial Distribution of the TCR/CD3

In addition to the valency of the receptor, also the spatial distribution of the TCR/CD3 complexes within the plasma membrane of T cells is a highly debated topic. For non-activated T cells, several studies have reported clustering of TCR/CD3 complexes and signaling proteins in nano-domains with radii of 20-100 nm [129, 185, 191]. Experimental evidence derived from electron microscopy [129, 190], biochemical experiments [115] and SMLM [129, 191, 230, 231]. While the first two methods involve harsh sample preparation procedures, the latter offers a possibility to visualize TCR/CD3 complexes even in living cells [129].

SMLM methods were first described in the mid-2000's [63, 64, 66] and while offering an easy-to-facilitate implementation, quantitative results of SMLM experiments often remain elusive and difficult to interpret. The lack of understanding novel and complex methods combined with their straight-forward realization can easily lead to misconceived models about the underlying biological processes. Nevertheless, due to reports on the artifactual character of SMLM methods when investigating the spatial nano-scale distribution of proteins [204, 232], we opted for a preceding in-depth characterization of our experimental methods, i.e. the use of PS-CFP2 for PALM. The deduction of quantitative information from SMLM data crucially depends on the photophysical character of the fluorescent label. In contrast to dSTORM with inherent repetitive blinking of organic dyes, in PALM it is often implicitly assumed that each fluorophore gives rise to a single localization. Nonetheless, it was found that this is far from being true for mEos2 [233].

This prompted us to study the emission properties of PS-CFP2 in detail. To this end, we developed a modular, experimental platform to study fluorophore blinking properties at the single-molecule level, which is generally applicable to any FP. Additionally, I used the newly gained insights from these experiments as quantitative basis for a SMLM analysis method recently developed in our lab [204] to re-investigate the spatial distribution of TCR/CD3 complexes on the membrane of non-activated T cells.

### C1) A System to Analyze Single Fluorophore Blinking

To study PS-CFP2 emission, we developed an experimental system based on immobile supported lipid bilayers which enables single-molecule emission analysis of recombinant PA/PS-FPs.

DPPC has a phase transition temperature of 41°C and is therefore suitable for generating gel-phase supported lipid bilayers at room temperature. We added trace amounts of DGS-NTA(Ni) to the supported lipid bilayers to couple his-tagged proteins. In principle, addition of recombinant, his-tagged PS-CFP2 should have allowed for investigation of the PS-FPs emission characteristics. However, when imaging the SLB without addition of PS-CFP2, we detected a high number of signals, with spectral characteristics similar to those of PS-CFP2. These unspecific signals likely originated from contaminations in the used buffers or lipids. For this reason,

a two-color system was chosen. The final platform consisted of a his-tagged tetrameric monovalent streptavidin molecule, with three of the four biotin-binding sites inactivated (mSav or 'A1D3'; **Figure 42A**). A mutation of an alanine residue at position 106 to a cysteine residue (A106C) enabled the site-specific coupling to AbberiorStar635 via maleimide conjugation (mSav-AS635). Size exclusion chromatography of a mixture of biotinylated PS-CFP2 (bio-PS-CFP2) and mSav-AS635 allowed purification of the full bio-PS-CFP2:mSav-AS635 complexes (**Figure 42B**).

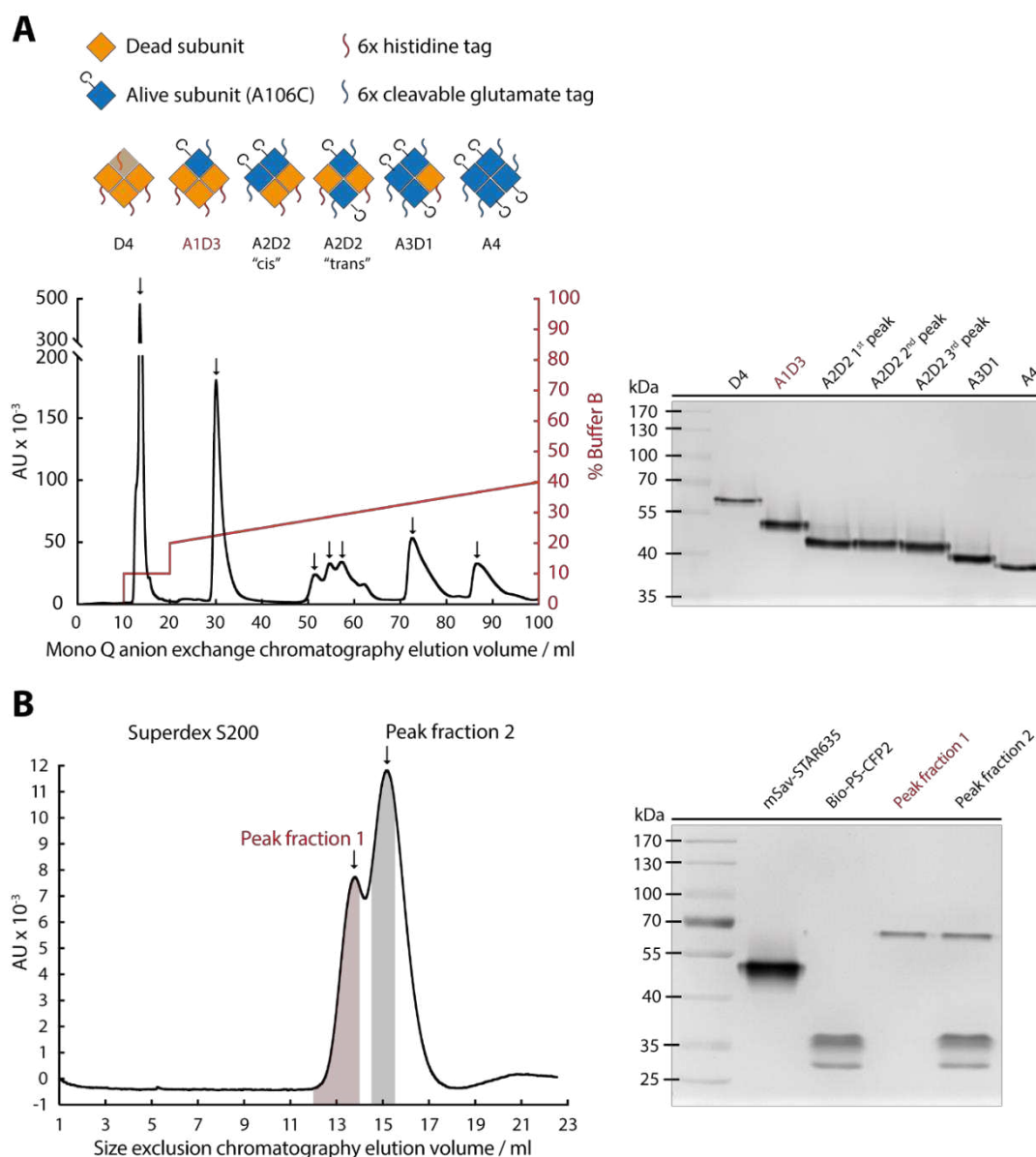


**Figure 42. Synthesis of the streptavidin-based measurement platform**

**A) Left:** Monovalent streptavidin (mSav; 'A1D3') was separated from other streptavidin species by the Glu6-tag within the active subunit. **Right:** SDS-PAGE analysis of the peak fractions from anion exchange chromatography confirmed the different streptavidin species. **B) Left:** Further size-exclusion chromatography allowed for selection of the conjugated bio-PS-CFP2:mSav-STAR635 complex, also confirmed by SDS-PAGE (right).

A full schematic of the final version of the measurement platform is shown in **Figure 43**.

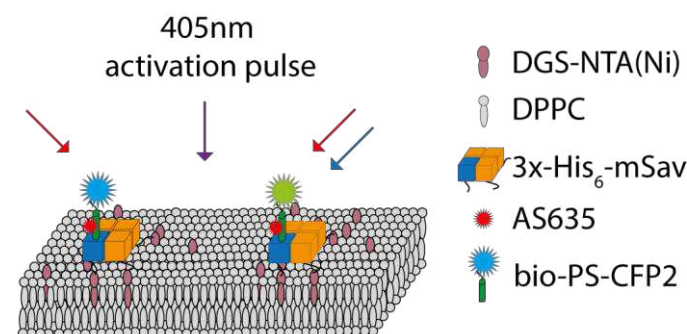


**Figure 43. Sketch of the final measurement platform**

The *bio-PS-CFP2:mSav-STAR635* complexes were coupled on immobile SLBs via DGS-NTA(Ni) and the 3x-His6 tag present on the monovalent streptavidin.

Co-localization analysis of the *bio-PS-CFP2* signals, detected after 405 nm photo-activation, with *mSav-AS635* signals minimized the amount of erroneous identification of *bio-PS-CFP2*.

In addition to contaminations, also membrane-adsorbed unconjugated *bio-PS-CFP2* or the presence of photobleached *mSav-AS635* could give rise to un-localized signals.

Single-molecule tracking of *mSav-AS635* revealed a diffusion coefficient of  $D \sim 9 \times 10^{-5} \mu\text{m}^2/\text{s}$ , confirming the low-mobility character of the SLB. In case of Brownian motion, the probability for a *bio-PS-CFP2* to stay within a circle of radius 240 nm during one full PALM recording of 60 s, is larger than 0.9:

$$p(dr) = \int_0^{r_{\max}} \frac{r}{2Dt} e^{-\frac{r^2}{4Dt}} dr \approx 0.93 \quad (26)$$

with  $r_{\max} = 0.24 \mu\text{m}$ ,  $D = 9 \times 10^{-5} \mu\text{m}^2/\text{s}$  and  $t = 60 \text{ s}$ . This confirms the applicability of the SLB system on recording emission traces of *bio-PS-CFP2* (**Figure 44**).

**Figure 45** depicts exemplary data showing *mSav-AS635* signals in an overlay with *bio-PS-CFP2* localizations recorded in a consecutive PALM sequence.

Emission traces of *bio-PS-CFP2* revealed a highly heterogeneous character ranging from single detections (**Figure 46, 1b**) over repetitive detections in consecutive frames (**Figure 46, 1a**) to multiple detections with non-emissive durations up to several seconds (**Figure 46, 2a**).

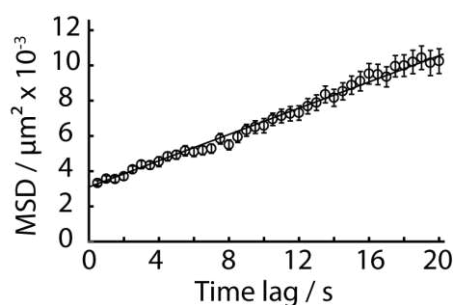


**Figure 44. Mobility determination of immobile SLBs**

A diffusion coefficient of  $D \sim 9.3 \times 10^{-5} \mu\text{m}^2/\text{s}$  was determined by single-molecule tracking of mSav-STAR635 on SLBs ( $n=79$  molecules; shown is mean  $\pm$  s.e.m.).

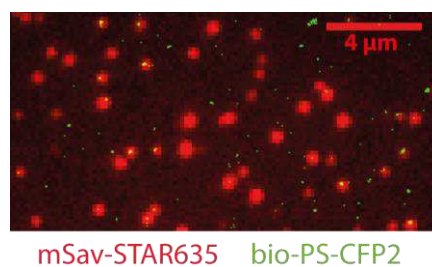


**Figure 45. Exemplary data of a co-localization experiment**

Images from a mSav-STAR635 tracking sequence are overlaid with localizations from the consecutive PALM recording of bio-PS-CFP2.

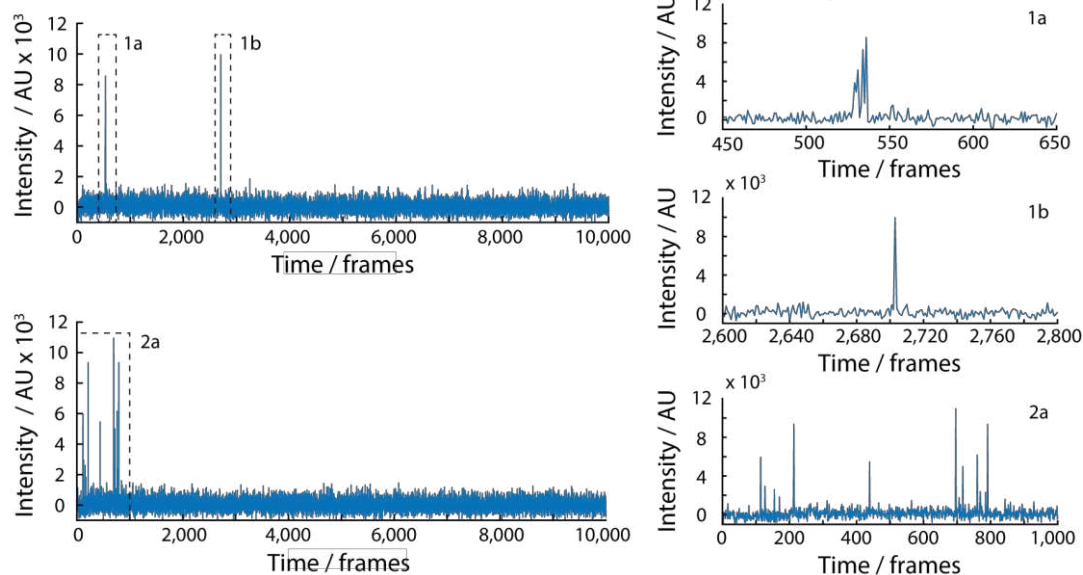


**Figure 46. Exemplary emission traces of two bio-PS-CFP2 molecules**

The intensity traces for two different PS-CFP2 molecules show multiple consecutive emission frames (1a), single-frame emission (1b) and multiple emissions with multiple gaps (2a).

## C2) Parameters to Describe Fluorophore Blinking

For quantitative analysis of the blinking traces, four parameters were investigated (Figure 47):

- The overall number of detections per single bio-PS-CFP2 molecule within the whole PALM sequence ( $N$ ),
- the number of non-emissive gaps per single bio-PS-CFP2 molecule (gaps,  $g$ ), and
- the duration of each single (non-)emissive state ( $t_{off}$ ,  $t_{on}$ ).

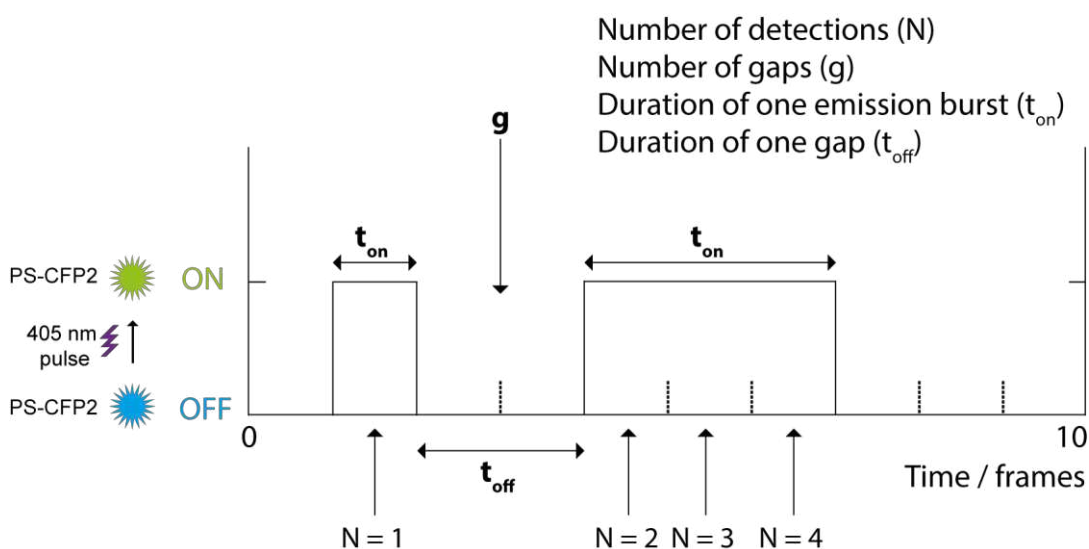


**Figure 47. Parameters for blinking characterization**

Four parameters were defined for the characterization of single-molecule blinking:  $N$ , the total number of detections per PS-CFP2 molecule;  $g$ , the number of off-gaps;  $t_{on}$ , the duration of an emission burst and  $t_{off}$ , the duration of each gap ( $g$ ).

Normalized histograms of the analysis of 1080 bio-PS-CFP2 emission traces from several experiments are shown in Figure 48. Approximately one third (35%) of bio-PS-CFP2 molecules were detected in only one frame ( $N = 1$ ), 31% were detected two to five times ( $2 \leq N \leq 5$ ), and 34% more often ( $N > 5$ ), with a maximum number of 38 detections for a single bio-PS-CFP2 molecule (Figure 48A).  $g$  gives additional information on whether a molecule turns dark and if so, how often it enters this state of absent fluorescence emission. 45% of the analyzed molecules did not enter such a dark state, leaving 55% molecules which turned non-emissive at least once. The pronounced abundancy of blinking is also supported by the maximum value of  $g = 31$  (Figure 48A, inset). The analysis of the duration of the emissive states ( $t_{on}$ ) showed that approximately 80% of the emission bursts were not longer than 1 frame. The remaining 20% of bursts lasted up to five frames (Figure 48B). Furthermore, we analyzed the durations of the non-emissive states ( $t_{off}$ ): Most off-states were shorter than 50 frames. However, the distribution showed an extremely long tail towards

several thousand frames; 8% of these dark-state gaps were longer than 200 frames (**Figure 48B, inset**).

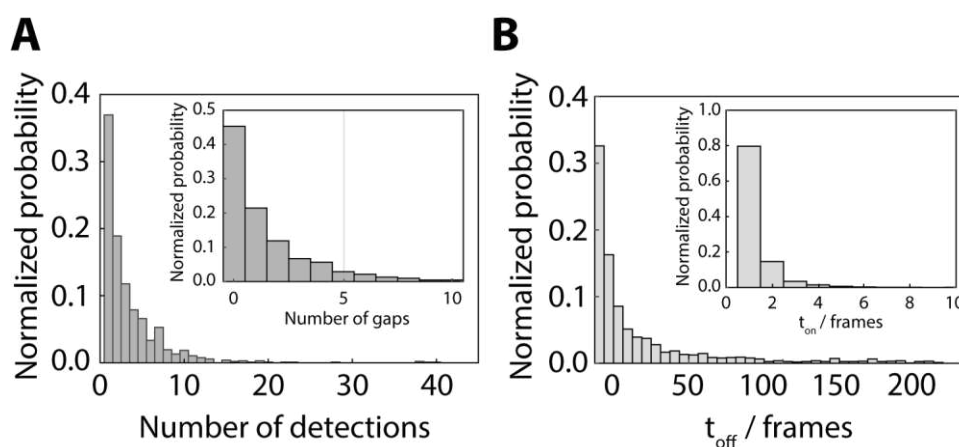


**Figure 48. Blinking parameters for bio-PS-CFP2 ( $n = 1080$  molecules)**

**A)** Normalized histograms for  $N$  and  $g$  (inset). **B)** Normalized histograms for  $t_{on}$  and  $t_{off}$  (inset).

### C3) Influence of Experimental Settings on Fluorophore Blinking

In attempts to maximize speed, illumination times down to only a few milliseconds were used, corresponding to acquisition rates of up to 250 Hz [129]. However, to maximize the signal of PA/PS-FPs, longer illumination times, i.e. lower acquisition rates (< 50 Hz) are also frequently used [191].

We were interested in how different illumination parameters, such as illumination time and imaging power, influence the blinking of bio-PS-CFP2. PALM sequences were recorded as reported by Lillemeier et al [129], who used short delay and illumination times to improve temporal resolution as a requirement for live-cell experiments. We compared the previous results, recorded at 2 ms illumination time and 3 kW/cm<sup>2</sup> intensity, to data recorded with a 7.5-fold longer illumination time at 7.5-fold reduced illumination intensity, thereby keeping the energy density at the sample identical. Using 15 ms illumination time and 0.4 kW/cm<sup>2</sup> intensity yielded an increased average  $N = 4.6$  (**Figure 49A**), and also the average duration of emissive states,  $t_{on}$ , increased (**Figure 49, inset**). The average number of non-emissive states per fluorescent protein,  $g$ , increased as well (**Figure 49B**), and the median duration of non-emissive states,  $t_{off}$ , decreased slightly (**Figure 49B, inset**).



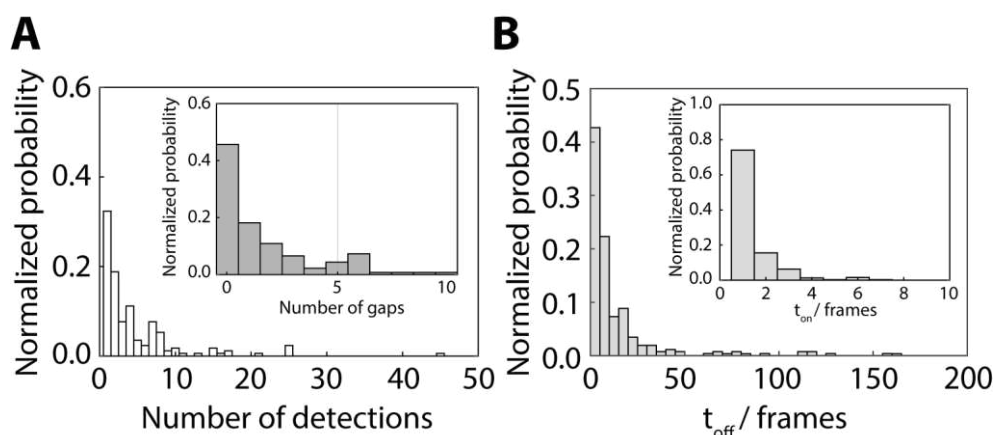


**Figure 49.** Blinking parameters for illumination with  $0.4 \text{ kW/cm}^2$  and  $15 \text{ ms}$  illumination time ( $n = 170$  molecules)

**A)** Normalized histograms for  $N$  and  $g$  (inset). **B)** Normalized histograms for  $t_{\text{on}}$  and  $t_{\text{off}}$  (inset).

PS-CFP2 is usually employed as fusion construct with other proteins. In many cases, PS-CFP2 faces the cytosol and is, because of a high glutathione (GSH) concentration [234], exposed to a reducing milieu. We imitated these conditions by performing the experiments in the presence of additional  $5 \text{ mM}$  GSH. A decrease in  $N$  to  $2.77$  combined with a decrease in the number of gaps,  $g$ , revealed an inhibitory effect of the reducing environment on the blinking of bio-PS-CFP2 (**Figure 50A**). While  $t_{\text{on}}$  did not change significantly, the median duration of dark states increased, yielding a reduction in the blinking frequency, while the duration of emission was not influenced (**Figure 50B**).

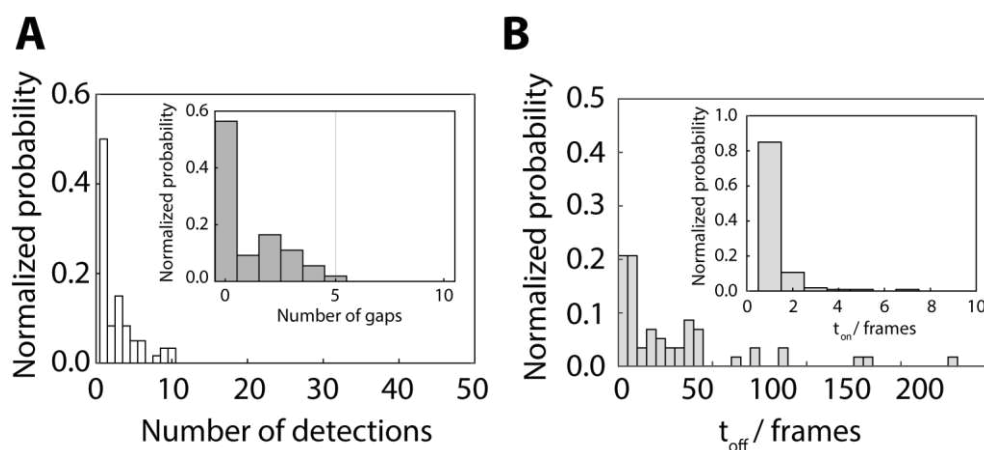


**Figure 50.** Blinking parameters for experiments with  $5 \text{ mM}$  GSH ( $n = 60$  molecules)

**A)** Normalized histograms for  $N$  and  $g$  (inset). **B)** Normalized histograms for  $t_{\text{on}}$  and  $t_{\text{off}}$  (inset).

To visualize the effect of multiple detections per fluorophore, we plotted the total number of localizations against the total number of bio-PS-CFP2 molecules. Ideal PALM experiments would yield one localization per fluorophore, which would give a 45° diagonal in this plot (**Figure 51, blue**). For our experimental data, we sorted the values of  $N$  in ascending order and normalized them to the number of molecules (**Figure 51, red**). This line starts to deviate from the ideal case at about 0.3, and reaches a final value of approximately 3.5, which is equivalent to the average number of detections per molecule. Experiments with decreased imaging power or with additional 5 mM GSH are shown in **Figure 51, magenta and green**, respectively. An overview over the performed experiments is given in **Table 11**.

| Laser-power            | Illumination Time | Buffer         | Fig.             |
|------------------------|-------------------|----------------|------------------|
| 3 kW/cm <sup>2</sup>   | 2 ms              | PBS            | <b>Figure 48</b> |
| 0.4 kW/cm <sup>2</sup> | 15 ms             | PBS            | <b>Figure 49</b> |
| 3 kW/cm <sup>2</sup>   | 2 ms              | PBS + 5 mM GSH | <b>Figure 50</b> |

**Table 11. Summary of single-molecule PS-CFP2 blinking experiments**

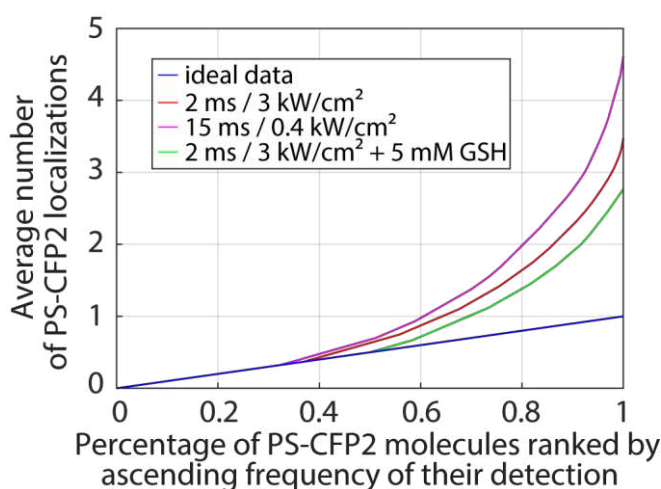


**Figure 51. Visualizing the effect of over-counting**

The detections per bio-PS-CFP2 were sorted and plotted against their rank. Both axes were normalized to the total number of bio-PS-CFP2 molecules. An ideal experimental scenario with a fluorophore-to-localization ratio of 1:1 is indicated by the blue line. All three examined experimental conditions (for color see key) showed clear deviations from this line.

#### C4) Ripley's K Analysis I: Effects of Blinking

SMLM methods do not result in an image *per se*, but in a list of localizations. This gave rise to a multitude of applications of statistical analyses on SMLM data [205, 235-237]. One commonly used method is Ripley's K statistics [238, 239]. Localizations within circles of increasing radius  $r$  are counted and normalized to their average density, for which a Poisson process would give  $K = \pi r^2$ . Typically,  $L(r)-r$  is plotted, with  $L = \sqrt{K/\pi}$ , yielding a horizontal line at zero for a Poissonian distribution (**Figure 52, blue**). When applied to SMLM data, deviations of this curve are often used as indications for protein clustering [240]. It is assumed in this

analysis that each localization represents one molecule. The effect of over-counting is furthermore neglected.

To evaluate the influence of overcounting on Ripley's K analysis, we performed simulations of random and clustered molecular distributions with and without PS-CFP2 blinking. For simulations of a random protein distribution, the positions of the molecules were randomly drawn within the simulated area; for clustered distributions, the centers of circular clusters were randomly drawn, followed by filling the clusters randomly with proteins. Blinking was simulated by drawing a value  $N_i$  from the empirically derived cumulative density function of  $N$  for each molecule and spreading the localizations within a Gaussian distribution, centered at the actual molecule position, with a width of the typical experimental localization errors of 25 nm. While the density of the molecules was kept constant at 70 molecules/ $\mu\text{m}^2$  as a basis for the simulation, the addition of blinking consequently increased the number of detected localizations.

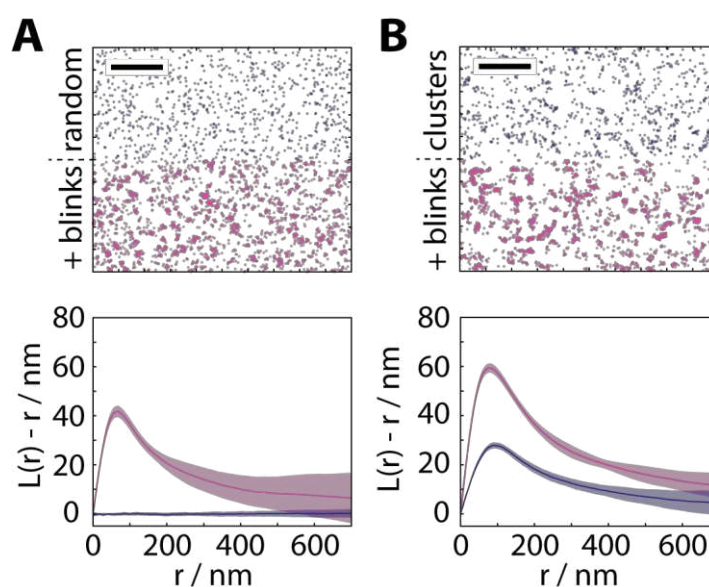


**Figure 52. Effect of blinking on Ripley's K analysis**

**A)** top: exemplary simulation of a random distribution of 70 molecules/ $\mu\text{m}^2$  without blinking (blue) and with blinking on the basis of bio-PS-CFP2 data (magenta). Bottom: 15 simulations were run, and Ripley's K analysis was done for distributions similar to top panel (Scale bar:  $2\mu\text{m}$ ; shown is mean  $\pm$  sd). **B)** top: exemplary simulation of a clustered distribution (cluster radius = 60 nm; cluster density = 20 clusters/ $\mu\text{m}^2$  and 80% of molecules within the clusters) of 70 molecules/ $\mu\text{m}^2$  without blinking (blue) and with blinking on the basis of bio-PS-CFP2 data (magenta). Bottom: 15 simulations were run, and Ripley's K analysis was done for distributions similar to top panel (Scale bar:  $2\mu\text{m}$ ; shown is mean  $\pm$  sd).

Upon the inclusion of blinking, the clusters of localizations in the simulation of a random molecular distribution became apparent (**Figure 52A, purple**), and  $L(r)$ - $r$  showed a clear peak (**Figure 52A, purple**).

Remarkably, non-blinking but clustered distributions of molecules gave rise to a similar peak in  $L(r)$ - $r$  (**Figure 52B, blue**), with the peak getting more pronounced after including blinks in the simulation (**Figure 52B, purple**). Ultimately, the effect of over-counting clearly disqualified Ripley's  $K$  analysis as a tool for detecting molecular clustering from SMLM data.

### C5) Label-density-variation SMLM of TCR/CD3 Subunits

Given the non-ideal behavior of recombinant bio-PS-CFP2 for PALM, we re-assessed the spatial distribution of the TCR/CD3 complex in T cells on non-activating supported lipid bilayers, utilizing a recently developed method termed label-density-variation microscopy [204]. Three different receptor subunits were imaged by dSTORM using fluorescent labels for TCR $\beta$  and CD3 $\epsilon$  or by PALM using retroviral transduction of the fusion protein CD3 $\zeta$ -PS-CFP2. As positive controls, all experiments were also performed on activating supported lipid bilayers (**Figure 28**). Label-density-variation microscopy is robust to over-counting artifacts and is based on titrating the label down to a level in which single label molecules are imaged [204]. The image characteristics are compared for different degrees of labeling. Specifically, images are described by the relative area covered by apparent localization clusters ( $\eta$ ) and the normalized localization density within clusters ( $\rho$ ). For a random distribution of molecules,  $\eta$  increases with labeling density, whereas  $\rho$  remains rather constant (**Figure 53A, C and D, magenta**). In case of real protein clustering, the relative clustered area  $\eta$  increases to a lesser extent while the localization density  $\rho$  within the clustered area increases (**Figure 53B, C and D, cyan**). **Figure 53E** shows a typical  $\rho$ -vs- $\eta$  plot. The black reference curve shows the result for a random distribution.

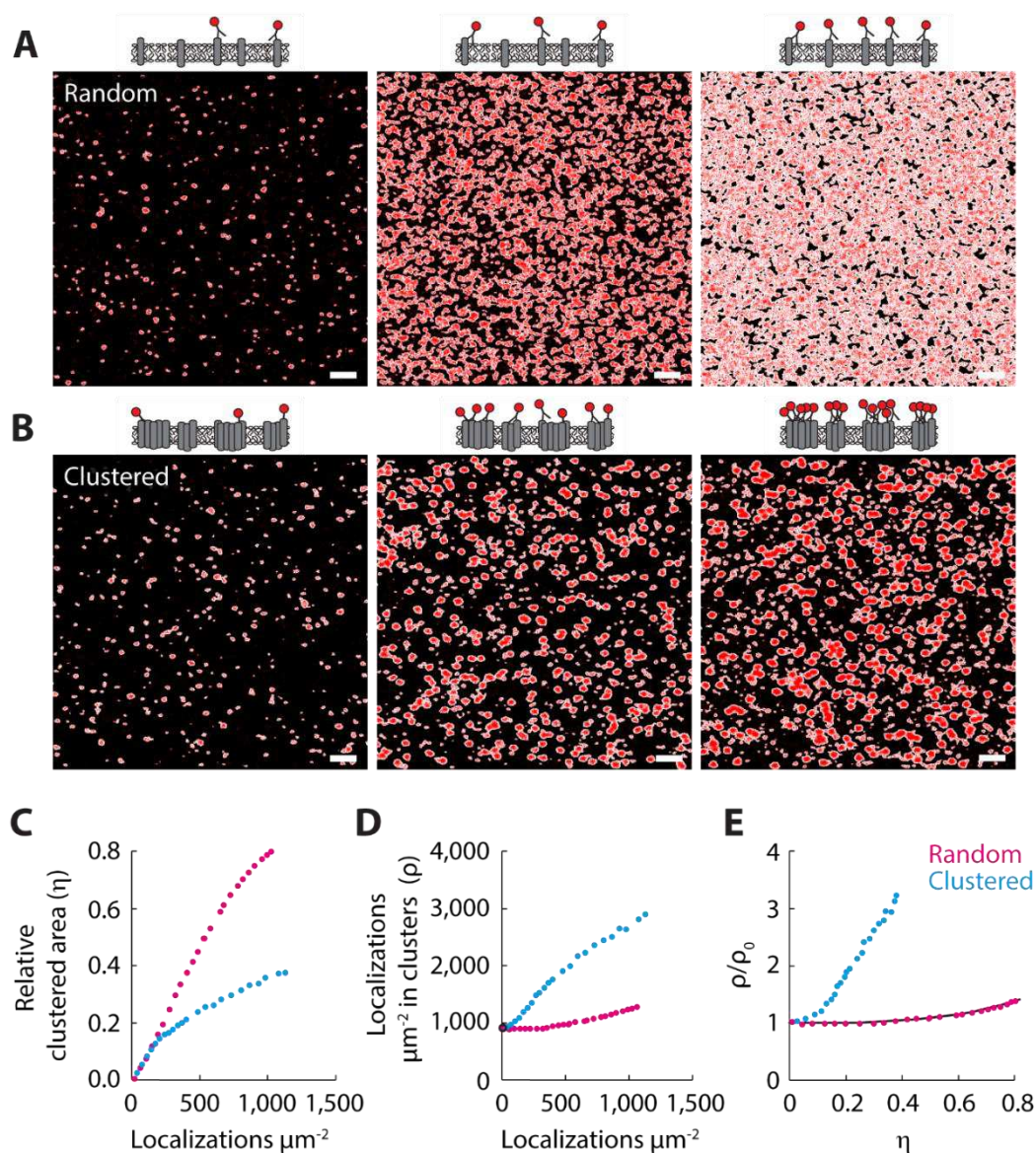


**Figure 53. Label-density-variation SMLM**

**A)** For a random protein distribution, a low concentration of the label leads to the presence of spurious localization clusters due to fluorophore blinking (left). Increasing the label density increases the relative clustered area  $\eta$  (red) while the density of localizations within this area,  $\rho$ , remains rather constant. **B)** For a clustered protein distribution, a low concentration of the label leads to a similar result as for the random protein distribution (left). Increasing the label density will fill up clusters with localizations, yielding an increase of  $\rho$  at rather constant values of  $\eta$ . **C)** Plotting  $\eta$  versus the density of localizations shows a more pronounced increase for a random distribution. **D)** Plotting  $\rho$  versus the density of localizations shows only an increase for clustered distributions. **E)** Plotting  $\rho$  versus  $\eta$  ( $\rho$ -vs- $\eta$  plot) allows for a clear discrimination between the case of random and clustered protein distributions. Reprinted as adapted version by permission from Springer Nature: Nature Methods, 'Varying label density allows artifact-free analysis of membrane-protein nanoclusters' by Baumgart F, Arnold AM, Leskovar K, Staszek K, Fölser M, Weghuber J, Stockinger H, Schütz GJ, ©2016.

For studying the spatial distribution of the TCR $\beta$  subunit, the monoclonal antibody H57 was conjugated to AF647 (H57-AF647) and used for labeling at varying concentrations (0.1, 1, 5 and 10  $\mu\text{g/ml}$ ). 5c.c7 T cells were seeded onto (non-)activating supported lipid bilayers, fixed, and diffraction-limited as well as dSTORM images were acquired. When labeled at saturating concentration, the distribution of fluorophores on the T cell membrane of non-activated cells looked slightly heterogenous even in the diffraction-limited image (**Figure 54, left**). These brightness variations could be due to pixel-to-pixel variations in the number of receptors or differences in fluorophores per labeled antibody. Investigation of dSTORM localization maps of non-activated T cells confirmed this seemingly heterogenous distribution (**Figure 54, right**). Even more so, when reconstructing diffraction-limited images by convolution of the localization data with the PSF of the microscope, strong inconsistencies between the diffraction-limited image and the reconstructed dSTORM image could be seen (**Figure 54, middle**). These inconsistencies include pronounced features in the diffraction-limited image, which are absent in the convolved dSTORM data (**Figure 54, red arrows**), or vice versa (**Figure 54, yellow arrows**).

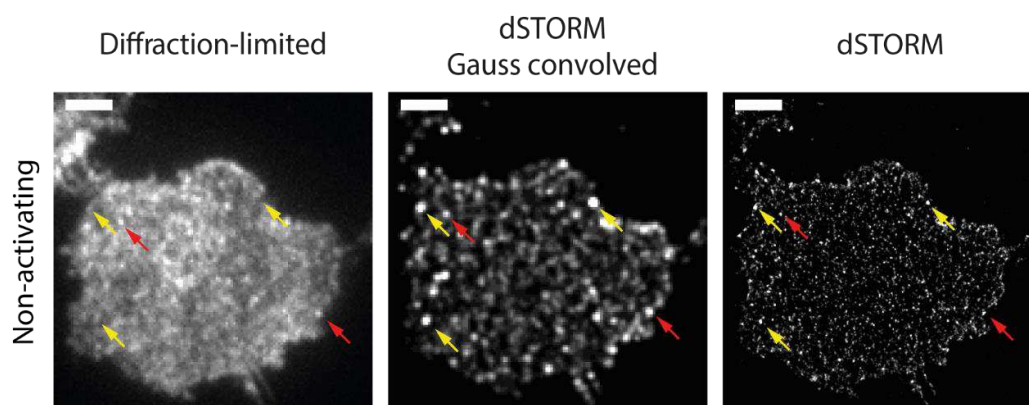


**Figure 54. Comparison of diffraction-limited and dSTORM images.**

Diffraction-limited images (left) were recorded before the dSTORM experiments (right). For comparison, the reconstructed dSTORM image was convolved with the PSF of the imaging system (middle). Red arrows highlight features which are present in all three images, yellow arrows highlight artifactual features not present in the diffraction-limited image. Scale bar: 3  $\mu\text{m}$ .

We hence aimed at determining the obtained single molecule localization microscopy images in a statistically correct way using label-density-variation analysis. For this, we first determined a reference curve for the case of a random distribution. To this end, we used Monte Carlo simulations based on the blinking statistics of the H57-AF647 antibody, derived from dSTORM data recorded with low labeling density (**Figure 55**). The molecular density in the simulations was adjusted to the number of localizations divided by the average number of localizations per antibody (mean of  $N$ ; **Figure 55B**), for fully-labeled cells. The densities approximated in this way ranged from 59 to 81 molecules/ $\mu\text{m}^2$  and fitted well to a previously

published surface density of  $\sim 70$  molecules/ $\mu\text{m}^2$  derived by brightness analysis [2]. dSTORM recordings of H57-AF647 labeled T cells on non-activating supported lipid bilayer

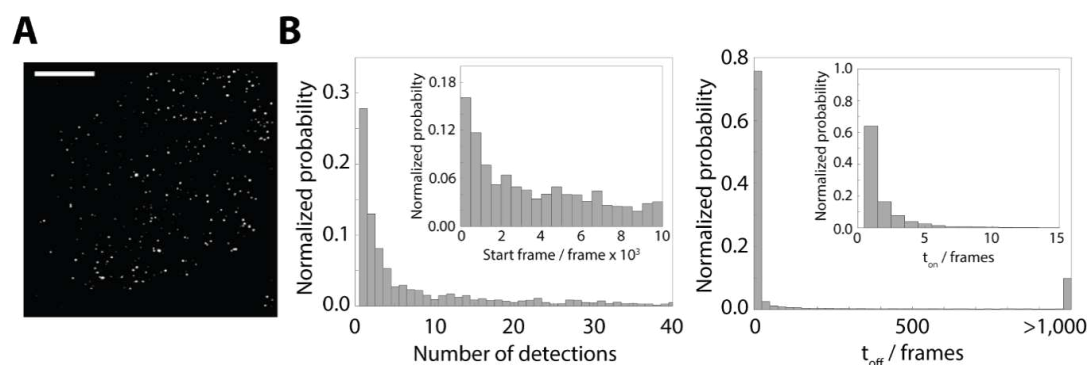


**Figure 55. Blinking estimation for H57-AF647**

**A)** T cells were labelled with H57-AF647 at low densities ( $c = 0.05 \mu\text{g/ml}$ ), fixed and imaged with dSTORM. Scale bar:  $3 \mu\text{m}$ . **B)** Blinking parameters were estimated, and normalized histograms are shown for  $n = 1,827$  H57-AF647 antibodies.

bilayers (**Figure 56A, top**) did not deviate from the simulated reference curve (**Figure 56B, red line & blue data**), which supports the view of a random distribution across the membrane.

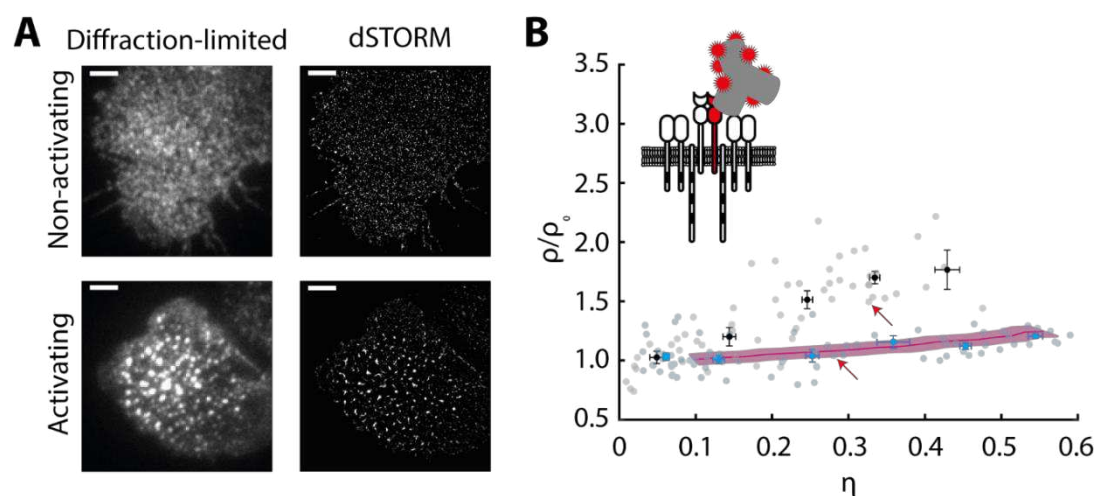


**Figure 56. Label-density-variation dSTORM of TCR $\beta$  with H57-AF64**

**A)** Before dSTORM experiments, diffraction-limited images of T cells on non-activating (top) or activating (bottom) SLBs were recorded (A, left). Reconstructed dSTORM images are shown in the right panel of A. Scale bars:  $3 \mu\text{m}$ . **B)**  $\rho$ -vs- $\eta$  plot for label-density-variation analysis of dSTORM experiments with H57-AF647. T cells on non-activating (blue,  $n = 75$  cells) or activating (black,  $n = 55$  cells) SLBs were labeled with H57-AF647 at varying concentrations (0.05, 1, 5 and  $10 \mu\text{g/ml}$ ). Cells shown in panel A are highlighted by a red arrow. Bold data points represent means  $\pm$  s.e.m. of binned data according to  $\eta$  (size: 0.1). The magenta line (mean  $\pm$  s.e.m.) represents the reference curve derived from simulations with a random distribution and H57-AF647 blinking statistics ( $n = 50$  simulations).

However, when T cells were added to activating supported lipid bilayers, micro-clustering of the TCR could readily be detected (**Figure 56A, bottom** and **Figure 56B, red line & black data**).

We repeated the experiments using an antibody specific to CD3 $\epsilon$  (clone KT3). Due to the reduced number of fluorophores per antibody, the number of detections per label was lower than for the H57 antibody (**Figure 57**).

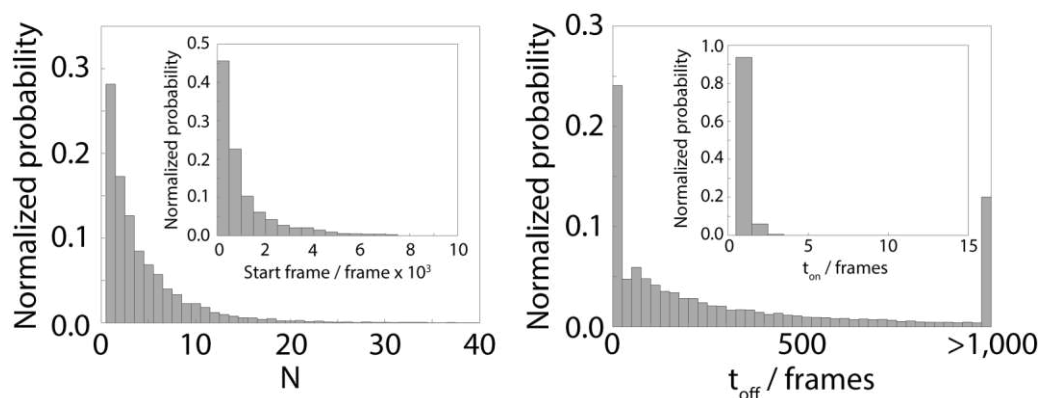


**Figure 57. Blinking determination for KT3-AF647**

T cells were labelled with KT3-AF647 at low densities ( $c = 0.02 \mu\text{g/ml}$ ) and imaged with dSTORM. Blinking parameters were estimated, and normalized histograms are shown for  $n = 6,151$  KT3-AF647 antibodies.

A surface density of 68-73 molecules/ $\mu\text{m}^2$  was determined. However, as two CD3 $\epsilon$  subunits are present per TCR/CD3 complex, we expected two-fold higher numbers. Steric hindrance and incomplete labeling might account for this: due to the potency of the KT3 antibody to induce activation via cross-linking, labeling had to be conducted after cell adhesion and fixation. For non-activated T cells (**Figure 58A, top**), the results confirmed the conclusions from H57-AF647 experiments (**Figure 58B, red line & blue data**). When performing labeling before adhesion and fixation, clustering was induced (**Figure 58A, bottom**) and could be readily detected by label-density-variation microscopy (**Figure 58B, red line & black data**).



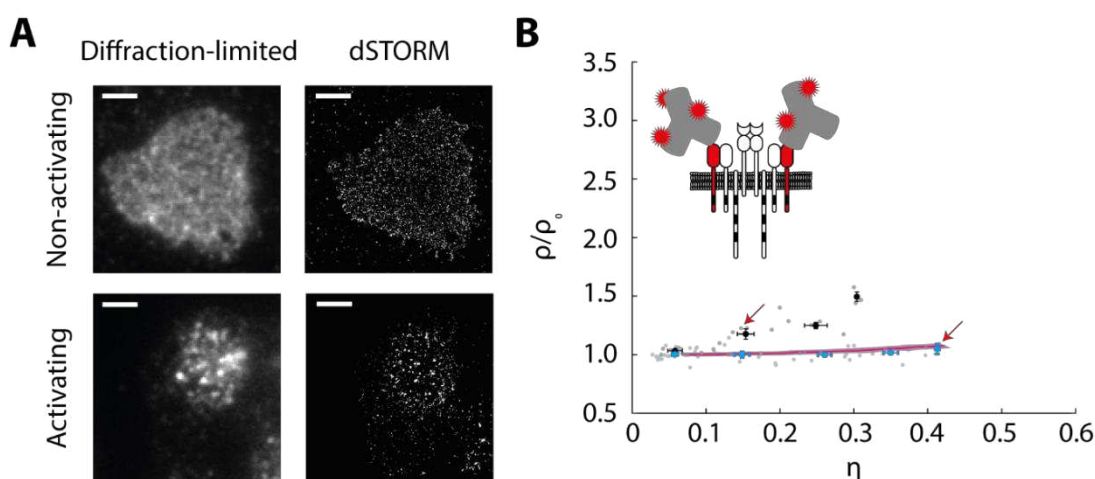


**Figure 58. Label-density-variation dSTORM for CD3 $\epsilon$  using KT3-AF647**

**A)** Before dSTORM experiments, diffraction-limited images of T cells on non-activating (top) or activating (bottom) SLBs were recorded (A, left). Reconstructed dSTORM images are shown in the right panel of A. Scale bars: 3  $\mu\text{m}$ . **B)**  $\rho$ -vs- $\eta$  plot for label-density-variation analysis of dSTORM experiments with KT3-AF647. T cells on non-activating (blue,  $n = 19$  cells) or activating (black,  $n = 10$  cells) SLBs were labeled with KT3-AF647 at varying concentrations (0.02, 0.2, 2 and 20  $\mu\text{g/ml}$ ). Cells shown in panel A are highlighted by a red arrow. Bold data points represent means  $\pm$  s.e.m. of binned data according to  $\eta$  (size: 0.1). The magenta line (mean  $\pm$  s.e.m.) represents the reference curve derived from simulations with a random distribution and KT3-AF647 blinking statistics ( $n = 50$  simulations).

Taken together, label-density-variation dSTORM experiments did not support nanoclustering for TCR $\beta$  and CD3 $\epsilon$ .

While dSTORM inherently relies on the repeated activation of organic dyes, PALM facilitates the use of PS- or PA-FPs, which allows for minimizing the influence of over-counting. Nevertheless, a significant fraction of FPs can still be detected multiple times as described in **Chapter 3 – Part C**. Unfortunately, efficient conjugation of recombinant PS-CFP2 to a H57-scFv could not be achieved. We also tried to label T cells with biotinylated H57-scFv conjugated to mSav-PS-CFP2, but also for this approach, the achieved labeling efficiency was poor. Finally, a decision was made towards retroviral expression of the fusion protein CD3 $\zeta$ -PS-CFP2.

As an advantage, this allowed to probe a third constituent of the TCR/CD3 complex, CD3 $\zeta$ . We applied label-density-variation PALM on T cells expressing CD3 $\zeta$ -PS-CFP2. To vary the labeling density, the natural variation in expression level of the transduced protein was exploited. For imaging the TCR/CD3 complex by diffraction-limited microscopy, T cells were labeled with H57-scFv-AF647. We analyzed the blinking behavior of CD3 $\zeta$ -PS-CFP2 from data of cells with low expression level (**Figure 59**).

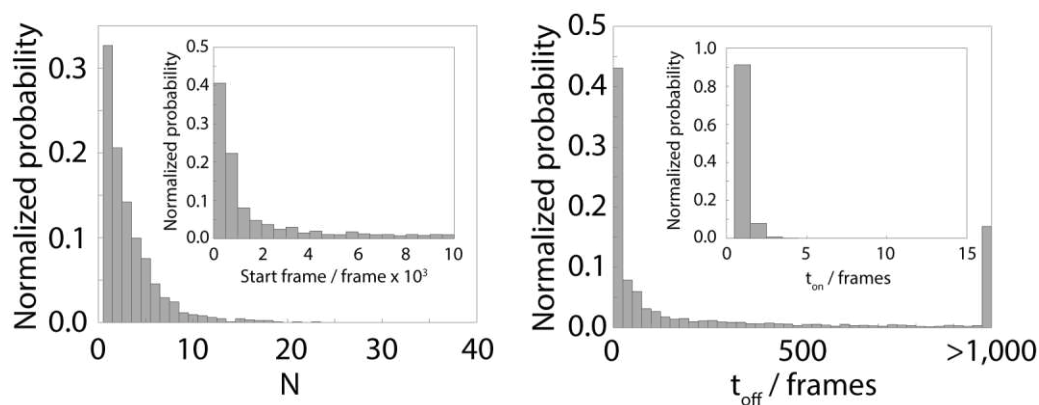


**Figure 59. Determination of blinking for CD3 $\zeta$ -PS-CFP2**

T cells with low expression levels of CD3 $\zeta$ -PS-CFP2 were imaged using PALM. Blinking parameters were estimated, and normalized histograms are shown for  $n = 1,409$  CD3 $\zeta$ -PS-CFP2 entities.

After the determination of the mean number of localizations per CD3 $\zeta$ -PS-CFP2 ( $N$ ), the surface densities were estimated by dividing the total number of localizations by  $N$ , yielding 37–141 molecules/ $\mu\text{m}^2$ . Contrary to dSTORM experiments, here, the presence of endogenous CD3 $\zeta$  complicates the analysis of expression levels. The discrimination between an overall low expression level of all CD3 $\zeta$  species or only a small fraction of CD3 $\zeta$  being fused to PS-CFP2 is therefore not possible. Nevertheless, assuming low endogenous levels of CD3 $\zeta$  as described by Lillemeier et al. [129] and a stoichiometric ratio of 1:2 for TCR $\beta$  and CD3 $\zeta$ , the measured surface densities are in accordance with previously reported levels of 20 – 120 TCR $\beta$  per  $\mu\text{m}^2$  [2].

Reconstructed PALM images showed again a seemingly heterogeneous distribution of CD3 $\zeta$ -PS-CFP2 similar to dSTORM images (**Figure 60A, top**). However, label-density-variation analysis did not reveal a deviation from the random reference curve (**Figure 60B, red line & blue data**). Upon activation (**Figure 60A, bottom**), the micro-clusters were readily detected (**Figure 60B, red line & black data**). Over-counting was considered to be overcome when recording live-cell PALM as molecules would move during the non-emissive state  $t_{\text{off}}$  [129].

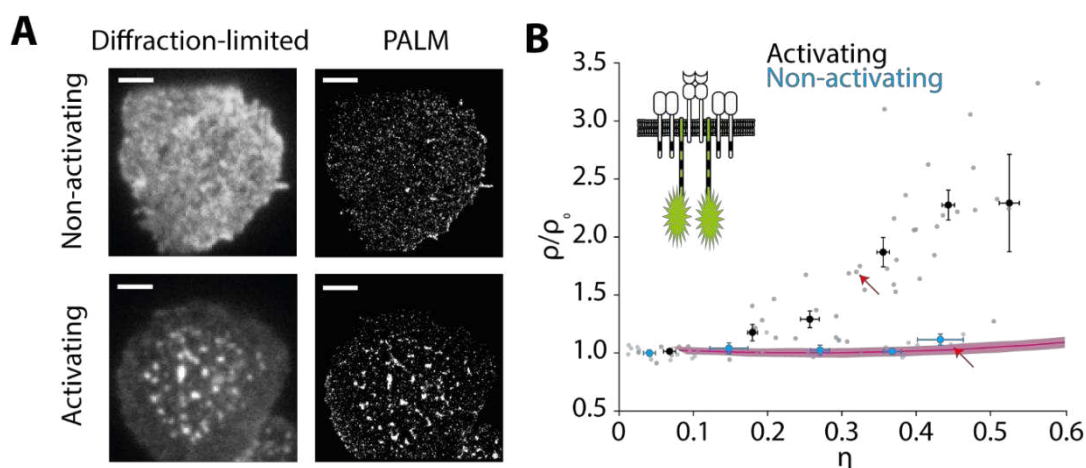


**Figure 60. Label-density-variation PALM for CD3 $\zeta$ -PS-CFP2**

**A)** Before PALM experiments were conducted, diffraction-limited images of T cells labeled with H57-scFv-AF647 on non-activating (top) or activating (bottom) SLBs were recorded (A, left). Reconstructed PALM images are shown in the right panel of A. Scale bars: 3  $\mu\text{m}$ . **B)**  $\rho$ -vs- $\eta$  plot for label-density-variation analysis of PALM experiments with T cells expressing CD3 $\zeta$ -PS-CFP2 on non-activating (blue,  $n = 30$  cells) or activating (black,  $n = 50$  cells) SLBs. Cells shown in panel A are highlighted by a red arrow. Bold data points represent means  $\pm$  s.e.m. of binned data according to  $\eta$  (size: 0.1). The magenta line (mean  $\pm$  s.e.m.) represents the reference curve derived from simulations with a random distribution and CD3 $\zeta$ -PS-CFP2 blinking statistics ( $n = 50$  simulations).

For this reason, we performed label-density-variation PALM experiments of CD3 $\zeta$ -PS-CFP2 on live T cells. However, the localization maps derived from the PALM data still showed clustered appearance (**Figure 61A**). For creating the reference curve for a random distribution, we included diffusion, that was measured earlier (see **Chapter 3 – Part A**), into the simulations. A fraction of 36% of all molecules was simulated to diffuse slowly with  $0.003 \mu\text{m}^2/\text{s}$ . This was combined with a fraction of 64% of molecules diffusing fast with  $0.047 \mu\text{m}^2/\text{s}$ . After the analysis using label-density-variation, no indication for a deviation from the random reference curve was found (**Figure 61B**).

Apparently, the overall low mobility for the TCR/CD3 complexes kept the probability for re-observations in close proximity high, especially when recording at high acquisition rates.

An overview over all performed SMLM experiments is shown in **Table 12**.

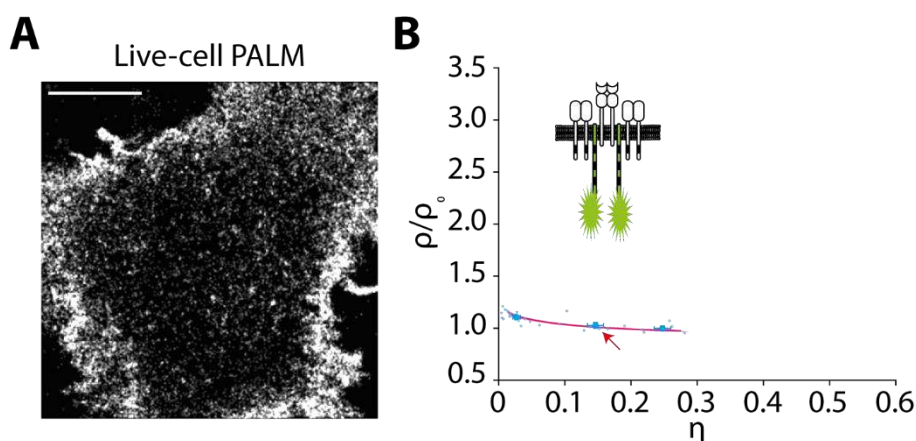


**Figure 61. Label-density-variation PALM on living cells for CD3 $\zeta$ -PS-CFP2**

**A)** T cells expressing CD3 $\zeta$ -PS-CFP2 were added on non-activating SLBs and PALM images were recorded. Scale bar: 3  $\mu\text{m}$ . **B)**  $\rho$ -vs- $\eta$  plot for label-density-variation analysis of living-cell PALM experiments with T cells expressing CD3 $\zeta$ -PS-CFP2 on non-activating SLBs (blue,  $n = 29$  cells). The cell shown in panel A is highlighted by a red arrow. Bold data points represent means  $\pm$  s.e.m. of binned data according to  $\eta$  (size: 0.1). The magenta line (mean  $\pm$  s.e.m.) represents the reference curve derived from simulations with a random distribution and CD3 $\zeta$ -PS-CFP2 blinking statistics ( $n = 50$  simulations).

| SMLM Method | Probe                    | Complex Subunit | Live/Fixed | Fig.             |
|-------------|--------------------------|-----------------|------------|------------------|
| dSTORM      | H57-<br>AF647            | TCR $\beta$     | Fixed      | <b>Figure 56</b> |
| dSTORM      | KT3-<br>AF647            | CD3 $\epsilon$  | Fixed      | <b>Figure 58</b> |
| PALM        | CD3 $\zeta$ -PS-<br>CFP2 | CD3 $\zeta$     | Fixed      | <b>Figure 60</b> |
| PALM        | CD3 $\zeta$ -PS-<br>CFP2 | CD3 $\zeta$     | Live       | <b>Figure 61</b> |

**Table 12. Summary of label-density-variation SMLM experiments**

## C6) Ripley's K Analysis II: T Cell Context

To study the effects of blinking and diffusion on Ripley's K analysis, we performed additional Monte Carlo simulations. We used the determined blinking statistics of H57-AF657, KT3-AF647 antibodies or CD3 $\zeta$ -PS-CFP2 to simulate the expected localization patterns of randomly distributed monomeric or dimeric molecules and analyzed the results with Ripley's K analysis.

**Figure 62A** shows a random distribution of signals and the corresponding Ripley's K analysis, yielding a constant line at  $L(r)-r = 0$ . Including the blinking statistics of H57-AF647 in the simulation, gave rise to a significant peak in the Ripley's K curve, which indicates clustering of localizations (**Figure 62B**).

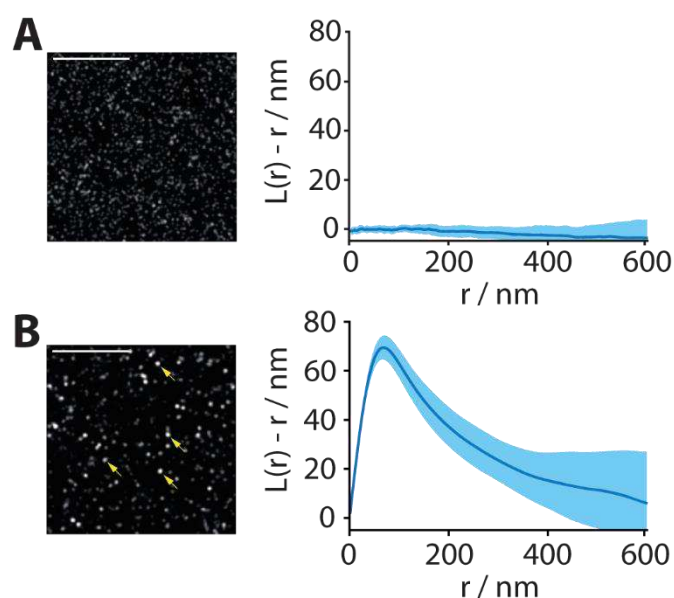


**Figure 62. Ripley's K analysis on randomly distributed monomers with and without blinking of H57-AF647**

Molecules were simulated at densities of 70 molecules/ $\mu\text{m}^2$  in  $5 \times 5 \mu\text{m}$  areas ( $n = 10$  simulations). Simulated, reconstructed SMLM images are shown (left) with corresponding Ripley's K results (right; mean  $\pm$  sd). Scale bars: 2  $\mu\text{m}$ . **A)** Distribution of randomly distributed non-blinking monomers. **B)** Distribution of randomly distributed monomers with H57-AF647 blinking. Yellow arrows highlight exemplary features occurring due to over-counting.

Simulations of randomly distributed dimers without blinking gave rise to a peak in the  $L(r)-r$  curve, showing the high sensitivity of Ripley's K analysis (**Figure 63A**). Addition of KT3-AF647 blinking increased the peak further (**Figure 63B**).

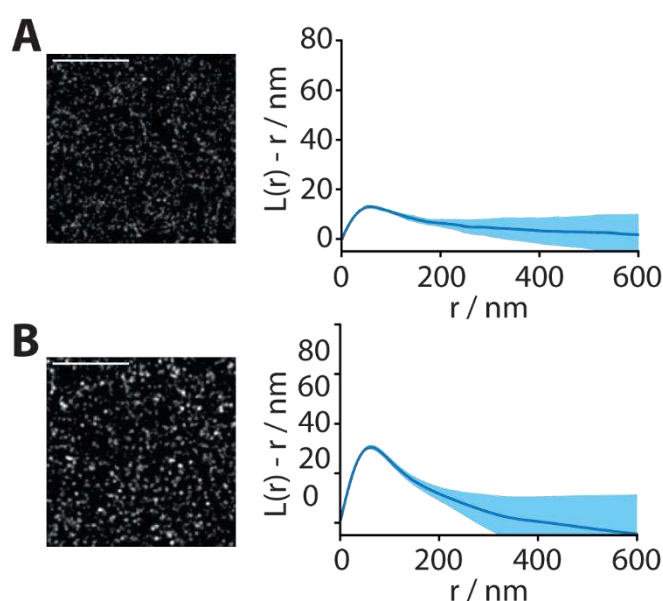


**Figure 63. Ripley's K analysis of randomly distributed dimers with and without blinking of KT3-AF647**

Molecules were simulated at densities of  $70 \text{ molecules}/\mu\text{m}^2$  in  $5 \times 5 \mu\text{m}$  areas ( $n = 10$  simulations). Simulated, reconstructed SMLM images are shown (left) with corresponding Ripley's K results (right; mean  $\pm$  sd). Scale bars:  $2 \mu\text{m}$ . **A)** Distribution of randomly distributed non-blinking dimers. **B)** Distribution of randomly distributed dimers with KT3-AF647 blinking.

Changing the blinking behavior of the randomly distributed dimers to that of CD3 $\zeta$ -PS-CFP2 yielded a similar result (**Figure 64A**).

First observations of protein nanoclusters were partially based on live-cell SMLM experiments [129]. Arguably, the blinking of fluorophores would not influence the results as the molecules will move between their emission gaps. This, however, strongly depends on the acquisition rate, the mean emission gap length and the mobility of the studied protein. Thus, knowledge of the diffusional characteristics of the protein is indispensable for interpretation of live-cell SMLM data. To study the effects of the rather low overall mobility of the TCR/CD3 complexes, and especially of the immobile fraction, we performed simulations including protein diffusion. Randomly distributed dimers were simulated, including the blinking characteristics as well as the determined mobility of CD3 $\zeta$ -PS-CFP2 (36% quasi-immobile with  $D = 0.003 \mu\text{m}^2/\text{s}$ , 64% diffusing with  $D = 0.047 \mu\text{m}^2/\text{s}$ ). Subsequent Ripley's K analysis showed a distinct peak, which indicated clusters of localizations in a randomized protein distribution (**Figure 64B**).

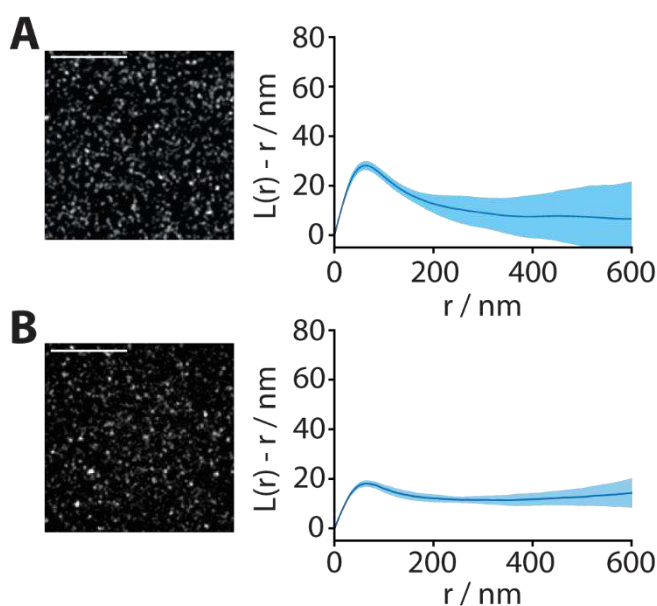


**Figure 64. Ripley's K analysis of randomly distributed dimers with blinking behavior of CD3 $\zeta$ -PS-CFP2 with and without TCR-like diffusion**

Molecules were simulated at densities of 70 molecules/ $\mu\text{m}^2$  in  $5 \times 5 \mu\text{m}$  areas ( $n = 10$  simulations). Simulated, reconstructed SMLM images are shown (left) with corresponding Ripley's K results (right; mean  $\pm$  sd). Scale bars: 2  $\mu\text{m}$ . **A)** Distribution of randomly distributed dimers with CD3 $\zeta$ -PS-CFP2 blinking. **B)** Distribution of randomly distributed dimers with CD3 $\zeta$ -PS-CFP2 blinking and additional diffusion according to the measured behavior (mobile fraction: 64% with  $D = 0.047 \mu\text{m}^2/\text{s}$ ; quasi-immobile fraction: 36% with  $D = 0.003 \mu\text{m}^2/\text{s}$ ).

Fluorophore blinking thus affects Ripley's K analysis also in live-cell SMLM data, especially if the protein shows a significant immobile fraction and/or a slow overall diffusion.

Due to incomplete maturation of CD3 $\zeta$ -PS-CFP2, molecules might be missed during a PALM experiment, giving rise to a bias of the dimeric distribution towards monomers. To account for such effects, we included a fraction of 30% monomers and simulated random distributions without blinking (**Figure 65A**), with blinking (**Figure 65B**), and with blinking and diffusion (**Figure 65C**). All three simulations revealed a peak within the  $L(r)$ - $r$  function indicative of clustering.

Taken together, Ripley's K does not represent an adequate tool for analysis of cellular SMLM data in the presence of fluorophore blinking.

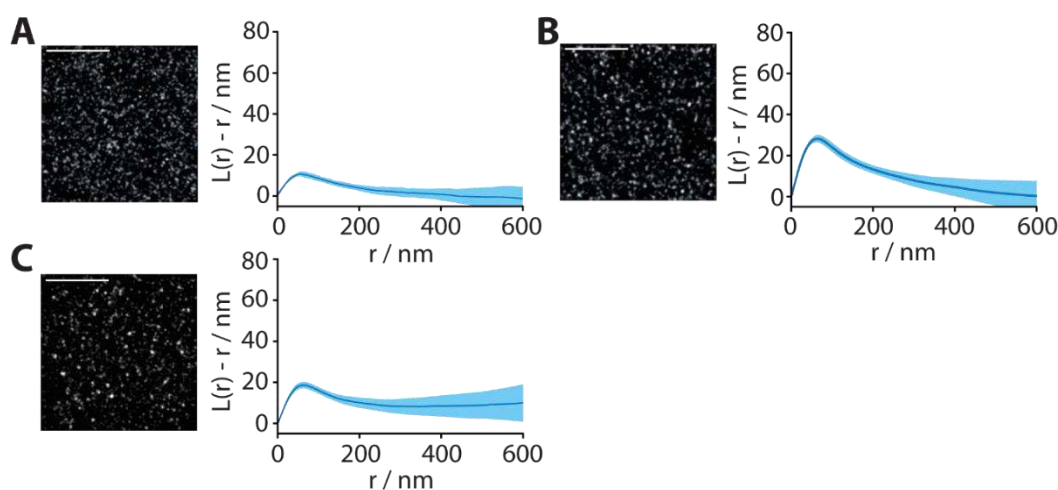


**Figure 65. Ripley's  $K$  analysis on randomly distributed dimers with additional 30% of monomers, with and without blinking and diffusion**

Molecules were simulated at densities of 70 molecules/ $\mu\text{m}^2$  in  $5 \times 5 \mu\text{m}$  areas ( $n = 10$  simulations). Simulated, reconstructed SMLM images are shown (left) with corresponding Ripley's  $K$  results (right; mean  $\pm$  sd). Scale bars:  $2 \mu\text{m}$ . **A)** Distribution of randomly distributed 70% of dimers with additional 30% of monomers without blinking.

**B)** Distribution of randomly distributed 70% of dimers with additional 30% of monomers with CD3 $\zeta$ -PS-CFP2 blinking. **C)** Distribution of randomly distributed 70% of dimers with additional 30% of monomers with CD3 $\zeta$ -PS-CFP2 blinking and additional diffusion according to the measured behavior (mobile fraction: 64% with  $D = 0.047 \mu\text{m}^2/\text{s}$ ; quasi immobile fraction: 36% with  $D = 0.003 \mu\text{m}^2/\text{s}$ ).



## C7) STED Imaging of TCR/CD3 Subunits

As a next important step within this thesis, we wanted to confirm our results with a super-resolution method which is not prone to the detection of false clusters originating from multiple observations of the same molecule. To this end, we used STED microscopy, in which the gain in resolution is realized solely by decreasing the size of the PSF. Imaging is facilitated in a single scan, thus blinking of fluorophores does not influence the analysis.

Unfortunately, the system at hand only allowed for measurement of red fluorophores, and the hitherto used AF647 could not be used for STED imaging. Hence, we had to test alternative organic dyes and their conjugation to the scFv. We did not achieve a DOL higher than 0.6 for site-specific conjugation of the scFv to AS635. The low DOL implies that only 60% of total TCR/CD3 complexes would have been probed, thus prohibiting comprehensive imaging and cluster analysis. However, using a phosphorylated derivative of AS635, AS635P, we could achieve a DOL close to one, similar to what was realized with AF dyes.

CD3 $\epsilon$  was labeled with KT3-scFv-AS635P and STED images of T cells on non-activating and on activating supported lipid bilayers were recorded (**Figure 66A**).

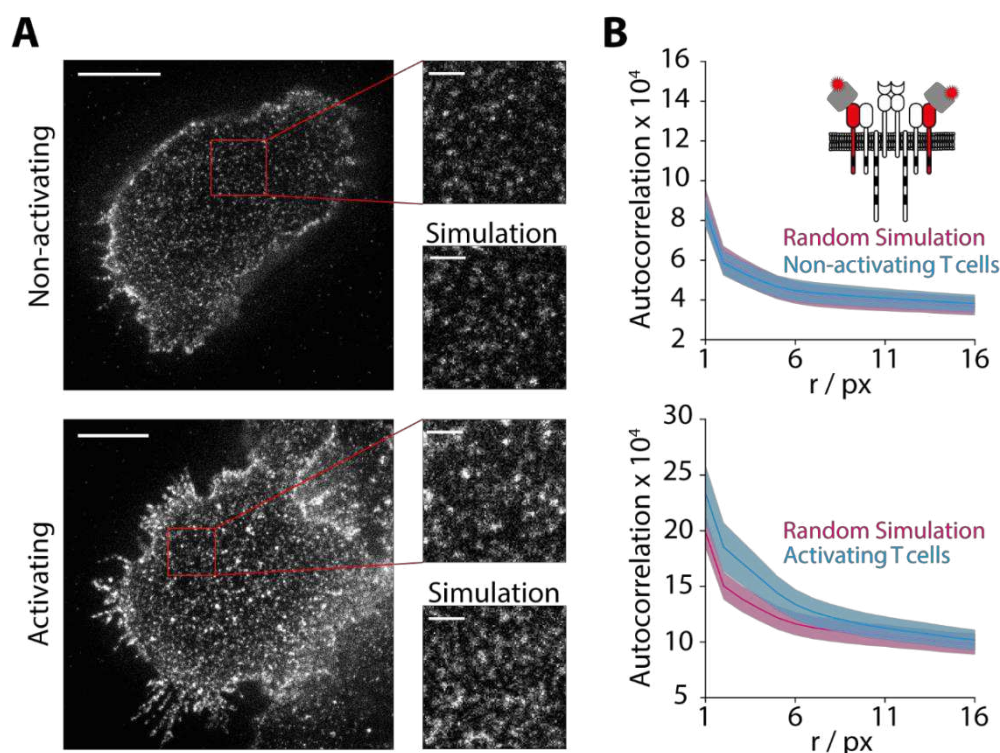


**Figure 66.** STED experiments with KT3-scFv-STAR635P on non-activating and activating SLBs

**A)** T cells were labeled with KT3-scFv-STAR635P, added on non-activating (top) or activating (bottom) SLBs, fixed, and imaged with STED. The red rectangles mark regions for the magnified display. Images of random distributions were simulated according to the measured density and PSF of the STED microscope. Scale bars: 3  $\mu m$  (full image), 500 nm (magnified image). **B)** 5 different ROIs within the cell borders were analyzed by image auto-correlation (1 px = 20 nm). Results of the experiment (blue) were compared to results from random simulations at the same densities (magenta) for non-activating (top) and activating (bottom) SLBs.

To analyze the STED images, we compared the average image autocorrelation (AC) functions of five regions-of-interest (ROIs) at the bottom surface of the cells to those of random simulations at the same density. Image Correlation Spectroscopy (ICS) is a powerful tool to infer on the spatial distribution of fluorophores within images [241]. The fluorescence image is correlated with itself as a function of a pixelated spatial shift in  $x$ - and  $y$ -direction [242]. The resulting correlation function is calculated from two contributors: First, the PSF of the microscope and secondly, the underlying spatial distribution of proteins. While the decay of the curve reports on the spatial size of potential clusters and the systems PSF, the amplitude indicates the protein density within the analyzed region and again the PSF.

For reference simulations, precise quantification of the PSF was required. We therefore recorded images of T cells labeled at single-molecule density (**Figure 67A**). The single-molecule signals were fit with a 2D-Gaussian function and the resulting intensity distribution was fit with a log-normal model (**Figure 67B**) [18]. Note that the width of the signals,  $\sigma$ , was found to depend on the intensity (**Figure 67C**), which was also accounted for in the simulations. This dependency might arise from fluorophores being bleached during the scanning process, yielding signals with a reduced intensity and width.

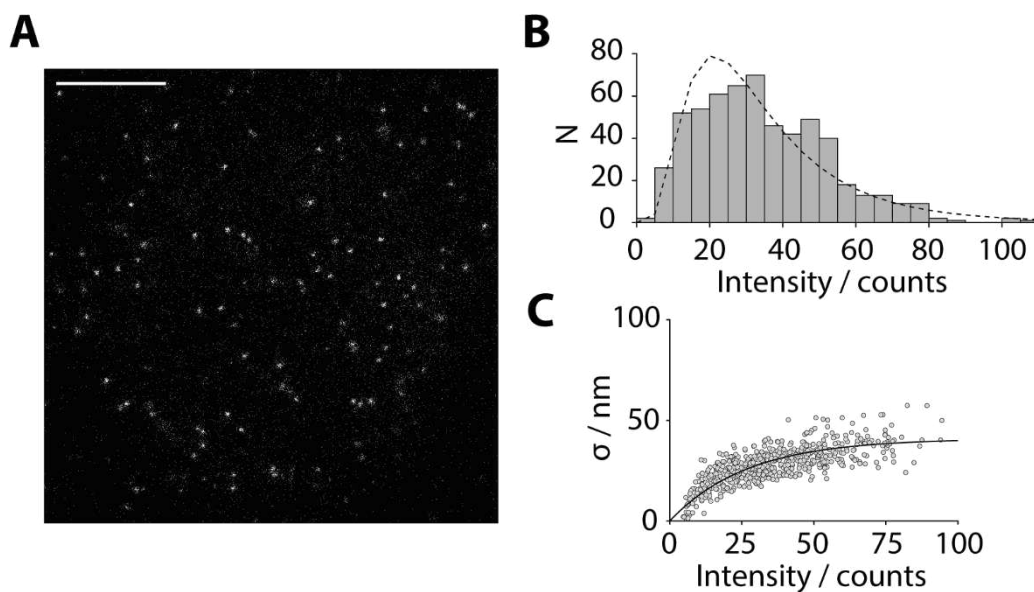


**Figure 67. Determination of the STED PSF by single-molecule imaging and fitting**

**A)** T cells were labeled with H57-scFv-STAR635P at low densities, added to non-activating SLBs, fixed and imaged with STED. Scale bar: 3  $\mu\text{m}$ . **B)** Single-molecule fitting with a 2D-Gaussian resulted in a distribution of integrated intensities ( $I$ ) and its width ( $\sigma$ ). Fitting of the distribution with a log-normal distribution yielded a mean intensity of 35.14 and a variance of 508.52. **C)**  $\sigma$  was found to depend on  $I$ , which was fitted by Equation (23); see Chapter 2.

The information on the PSF was used to simulate random distributions of STED images at the same density as recorded on T cells (**Figure 66A**). We compared the random curve to the experimental results of labeled T cells (**Figure 66B, top**), which reveals no deviation in the case of non-activated T cells. Upon stimulation with MCC/IE<sup>k</sup>, formation of micro-clusters was observed and resulted in deviations from the AC curve for a random distribution (**Figure 66B, bottom**).

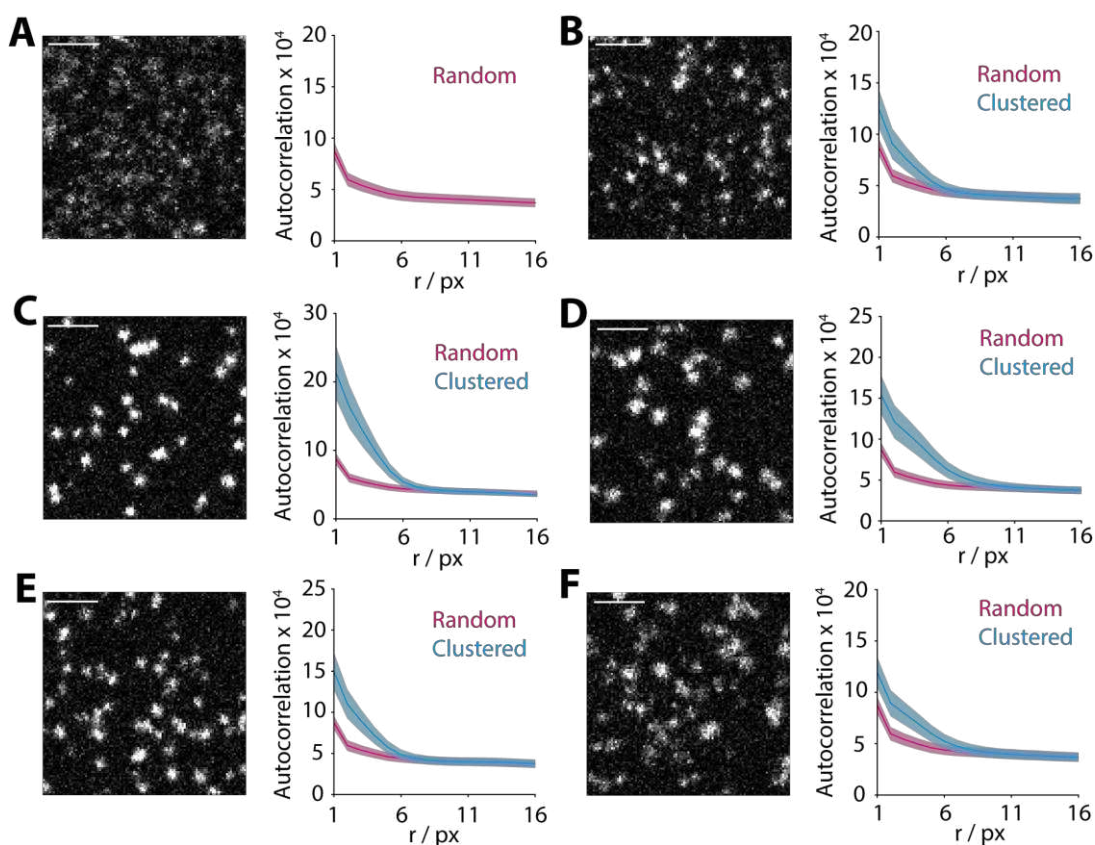


**Figure 68. STED image simulation for different cluster scenarios**

Molecules were simulated at densities that matched the experiment in  $2 \times 2 \mu\text{m}$  areas ( $n = 5$  simulations). Simulated STED images are shown (left) with corresponding image auto-correlation results (right; mean  $\pm$  s.e.m.). Magenta line with confidence interval represents the random distribution and blue lines correspond to the clustered scenario. Scale bars: 500 nm. **A)** Random distribution of molecules. **B)** Clusters with radius of 20 nm, cluster density of 20 clusters/ $\mu\text{m}^2$  and 80% of molecules within clusters. **C)** Clusters with radius of 20 nm, cluster density of 10 clusters/ $\mu\text{m}^2$  and 100% of molecules within clusters. **D)** Clusters with radius of 60 nm, cluster density of 10 clusters/ $\mu\text{m}^2$  and 100% of molecules within clusters. **E)** Clusters with radius of 20 nm, cluster density of 20 clusters/ $\mu\text{m}^2$  and 100% of molecules within clusters. **F)** Clusters with radius of 60 nm, cluster density of 20 clusters/ $\mu\text{m}^2$  and 100% of molecules within clusters.

To test the method for its applicability, we simulated STED images based on clusters and random distributions of molecules and analyzed them. The selection of cluster parameters was based on values published earlier [129, 191]. Clear deviations from the random curve should have been observable for all scenarios, confirming the usability of the auto-correlation method to identify protein clustering (**Figure 68**).

The reason for rather small deviations in case of TCR microclusters observed in **Figure 66B** is most likely due to the minute fraction of molecules located in micro-clusters ( $\sim 10\%$ ) and the sparsity of micro-clusters ( $< 0.5$  clusters/ $\mu\text{m}^2$ ; **Figure 69**).

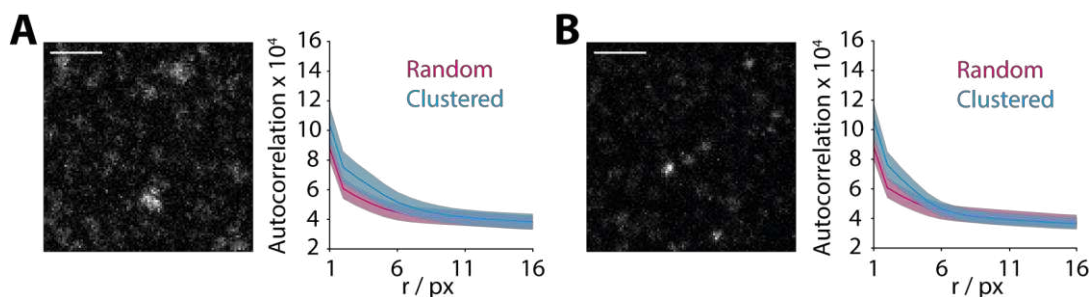


**Figure 69.** STED image simulations for cluster scenarios representative of micro-clustering. Molecules were simulated at densities that matched the experiment in  $2 \times 2 \mu\text{m}$  areas ( $n = 5$  simulations). Simulated STED images are shown (left) with corresponding image auto-correlation results (right; mean  $\pm$  s.e.m.). Magenta line with confidence interval represents the random distribution and blue lines correspond to the clustered scenario. Scale bars: 500 nm. **A)** Clusters with radius of 100 nm, cluster density of 0.5 clusters/ $\mu\text{m}^2$  and 15% of molecules within clusters. **B)** Clusters with radius of 40 nm, cluster density of 0.5 clusters/ $\mu\text{m}^2$  and 10% of molecules within clusters.

Analogous experiments were performed by labeling the TCR $\beta$  subunit with H57-scFv-AS635P (**Figure 70**), yielding consistent results.

**Table 13** summarizes all performed STED microscopy experiments.

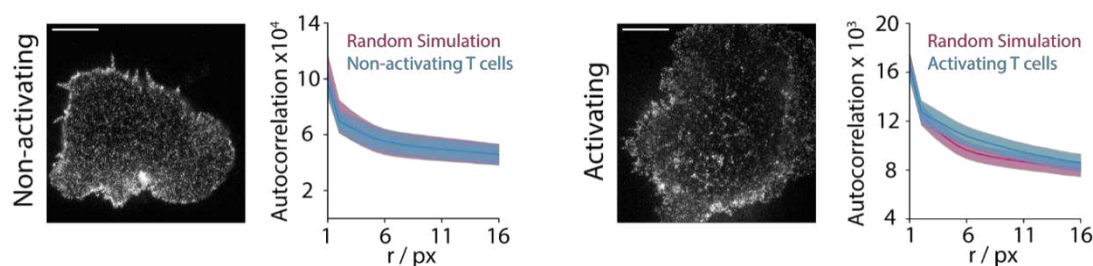


**Figure 70.** STED experiments with H57-scFv-STAR635P on non-activating and activating SLBs

**A)** left: T cells were labeled with H57-scFv-STAR635P, added to non-activating SLBs, fixed, and imaged with STED. Scale bar: 3  $\mu\text{m}$ . right: 5 different ROIs within the cell borders were analyzed by image auto-correlation (1 px = 20 nm; mean  $\pm$  s.e.m.). Results of the experiment (blue) were compared to results from random simulations at the same densities (magenta). **B)** left: T cells were labeled with H57-scFv-STAR635P, added to activating SLBs, fixed, and imaged with STED. Scale bar: 3  $\mu\text{m}$ . right: 5 different ROIs within the cell borders were analyzed by image auto-correlation (1 px = 20 nm; mean  $\pm$  s.e.m.). Results of the experiment (blue) were compared to results from random simulations at the same densities (magenta).

| Probe          | Complex Subunit | Live/Fix | Fig.             |
|----------------|-----------------|----------|------------------|
| scFv-H57-AF647 | TCR $\beta$     | Fixed    | <b>Figure 66</b> |
| scFv-KT3-AF647 | CD3 $\epsilon$  | Fixed    | <b>Figure 70</b> |

**Table 13.** Summary of STED experiments

## C8) Estimations of Sensitivity for Cluster Detection

To assess the sensitivity of the applied methods, holistic Monte Carlo simulations of well-defined cluster scenarios were performed. The size, number and the occupancy of the clusters were varied. The simulations covered particularly the published scenarios, i.e. the works of Lillemeier et al [129] and Pagoon et al [191]. **Table 14** shows the selected values for the parameters.

| Parameter                              | Values                   |
|--|--------------------------|
| Radius [nm]                            | 20, 40, 60, 80, 100, 150 |
| Number [clusters/ $\mu\text{m}^2$ ]    | 3, 5, 10, 15, 20         |
| Occupancy [% of molecules in clusters] | 40, 60, 80, 100          |

**Table 14.** Cluster parameters for sensitivity simulations

For sensitivity estimations of the label-density-variation method, molecules were spatially distributed according to the varying cluster scenarios, using average label densities as determined for the T cell plasma membrane. In addition, the number of detections per molecule was added according to the experimentally determined blink statistics on sparsely labeled cells.

These simulations were compared to the results of a random distribution of molecules and the simulated scenarios were classified into detectable, borderline and not detectable (**Figure 71**).

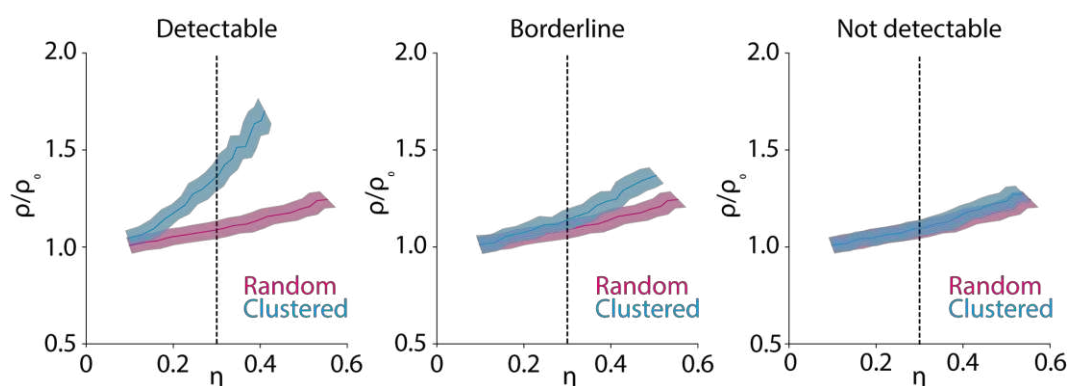


**Figure 71.** Detectability definition for SMLM experiments

Three classes of detectability were defined, depending on the overlap of error estimates (s.e.m.) at  $\eta = 0.3$ . No overlap of the confidence intervals was classified as detectable; overlap of confidence intervals, but mean curves outside of the confidence intervals was classified as borderline; and a mean curve within the confidence interval was classified as not detectable.

If a scenario was classified as detectable within the context of these simulations, we concluded that our experimental approach would be able to identify a non-random distribution clustered according to these simulated parameters. Not detectable combinations of cluster parameters, however, would also not be detected as clusters

within a real experiment, and thus evade detection by our approach. Sensitivity maps were derived for all three SMLM probes used (H57-AF647, KT3-AF647 and CD3 $\zeta$ -PS-CFP2) and all simulated parameter combinations (**Figure 72**, **Figure 73** and **Figure 74**). Combining this holistic simulation framework with the experimental results from our label-density-variation SMLM method, we were confidently able to rule out clustering of the TCR/CD3 complex down to three molecules per cluster. This result also negates previously proposed clustered complex distributions with ~7-20 molecules per cluster [129, 191]. Larger clusters ( $r \geq 100$  nm) could not be detected and hence cannot be ruled out by our method. In this case, however, there is rather low relative enrichment within clusters. Additionally, the method is not sensitive to high numbers of clusters per area combined with a high number of non-clustered background. In this case, each cluster contains only low numbers of molecules, which cannot be distinguished from random co-localization of non-clustered molecules.

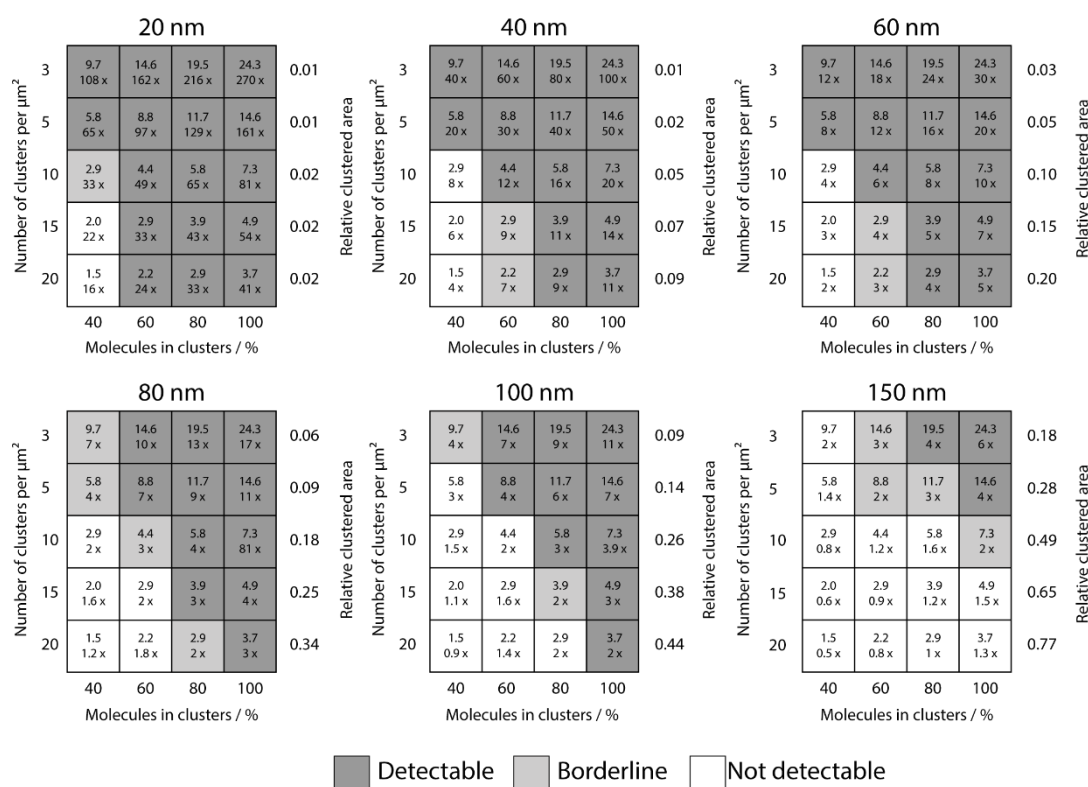


**Figure 72. Sensitivity map for H57-AF647 dSTORM experiments**

Varying clustering scenarios were tested on their detectability by simulation of well-defined distributions of molecules. Three cluster parameters were varied: i) the cluster size ( $r = 20, 40, 60, 80, 100$  and  $150$  nm), ii) the cluster density (3, 5, 10, 15 and 20 clusters/ $\mu\text{m}^2$ ) and iii) the fraction of molecules in clusters (40, 60, 80 and 100%). The different scenarios were compared to a random distribution of molecules and classified according to **Figure 71**. Dark gray rectangles were detectable, light gray rectangles were borderline and white rectangles were not detectable. The numbers within the fields indicate the mean number of molecules per cluster and the density in clusters in relation to the total density.

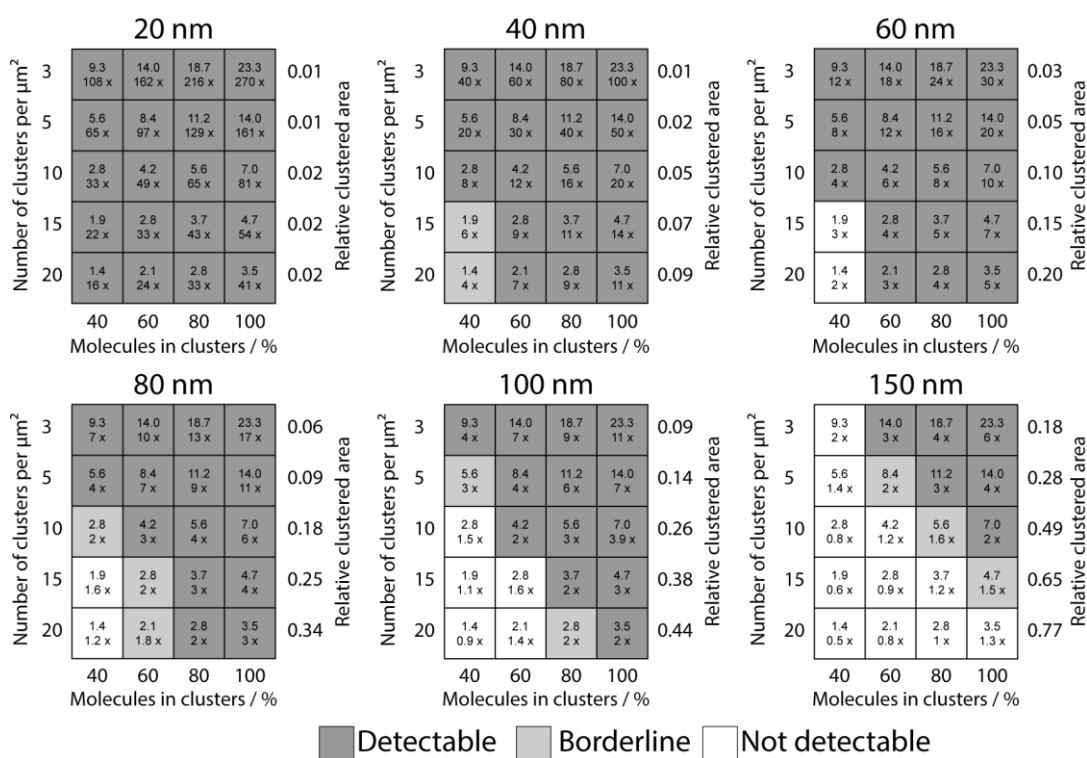


**Figure 73. Sensitivity map for KT3-AF647 dSTORM experiments**

Varying clustering scenarios were tested on their detectability by simulation of well-defined distributions of molecules. Three cluster parameters were varied: i) the cluster size ( $r = 20, 40, 60, 80, 100$  and  $150$  nm), ii) the cluster density (3, 5, 10, 15 and 20 clusters/ $\mu\text{m}^2$ ) and iii) the fraction of molecules in clusters (40, 60, 80 and 100%). The different scenarios were compared to a random distribution of molecules and classified according to **Figure 71**. Dark gray rectangles were detectable, light gray rectangles were borderline and white rectangles were not detectable. The numbers within the fields indicate the mean number of molecules per cluster and the density in clusters in relation to the total density.

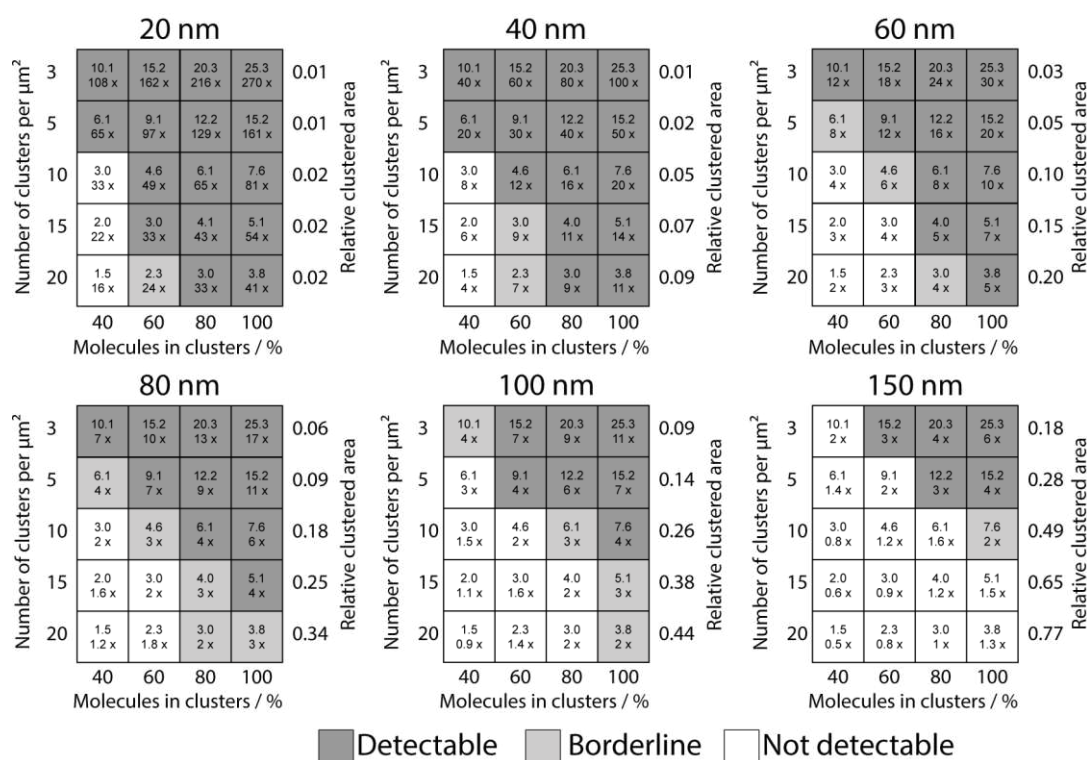


**Figure 74. Sensitivity map for CD3 $\zeta$ -PS-CFP2 PALM experiments**

Varying clustering scenarios were tested on their detectability by simulation of well-defined distributions of molecules. Three cluster parameters were varied: i) the cluster size ( $r = 20, 40, 60, 80, 100$  and  $150$  nm), ii) the cluster density (3, 5, 10, 15 and 20 clusters/ $\mu\text{m}^2$ ) and iii) the fraction of molecules in clusters (40, 60, 80 and 100%). The different scenarios were compared to a random distribution of molecules and classified according to **Figure 71**. Dark gray rectangles were detectable, light gray rectangles were borderline and white rectangles were not detectable. The numbers within the fields indicate the mean number of molecules per cluster and the density in clusters in relation to the total density.

We also performed similar sensitivity estimations for the STED auto-correlation analysis. Here, no blinking was included in the simulations; however, the molecular positions were convolved with the PSF of the STED system, and compared to random distributions. The same set of parameters was simulated (**Table 14**) and analyzed with the auto-correlation method. The results were again classified into detectable, borderline and not detectable (**Figure 76**), and sensitivity maps were generated (**Figure 75**). The sensitivity was estimated to be comparable to the SMLM experiments, further allowing to rule out the presence of substantial global nanoclustering in non-activated T cells.



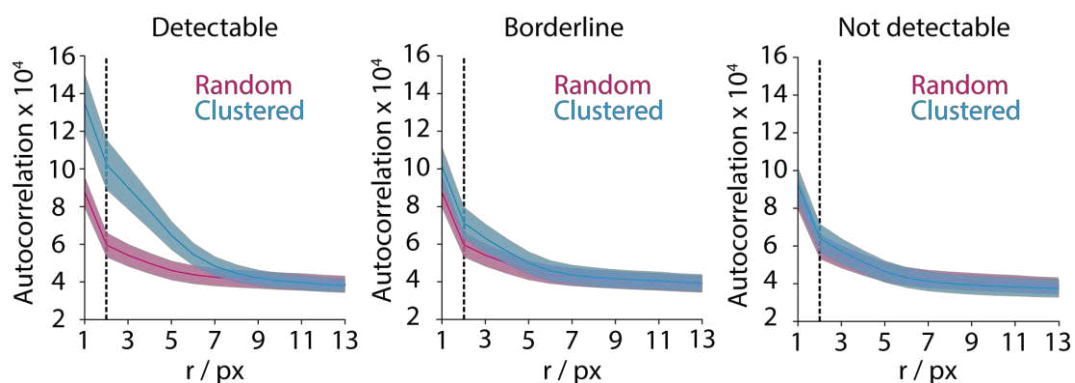


**Figure 76. Detectability definition for STED experiments**

Three classes of detectability were defined, depending on the overlap of error estimates (s.e.m.) at a displacement distance of 2 px. No overlap of the confidence intervals was classified as detectable; overlap of confidence intervals, but mean curves outside of the confidence intervals was classified as borderline; and a mean curve within the confidence interval was classified as not detectable.

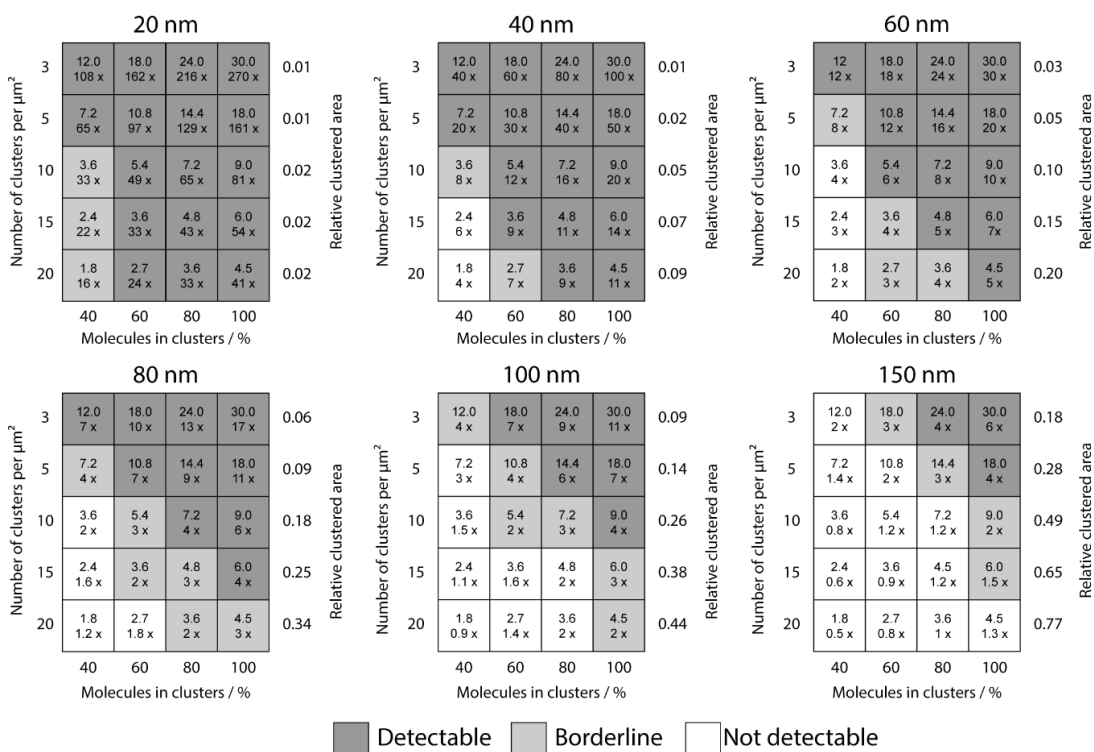


**Figure 75. Sensitivity map for STED experiments**

Varying clustering scenarios were tested on their detectability by simulation of well-defined distributions of molecules. Three cluster parameters were varied: i) the cluster size ( $r = 20, 40, 60, 80, 100$  and  $150$  nm), ii) the cluster density (3, 5, 10, 15 and 20 clusters/ $\mu\text{m}^2$ ) and iii) the fraction of molecules in clusters (40, 60, 80 and 100%). The different scenarios were then compared to a random distribution of molecules and classified according to **Figure 76**. Dark gray rectangles were detectable, light gray rectangles were borderline and white rectangles were not detectable. The numbers within the fields indicate the mean number of molecules per cluster and the density in clusters in relation to the total density.

## C9) Discussion

In the same way as the knowledge on the diffusion of a protein is detrimental for live-cell experiments, the information on the blinking of fluorophores is crucial when aiming at interpreting SMLM data in a quantitative manner. While the influence of diffusion on live-cell experiments is widely acknowledged, blinking-based bias in SMLM is often omitted. This neglect persists despite many reports on the stochasticity of blinking, even for PS-FPs [15, 16].

To this end, we developed a modular platform that allowed us to investigate the blinking behaviour of PA-FPs in any customary surrounding. We used this platform to study the emission pattern of purified PS-CFP2 under commonly applied imaging conditions, using different buffer compositions and variations in illumination time and power. This allowed us to simulate different spatial distributions of molecules while including the empirically measured blinking of fluorophores. Consequently, this enabled us to study the influences of blinking on a widely applied analysis method called Ripley's K analysis.

The issue of photo-blinking was identified as being problematic for quantitative measurements already in 2011 [232], and, thus, several studies on the characterisation of emission patterns of PA/PS-FPs have already been realized by now. These reports studied the emission of fluorophores embedded within PAGE gels [233], on glass surfaces [243, 244] or using reference proteins within the cellular context [245, 246]. Zanicchi et al presented an elegant way to estimate the blinking of organic dyes used in dSTORM by constructing a two-color DNA origami system [247]. A DNA chassis was biotinylated and crosslinked to streptavidin on a glass surface. However, up to now, our platform is the only one enabling single-molecule emission measurements within a well-defined environment that is not glass or gel. Both substrates might influence the FPs emissive behaviour. An additional environment to study the blinking of an isolated PA/PS-FP for quantitative estimations is within the cellular context. However, to ensure the measurement of a single fluorophore, one needs i) the expression of a purely monomeric fluorescent fusion protein and ii) fixation by any means. This approach was realized by Fricke et al [246] using CD86-mEos2 as monomeric reference. Nevertheless, for the translation to live-cell experiments, our platform enables immobilization without any chemical fixation, thus preventing any potential effects on blinking by fixatives. We refrained from modelling the exact kinetics of the emissive behaviour because we did not aim to characterize the exact photophysics of PS-CFP2, but the empirical emission patterns encountered during a realistic experiment. While a better photophysical understanding of fluorophores can guide decision making in the optimization of methods [243, 248], the knowledge of blinking behaviour under well-defined experimental conditions suffices to make valid assumptions on the spatial distribution of the studied proteins.

Most methods in which known blinking characteristics are included in the analysis, are based on fitting a model to the number of localizations per isolated entity. The used distributions include negative binomial [246], geometric [243] or binomial [245], notably, all for the same PS-FP, mEos2. Contrary to these studies, we refrained

from fitting the number of localizations per emitter as the prolonged tails of the empirical distribution would not be captured. Instead, we utilized the blinking information to simulate localization maps originating from different spatial distributions of fluorophores. Analysis of these simulated distributions allowed us to characterize the influence of blinking on the corresponding analysis algorithm. While this inherently reduced the sensitivity of the method, it effectively precluded erroneous detection of clustering, which appeared when SMLM localization maps were compared to simulations exclusively based on the positions of molecules [129]. With our approach, we were able to investigate global scenarios of clustering or oligomerisation. This is analogous to other proposed methods, which report either the mean number of emitters per entity or the mean number of emitters per area [232, 245-247, 249]. However, until now, it was only possible to determine average numbers, as the estimation of emitter numbers for a single entity is aggravated by the stochastic character of the blinking itself.

The addition of the empirical blinking behaviour of PS-CFP2 to simulations confirmed the bias of PALM towards detecting clusters via Ripley's K analysis. This was already reported for other PA/PS-FPs, most prominently mEos2 [204, 232, 250]. To this end, Baumgart et al developed label-density-variation SMLM [204], which has already been described in more detail above (**Chapter 3 – Part C**). This method already allowed to disprove Lck nanoclustering [204]. The basic approach of label-density-variation SMLM is similar to some other approaches: the blinking behaviour of the label is measured (low density labeling) and compared to the results from a fully labeled sample; the localizations per cluster for varying labeling densities are compared. The titration of the label, however, adds several advantages: i) a binding curve can be determined by the titration, which allows to estimate whether the labeling is at saturation, or whether complexes could still be unlabeled at the highest labeling concentration, ii) the resulting  $\varrho$ -vs- $\eta$  plot can be compared to simulations of different cluster scenarios, hence giving an idea about cluster sizes, occupancy and numbers and iii) the simulation of a purely random distribution adds a reliable baseline. However, this method, lacks a true quantitative character, i.e. it does not allow for estimation of the exact number of proteins per each cluster.

In label-density-variation SMLM, one cell represents one data point within the  $\varrho$ -vs- $\eta$  plot. This renders label-density-variation SMLM time consuming, even when the experimental settings are already well established. Additionally, some spread in the  $\varrho$ -vs- $\eta$  plot will most likely be due to the biological cell-to-cell variations. Acquisition of an increased number of cells therefore increases the clarity of potential trends within the  $\varrho$ -vs- $\eta$  plot. Several approaches have already been designed to drive SMLM methods towards higher throughput: these include an automated nanofluidics device, based on a low-cost Lego pump, for fixation and buffer exchange [251]. The change from gaussian beam to flat-field illumination allowed to increase the observation area of one movie from  $\sim 20 \mu\text{m}^2$  ( $\sim 1$  cell) realized within this work to  $10^4 \mu\text{m}^2$  [252]. Even more so, fully automated systems have been developed, which allow to study a full 96-well plate, and to record data on 1,600 cells in only one day [253-255]. High-throughput methods are paving their way not only for the

realization of experiments, but also for analysis: machine learning did not stop at SMLM and the manifold implementations of different algorithms for emitter fitting, mainly based on neural networks, all have a strongly decreased processing time compared to common MLE or least-squares fitting procedures [7, 255-258].

After having identified the emissive behaviour of PS-CFP2, we saw the need to re-address the spatial distribution of the TCR/CD3 complex, since many studies on the receptor complex were realized by utilization of PS-CFP2 [129, 191]. To strengthen the results, we further extended the range of experiments to dSTORM experiments and to multiple subunits of the receptor complex. Combined with extensive Monte Carlo simulations, the results of our label-density-variation SMLM experiments let us preclude the existence of clusters consisting of down to 3 molecules and being smaller than 80 nm in radius.

We initially opted for studying the spatial distribution of the TCR/CD3 complex on fixed cells. This was motivated mainly by the low temporal resolution of SMLM arising from the necessity to record thousands of frames to obtain a comprehensive image of all abundant complexes. However, inadequate fixation protocols were reported to not fix membrane receptors sufficiently or alter the true underlying structures of the probed molecules [259-262]. Importantly, fixation might not only alter the protein distribution on the cells' membrane but might even block the binding of labels, thereby decreasing the number of complexes subjected to the experiment [263, 264]. We particularly took care of these issues by selecting the most adequate fixation protocol that has been reported [262], nevertheless, the effects on nanoclustering might still not be negligible. To this end, we also performed measurements on living T cells.

While live-cell experiments are not hampered by potential fixation artifacts, they raise other significant issues. Several researchers assumed that, when imaging living cells, the problem of repetitive detection of the same PS/PA-FP would become irrelevant. Movement of the protein during its dark state would yield a new localization at a distinct place compared to the location of the initial detection. For such assumptions, diffusion studies of the TCR/CD3 complex as realized in the first part of this thesis (**Chapter 3 – Part A**) are indispensable. To estimate this effect of mobility on live-cell SMLM experiments, **Figure 77** shows the probabilities of a molecule to stay within a circle with diameter  $d = 160$  nm ( $\sim 1$  camera pixel) during the acquisition of 100 frames or 5,000 frames at 167 Hz in magenta or cyan, respectively, as a function of the molecule's diffusion coefficient,  $D$ .

The three vertical lines indicate the two mobilities obtained in **Chapter 3 – Part A** ( $D = 0.003 \mu\text{m}^2/\text{s}$  and  $D = 0.046 \mu\text{m}^2/\text{s}$  for the quasi-immobile and mobile fraction, respectively), while the third one represents a typical value of residual diffusion after fixation ( $D = 1.6 \times 10^5 \mu\text{m}^2/\text{s}$ ). The quasi-immobile fraction of TCR/CD3 complexes shows a probability of  $\sim 0.60$  to stay within this area during a typical off-time of PS-CFP2 of about 100 frames, and even about 5% of mobile complexes will not leave this area during that time. Thus, these molecules still contribute to the detection of artificial clustering. Blinking with larger off times (**Figure 77, cyan**) or

increased  $D$  would genuinely reduce the probability to stay within the mentioned area, and hence dissipate the problem of overcounting.

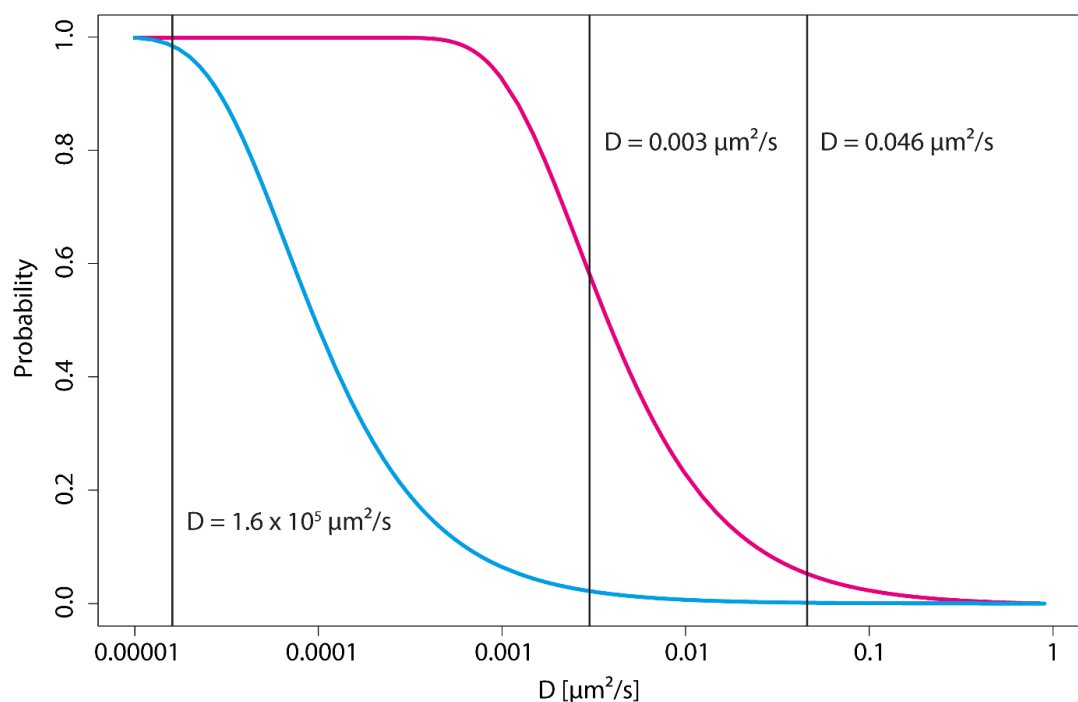


**Figure 77. Probability to stay within a circle with a radius of 80 nm**

The figure shows the probability of a protein with mobility  $D$  to stay within a circle with a radius of 80 nm within 100 frames (= 0.6 s) or 5,000 frames (= 30 s) in magenta and cyan, respectively. Marked are three values of  $D$ , typically measured within TCR/CD3 mobility measurements: i)  $D = 1.6 \times 10^5 \mu\text{m}^2/\text{s}$  for residual diffusion after fixation, ii)  $D = 0.003 \mu\text{m}^2/\text{s}$  for the quasi-immobile fraction of TCR/CD3 complexes and iii)  $D = 0.046 \mu\text{m}^2/\text{s}$  for the mobile fraction of complexes.

To this end, label-density-variation SMLM was applied to living cells, and the recorded data was compared to simulations incorporating both blinking of the label and diffusion of the TCR/CD3 complexes, as measured in the previous two chapters. Consistently, no indications of substantial nanoclustering could be measured.

Potential nanoclusters of the TCR/CD3 complex were first observed via PALM by Lillemeier et al in 2010 [129]. Since then, many studies were reported, which confirmed this idea, all of them were based on SMLM data [187, 191, 230, 231, 236]. The analysis methods used in these reports (Ripley's K, DBSCAN or a novel Bayesian cluster detection [236, 238, 265]), however, do not account for the blinking of molecules. Some of those studies have tried to correct for blinking of PS-CFP2 by merging localizations within consecutive frames and within a certain spatial distance. However, it is apparent from the blinking data recorded within my thesis, that merging does not completely abrogate overcounting effects. To this end, the label-density-variation SMLM experiments on the TCR/CD3 complex were the first SMLM experiments that cope with blinking, and largely narrow down the possible degrees of clustering. The risk of combining SMLM with inappropriate analysis methods is highlighted by the enormous amount of studies describing

nanoclustering of other membrane proteins or lipids [185, 186, 266-279]. Importantly, the referred studies represent the peak of the iceberg, and, while the concept of protein nanoclusters should not be rejected in a general scope, many of the reports should be carefully readdressed in a more critical light of blinking bias. Several estimations can help to assess the influence of blinking.

In our study, the number of localizations at saturated degree of labelling divided by the number of detections per cluster matched very well the reported overall densities of TCR/CD3 complexes on the membrane. However, a calculation based on cluster characteristics reported by Pigeon et al would result in an overall TCR/CD3 complex density of about 700 complexes per  $\mu\text{m}^2$  - about 7 times higher than described elsewhere [2]. Of note, one is not reliant on single-molecule methods to derive the approximate expression level of membrane proteins; diffraction-limited, intensity-based estimations already show good accuracy.

Based on a diffraction-limited image recorded before the actual SMLM experiment, Culley et al introduced another quantitative quality control method for SMLM data called SQUIREL [280]. Using SQUIREL one can estimate the overall quality of SMLM data as well as locally assess whether SMLM structures were detected erroneously.

To strengthen our conclusions drawn from SMLM experiments, we performed STED experiments. As described earlier, STED is not based on the blinking of fluorescent proteins, and thus it is not prone to cluster artifacts. In several reports, protein nanoclustering has already been identified using STED microscopy. However, common analysis methods have not been established up to now. While in some reports, the analysis was initialised by a user-guided selection of fluorescent signals with consecutive fitting of signals and analysis of the distribution of FWHM, other groups used more sophisticated methods [281, 282] such as multi-emitter fitting combined with pair correlation analysis or signal-fitting combined with fitting linear combinations of single-molecule intensities [283-285]. Within our analysis, we refrained from fitting signals from potential clusters; the emission of a randomly shaped cluster might deviate from the idealized Gaussian emission profile used when fitting single, isolated molecules. We thus used fitting only in the case of characterizing the PSF of our STED system after having measured emission of single molecules. We realized this in a cellular context by using a largely decreased concentration of fluorescently conjugated label, avoiding any potential influences of altered emission when measuring the fluorophore directly on a glass surface [284]. Instead of fitting potential randomly-shaped clusters with Gaussian curves, or measuring dimensions by user defined ROIs, we opted to use Image Correlation Spectroscopy, a method used for investigation of membrane protein distribution already in 1993 [241]. Combined with the holistic Monte Carlo simulation approach used in SMLM studies, it allowed us to determine the degree of TCR nanoclustering that would still be consistent with the observations. As these sensitivity estimations showed, large scale domains or clusters with small occupancies cannot be fully negated. However, if present, these clusters would be rather faint: for example, clusters with a radius of 150 nm, having 80% of molecules within clusters and

showing a cluster density of 10 cluster per  $\mu\text{m}^2$  would have been missed by our approach. Such clusters would show a TCR density, which is increased only 1.6-fold compared to the area outside the cluster.

All experiments within this work, except for PA/FCS and STED, were performed using two-dimensional TIRF microscopy. However, if the three-dimensional structure of a T cell is considered, questions arise on how flat the interaction area of the cell on a two-dimensional surface really is. As TIRF imaging will only result in the measurement of the projection of all coordinates on the focal plane, three-dimensional information is lost. While our experiments showed that the plasma membrane of T cells is able to flatten out to a high degree, the problem is highlighted when trying to measure e.g. Dendritic Cells on adhesive surfaces. Their increased membrane ruffling can easily give rise to several layers of membranes stacked up on each other, thus distorting a two-dimensional experiment.

For these reasons, attempts were initiated to measure T cells not on adhesive surfaces, but suspended within an agarose gel followed by imaging with either 3D-STED [286], double-helix PSF engineering [134] or Light-Sheet Microscopy [132]. These experiments did indeed reveal changes in diffusion and activation behavior of the cells.

One three-dimensional structure possibly neglected by TIRF imaging regards activation-dependent microclusters: in a very elegant study by Choudhuri et al [287], correlative imaging with transmission EM and fluorescence microscopy was used to derive the three-dimensional structure of the immune synapse. They found that the microclusters in activated T cells correlate with extracellular micro-vesicles.

## C10) A Two-Phase Activation Model for T Cells

While many different models exist for the activation of T cells (see **Chapter 1**), most of them neglect the challenge of identifying rare antigenic pMHC molecules in the first place. The essentially un-clustered distribution of TCR/CD3 complexes has direct implications on the time a T cell needs to scan the entirety of antigens presented on an APC. A clustered distribution would lead to a more rapid rebinding of the pMHC to nearby TCR/CD3 complexes and eventually even cooperative binding effects, thereby decreasing the effective on-rate of the TCR:pMHC binding and slowing down the scanning process, when compared to a random receptor distribution. This effect on the time necessary to scan all pMHCs motivated the decision to introduce a two-phase model of antigen identification and the activation of T cells. The following two-phase activation model was introduced previously [3] and was more thoroughly discussed by Baumgart et al [288].

Out of tens of millions of APCs, only few of them carry one particular antigen. In addition, very few T cells or even only one might show specificity to that antigen [289]. Single antigenic MHCs are reported to readily initiate T cell reactions [290, 291]. However, most of the presented antigens are endogenous, with probably only 1 – 5 MHC complexes presenting antigenic peptides within a total of ~ 200,000 pMHC complexes being present [292, 293].

To this end, Baumgart et al drew the nice analogy between the T cells' task to identify agonistic pMHC within the vast amount of endogenous antigens, and the popular problem of finding 'a needle in the haystack' [288]. But while time is often not of primary importance when looking for a needle in a barn, it most probably will be critical for a T cell to be fast in the identification of the antigenic pMHC.

Using the statistical merits of *sensitivity* and *fall-out* as performance indicators for search algorithms, Baumgart et al showed that in a two-phase model, the required searching time is decreased significantly [288].

| Merit | Description                         |
|-------|-------------------------------------|
| TP    | Infected APC classified as infected |
| FP    | Healthy APC classified as infected  |
| TN    | Healthy APC classified as healthy   |
| FN    | Infected APC classified as healthy  |

Table 15. Statistical merits of performance

Based on the definitions in **Table 15**, these merits are given by the following equations:

$$\text{sensitivity (TPR)} = \frac{TP}{TP + FN} \quad (27)$$

$$\text{fall-out (FPR)} = \frac{FP}{TN + FP} \quad (28)$$



The *sensitivity* represents the fraction of identified *infected* APCs amongst all *infected* APCs, and is maximized, if FN is minimized. The *fall-out* represents the fraction of APCs erroneously identified as *infected* from all *healthy* APCs. A search with a large *fall-out* offers only little discriminative power.

Thus, in an efficient search, such as the T cells' search for antigenic pMHC, FN and FP need to be minimized. For rare cases, it is difficult to optimize both at the same time, while also minimizing the search time: A two-phase approach is described to be more efficient [294].

Within the T cell model for antigen identification, the first phase serves to optimize the *sensitivity* without considering a low *fall-out*. Many APCs without agonistic pMHC are classified wrongly as *infected*. Only these identified APCs are then screened more thoroughly in the second phase with the *fall-out* being kept low (**Figure 78**).

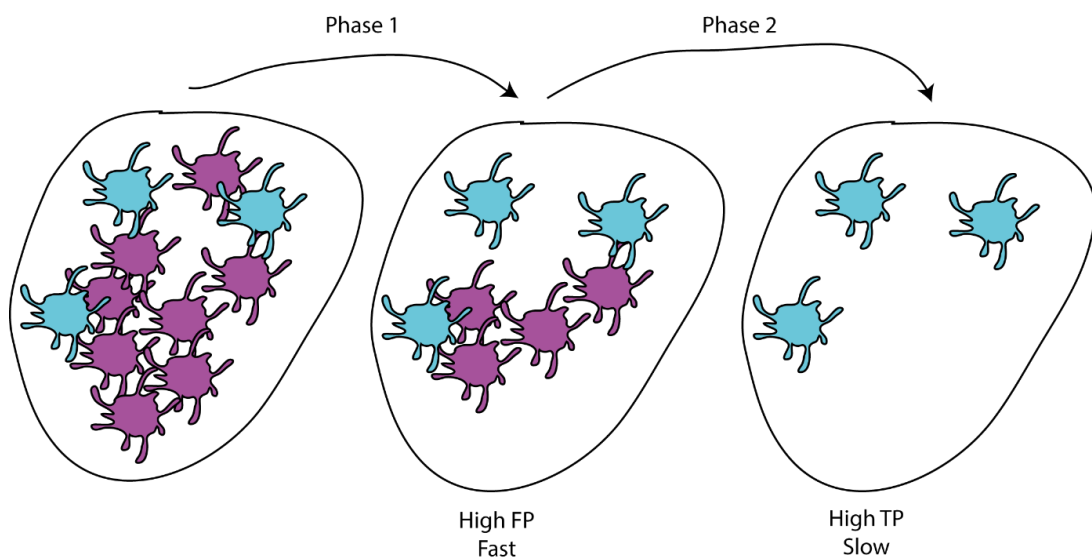


**Figure 78.** Sketch for the two phases proposed within this model

In the first phase, a high number of FPs are allowed, which decreases the time needed for a first decision. The second phase consecutively has a reduced number of cells to investigate. A more thorough search leads to high TPs but takes more time. Both phases combined yield a largely decreased time, when compared to a 1-phase approach.

A comparison of a two-phase model with a *fall-out* during phase 1 of  $10^{-2}$  and a *fall-out* during phase 2 of  $10^{-4}$  and a one-phase model with a *fall-out* of  $10^{-6}$  highlights the massive increase in search speed of a factor of  $\sim 5,000$  (**Figure 79**; [288]). This speed can be optimized even further by immediately starting phase 2 after having detected agonistic pMHC in phase 1, which might model the real scenario even better.

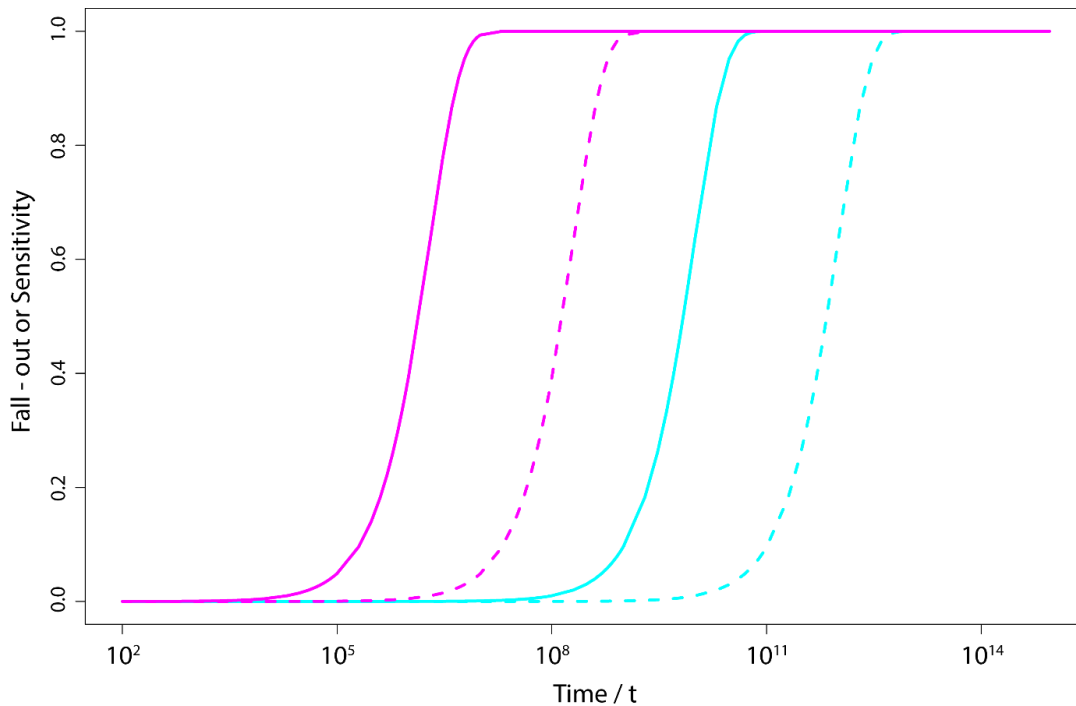


**Figure 79. Time comparison of 1-phase and 2-phase model**

The combined time from phase 1 and phase 2 of the 2-phase model are shorter, when compared to the 1-phase model. Here, both models were calculated with a combined local fall-out of  $10^{-6}$ , and a fraction of  $p = 0.0001$  MHCs showing antigenic peptides. While the discriminative power is the same for both approaches (same combined local fall-out), the time for the 2-phase approach is about 5,000 times faster.

## The T cells' Hunt for Agonistic pMHC

Approximately  $50 \times 10^6$  DCs are present in a human body [289]. During infection,  $10^3 - 10^5$  of those gather at the lymph nodes, where they encounter the T cells [295]. When studying the identification process of a single T cell, the specificity of the T cell to one APC out of  $\sim 10^5 - 10^6$  has to be taken into account [296]. This gives rise to the need of identifying one *infected* out of  $10^4$  APCs. A further justification for a random search approach is, that the movement of T cells, once recruited to the lymph nodes, is random [297].

Regarding the time of interaction between a T cell and an APC, three aspects are of interest. First, the T cell's movement from one APC to the next, second, the time to scan the pMHCs on the APC, and third, the time needed for a first decision. While it usually takes a T cell less than a second to get to the next APC [298], the time to an encounter with a cognate pMHC can be as long as several minutes. Here, the implications of the random distribution of TCR/CD3 complexes manifest. Further aspects influencing this time are the surface density as well as the diffusion coefficient  $D$  of both pMHC and TCR/CD3 complexes.

Several models were proposed that might describe the phase 1 of this decision making. These models include kinetic segregation [299, 300] and/or proofreading [301, 302], cooperativity [303, 304], conformational changes [166, 169] and mechano-

sensitivity [171, 305, 306]. Cai et al additionally suggested a sensing functionality for a T cell's microvilli when scanning over the APCs plasma membrane [307]. This would allow to scan the entire plasma membrane of the APC for cognate pMHCs in under a minute [288]. A low mobility of pMHC complexes ( $D \approx 0.02 \mu\text{m}^2/\text{s}$ ) renders this approach highly efficient [308]. The herein discovered random distribution of the TCR/CD3 complexes optimizes the scanning speed further by increasing the probability to encounter a cognate pMHC. The effect of decreased nearest neighbour distances in the case of random distributions of the TCR and the MHC is shown in Figure 80.

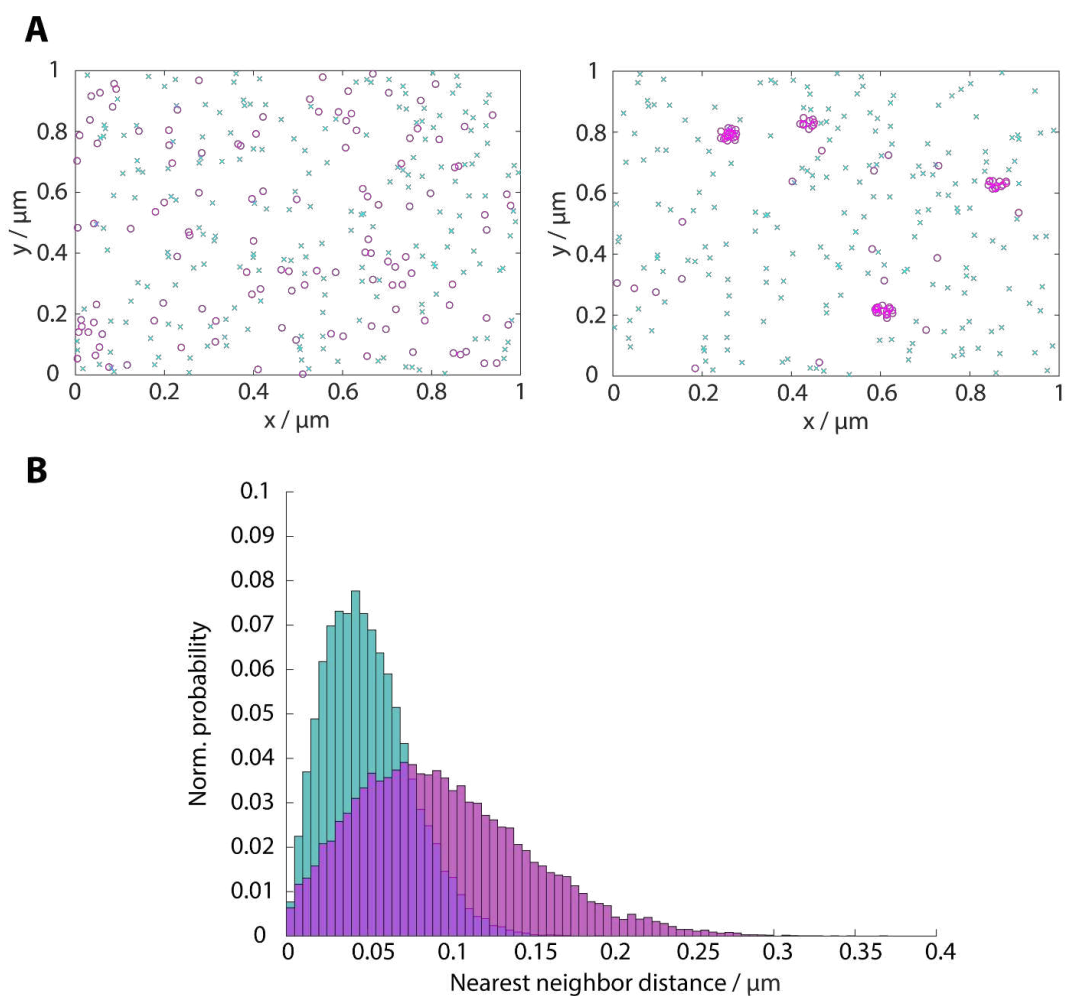


**Figure 80. Effect of clustering on the nearest neighbor distances**

*A) Plots of simulated positions of pMHC (cyan) or TCR/CD3 complexes (magenta). In the left panel, a random distribution is assumed for both protein complexes, while in the right panel clusters are assumed with radius of 25 nm, cluster density of 20 clusters/ $\mu\text{m}^2$  and 80% of molecules within clusters. The density is 100 molecules/ $\mu\text{m}^2$  in both cases. B) The nearest-neighbor analysis shows increased nearest neighbor distances in the case of clustered TCR/CD3 complexes (magenta) when compared to a random distribution (cyan).*

The proposed enrichment of TCR/CD3 complexes at the tip of microvilli before adhesion and formation of the full synapse would also support the recognition in the very first encounters [230].

In this second phase of T cell activation, the large-scale rearrangement of the T cells surface molecules and cytoskeleton, i.e. the immunological synapse (see **Chapter 1**) might play a central role [149]. In addition to that, the duration of the interaction between the T cell and the APC is significantly extended [291, 309, 310]. First steps of rearrangements within the T cells plasma membrane include the formation of microclusters, which are widely acknowledged as the fundamental signalling unit [189, 311, 312]. According to the proposed two-phase model, false positive identification of an APC as *infected*, would allow the T cell to initiate this membrane rearrangement while cognate pMHCs are absent. Crites et al reported on micro-cluster formation even in non-activating conditions, and detachment of the T cell from the APC before having initiated activation showed revoking of T cell differentiation [313-315].

Those aspects make it evident, that for the second phase of T cell activation, pending questions are yet to be resolved. The presented thesis should not only be of relevance due to the presented results but should also pave the way to studies that investigate the addressed topics further.



Die approbierte gedruckte Originalversion dieser Dissertation ist an der TU Wien Bibliothek verfügbar.  
The approved original version of this doctoral thesis is available in print at TU Wien Bibliothek.



Die approbierte gedruckte Originalversion dieser Dissertation ist an der TU Wien Bibliothek verfügbar.  
The approved original version of this doctoral thesis is available in print at TU Wien Bibliothek.

## Chapter 4

# Appendix

## Abbreviations

|                  |  |        |  |
|------------------|--|--------|--|
| AC               | <i>Auto-Correlation</i>  | DCs    | <i>Dendritic Cell</i>                                      |
| AF488            | <i>AlexaFluor488</i>   | DGS    | <i>1,2-Dioleoyl-sn-Glycero Succinyl</i>                    |
| AF555            | <i>AlexaFluor555</i>   | DN     | <i>Double Negative</i>                                     |
| AF568            | <i>AlexaFluor568</i>   | DNA    | <i>Deoxyribonucleic Acid</i>                               |
| AF647            | <i>AlexaFluor647</i>   | DOL    | <i>Degree of Labeling</i>                                  |
| AIDS             | <i>Acquired Immune Deficiency Syndrome</i>                         | DP     | <i>Double Positive</i>                                     |
| AOM              | <i>Acousto-Optic Modulators</i>                                    | DPPC   | <i>1,2-Dipalmitoyl-sn-Glycero-3-Phosphocholine</i>         |
| APC              | <i>Antigen-Presenting Cell</i>                                     | dSMAC  | <i>Distal Supramolecular Activation Cluster</i>            |
| APD              | <i>Avalanche Photodiode</i>  | dSTORM | <i>Direct Stochastic Optical Reconstruction Microscopy</i> |
| AS635            | <i>AbberiorStar635</i>   |        |  |
| AS635P           | <i>AbberiorStar 635P</i>   | eGFP   | <i>Enhanced GFP</i>  |
| AUC              | <i>Area-Under-Curve</i>  | EM     | <i>Electron Microscopy</i>                                 |
|                  |  | ER     | <i>Endoplasmic Reticulum</i>                               |
| BCR              | <i>B Cell Receptor</i>   |        |  |
| bio              | <i>Biotin</i>  | Fabs   | <i>Antigen-Binding Fragment</i>                            |
| BSA              | <i>Bovine Serum Albumin</i>  | FBS    | <i>Fetal Bovine Serum</i>                                  |
|                  |  | FCS    | <i>Fluorescence Correlation Spectroscopy</i>               |
| CaF <sub>2</sub> | <i>Fluorite</i>  | FN     | <i>False Negative</i>                                      |
| CBTL             | <i>Cord Blood T Lymphocyte</i>                                     | FP     | <i>False Positive, Fluorescent Protein</i>                 |
| CD               | <i>Cluster of Differentiation</i>                                  | FPR    | <i>False Positive Rate</i>                                 |
| cdf              | <i>Cumulative Density Function</i>                                 | FRAP   | <i>Fluorescence Recovery After Photobleaching</i>          |
| CFP              | <i>Cyan Fluorescent Protein</i>                                    | FRET   | <i>Förster Resonance Energy Transfer</i>                   |
| cSMAC            | <i>Central Supramolecular Activation Cluster</i>                   | FWHM   | <i>Full Width Half Maximum</i>                             |
| CTLA-4           | <i>Cytotoxic T-Lymphocyte-Associated-Protein 4</i>                 | GA     | <i>Glutaraldehyde</i>                                      |
|                  |  | GADS   | <i>GRB2-Related Adaptor Downstream of Shc</i>              |
| DAG              | <i>Diacylglycerol</i>  |        |  |
| DBSCAN           | <i>Density-Based Spatial Clustering of Applications with Noise</i> |        |  |
| dcFCCS           | <i>Dual-Color Fluorescence Cross-Correlation Spectroscopy</i>      |        |  |



|  |  |
|--|--|
| GFP <i>Green Fluorescent Protein</i>                       |  |
| GSH <i>Glutathion</i>                                      | <i>n.d. Not Determined</i>   |
| HBSS <i>Hank's Balanced Salt Solution</i>                  | NA <i>Numerical Aperture</i>   |
| HDL <i>High-Density Lipoprotein</i>                        | NFAT <i>Nuclear Factor of Activated T cells</i>                                |
| HILO <i>Highly-Inclined and Laminated Optical Sheet</i>    | NF- $\kappa$ B <i>Nuclear Factor Kappa-Light-Chain-Enhancer of B Cells</i>     |
| His <i>Histidin</i>  | NR <i>Not Reported</i>   |
| HIV <i>Human Immunodeficiency Virus</i>                    | NTA <i>Nitrilotriacetic Acid</i>   |
| HPLC <i>High-Performance Liquid Chromatography</i>         | NTA(Ni) <i>3-(N-(5-Amino-1-Carboxypentyl)iminodiacetic acid) (nickel salt)</i> |
| ICAM-1 <i>Intercellular Adhesion Molecule 1</i>            | PA <i>Photo-Activatable</i>  |
| ICS <i>Image Correlation Spectroscopy</i>                  | PA/FCS <i>Photon Arrival Time Analysis FCS</i>                                 |
| IL-2 <i>Interleukin 2</i>                                  | PAGE <i>Polyacrylamide Gel Electrophoresis</i>                                 |
| IP <sub>3</sub> <i>Inositol 1,4,5-Triphosphate</i>         | PAINT <i>Point Accumulation for Imaging in Nanoscale Topography</i>            |
| ITAM <i>Immunoreceptor Tyrosine-Based Activation Motif</i> | PALM <i>Photoactivated Localization Microscopy</i>                             |
| LAT <i>Linker for Activation of T Cells</i>                | PAMPs <i>Pathogen-Associated Molecular Patterns</i>                            |
| Lck <i>Lymphocyte-specific Tyrosine Kinase</i>             | PBL <i>Peripheral Blood T Lymphocyte</i>                                       |
| LFA-1 <i>Lymphocyte Function-Associated Antigen 1</i>      | PBS <i>Phosphate-Buffered Saline</i>   |
| MAPK <i>Mitogen-Activated Protein Kinase</i>               | PDF <i>Probability Density Function</i>  |
| MCC <i>Moth Cytochrome C</i>                               | PDL <i>Poly-D-Lysine</i>   |
| MHC <i>Major Histocompatibility Complex</i>                | PFA <i>Paraformaldehyde</i>  |
| MLE <i>Maximum-Likelihood Estimation</i>                   | PIP <sub>2</sub> <i>Phosphatidylinositol 4,5-Biphosphate</i>                   |
| mRNA <i>Messenger Ribonucleic Acid</i>                     | PLC $\gamma$ 1 <i>Phospholipase C-Gamma 1</i>                                  |
| mSav <i>Monovalent Streptavidin</i>                        | PLL <i>Poly-L-Lysine</i>   |
| MSD <i>Mean Square Displacement</i>                        | pMHC <i>Peptide MHC</i>  |
|  | POPC <i>1-Palmitoyl-2-Oleoyl-sn-Glycero-3-Phosphocholine</i>                   |

|  |  |
|--|--|
| PS Photo-Switchable  | SMT <i>Single-Molecule Tracking</i>  |
| PS-CFP2 <i>Photo-Switchable Cyan<br/>Fluorescent Protein 2</i>     | SP <i>Single Positive</i>  |
| PSF <i>Point Spread Function</i>                                   | STED <i>Stimulated Emission Depletion</i>  |
| pSMAC <i>Periphereal Supramolecular<br/>Activation Cluster</i>     | TCR <i>T cell receptor</i>   |
| ROC <i>Receiver Operator Characteristics</i>                       | TIRF <i>Total Internal Reflection<br/>Fluorescence</i>                             |
| ROI <i>Region of Interest</i>                                      | TMR <i>Tetramethylrhodamine</i>  |
| ROXS <i>Reduction/Oxidation Buffer<br/>System</i>                  | TN <i>True Negative</i>  |
| scFv <i>Single-Chain Variable Fragment</i>                         | TOCCSL <i>Thinning out clusters while<br/>conserving stoichiometry of labeling</i> |
| SDS <i>Sodium Dodecyl Sulfate</i>                                  | TP <i>True Positive</i>  |
| SLB <i>Supported Lipid Bilayer</i>                                 | TPR <i>True Positive Rate</i>  |
| SLP-76 <i>SH2 Domain Containing<br/>Leukocyte Protein of 76kDa</i> | UV <i>Ultra-Violet</i>   |
| smFRET <i>Single-Molecule FRET</i>                                 | ZAP-70 <i>Zeta-Chain Associated Protein<br/>Kinase 70</i>                          |
| SMLM <i>Single-Molecule Localization<br/>Microscopy</i>            |  |

## List of Figures

|   |    |
|---|----|
| Figure 1. Principle of a Microscope and of Immersion Oil .....                                      | 9  |
| Figure 2. Jablonski Diagram and Stoke's Shift .....   | 10 |
| Figure 3. Major Groups of Organic Dyes.....   | 11 |
| Figure 4. TIRF and HILO Illumination for Contrast Increase.....                                     | 13 |
| Figure 5. The Physical Limitation of Resolution.....  | 15 |
| Figure 6. Gaussian Fitting of the PSF .....   | 16 |
| Figure 7. Single Molecule Localization Microscopy.....  | 18 |
| Figure 8. STED Microscopy .....   | 21 |
| Figure 9. Methods to Determine Mobility .....   | 23 |
| Figure 10. Thinning Out Clusters while Conserving Stoichiometry of Labeling (TOCCSL).....           | 24 |
| Figure 11. Förster Resonance Energy Transfer (FRET).....  | 25 |
| Figure 12. Response Times of the Innate and Adaptive Immune System .....                            | 27 |
| Figure 13. Selected Cells of the Immune System.....   | 28 |
| Figure 14. Antigen Processing and Presentation.....   | 29 |
| Figure 15. T Cell Differentiation and Effector Tasks of CD4 and CD8-positive T Cells .....          | 30 |
| Figure 16. Structure of the TCR.....  | 31 |
| Figure 17. TCR/CD3 Complex Structure.....   | 32 |
| Figure 18. Signaling pathway and spatial redistribution induced by T cell activation .....          | 37 |
| Figure 19. Proposed Activation Models: Kinetic Proof-Reading Model.....                             | 38 |
| Figure 20. Proposed Activation Models: Kinetic Segregation .....                                    | 39 |
| Figure 21. Proposed Activation Models: Membrane-Associated ITAMs .....                              | 40 |
| Figure 22. Proposed Activation Models: Cholesterol Allosterity .....                                | 41 |
| Figure 23. Proposed Activation Models: Force Sensing .....  | 41 |
| Figure 24. Proposed Activation Models: Conformational Changes .....                                 | 41 |
| Figure 25. Amino acid sequence and DNA sequence of the PS-CFP2-AVI-3C-His12 construct .....         | 48 |
| Figure 26. Amino acid sequence and DNA sequence of the active streptavidin subunit construct.....   | 49 |
| Figure 27. Amino acid sequence and DNA sequence of the inactive streptavidin subunit construct..... | 49 |

|  |     |
|--|-----|
| Figure 28. Experimental System.....  | 64  |
| Figure 29. Ca <sup>2+</sup> experiments .....  | 65  |
| Figure 30. TCR/CD3 mobility determination with two different fluorophores .....  | 66  |
| Figure 31. TCR Mobility Estimation in T cells placed on two different surfaces using two different illumination configurations ..... | 67  |
| Figure 32. TCR Mobility Estimation .....   | 68  |
| Figure 33. TOCCSL studies on TCR/CD3 complex stoichiometry .....   | 72  |
| Figure 34. Two-color TOCCSL studies on TCR/CD3 complex stoichiometry .....   | 74  |
| Figure 35. Studies on TCR/CD3 complex stoichiometry by PA/FCS .....  | 76  |
| Figure 36. H57-scFv FRET experiments on non-activating SLBs.....   | 78  |
| Figure 37. H57-scFv FRET experiments on activating SLBs.....   | 79  |
| Figure 38. H57-scFv FRET experiments on non-activating SLBs with streptavidin crosslinking .....                                     | 80  |
| Figure 39. MCC/IE <sup>k</sup> FRET simulations .....  | 81  |
| Figure 40. MCC/IE <sup>k</sup> FRET experiments on SLBs.....   | 82  |
| Figure 41. FRET efficiencies of AF dyes .....  | 85  |
| Figure 42. Synthesis of the streptavidin-based measurement platform .....  | 88  |
| Figure 43. Sketch of the final measurement platform .....  | 89  |
| Figure 44. Mobility determination of immobile SLBs .....   | 90  |
| Figure 45. Exemplary data of a co-localization experiment .....  | 90  |
| Figure 46. Exemplary emission traces of two bio-PS-CFP2 molecules .....  | 90  |
| Figure 47. Parameters for blinking characterization .....  | 91  |
| Figure 48. Blinking parameters for bio-PS-CFP2 (n = 1080 molecules).....   | 92  |
| Figure 49. Blinking parameters for illumination with 0.4 kW/cm <sup>2</sup> and 15 ms illumination time (n = 170 molecules) .....    | 93  |
| Figure 50. Blinking parameters for experiments with 5 mM GSH (n = 60 molecules) .....  | 93  |
| Figure 51. Visualizing the effect of over-counting.....  | 94  |
| Figure 52. Effect of blinking on Ripley's K analysis .....   | 95  |
| Figure 53. Label-density-variation SMLM.....   | 97  |
| Figure 54. Comparison of diffraction-limited and dSTORM images.....  | 98  |
| Figure 55. Blinking estimation for H57-AF647.....  | 99  |
| Figure 56. Label-density-variation dSTORM of TCRβ with H57-AF64.....   | 99  |
| Figure 57. Blinking determination for KT3-AF647 .....  | 100 |
| Figure 58. Label-density-variation dSTORM for CD3ε using KT3-AF647.....  | 101 |
| Figure 59. Determination of blinking for CD3ζ-PS-CFP2.....   | 102 |

|  |     |
|--|-----|
| Figure 60. Label-density-variation PALM for CD3 $\zeta$ -PS-CFP2 .....   | 103 |
| Figure 61. Label-density-variation PALM on living cells for CD3 $\zeta$ -PS-CFP2 .....   | 104 |
| Figure 62. Ripley's K analysis on randomly distributed monomers with and without blinking of H57-AF647 .....   | 105 |
| Figure 63. Ripley's K analysis of randomly distributed dimers with and without blinking of KT3-AF647 .....   | 106 |
| Figure 64. Ripley's K analysis of randomly distributed dimers with blinking behavior of CD3 $\zeta$ -PS-CFP2 with and without TCR-like diffusion ..... | 107 |
| Figure 65. Ripley's K analysis on randomly distributed dimers with additional 30% of monomers, with and without blinking and diffusion.....            | 108 |
| Figure 66. STED experiments with KT3-scFv-STAR635P on non-activating and activating SLBs .....   | 109 |
| Figure 67. Determination of the STED PSF by single-molecule imaging and fitting .....  | 110 |
| Figure 68. STED image simulation for different cluster scenarios.....  | 111 |
| Figure 69. STED image simulations for cluster scenarios representative of micro-clustering.....  | 112 |
| Figure 70. STED experiments with H57-scFv-STAR635P on non-activating and activating SLBs .....   | 112 |
| Figure 71. Detectability definition for SMLM experiments .....   | 113 |
| Figure 72. Sensitivity map for H57-AF647 dSTORM experiments .....  | 114 |
| Figure 73. Sensitivity map for KT3-AF647 dSTORM experiments .....  | 115 |
| Figure 74. Sensitivity map for CD3 $\zeta$ -PS-CFP2 PALM experiments .....   | 116 |
| Figure 75. Sensitivity map for STED experiments.....   | 117 |
| Figure 76. Detectability definition for STED experiments .....   | 117 |
| Figure 77. Probability to stay within a circle with a radius of 80nm .....   | 121 |
| Figure 78. Sketch for the two phases proposed within this model .....  | 125 |
| Figure 79. Time comparison of 1-phase and 2-phase model .....  | 126 |
| Figure 80. Effect of clustering on the nearest neighbor distances .....  | 127 |

## Equations

|           |     |
|-----------|-----|
| (1).....  | 8   |
| (2).....  | 8   |
| (3).....  | 12  |
| (4).....  | 14  |
| (5).....  | 14  |
| (6).....  | 14  |
| (7).....  | 16  |
| (8).....  | 17  |
| (9).....  | 20  |
| (10)..... | 22  |
| (11)..... | 22  |
| (12)..... | 22  |
| (13)..... | 26  |
| (14)..... | 56  |
| (15)..... | 56  |
| (16)..... | 57  |
| (17)..... | 58  |
| (18)..... | 58  |
| (19)..... | 58  |
| (20)..... | 58  |
| (21)..... | 58  |
| (22)..... | 58  |
| (23)..... | 59  |
| (24)..... | 60  |
| (25)..... | 77  |
| (26)..... | 89  |
| (27)..... | 124 |
| (28)..... | 124 |

## List of Tables

|   |     |
|---|-----|
| Table 1. Summary of reported mobility estimations of the TCR/CD3 complex .....  | 34  |
| Table 2. Proteins involved in T cell activation .....   | 36  |
| Table 3. Summary of tracking experiments.....   | 68  |
| Table 4. Summary of TOCCSL experiments .....  | 73  |
| Table 5. Summary of two-color TOCCSL and single-molecule FRET experiments   | 74  |
| Table 6. Summary of PA/FCS experiments .....  | 75  |
| Table 7. Summary of donor recovery after acceptor photobleaching TCR/CD3 FRET experiments.....                                  | 79  |
| Table 8. Summary of MCC/IE <sup>k</sup> FRET experiments.....   | 81  |
| Table 9. Summary of experiments on the TCR/CD3 complex stoichiometry.....   | 83  |
| Table 10. Summary of experiments by Brameshuber et al. using Fab-KJ25, and comparison to results obtained within this work..... | 84  |
| Table 11. Summary of single-molecule PS-CFP2 blinking experiments .....   | 94  |
| Table 12. Summary of label-density-variation SMLM experiments .....   | 104 |
| Table 13. Summary of STED experiments .....   | 112 |
| Table 14. Cluster parameters for sensitivity simulations .....  | 113 |
| Table 15. Statistical merits of performance.....  | 124 |

# Curriculum Vitae

## Personal Information

Name **DI Benedikt Klaus Rossboth, BSc.**  
 Address Johann-Lehnerstraße 13/5  
 4061 Pasching, Austria  
 Mobile +43 664 5443909  
 E-Mail benedikt@rossboth.at



## Education

- 10/2015 - present **PhD Studies in Physics**  
 Technical University of Vienna, Austria
- 09/2012 – 10/2015 **MSc in Biomedical Engineering**  
*Focus on Medical Physics and Imaging*  
 Technical University of Vienna, Austria
- 9/2009 – 06/2012 **BSc in Biomedical Engineering**  
 University of Applied Sciences Technikum Vienna, Austria
- 2011, 2012 & 2013 **ERASMUS** (Universitat Politècnica de València, Spain) and  
**2 Summer Schools** (DTU, Copenhagen, Denmark & ETH Zurich,  
 Switzerland)

## Internships & Work Experience

- 11/2018 – present **Quantitative Analyst**  
 Sportradar AG  
 Leonding, Austria
- 10/2015 – 10/2018 **Project Assistant**  
 Institute of Applied Physics, Biophysics  
 Technical University of Vienna, Austria
- 04/2014 – 09/2015 **Research Assistant (Master Thesis & Project Work)**  
 11/2013 – 12/2013 Institute of Applied Physics, Biophysics  
 Technical University of Vienna, Austria
- 01/2012 – 04/2012 **Research Assistant (Bachelor Thesis)**  
 Health & Environment Dept.  
 Austrian Institute of Technology GmbH, Vienna, Austria



## Publications

### First authored

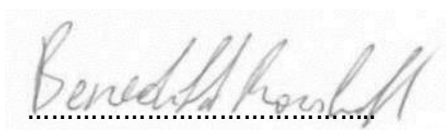
- 02/2019 *'Unscrambling Fluorophore Blinking for Comprehensive Cluster Detection via PALM'*, preprint at bioRxiv
- 07/2018 *'The TCR is randomly distributed over the plasma membrane of resting antigen-experienced T cells on non-activating surfaces'*, Nature Immunology 19, 821-7

### Co-authored

- 12/2018 *'Three-dimensional localization microscopy using deep learning'*, co-authored publication, Optics Express 26, 33166-79
- 11/2018 *'What we talk about when we talk about nanoclusters'*, co-authored publication, Methods and Applications in Fluorescence 7, 013001
- 10/2018 *'Direct observation of cargo transfer from HDL particles to the plasma membrane'*, co-authored publication, Atherosclerosis 277, 53-9
- 09/2018 *'Single-molecule optical absorption imaging by nanomechanical photothermal sensing'*, co-authored publication, PNAS 115, 11150-5
- 04/2018 *'Monomeric TCRs Drive T-Cell Antigen Recognition'*, co-authored publication, Nature Immunology 19, 487-96
- 01/2016 *'Oxidized Phospholipids Inhibit the Formation of Cholesterol-Dependent Plasma Membrane Nanoplatfoms'*, co-authored publication, Biophysical Journal 110:1, 205-213

## Scientific Talks & Poster Presentations

- 06/2018 *'The TCR is randomly distributed in non-activated T cells'*, Talk at the European Light Microscopy Initiative Meeting, Dublin, Ireland.
- 01/2018 *'Revisiting the nano-scale distribution of T cell membrane proteins'*, Conference talk at JKU Linz, Austria.
- 2016 - 2018 Poster presentations at five international conferences in Austria, Italy and USA.



Pasching, 20<sup>th</sup> of June 2019

## References

- [1] Murphy K., *Janeway's Immunobiology*. 8th ed. 2012: Garland Science.
- [2] Brameshuber M. et al, *Monomeric Tcrs Drive T Cell Antigen Recognition*. *Nat Immunol*, 2018. 19(5): p. 487-496.
- [3] Rossboth B. et al, *Tcrs Are Randomly Distributed on the Plasma Membrane of Resting Antigen-Experienced T Cells*. *Nature Immunology*, 2018.
- [4] Baumgart F. et al, *What We Talk About When We Talk About Nanoclusters*. *Methods Appl Fluoresc*, 2018. 7(1): p. 013001.
- [5] Plochberger B. et al, *Direct Observation of Cargo Transfer from Hdl Particles to the Plasma Membrane*. *Atherosclerosis*, 2018. 277: p. 53-59.
- [6] Chien M.-H. et al, *Single-Molecule Optical Absorption Imaging by Nanomechanical Photothermal Sensing*. *Proceedings of the National Academy of Sciences*, 2018: p. 201804174.
- [7] Zelger P. et al, *Three-Dimensional Localization Microscopy Using Deep Learning*. *Opt Express*, 2018. 26(25): p. 33166-79.
- [8] van Helden A. et al, *The Origins of the Telescope*. 2010.
- [9] Wayne R., *Light and Video Microscopy*. 2nd ed. 2014: Elsevier.
- [10] van Zuylen J., *The Microscopes of Antoni Van Leeuwenhoek*. *J Microsc*, 1980. 121(3): p. 309-28.
- [11] Abbe E., *Beiträge Zur Theorie Des Mikroskops Und Der Mikroskopischen Wahrnehmung*. *Archiv f. mikrosk. Anatomie*, 1873. 9.
- [12] Murphy D.B., *Fundamentals of Light Microscopy and Electronic Imaging*. 2001: Wiley-Liss.
- [13] Monardes N., *Historia Medicinal De Las Cosas Que Se Traen De Nuestras Indias Occidentales*. 1565.
- [14] Clarke E.D., *Account of a Newly Discovered Variety of Green Fluor Spar, of Very Uncommon Beatuy, and with Remarkable Properties of Colour and Phosphorescence*. *Annals of Phil*, 1819. 14.
- [15] Stokes G.G., *On the Change of Refrangibility of Light*. *Philos Trans R Soc Lond*, 1852. 142: p. 463-562.
- [16] Jablonski A., *Efficiency of Anti-Stokes Fluorescence in Dyes*. *Nature*, 1933. 131(363).
- [17] Xiao J., *Single-Molecule Imaging in Live Cells*, in *Handbook of Single-Molecule Biophysics*, P. Hinterdorfer and A.M. Van Oijen, Editors. 2009, Springer.
- [18] Mutch S.A. et al, *Deconvolving Single-Molecule Intensity Distributions for Quantitative Microscopy Measurements*. *Biophys J*, 2007. 92(8): p. 2926-43.
- [19] Willig K.I. et al, *Sted Microscopy Reveals That Synaptotagmin Remains Clustered after Synaptic Vesicle Exocytosis*. *Nature*, 2006. 440: p. 935-9.
- [20] Coons A.H., Creech H.J., and Jones R.N., *Immunological Properties of an Antibody Containing a Fluorescent Group*. *Experimental Biology and Medicine*, 1941. 47(2): p. 200-202.
- [21] Gürses A. et al, *Dyes and Pigments*. *Springer Briefs in Molecular Science*. 2016: Springer. 13-29.

- [22] Sauer M., Hofkens J., and Enderlein J., *Handbook of Fluorescence Spectroscopy and Imaging*. 2011: Wiley-VCH.
- [23] Kiernan J.A., *Classification and Naming of Dyes, Stains and Fluorochromes*. Biotechnic & Histochemistry, 2009. 76(5-6): p. 261-278.
- [24] Shimomura O., Johnson F.H., and Saiga Y., *Extraction, Purification and Properties of Aequorin, a Bioluminescent Protein from the Luminous Hydromedusan, Aequorea*. J Cell Physio, 1962. 59(3).
- [25] Chalfie M. et al, *Green Fluorescent Protein as a Marker for Gene Expression*. Science, 1994. 263.
- [26] Patterson G., Day R.N., and Piston D.W., *Fluorescent Protein Spectra*. J Cell Sci, 2001. 114(5): p. 837-8.
- [27] Heim R., Prasher D.C., and Tsien R.Y., *Wavelength Mutations and Posttranslational Autoxidation of Green Fluorescent Protein*. Proc Natl Acad Sci U S A, 1994. 91: p. 12501-4.
- [28] Matz M.V. et al, *Fluorescent Proteins from Nonbioluminescent Anthozoa Species*. Nat Biotechnol, 1999. 17.
- [29] Day R.N. and Davidson M.W., *The Fluorescent Protein Palette: Tools for Cellular Imaging*. Chem Soc Rev, 2009. 38(10): p. 2887-921.
- [30] Brown J.K. et al, *Primary Antibody-Fab Fragment Complexes: A Flexible Alternative to Traditional Direct and Indirect Immunolabeling Techniques*. J Histochem Cytochem, 2004. 52(9): p. 1219-30.
- [31] Huston J.S. et al, *Protein Engineering of Antibody Binding Sites: Recovery of Specific Activity in an Anti-Digoxin Single-Chain Fv Analogue Produced in Escherichia Coli*. Proc Natl Acad Sci U S A, 1988. 85: p. 5879-83.
- [32] Zlatanova J. and van Holde K., *Single-Molecule Biology: What Is It and How Does It Work?* Mol Cell, 2006. 24(3): p. 317-29.
- [33] Basche T., Nie S., and Fernandez J.M., *Single Molecules*. Proc Natl Acad Sci U S A, 2001. 98(19): p. 10527-8.
- [34] Schrödinger E., *Are There Quantum Jumps?* Brit J Philo Sci, 1952. 3(11): p. 233-42.
- [35] Gimzewski J.K. and Joachim C., *Nanoscale Science of Single Molecules Using Local Probes*. Science, 1999. 283: p. 1683-8.
- [36] Weiss S., *Fluorescence Spectroscopy of Single Biomolecules*. Science, 1999. 283: p. 1676-83.
- [37] Hirschfeld T., *Optical Microscopic Observation of Single Small Molecules*. Applied Optics, 1976. 15(12).
- [38] Moerner W.E. and Kador L., *Finding a Single Molecule in a Haystack: Optical Detection and Spectroscopy of Single Absorbers in Solids*. Anal Chem, 1989. 81(21).
- [39] Brooks Shera E. et al, *Detection of Single Fluorescent Molecules*. Chem Phys Lett, 1990. 174(6).
- [40] Moerner W.E. and Kador L., *Optical Detection and Spectroscopy of Single Molecules in a Solid*. Phys Rev Lett, 1989. 62(21): p. 2535-2538.

- [41] Dickson R.M. et al, *Three-Dimensional Imaging of Single Molecules Solvated in Pores of Poly(Acrylamide) Gels*. Science, 1996. 274: p. 966-9.
- [42] Schmidt T. et al, *Characterization of Photophysics and Mobility of Single Molecules in a Fluid Lipid Membrane*. J Phys Chem, 1995. 99: p. 17662-8.
- [43] Funatsu T. et al, *Imaging of Single Fluorescent Molecules and Individual Atp Turnovers by Single Myosin Molecules in Aqueous Solution*. Nature, 1995. 374: p. 555-9.
- [44] Vale R.D. et al, *Direct Observation of Single Kinesin Molecules Moving Along Microtubules*. Nature, 1996. 380: p. 451-3.
- [45] Ambrose K.J., *A Surface Contact Microscope for the Study of Cell Movements*. Nature, 1956. 178.
- [46] Axelrod D., *Cell-Substrate Contacts Illuminated by Total Internal Reflection Fluorescence*. The Journal of Cell Biology, 1981. 89(1): p. 141-145.
- [47] Martin-Fernandez M.L., Tynan C.J., and Webb S.E., *A 'Pocket Guide' to Total Internal Reflection Fluorescence*. J Microsc, 2013. 252(1): p. 16-22.
- [48] Tokunaga M., Imamoto N., and Sakata-Sogawa K., *Highly Inclined Thin Illumination Enables Clear Single-Molecule Imaging in Cells*. Nat Methods, 2008. 5(2).
- [49] Huygens C., *Traite De La Lumiere*. 1690.
- [50] Kubitscheck U., *Fluorescence Microscopy - from Principles to Biological Applications*. 2013, Weinheim, Germany: Wiley-Blackwell.
- [51] Airy G.B., *On the Diffraction of an Object-Glass with Circular Aperture*. Trans Cam Phil Soc, 1835. 5: p. 283-91.
- [52] Lord Rayleigh F.R.S., *Investigations in Optics, with Special Reference to the Spectroscope*. Phil Mag S, 1879. 8(49).
- [53] Wallace W., Schaefer L.H., and Swedlow J.R. *Resolution Criteria and Performance Issues*. 31.8.2018]; Available from: <https://www.olympus-lifescience.com/ko/microscope-resource/primer/digitalimaging/deconvolution/deconresolution/>.
- [54] Sigal Y.M., Zhou R., and Zhuang X., *Visualizing and Discovering Cellular Structures with Super-Resolution Microscopy*. Science, 2018. 361: p. 880-7.
- [55] Huang B., Bates M., and Zhuang X., *Super-Resolution Fluorescence Microscopy*. Annu Rev Biochem, 2009. 78: p. 993-1016.
- [56] Seyforth J., *Realisation of a Digitally Scanned Laser Light Sheet Fluorescent Microscope with Determination of the System Resolution*, in Department of Physics. 2016, King's College London: London.
- [57] Shroff H. et al. *Fitting Single-Molecule Pixel Data to a Gaussian Function*. Practical Aspects of PALM imaging 31.8.2018]; Available from: <http://zeiss-campus.magnet.fsu.edu/articles/superresolution/palm/practicalaspects.html>.
- [58] Gelles J., Schnapp B.J., and Sheetz M.P., *Tracking Kinesin-Driven Movements with Nanometre-Scale Precision*. Nature, 1988. 331.
- [59] Yildiz A. et al, *Myosin V Walks Hand-over-Hand: Single Fluorophore Imaging with 1.5-Nm Localization*. Science, 2003. 300.

- [60] Pertsinidis A., Zhang Y., and Chu S., *Subnanometre Single-Molecule Localization, Registration and Distance Measurements*. Nature, 2010. 466(7306): p. 647-51.
- [61] Thompson R.E., Larson D.R., and Webb W.W., *Precise Nanometer Localization Analysis for Individual Fluorescent Probes*. Biophys J, 2002. 82: p. 2775-83.
- [62] Quan T., Zeng S., and Huang Z.L., *Localization Capability and Limitation of Electron-Multiplying Charge-Coupled, Scientific Complementary Metal-Oxide Semiconductor, and Charge-Coupled Devices for Superresolution Imaging*. J Biomed Opt, 2010. 15(6).
- [63] Betzig E. et al, *Imaging Intracellular Fluorescent Proteins at Nanometer Resolution*. Science, 2006. 313.
- [64] Rust M.J., Bates M., and Zhuang X., *Sub-Diffraction-Limit Imaging by Stochastic Optical Reconstruction Microscopy (Storm)*. Nat Methods, 2006. 3(10): p. 793-5.
- [65] Vogelsang J. et al, *A Reducing and Oxidizing System Minimizes Photobleaching and Blinking of Fluorescent Dyes*. Angew Chem Int Ed Engl, 2008. 47(29): p. 5465-9.
- [66] Heilemann M. et al, *Subdiffraction-Resolution Fluorescence Imaging with Conventional Fluorescent Probes*. Angew Chem Int Ed Engl, 2008. 47(33): p. 6172-6.
- [67] Dickson R.M. et al, *On/Off Blinking and Switching Behaviour of Single Molecules of Green Fluorescent Protein*. Nature, 1997. 388(6640): p. 355-358.
- [68] Patterson G. and Lippincott-Schwartz J., *A Photoactivatable Gfp for Selective Photolabeling of Proteins and Cells*. Science, 2002. 297: p. 1873-7.
- [69] Henderson J.N. et al, *Structure and Mechanism of the Photoactivatable Green Fluorescent Protein*. J A C S, 2009. 131: p. 4176-7.
- [70] Subach F.V. et al, *Photoactivatable Mcherry for High-Resolution Two-Color Fluorescence Microscopy*. Nat Methods, 2009. 6(2): p. 153-9.
- [71] Chudakov D.M. et al, *Photoswitchable Cyan Fluorescent Protein for Protein Tracking*. Nat Biotechnol, 2004. 22(11): p. 1435-9.
- [72] Chudakov D.M., Lukyanov S., and Lukyanov K.A., *Tracking Intracellular Protein Movements Using Photoswitchable Fluorescent Proteins Ps-Cfp2 and Dendra2*. Nat Protoc, 2007. 2(8): p. 2024-32.
- [73] Zhang M. et al, *Rational Design of True Monomeric and Bright Photoactivatable Fluorescent Proteins*. Nat Methods, 2012. 9(7): p. 727-9.
- [74] Ando R., Mizuno H., and Miyasaka M., *Regulated Fast Nucleocytoplasmic Shuttling Observed by Reversible Protein Highlighting*. Science, 2004. 306: p. 1370-3.
- [75] Sharonov A. and Hochstrasser R.M., *Wide-Field Subdiffraction Imaging by Accumulated Binding of Diffusing Probes*. Proc Natl Acad Sci U S A, 2006. 103(50): p. 18911-6.
- [76] Jungmann R. et al, *Single-Molecule Kinetics and Super-Resolution Microscopy by Fluorescence Imaging of Transient Binding on DNA Origami*. Nano Lett, 2010. 10(11): p. 4756-61.

- [77] Hell S.W. and Wichmann J., *Breaking the Diffraction Resolution Limit by Stimulated Emission: Stimulated-Emission-Depletion Fluorescence Microscopy*. *Opt Lett*, 1994. 19(11): p. 780-3.
- [78] Klar T.A. et al, *Fluorescence Microscopy with Diffraction Resolution Barrier Broken by Stimulated Emission*. *Proc Natl Acad Sci U S A*, 2000. 97(15).
- [79] Einstein A., *Zur Quantentheorie Der Strahlung*. *Phys Z*, 1916. 18: p. 121-8.
- [80] Klar T.A., Engel E., and Hell S.W., *Breaking Abbe's Diffraction Resolution Limit in Fluorescence Microscopy with Stimulated Emission Depletion Beams of Various Shapes*. *Physical Review E*, 2001. 64(6).
- [81] Vicidomini G., Bianchini P., and Diaspro A., *Sted Super-Resolved Microscopy*. *Nat Methods*, 2018. 15(3): p. 173-182.
- [82] Westphal V. and Hell S.W., *Nanoscale Resolution in the Focal Plane of an Optical Microscope*. *Phys Rev Lett*, 2005. 94(14): p. 143903.
- [83] Berg J.M., Tymoczko J.K., and Stryer L., *Biochemistry*. 5th ed. 2002, New York: W H Freeman.
- [84] Wieser S. and Schutz G.J., *Tracking Single Molecules in the Live Cell Plasma Membrane-Do's and Don't's*. *Methods*, 2008. 46(2): p. 131-40.
- [85] Sprague B.L. and McNally J.G., *Frap Analysis of Binding: Proper and Fitting*. *Trends Cell Biol*, 2005. 15(2): p. 84-91.
- [86] Eggeling C. et al, *Direct Observation of the Nanoscale Dynamics of Membrane Lipids in a Living Cell*. *Nature*, 2009. 457(7233): p. 1159-62.
- [87] Lenne P.-F. et al, *Dynamic Molecular Confinement in the Plasma Membrane by Microdomains and the Cytoskeleton Meshwork*. *EMBO J*, 2006. 25: p. 3245-3256.
- [88] Wawrezynieck L. et al, *Fluorescence Correlation Spectroscopy Diffusion Laws to Probe the Submicron Cell Membrane Organization*. *Biophys J*, 2005. 89(6): p. 4029-42.
- [89] Honigsmann A. et al, *Scanning Sted-Fcs Reveals Spatiotemporal Heterogeneity of Lipid Interaction in the Plasma Membrane of Living Cells*. *Nat Commun*, 2014. 5: p. 5412.
- [90] Schneider F. et al, *Nanoscale Spatio-Temporal Diffusion Modes Measured by Simultaneous Confocal and Sted Imaging*. *Nano Lett*, 2018.
- [91] Dushek O. and van der Merwe P.A., *An Induced Rebinding Model of Antigen Discrimination*. *Trends Immunol*, 2014. 35(4): p. 153-8.
- [92] Moertelmaier M. et al, *Thinning out Clusters While Conserving Stoichiometry of Labeling*. *Applied Physics Letters*, 2005. 87(26): p. 263903.
- [93] Brameshuber M. et al, *Imaging of Mobile Long-Lived Nanoplatfoms in the Live Cell Plasma Membrane*. *J Biol Chem*, 2010. 285(53): p. 41765-71.
- [94] Ruprecht V., Brameshuber M., and Schütz G.J., *Two-Color Single Molecule Tracking Combined with Photobleaching for the Detection of Rare Molecular Interactions in Fluid Biomembranes*. *Soft Matter*, 2010. 6(3): p. 568-581.
- [95] Ta H. et al, *Experimental Approach to Extend the Range for Counting Fluorescent Molecules Based on Photon-Antibunching*. *Phys Chem Chem Phys*, 2010. 12(35): p. 10295-300.

- [96] Sykora J. et al, *Exploring Fluorescence Antibunching in Solution to Determine the Stoichiometry of Molecular Complexes*. Anal Chem, 2007. 79: p. 4040-9.
- [97] Kimble H.J., Dagenais M., and Mandel L., *Photon Antibunching in Resonance Fluorescence*. Physical Review Letters, 1977. 39(11): p. 691-695.
- [98] Basche T. et al, *Photon Antibunching in the Fluorescence of a Single Dye Molecule Trapped in a Solid*. Phys Rev Lett, 1992. 69(10): p. 1516-1519.
- [99] Sykora J. et al, *Exploring Fluorescence Antibunching in Solution to Determine the Stoichiometry of Molecular Complexes*. Anal Chem, 2007. 79: p. 4040-49.
- [100] Förster T., *Zwischenmolekulare Energiewanderung Und Fluoreszenz*. Ann Phys, 1948. 2: p. 55-75.
- [101] Bastiaens P.I.H. and Jovin T.M., *Microspectroscopic Imaging Tracks the Intracellular Processing of a Signal Transduction Protein: Fluorescent-Labeled Protein Kinase C Beta1*. Proc Natl Acad Sci U S A, 1996. 93: p. 8407-12.
- [102] Szabo Jr. G. et al, *Epitope Mapping by Photobleaching Fluorescence Resonance Energy Transfer Measurements Using a Laser Scanning Microscope System*. Biophys J, 1992. 61: p. 661-70.
- [103] Uster P.S. and Pagano R.E., *Resonance Energy Transfer Microscopy: Observations of Membrane-Bound Fluorescent Probes in Model Membranes and in Living Cells*. J Cell Bio, 1986. 103: p. 1221-34.
- [104] Piston D.W. and Kremers G.J., *Fluorescent Protein FRET: The Good, the Bad and the Ugly*. Trends Biochem Sci, 2007. 32(9): p. 407-14.
- [105] van Rheejen J., Langeslag M., and Jalink K., *Correcting Confocal Acquisition to Optimize Imaging of Fluorescence Resonance Energy Transfer by Sensitized Emission*. Biophys J, 2004. 86: p. 2517-29.
- [106] Reth M., *Antigen Receptor Tail Clue*. Nat, 1989. 338: p. 383-4.
- [107] Love P.E. and Hayes S.M., *Itam-Mediated Signaling by the T-Cell Antigen Receptor*. Cold Spring Harb Perspect Biol, 2010. 2(6): p. a002485.
- [108] Blumberg R. et al, *Structure of the T-Cell Antigen Receptor: Evidence for Two Cd3 $\epsilon$  Subunits in the T-Cell Receptor-Cd3 Complex*. Proc Natl Acad Sci U S A, 1990. 87: p. 7220-7224.
- [109] de la Hera A. et al, *Structure of the T Cell Antigen Receptor (Tcr): Two Cd3 $\epsilon$  Subunits in a Functional Tcr/Cd3 Complex*. J Exp Med, 1991. 173: p. 7-17.
- [110] Wang J.-H. et al, *Atomic Structure of an Alphabeta T Cell Receptor (Tcr) Heterodimer in Complex with an Anti-Tcr Fab Fragment Derived from a Mitogenic Antibody*. EMBO J, 1998. 17(1): p. 10-26.
- [111] Call M.E. et al, *The Structure of the  $\zeta$  Transmembrane Dimer Reveals Features Essential for Its Assembly with the T Cell Receptor*. Cell, 2006. 127(2): p. 355-68.
- [112] Call M.E. et al, *The Organizing Principle in the Formation of the T Cell Receptor-Cd3 Complex*. Cell, 2002. 111: p. 967-979.
- [113] Kuhns M.S. et al, *Evidence for a Functional Sidedness to the  $\alpha$  $\beta$ Tcr*. Proc Natl Acad Sci U S A, 2010. 107(11): p. 5094-9.

- [114] Fernandez-Miguel G. et al, *Multivalent Structure of an  $\alpha\beta$  T Cell Receptor*. Proc Natl Acad Sci U S A, 1999. 96: p. 1547-1552.
- [115] Schamel W.W. et al, *Coexistence of Multivalent and Monovalent Tcrs Explains High Sensitivity and Wide Range of Response*. J Exp Med, 2005. 202(4): p. 493-503.
- [116] James J.R. et al, *The T Cell Receptor Triggering Apparatus Is Composed of Monovalent or Monomeric Proteins*. J Biol Chem, 2011. 286(37): p. 31993-2001.
- [117] Rutledge T. et al, *Transmembrane Helical Interactions:  $\zeta$  Chain Dimerization and Functional Association with the T Cell Antigen Receptor*. EMBO J, 1992. 11(9): p. 3245-3254.
- [118] Göbe T.W.F. and Bolliger L., *Cutting Edge: The Chicken Tcr  $\zeta$ -Chain Restores the Function of a Mouse T Cell Hybridoma*. J Immunol, 1998. 160: p. 1552-1554.
- [119] Caplan S. et al, *Cell-Surface-Expressed T-Cell Antigen-Receptor  $\zeta$  Chain Is Associated with the Cytoskeleton*. Proc Natl Acad Sci U S A, 1995. 92: p. 4768-4772.
- [120] Wucherpfennig K.W. et al, *Structural Biology of the T-Cell Receptor: Insights into Receptor Assembly, Ligand Recognition, and Initiation of Signaling*. Cold Spring Harb Perspect Biol, 2010. 2(4).
- [121] Kuhns M.S., Davis M.M., and Garcia K.C., *Deconstructing the Form and Function of the Tcr/Cd3 Complex*. Immunity, 2006. 24(2): p. 133-9.
- [122] Kuhns M.S. and Davis M.M., *Disruption of Extracellular Interactions Impairs T Cell Receptor-Cd3 Complex Stability and Signaling*. Immunity, 2007. 26(3): p. 357-69.
- [123] Geisler C., Kuhlmann J., and Rubin B., *Assembly, Intracellular Processing, and Expression at the Cell Surface of the Human  $\alpha\beta$  T Cell Receptor/Cd3 Complex - Function of the Cd3 $\zeta$  Chain*. J Immunol, 1989. 143(12): p. 4069-4077.
- [124] Minami Y. et al, *Building a Multichain Receptor: Synthesis, Degradation, and Assembly of the T-Cell Antigen Receptor*. Proc Natl Acad Sci USA, 1987. 84: p. 2688-2692.
- [125] Ashwell J.D. and Klausner R.D., *Genetic and Mutational Analysis of the T-Cell Antigen Receptor*. Annu Rev Immunol, 1990. 8: p. 139-167.
- [126] Weissman A.M. et al, *Role of the  $\zeta$  Chain in the Expression of the T Cell Antigen Receptor: Genetic Reconstitution Studies*. The EMBO J, 1989. 8(12): p. 3651-3656.
- [127] Sloan-Lancaster J. et al, *Zap-70 Association with T Cell Receptor  $\zeta$ : Fluorescence Imaging of Dynamic Changes Upon Cellular Stimulation*. J Cell Bio, 1998. 143(3): p. 613-624.
- [128] Dushek O. et al, *Effects of Intracellular Calcium and Actin Cytoskeleton on Tcr Mobility Measured by Fluorescence Recovery*. PLoS One, 2008. 3(12): p. 3913.
- [129] Lillemeier B.F. et al, *Tcr and Lat Are Expressed on Separate Protein Islands on T Cell Membranes and Concatenate During Activation*. Nat Immunol, 2010. 11(1): p. 90-6.



- [130] Ito Y., Sakata-Sogawa K., and Tokunaga M., *Multi-Color Single-Molecule Tracking and Subtrajectory Analysis for Quantification of Spatiotemporal Dynamics and Kinetics Upon T Cell Activation*. *Sci Rep*, 2017. 7(1): p. 6994.
- [131] Santos A.M. et al, *Capturing Resting T Cells: The Perils of Pll*. *Nat Immunol*, 2018.
- [132] Ponjavic A. et al, *Single-Molecule Light-Sheet Imaging of Suspended T Cells*. *Biophys J*, 2018. 114(9): p. 2200-2211.
- [133] Favier B. et al, *Tcr Dynamics on the Surface of Living T Cells*. *Int Immunol*, 2001. 13(12): p. 1525-1532.
- [134] Carr A.R. et al, *Three-Dimensional Super-Resolution in Eukaryotic Cells Using the Double-Helix Point Spread Function*. *Biophys J*, 2017. 112(7): p. 1444-1454.
- [135] James J.R. et al, *Single-Molecule Level Analysis of the Subunit Composition of the T Cell Receptor on Live T Cells*. *Proc Natl Acad Sci U S A*, 2007. 104(45): p. 17662-7.
- [136] Rheinlander A., Schraven B., and Bommhardt U., *Cd45 in Human Physiology and Clinical Medicine*. *Immunol Lett*, 2018. 196: p. 22-32.
- [137] Hermiston M.L., Xu Z., and Weiss A., *Cd45: A Critical Regulator of Signaling Thresholds in Immune Cells*. *Annu Rev Immunol*, 2003. 21: p. 107-37.
- [138] Charbonneau H. et al, *The Leukocyte Common Antigen (Cd45): A Putative Receptor-Linked Protein Tyrosine Phosphatase*. *Proc Natl Acad Sci U S A*, 1988. 85: p. 7182-6.
- [139] Salmond R.J. et al, *T-Cell Receptor Proximal Signaling Via the Src-Family Kinases, Lck and Fyn, Influences T-Cell Activation, Differentiation, and Tolerance*. *Immu Rev*, 2009. 228: p. 9-22.
- [140] Weiss A. and Littman D.R., *Signal Transduction by Lymphocyte Antigen Receptors*. *Cell*, 1994. 76: p. 263-274.
- [141] Zhang W. et al, *Lat: The Zap-70 Tyrosine Kinase Substrate That Links T Cell Receptor to Cellular Activation*. *Cell*, 1998. 92: p. 83-92.
- [142] Su X. et al, *Phase Separation of Signaling Molecules Promotes T Cell Receptor Signal Transduction*. *Science*, 2016. 352(6285).
- [143] Balagopalan L. et al, *The Linker for Activation of T Cells (Lat) Signaling Hub: From Signaling Complexes to Microclusters*. *J Biol Chem*, 2015. 290(44): p. 26422-9.
- [144] Brownlie R.J. and Zamoyska R., *T Cell Receptor Signalling Networks: Branched, Diversified and Bounded*. *Nat Rev Immunol*, 2013. 13(4): p. 257-69.
- [145] Bubeck Wardenburg J. et al, *Phosphorylation of Slp-76 by the Zap-70 Protein-Tyrosine Kinase Is Required for T-Cell Receptor Function*. *J Biol Chem*, 1996. 271(33): p. 19641-4.
- [146] Rowshanravan B., Halliday N., and Sansom D.M., *Ctla-4: A Moving Target in Immunotherapy*. *Blood*, 2018. 131(1): p. 58-67.
- [147] Hogg N., Patzak I., and Willenbrock F., *The Insider's Guide to Leukocyte Integrin Signalling and Function*. *Nat Rev Immunol*, 2011. 11(6): p. 416-26.

- [148] Jankowska K.I. et al, *Integrins Modulate T Cell Receptor Signaling by Constraining Actin Flow at the Immunological Synapse*. *Front Immunol*, 2018. 9: p. 25.
- [149] Monks C.R.F. et al, *Three-Dimensional Segregation of Supramolecular Activation Clusters in T Cells*. *Nature*, 1998. 395.
- [150] Freiberg B.A. et al, *Staging and Resetting T Cell Activation in Smacs*. *Nat Immunol*, 2002. 3(10): p. 911-7.
- [151] Rhee S.G., *Regulation of Phosphoinositide-Specific Phospholipase C*. *Annu Rev Biochem*, 2001. 70: p. 281-312.
- [152] Schulze-Luehrmann J. and Ghosh S., *Antigen-Receptor Signaling to Nuclear Factor Kappa B*. *Immunity*, 2006. 25(5): p. 701-15.
- [153] Joseph N., Reicher B., and Barda-Saad M., *The Calcium Feedback Loop and T Cell Activation: How Cytoskeleton Networks Control Intracellular Calcium Flux*. *Biochim Biophys Acta*, 2014. 1838(2): p. 557-68.
- [154] Abbas A.K. et al, *Revisiting Il-2: Biology and Therapeutic Prospects*. *Sci Immunol*, 2018. 3.
- [155] Lever M. et al, *Architecture of a Minimal Signaling Pathway Explains the T-Cell Response to a 1 Million-Fold Variation in Antigen Affinity and Dose*. *Proc Natl Acad Sci U S A*, 2016: p. E6630-8.
- [156] Manz B.N. et al, *Small Molecule Inhibition of Csk Alters Affinity Recognition by T Cells*. *Elife*, 2015. 4.
- [157] McKeithan T.W., *Kinetic Proofreading in T-Cell Receptor Signal Transduction*. *PNAS*, 1995. 92: p. 5042-6.
- [158] Yousefi O.S. et al, *Optogenetic Control Shows That Kinetic Proofreading Regulates the Activity of the T Cell Receptor*. *bioRxiv*, 2018.
- [159] Springer T.A., *Adhesion Receptors of the Immune System*. *Nature*, 1990. 346.
- [160] Van der Merwe P.A. et al, *Cytoskeletal Polarization and Redistribution of Cell-Surface Molecules During T Cell Antigen Recognition*. *Semin Immunol*, 2000. 12: p. 5-21.
- [161] Secrist J.P. et al, *Stimulatory Effects of the Protein Tyrosine Phosphatase Inhibitor, Pervanadate, on T-Cell Activation Events*. *J Biol Chem*, 1993. 268(8): p. 5886-93.
- [162] Penninger J.M. et al, *Cd45: New Jobs for an Old Acquaintance*. *Nat Immunol*, 2001. 2(5).
- [163] Davis S.J. and Van der Merwe P.A., *The Structure and Ligand Interactions of Cd2: Implications for T-Cell Function*. *Immu Today*, 1996. 17(4).
- [164] Reiser J.-B. et al, *A T Cell Receptor Cdr3beta Loop Undergoes Conformational Changes of Unprecedented Magnitude Upon Binding to a Peptide/Mhc Class I Complex*. *Immunity*, 2002. 16: p. 345-54.
- [165] Aivazian D. and Stern L.J., *Phosphorylation of T Cell Receptor  $\zeta$  Is Regulated by a Lipid Dependent Folding Transition*. *Nat Struct Bio*, 2000. 7(11): p. 1023-1026.
- [166] Xu C. et al, *Regulation of T Cell Receptor Activation by Dynamic Membrane Binding of the Cd3epsilon Cytoplasmic Tyrosine-Based Motif*. *Cell*, 2008. 135(4): p. 702-13.

- [167] Ma Y. et al, *A FRET Sensor Enables Quantitative Measurements of Membrane Charges in Live Cells*. Nat Biotechnol, 2017. 35(4): p. 363-370.
- [168] Filipp D., Ballek O., and Manning J., *Lck, Membrane Microdomains, and Tcr Triggering Machinery: Defining the New Rules of Engagement*. Front Immunol, 2012. 3: p. 155.
- [169] Swamy M. et al, *A Cholesterol-Based Allosteric Model of T Cell Receptor Phosphorylation*. Immunity, 2016. 44(5): p. 1091-101.
- [170] Aramesh M. et al, *Engineering T-Cell Activation for Immunotherapy by Mechanical Forces*. Current Opinion in Biomedical Engineering, 2019.
- [171] Feng Y. et al, *Mechanosensing Drives Acuity of Alphabeta T-Cell Recognition*. Proc Natl Acad Sci U S A, 2017.
- [172] Das D.K. et al, *Force-Dependent Transition in the T-Cell Receptor Beta-Subunit Allosterically Regulates Peptide Discrimination and Pmhc Bond Lifetime*. Proc Natl Acad Sci U S A, 2015. 112(5): p. 1517-22.
- [173] Klotzsch E. et al, *Do Mechanical Forces Contribute to Nanoscale Membrane Organisation in T Cells?* Biochim Biophys Acta, 2014.
- [174] Lee M.S. et al, *A Mechanical Switch Couples T Cell Receptor Triggering to the Cytoplasmic Juxtamembrane Regions of Cd3zetazeta*. Immunity, 2015. 43(2): p. 227-39.
- [175] Singer S.J. and Nicolson G.L., *The Fluid Mosaic Model of the Structure of Cell Membranes*. Science, 1972. 175: p. 726.
- [176] van Meer G., *Sorting of Sphingolipids in Epithelial (Madin-Darby Canine Kidney) Cells*. The Journal of Cell Biology, 1987. 105(4): p. 1623-1635.
- [177] Lingwood D. and Simons K., *Lipid Rafts as a Membrane-Organizing Principle*. Science, 2010. 327(5961): p. 46-50.
- [178] Kusumi A. et al, *Hierarchical Mesoscale Domain Organization of the Plasma Membrane*. Trends Biochem Sci, 2011. 36(11): p. 604-15.
- [179] Klotzsch E. and Schutz G.J., *A Critical Survey of Methods to Detect Plasma Membrane Rafts*. Philos Trans R Soc Lond B Biol Sci, 2013. 368(1611): p. 20120033.
- [180] Sevcsik E. et al, *Gpi-Anchored Proteins Do Not Reside in Ordered Domains in the Live Cell Plasma Membrane*. Nat Commun, 2015. 6: p. 6969.
- [181] Sevcsik E. and Schutz G.J., *With or without Rafts? Alternative Views on Cell Membranes*. Bioessays, 2015.
- [182] Sheetz M.P., *Membrane Skeletal Dynamics: Role in Modulation of Red Cell Deformability, Mobility of Transmembrane Proteins, and Shape*. Semin Hematol, 1983. 20: p. 175-88.
- [183] Kusumi A. et al, *Paradigm Shift of the Plasma Membrane Concept from the Two-Dimensional Continuum Fluid to the Partitioned Fluid: High-Speed Single-Molecule Tracking of Membrane Molecules*. Annu Rev Biophys Biomol Struct, 2005. 34: p. 351-78.
- [184] Lillemeier B.F. et al, *Plasma Membrane-Associated Proteins Are Clustered into Islands Attached to the Cytoskeleton*. Proc Natl Acad Sci U S A, 2006. 103(50): p. 18992-7.

- [185] Sherman E. et al, *Functional Nanoscale Organization of Signaling Molecules Downstream of the T Cell Antigen Receptor*. *Immunity*, 2011. 35(5): p. 705-20.
- [186] Rossy J. et al, *Conformational States of the Kinase Lck Regulate Clustering in Early T Cell Signaling*. *Nat Immunol*, 2013. 14(1): p. 82-9.
- [187] Roh K.-H. et al, *The Coreceptor Cd4 Is Expressed in Distinct Nanoclusters and Does Not Colocalize with T-Cell Receptor and Active Protein Tyrosine Kinase P56lck*. *Proc Natl Acad Sci U S A*, 2015.
- [188] Molnar E. et al, *Cholesterol and Sphingomyelin Drive Ligand-Independent T-Cell Antigen Receptor Nanoclustering*. *J Biol Chem*, 2012. 287(51): p. 42664-74.
- [189] Campi G., Varma R., and Dustin M.L., *Actin and Agonist Mhc-Peptide Complex-Dependent T Cell Receptor Microclusters as Scaffolds for Signaling*. *J Exp Med*, 2005. 202(8): p. 1031-6.
- [190] Kumar R. et al, *Increased Sensitivity of Antigen-Experienced T Cells through the Enrichment of Oligomeric T Cell Receptor Complexes*. *Immunity*, 2011. 35(3): p. 375-87.
- [191] Pagoon S.V. et al, *Functional Role of T-Cell Receptor Nanoclusters in Signal Initiation and Antigen Discrimination*. *Proc Natl Acad Sci U S A*, 2016. 113(37): p. E5454-63.
- [192] Cai H. et al, *Full Control of Ligand Positioning Reveals Spatial Thresholds for T Cell Receptor Triggering*. *Nat Nanotechnol*, 2018.
- [193] Huppa J.B. et al, *Continuous T Cell Receptor Signaling Required for Synapse Maintenance and Full Effector Potential*. *Nat Immunol*, 2003. 4(8): p. 749-55.
- [194] Zhong S. et al, *Retroviral Transduction of T-Cell Receptors in Mouse T-Cells*. *J Vis Exp*, 2010. 44.
- [195] Huppa J.B. et al, *Tcr-Peptide-Mhc Interactions in Situ Show Accelerated Kinetics and Increased Affinity*. *Nature*, 2010. 463(7283): p. 963-7.
- [196] Fairhead M. et al, *Plug-and-Play Pairing Via Defined Divalent Streptavidins*. *J Mol Biol*, 2014. 426(1): p. 199-214.
- [197] Howarth M. et al, *A Monovalent Streptavidin with a Single Femtomolar Biotin Binding Site*. *Nature methods*, 2006. 3(4): p. 267-273.
- [198] Abberior G. *Recommended Labeling Protocols*. 2019 [cited 2019 18.06.2019]; Available from: [https://www.abberior.com/site/assets/files/1857/20120316-labeling\\_protocol-1.pdf](https://www.abberior.com/site/assets/files/1857/20120316-labeling_protocol-1.pdf).
- [199] Chevallet M., Luche S., and Rabilloud T., *Silver Staining of Proteins in Polyacrylamide Gels*. *Nat. Protocols*, 2006. 1(4): p. 1852-1858.
- [200] Stratagene. *Quikchange Site-Directed Mutagenesis Kit*. 2019 [cited 2019 18.06.2019]; Available from: [https://www.chemistry.mcmaster.ca/berti/safety/Manuals/Quikchange\\_Stratagene.pdf](https://www.chemistry.mcmaster.ca/berti/safety/Manuals/Quikchange_Stratagene.pdf).
- [201] Gao Y. and Kilfoil M.L., *Accurate Detection and Complete Tracking of Large Populations of Features in Three Dimensions*. *Optical Express*, 2009. 17(6): p. 4685-704.

- [202] Ovesny M. et al, *Thunderstorm: A Comprehensive ImageJ Plug-in for Palm and Storm Data Analysis and Super-Resolution Imaging*. *Bioinformatics*, 2014. 30(16): p. 2389-90.
- [203] Schütz G.J., Schindler H., and Schmidt T., *Single-Molecule Microscopy on Model Membranes Reveals Anomalous Diffusion*. *Biophys J*, 1997. 73: p. 1073-80.
- [204] Baumgart F. et al, *Varying Label Density Allows Artifact-Free Analysis of Membrane-Protein Nanoclusters*. *Nat Methods*, 2016. 13(8): p. 661-4.
- [205] Sengupta P. et al, *Probing Protein Heterogeneity in the Plasma Membrane Using Palm and Pair Correlation Analysis*. *Nat Methods*, 2011. 8(11): p. 969-75.
- [206] Gestwicki J.E. et al, *Influencing Receptor-Ligand Binding Mechanisms with Multivalent Ligand Architecture*. *J A C S*, 2002. 124: p. 14922-33.
- [207] Goldstein B. and Wiegel F.W., *The Effect of Receptor Clustering on Diffusion-Limited Forward Rate Constants*. *Biophys J*, 1983. 43: p. 121-5.
- [208] Shoup D. and Szabo A., *Role of Diffusion in Ligand Binding to Macromolecules and Cell-Bound Receptors*. *Biophys J*, 1982. 40: p. 33-9.
- [209] Adler J. et al, *Plasma Membrane Topography and Interpretation of Single-Particle Tracks*. *Nat Methods*, 2010. 7(3): p. 170-1.
- [210] Mazia D., *Adhesion of Cells to Surfaces Coated with Polylysine. Applications to Electron Microscopy*. *The Journal of Cell Biology*, 1975. 66(1): p. 198-200.
- [211] Ono S., Ohno H., and Saito T., *Rapid Turnover of the Cd3 $\zeta$  Chain Independent of the Tcr-Cd3 Complex in Normal T Cells*. *Immunity*, 1995. 2: p. 639-644.
- [212] Exley M. et al, *Evidence for Multivalent Structure of T-Cell Antigen Receptor Complex*. *Mol Immunol*, 1995. 32(11): p. 829-39.
- [213] Yarden Y. and Schlessinger J., *Epidermal Growth Factor Induces Rapid, Reversible Aggregation of the Purified Epidermal Growth Factor Receptor*. *Biochemistry*, 1987. 26: p. 1443-51.
- [214] Krogsgaard M. et al, *Agonist/Endogeneous Peptide-Mhc Heterodimers Drive T Cell Activation and Sensitivity*. *Nature*, 2005. 434(7030): p. 238-243.
- [215] Tang Q. et al, *The Src Family Kinase Fyn Mediates Signals Induced by Tcr Antagonists*. *The Journal of Immunology*, 2002. 168(9): p. 4480-4487.
- [216] Cochran J.R., Cameron T.O., and Stern L.J., *The Relationship of Mhc-Peptide Binding and T Cell Activation Probed Using Chemically Defined Mhc Class II Oligomers*. *Immunity*, 2000. 12: p. 241-50.
- [217] Brameshuber M. and Schutz G.J., *Detection and Quantification of Biomolecular Association in Living Cells Using Single-Molecule Microscopy*. *Methods Enzymol*, 2012. 505: p. 159-86.
- [218] Varma R. et al, *T Cell Receptor-Proximal Signals Are Sustained in Peripheral Microclusters and Terminated in the Central Supramolecular Activation Cluster*. *Immunity*, 2006. 25(1): p. 117-27.
- [219] Xie J. et al, *Photocrosslinkable Pmhc Monomers Stain T Cells Specifically and Cause Ligand-Bound Tcrs to Be 'Preferentially' Transported to the Csmac*. *Nat Immunol*, 2012. 13(7): p. 674-80.

- [220] Sunyer R. et al, *The Temperature Dependence of Cell Mechanics Measured by Atomic Force Microscopy*. *Phys Biol*, 2009. 6(2): p. 025009.
- [221] Fang C. et al, *Determination of the Temperature-Dependent Cell Membrane Permeabilities Using Microfluidics with Integrated Flow and Temperature Control*. *Lab Chip*, 2017. 17(5): p. 951-960.
- [222] Weiss K. et al, *Quantifying the Diffusion of Membrane Proteins and Peptides in Black Lipid Membranes with 2-Focus Fluorescence Correlation Spectroscopy*. *Biophys J*, 2013. 105(2): p. 455-62.
- [223] Bag N., Yap D.H.X., and Wohland T., *Temperature Dependence of Diffusion in Model and Live Cell Membranes Characterized by Imaging Fluorescence Correlation Spectroscopy*. *Biochimica et Biophysica Acta (BBA) - Biomembranes*, 2014. 1838(3): p. 802-813.
- [224] van der Meer B.W., *Kappa-Squared: From Nuisance to New Sense*. *Mol Biotech*, 2002. 82: p. 181-96.
- [225] Brown J.H. et al, *Three-Dimensional Structure of the Human Class II Histocompatibility Antigen Hla-Dr1*. *Nature*, 1993. 364.
- [226] Jardetzky T.S. et al, *Three-Dimensional Structure of a Human Class II Histocompatibility Molecule Complexed with Superantigen*. *Nature*, 1994. 368: p. 711-8.
- [227] Schafer P.H. and Pierce S.K., *Evidence for Dimers of Mhc Class II Molecules in B Lymphocytes and Their Role in Low Affinity T Cell Responses*. *Immunity*, 1994. 1: p. 699-707.
- [228] Reich Z. et al, *Ligand-Specific Oligomerization of T-Cell receptor Molecules*. *Nat Lett*, 1997. 387.
- [229] Dushek O. and Coombs D., *Analysis of Serial Engagement and Peptide-Mhc Transport in T Cell Receptor Microclusters*. *Biophys J*, 2008. 94(9): p. 3447-60.
- [230] Jung Y. et al, *Three-Dimensional Localization of T-Cell Receptors in Relation to Microvilli Using a Combination of Superresolution Microscopies*. *Proc Natl Acad Sci U S A*, 2016.
- [231] Hu Y.S., Cang H., and Lillemeier B.F., *Superresolution Imaging Reveals Nanometer- and Micrometer-Scale Spatial Distributions of T-Cell Receptors in Lymph Nodes*. *Proc Natl Acad Sci U S A*, 2016. 113(26): p. 7201-6.
- [232] Annibale P. et al, *Identification of Clustering Artifacts in Photoactivated Localization Microscopy*. *Nat Methods*, 2011. 8(7): p. 527-8.
- [233] Annibale P. et al, *Quantitative Photo Activated Localization Microscopy: Unraveling the Effects of Photoblinking*. *PLoS One*, 2011. 6(7): p. e22678.
- [234] Montero D. et al, *Intracellular Glutathione Pools Are Heterogeneously Concentrated*. *Redox Biol*, 2013. 1: p. 508-13.
- [235] Owen D.M. et al, *Palm Imaging and Cluster Analysis of Protein Heterogeneity at the Cell Surface*. *J Biophotonics*, 2010. 3(7): p. 446-54.
- [236] Rubin-Delanchy P. et al, *Bayesian Cluster Identification in Single-Molecule Localization Microscopy Data*. *Nat Methods*, 2015. 12(11): p. 1072-6.
- [237] Paparelli L. et al, *Inhomogeneity Based Characterization of Distribution Patterns on the Plasma Membrane*. *PLoS Comput Biol*, 2016. 12(9): p. e1005095.

- [238] Ripley B.D., *Modelling Spatial Patterns*. J Royal Stat Soc: B Meth, 1977. 39(2): p. 172-212.
- [239] Dixon P.M., *Ripley's K Function*. Encyclopedia of Environmetrics, 2002. 3: p. 1796-1803.
- [240] Kiskowski M.A., Hancock J.F., and Kenworthy A.K., *On the Use of Ripley's K-Function and Its Derivatives to Analyze Domain Size*. Biophys J, 2009. 97(4): p. 1095-103.
- [241] Petersen N.O. et al, *Quantitation of Membrane Receptor Distributions by Image Correlation Spectroscopy: Concept and Application*. Biophys J, 1993. 65: p. 1135-46.
- [242] Wiseman P.W., *Image Correlation Spectroscopy: Principles and Applications*. Cold Spring Harb Protoc, 2015. 2015(4): p. 336-48.
- [243] Lee S.H. et al, *Counting Single Photoactivatable Fluorescent Molecules by Photoactivated Localization Microscopy (Palm)*. Proc Natl Acad Sci U S A, 2012. 109(43): p. 17436-41.
- [244] Coltharp C., Kessler R.P., and Xiao J., *Accurate Construction of Photoactivated Localization Microscopy (Palm) Images for Quantitative Measurements*. PLoS One, 2012. 7(12): p. e51725.
- [245] Puchner E.M. et al, *Counting Molecules in Single Organelles with Superresolution Microscopy Allows Tracking of the Endosome Maturation Trajectory*. Proc Natl Acad Sci U S A, 2013. 110(40): p. 16015-20.
- [246] Fricke F. et al, *One, Two or Three? Probing the Stoichiometry of Membrane Proteins by Single-Molecule Localization Microscopy*. Sci Rep, 2015. 5: p. 14072.
- [247] Zanicchi F.C. et al, *A DNA Origami Platform for Quantifying Protein Copy Number in Super-Resolution*. Nat Methods, 2017.
- [248] Habuchi S. et al, *Reversible Single-Molecule Photoswitching in the Gfp-Like Fluorescent Protein Dronpa*. Proc Natl Acad Sci U S A, 2005. 102(27): p. 9511-6.
- [249] Hummer G., Fricke F., and Heilemann M., *Model-Independent Counting of Molecules in Single-Molecule Localization Microscopy*. Mol Biol Cell, 2016. 27: p. 3637-44.
- [250] Vandenberg W. et al, *Diffraction-Unlimited Imaging: From Pretty Pictures to Hard Numbers*. Cell Tissue Res, 2015. 360(1): p. 151-78.
- [251] Almada P. et al, *Automating Multimodal Microscopy with Nanofluidics*. bioRxiv, 2018.
- [252] Douglass K.M. et al, *Super-Resolution Imaging of Multiple Cells by Optimised Flat-Field Epi-Illumination*. Nat Photonics, 2016. 10(11): p. 705-708.
- [253] Beghin A. et al, *Localization-Based Super-Resolution Imaging Meets High-Content Screening*. Nat Methods, 2017.
- [254] Yasui M. et al, *Automated Single-Molecule Imaging in Living Cells*. Nat Commun, 2018. 9(1): p. 3061.
- [255] Ouyang W. et al, *Deep Learning Massively Accelerates Super-Resolution Localization Microscopy*. Nature Biotechnology, 2018.
- [256] Nehme E. et al, *Deep-Storm: Super-Resolution Single-Molecule Microscopy by Deep Learning*. Optica, 2018. 5(4): p. 458.

- [257] Li Y. et al, *Dlbi: Deep Learning Guided Bayesian Inference for Structure Reconstruction of Super-Resolution Fluorescence Microscopy*. Bioinformatics, 2018. 34(13): p. i284-i294.
- [258] Boyd N. et al, *Deeploco: Fast 3d Localization Microscopy Using Neural Networks*. bioRxiv, 2018.
- [259] Tanaka K.A. et al, *Membrane Molecules Mobile Even after Chemical Fixation*. Nat Methods, 2010. 7(11): p. 865-6.
- [260] Whelan D.R. and Bell T.D., *Image Artifacts in Single Molecule Localization Microscopy: Why Optimization of Sample Preparation Protocols Matters*. Sci Rep, 2015. 5: p. 7924.
- [261] Pereira P.M. et al, *Fix Your Membrane Receptor Imaging: Actin Cytoskeleton and Cd4 Membrane Organization Disruption by Chemical Fixation*. BioRxiv, 2018.
- [262] van de Linde S. et al, *Direct Stochastic Optical Reconstruction Microscopy with Standard Fluorescent Probes*. Nat Protoc, 2011. 6(7): p. 991-1009.
- [263] Scalia C.R. et al, *Antigen Masking During Fixation and Embedding, Dissected*. J Histochem Cytochem, 2017. 65(1): p. 5-20.
- [264] Klockenbusch C. and Kast J., *Optimization of Formaldehyde Cross-Linking for Protein Interaction Analysis of Non-Tagged Integrin Beta1*. J Biomed Biotechnol, 2010. 2010: p. 927585.
- [265] Ester M. et al, *A Density-Based Algorithm for Discovering Clusters in Large Spatial Databases with Noise*. Proceedings of the Second International Conference on Knowledge Discovery and Data Mining (KDD-96), 1996.
- [266] Scarselli M., Annibale P., and Radenovic A., *Cell Type-Specific Beta2-Adrenergic Receptor Clusters Identified Using Photoactivated Localization Microscopy Are Not Lipid Raft Related, but Depend on Actin Cytoskeleton Integrity*. J Biol Chem, 2012. 287(20): p. 16768-80.
- [267] Jayasinghe I. et al, *True Molecular Scale Visualization of Variable Clustering Properties of Ryanodine Receptors*. Cell Rep, 2018. 22(2): p. 557-567.
- [268] Williamson D.J. et al, *Pre-Existing Clusters of the Adaptor Lat Do Not Participate in Early T Cell Signaling Events*. Nat Immunol, 2011. 12(7): p. 655-62.
- [269] Gudheti M.V. et al, *Actin Mediates the Nanoscale Membrane Organization of the Clustered Membrane Protein Influenza Hemagglutinin*. Biophys J, 2013. 104(10): p. 2182-92.
- [270] Mattila P.K. et al, *The Actin and Tetraspanin Networks Organize Receptor Nanoclusters to Regulate B Cell Receptor-Mediated Signaling*. Immunity, 2013. 38(3): p. 461-74.
- [271] Levet F. et al, *Sr-Tesseler: A Method to Segment and Quantify Localization-Based Super-Resolution Microscopy Data*. Nat Methods, 2015. 12(11): p. 1065-71.
- [272] Oszmiana A. et al, *The Size of Activating and Inhibitory Killer Ig-Like Receptor Nanoclusters Is Controlled by the Transmembrane Sequence and Affects Signaling*. Cell Rep, 2016. 15: p. 1957-72.
- [273] Burgert A. et al, *Characterization of Plasma Membrane Ceramides by Super-Resolution Microscopy*. Angew Chem Int Ed Engl, 2017. 56(22): p. 6131-6135.



- [274] Balint S., Lopes F.B., and Davis D.M., *A Nanoscale Reorganization of the Il-15 Receptor Is Triggered by Nkg2d in a Ligand-Dependent Manner*. *Sci Signal*, 2018. 11.
- [275] Lopes F.B. et al, *Membrane Nanoclusters of Fcγm1 Segregate from Inhibitory SIRPα Upon Activation of Human Macrophages*. *J Cell Biol*, 2017. 216(4): p. 1123-1141.
- [276] Rahbek-Clemmensen T. et al, *Super-Resolution Microscopy Reveals Functional Organization of Dopamine Transporters into Cholesterol and Neuronal Activity-Dependent Nanodomains*. *Nat Commun*, 2017. 8(1): p. 740.
- [277] Chandra Maity P. et al, *B Cell Antigen Receptors of the Igm and Igd Classes Are Clustered in Different Protein Islands That Are Altered During B Cell Activation*. *Sci Signal*, 2015. 8(394).
- [278] Shelby S.A. et al, *Functional Nanoscale Coupling of Lyn Kinase with Ige-FcεR1 Is Restricted by the Actin Cytoskeleton in Early Antigen-Stimulated Signaling*. *MBoC*, 2016. 27: p. 3645-59.
- [279] Wasim L. et al, *N-Linked Glycosylation Regulates Cd22 Organization and Function*. *Frontiers in Immunology*, 2019. 10.
- [280] Culley S. et al, *Quantitative Mapping and Minimization of Super-Resolution Optical Imaging Artifacts*. *Nat Methods*, 2018.
- [281] Kellner R.R. et al, *Nanoscale Organization of Nicotinic Acetylcholine Receptors Revealed by Stimulated Emission Depletion Microscopy*. *Neuroscience*, 2007. 144(1): p. 135-43.
- [282] Broadhead M.J. et al, *Psd95 Nanoclusters Are Postsynaptic Building Blocks in Hippocampus Circuits*. *Sci Rep*, 2016. 6: p. 24626.
- [283] Torreno-Pina J.A. et al, *The Actin Cytoskeleton Modulates the Activation of Inkt Cells by Segregating Cd1d Nanoclusters on Antigen-Presenting Cells*. *PNAS*, 2015.
- [284] Martinez-Munoz L. et al, *Separating Actin-Dependent Chemokine Receptor Nanoclustering from Dimerization Indicates a Role for Clustering in Cxcr4 Signaling and Function*. *Mol Cell*, 2018. 70(1): p. 106-119 e10.
- [285] Manzo C. et al, *Psf Decomposition of Nanoscopy Images Via Bayesian Analysis Unravels Distinct Molecular Organization of the Cell Membrane*. *Sci Rep*, 2014. 4: p. 4354.
- [286] Fritzsche M. et al, *Cytoskeletal Actin Dynamics Shape a Ramifying Actin Network Underpinning Immunological Synapse Formation*. *Sci Adv*, 2017. 3.
- [287] Choudhuri K. et al, *Polarized Release of T-Cell-Receptor-Enriched Microvesicles at the Immunological Synapse*. *Nature*, 2014. 507(7490): p. 118-23.
- [288] Baumgart F., Schneider M., and Schütz G., *How T Cells Do the 'Search for the Needle in the Haystack'*. *Front Phys*, 2019. 7.
- [289] Fearnley D.B. et al, *Monitoring Human Blood Dendritic Cell Numbers in Normal Individuals and in Stem Cell Transplantation*. *Blood*, 1999. 93(2): p. 728-36.
- [290] Sykulev Y. et al, *Evidence That a Single Peptide-Mhc Complex on a Target Cell Can Elicit a Cytolytic T Cell Response*. *Immunity*, 1996. 4: p. 565-72.

- [291] Huang J. et al, *A Single Peptide-Major Histocompatibility Complex Ligand Triggers Digital Cytokine Secretion in Cd4(+) T Cells*. *Immunity*, 2013. 39(5): p. 846-57.
- [292] Irvine D.J. et al, *Direct Observation of Ligand Recognition by T Cells*. *Nat Lett*, 2002. 419.
- [293] Harding C.V. and Unanue E.R., *Quantitation of Antigen-Presenting Cell Mhc Class Ii/Peptide Complexes Necessary for T-Cell Stimulation*. *Nature*, 1990. 346.
- [294] Maimon O. and Rokach L., *Data Mining and Knowledge Discovery Handbook*. 2005: Springer.
- [295] Usherwood E.J., Hogg T.L., and Woodland D.L., *Enumeration of Antigen-Presenting Cells in Mice Infected with Sendai Virus*. *J Immunol*, 1999. 162: p. 3350-5.
- [296] Krummel M.F., Bartumeus F., and Gerard A., *T Cell Migration, Search Strategies and Mechanisms*. *Nat Rev Immunol*, 2016. 16(3): p. 193-201.
- [297] Miller M.J. et al, *Autonomous T Cell Trafficking Examined in Vivo with Intravital Two-Photon Microscopy*. *Proc Natl Acad Sci U S A*, 2003. 100(5): p. 2604-9.
- [298] Fooksman D.R. et al, *Functional Anatomy of T Cell Activation and Synapse Formation*. *Annu Rev Immunol*, 2010. 28: p. 79-105.
- [299] Davis S.J. and van der Merwe P.A., *The Kinetic-Segregation Model: Tcr Triggering and Beyond*. *Nat Immunol*, 2006. 7(8): p. 803-809.
- [300] Chang V.T. et al, *Initiation of T Cell Signaling by Cd45 Segregation at 'Close Contacts'*. *Nat Immunol*, 2016. 17(5): p. 574-582.
- [301] McKeithan T.W., *Kinetic Proofreading in T-Cell Receptor Signal Transduction*. *Proc Natl Acad Sci U S A*, 1995. 92: p. 5042-6.
- [302] Lever M. et al, *Phenotypic Models of T Cell Activation*. *Nat Rev Immunol*, 2014. 14(9): p. 619-29.
- [303] Su X. et al, *Phase Separation of Signaling Molecules Promotes T Cell Receptor Signal Transduction*. *Science*, 2016. 352(6285).
- [304] Huang W.Y.C. et al, *Phosphotyrosine-Mediated Lat Assembly on Membranes Drives Kinetic Bifurcation in Recruitment Dynamics of the Ras Activator Sos*. *Proc Natl Acad Sci U S A*, 2014. 113(29): p. 8218-23.
- [305] Klotzsch E. and Schutz G.J., *Improved Ligand Discrimination by Force-Induced Unbinding of the T Cell Receptor from Peptide-Mhc*. *Biophys J*, 2013. 104(8): p. 1670-5.
- [306] Liu B. et al, *Accumulation of Dynamic Catch Bonds between Tcr and Agonist Peptide-Mhc Triggers T Cell Signaling*. *Cell*, 2014. 157(2): p. 357-368.
- [307] Cai E. et al, *Visualizing Dynamic Microvillar Search and Stabilization During Ligand Detection by T Cells*. *Science*, 2017. 356(6338).
- [308] Qiu Y. et al, *Lateral Dynamics of Major Histocompatibility Complex Class Ii Molecules Bound with Agonist Peptide or Altered Peptide Ligands*. *Immunol Lett*, 1996. 53: p. 19-23.
- [309] Bousso P. and Robey E., *Dynamics of Cd8+ T Cell Priming by Dendritic Cells in Intact Lymph Nodes*. *Nat Immunol*, 2003. 4(6): p. 579-85.

- [310] Mempel T.R., Henricksen S.E., and von Andrian U.H., *T-Cell Priming by Dendritic Cells in Lymph Nodes Occurs in Three Distinct Phases*. *Nature*, 2004. 427.
- [311] Yokosuka T. et al, *Newly Generated T Cell Receptor Microclusters Initiate and Sustain T Cell Activation by Recruitment of Zap70 and Slp-76*. *Nat Immunol*, 2005. 6(12): p. 1253-62.
- [312] Hashimoto-Tane A. et al, *T-Cell Receptor Microclusters Critical for T-Cell Activation Are Formed Independently of Lipid Raft Clustering*. *Mol Cell Biol*, 2010. 30(14): p. 3421-9.
- [313] Mayya V. and Dustin M.L., *What Scales the T Cell Response?* *Trends Immunol*, 2016. 37(8): p. 513-522.
- [314] Marangoni F. et al, *The Transcription Factor Nfat Exhibits Signal Memory During Serial T Cell Interactions with Antigen-Presenting Cells*. *Immunity*, 2013. 38(2): p. 237-49.
- [315] Das J. et al, *Digital Signaling and Hysteresis Characterize Ras Activation in Lymphoid Cells*. *Cell*, 2009. 136(2): p. 337-51.